Enhancing Self-Sensing Estimation Accuracy Through Current Image Tracking

by

Timothy S. Slininger

A dissertation submitted in partial fulfillment

of the requirements for the degree of

Doctor of Philosophy

(Mechanical Engineering)

at the

University of Wisconsin-Madison

2020

Date of Final Exam: 04/13/2020

The dissertation is approved by the following members of the Final Oral Committee:

Peter Adamczyk, Assistant Professor, Mechanical Engineering

Thomas M. Jahns, Professor, Electrical and Computer Engineering

Daniel C. Ludois, Associate Professor, Electrical and Computer Engineering

Dan Negrut, Professor, Mechanical Engineering

Eric L. Severson, Assistant Professor, Electrical and Computer Engineering

Abstract

This work presents the development of methods for improving the estimation accuracy and bandwidth of self-sensing techniques which utilize a high frequency voltage injection and analyze the current response to estimate position. In particular a method is developed of accumulating time series current samples and applying image tracking methods to extract position information. The time samples are analyzed for properties of the high frequency current response which relate directly to rotor position. This project pays special attention to the generation of the current image, specifically selecting the reference frames used to isolate patterns with rotor position dependent properties. Pattern matching methods are applied to extract this information and associate it with a position to replace state-of-the-art heterodyning demodulation and improve estimation accuracy, increase system bandwidths, and remove lagging filters from the self-sensing system. To analyze the effectiveness of these methods, offline estimation accuracy using experimental data was performed, as well as online closed-loop simulation, and online closed-loop experiments all showing an improvement in estimation accuracy and bandwidth over state-of-the-art demodulation methods. This is due to the use of a template which associates current response with rotor position and captures non-ideal system properties without the need for further measurement and decoupling. To determine system properties when unexpected non-ideal inductance effects are present, as can be the case during machine faults, operating conditions, or due to aging the simulation was extended and results show graceful degradation of closed-loop error to a similar magnitude and phase of state-of-the-art demodulation.

Additionally, a method for modeling estimation errors due to speed effects related to the typically unmodeled stationary frame latch and reference frame transforms to

return to the synchronous frame is developed. A compensation method is proposed and evaluated in simulation.

Acknowledgements

First, I would like to thank Kimberly Slininger for being my normal force.

Secondly, I would like to thank my Advisor Professor Lorenz for giving me the opportunity to make the journey from Computer Science to Electro-Mechanical Engineering, for offering a never-ending fount of knowledge, and the best guidance a student could hope to receive.

Third, I would like to thank the WEMPEC Staff and Faculty for all their support through the entire process and in particular the challenges of the final year. In particular, Professor Dan Ludois and Jim Sember for their support in the last year of this project.

Finally, I would like to thank the staff and my colleagues at WEMPEC. The environment and vast amount of knowledge and resources available in these people made this work possible.

Table of Contents

List of Figures

List of Tables

Nomenclature

Symbol	Description
b_a or b_o	active or observer damping gain
b_p	viscous damping
i_{dq}	stator current complex space vector
J_p	inertia
k_{isa} or k_{iso}	active or observer integral spring gain
k_{sa} or k_{so}	active or observer spring gain
K_t	motor torque constant
L_d, L_q, L_{dq}	d-axis, q-axis, and cross-coupled stator inductance
R_s	stator resistance
T_d	torque disturbance
T_{delay}	computational delay
T_{em}	electro-mechanical torque
T_s	sample period
T_μ	Coulomb friction
v_{dq}	stator voltage complex space vector
λ_{pm}	Permanent magnet flux linkage
ω_r or ω_e	rotor electrical velocity
ω_m	rotor mechanical velocity

Superscripts

$(\ )^s$	stationary reference frame
$(\ )^r$	rotor reference frame
$(\ )^{\hat{r}}$	Estimated rotor reference frame
$(\ )^e$	excitation/synchronous reference frame
$(\ )^*$	commanded or reference quantity
$\bar{(\ )}$	average value

Subscripts

$(\ )_e$	rotor electrical
$(\ )_{rm}$	rotor mechanical
$(\ )_{dq}$	vector of the form $(\ )_q - j(\ )_d$ in the rotor reference frame
$(\ )_{\alpha\beta}$	vector of the form $(\ )_\alpha - j(\ )_\beta$ in the stationary reference frame
$(\ )_h$ or $(\ )_{hf}$	high frequency
$(\ )_c$	carrier
$(\ )_{cn}$	negative carrier portion of the signal

Abbreviations

AC	Alternating Current
AMR	Anisotropic Magnetoresistance
BPF	Band-pass Filter
CAST	Controls and Sensor Technologies
CVCR	Complex Vector Current Regulator
CW	Concentrated Windings
DB-DTFC	Deadbeat-Direct Torque and Flux Control
DC	Direct Current
DFT	Discrete Fourier Transform
DID	Disturbance Input Decoupling
DSP	Digital Signal Processor
DW	Distributed Windings
ELSO	Extended Luenberger-Style Observer
EMF	Electromotive Force
EV	Eigenvalue
FEA	Finite Element Analysis
FOC	Field Oriented Control
FPGA	Field Programmable Gate Array
FRF	Frequency Response Function
HF	High Frequency
HFI	High Frequency Injection
IPM	Interior Permanent Magnet
IPMSM	Interior Permanent Magnet Synchronous Machine
LPF	Low-pass Filter
LUT	Lookup Table
PI	Proportional-Integral
PM	Permanent Magnet
PNN	Probabilistic Neural Network
PWM	Pulse Width Modulation
PWM-VSI	Pulse Width Modulation – Voltage Source Inverter
RPM	Revolution Per Minute
SIFT	Scale-Invariant Feature Transform
SNR	Signal-to-Noise Ratio
SPM	Surface-mounted Permanent Magnet
SPMSM	Surface-mounted Permanent Magnet Synchronous Machine
SURF	Speeded Up Robust Features
WEMPEC	Wisconsin Electric Machines and Power Electronics Consortium

Introduction

This section provides research background and motivation, an overview of the research, and a chapter-by-chapter list of the material discussed in this report.

Research Motivation

Self-sensing methodologies have been researched for several decades and have been shown to be an acceptable sensor replacement particularly in high-speed cases that enable the use of back electromotive force (back-EMF) tracking. Removal of mechanical sensors allows for a reduction in cost, weight, and operational noise. However, in low-speed conditions, an external excitation of a spatially variant machine property is required to generate a position estimate.

All of these low-speed methods have relatively poor dynamic performance due to the extensive use of filters in the demodulation process, especially in low signal-to-noise ratio conditions such as those found in a surface-mounted permanent magnet synchronous machine SPMSM. Furthermore, estimation accuracy is relatively poor compared with traditional mechanical sensors, especially in the presence of non-ideal conditions such as cross-saturation, multiple saliencies, resistance, and inverter non-linearities.

Traditionally, high frequency injection based self-sensing has been focused on interior permanent magnet synchronous machines (IPMSM) and specially modified machines that induce a spatially variant inductance or resistance which can be tracked. Numerous projects have focused on creating small spatial saliencies in SPMSMs, typically through modification of the rotor. This allows for reuse of the simple SPMSM rotor structure and keeps production costs in check. Self-sensing with both inductive and resistive based methods were shown to be possible. However, they are both limited by the SPMSM's low saliency ratio as well as the multiple saliencies and cross-saturation which are load dependent in the machine.

Signal and image processing techniques often must deal with noisy environments and low signal-to-noise ratios. A number of methods have been utilized to extract small signals from environments with large amounts of noise. It is expected that by looking at the current response of a machine to a high frequency injection, image processing techniques will allow for improved estimation accuracy of rotor position. Furthermore, by considering a number of samples as an image it is expected that the number of filters required to successfully extract the signal will be reduced which will improve the dynamic capabilities of the system.

Overview

This work encompasses two main portions, both aimed at increasing the accuracy and bandwidth of self-sensing methods. The first deals with a modeling and compensation technique of the voltage latched in the stationary frame which is typically neglected and causes small position estimation errors. The second deals with the development and evaluation of self-sensing methods utilizing time series of the current response to a high frequency injection. This time series of a properly experimentally captured template is compared to samples collected in real time to generate position estimates. Results and analysis are presented for simulation, offline, as well as online experiments.

Research Contributions

The following list summarizes the key contributions made by this research.

- Analysis of the effects of the voltage latched in the stationary frame upon self-sensing methods.
- Development of a pattern-matching image tracking methodology utilizing a rotating vector injection in the stationary reference frame to perform position self-sensing.

- Comparison of the estimation accuracy, computational complexity, and system components of image tracking methodologies to traditional rotating and pulsating vector injection self-sensing methodologies.
- Documentation of non-ideal cross-saturation, multiple saliencies, resistance, and the stationary voltage latch effects upon the current image.
- Documentation of non-ideal effects on image tracking and comparison with traditional rotating self-sensing.
- Documentation of non-ideal effects which are not captured by the template, such as those which can arise from load dependent machine properties on image tracking.
- Documentation of relative performance in simulation, offline, and online experiments comparing heterodyning demodulation and image tracking methodologies.

Summary of Chapters

In Chapter 1, a state-of-the-art review is given on permanent magnet (PM) machine self-sensing methodologies, as well as the background required for image registration.

In Chapter 2, modeling of the effects of the stationary frame voltage latch on the current response to a pulsating voltage injection in the synchronous frame is provided. A method for compensating for these effects is developed and evaluated.

In Chapter 3 the development of a new form of position estimation via self-sensing is documented. This includes image formulation, effects of non-ideal and unmodeled inductances on the image and response, analysis of speed varying effects, and an analysis of the costs and tradeoffs associated with this method are presented.

In Chapter 4 the image tracking method is evaluated in simulation and offline experiments to demonstrate the viability and improvements of the method on a low-power, low-saliency, SPMSM.

In Chapter 5 the image tracking method is evaluated in simulation and online experiments to demonstrate the improvements of the method over existing methods on a 1.5kW, low-saliency, SPMSM.

In Chapter 6 presents key conclusions and contributions generated by this research. Recommended future work in the area of self-sensing and image tracking are discussed.

In 6.3Appendix A the development of the state-of-the-art control methods used in this project, as well as the experimental validation on a 13W low saliency SPMSM are provided.

In 6.3Appendix B the experimental validation of the control methods as well as evaluation of non-ideal conditions is provided for a 1.5kW low saliency SPMSM.

Chapter 1 State-of-the-Art Review

This chapter presents a summary of the state-of-the-art of position sensing. In general, position sensing is achieved with a standalone position sensor utilizing technology based on optics, electric machines, or the sensing of magnets. A newer field of self-sensing utilizes signals from the machine itself to estimate the rotor's position. These broadly fall into two categories, back-EMF tracking methods, which are suitable for medium-to-high speed applications, and high frequency injection (HFI) based methods, which are suitable in the zero-to-low speed range. Figure 1.1 shows a breakdown of the types of sensing which will be reviewed.

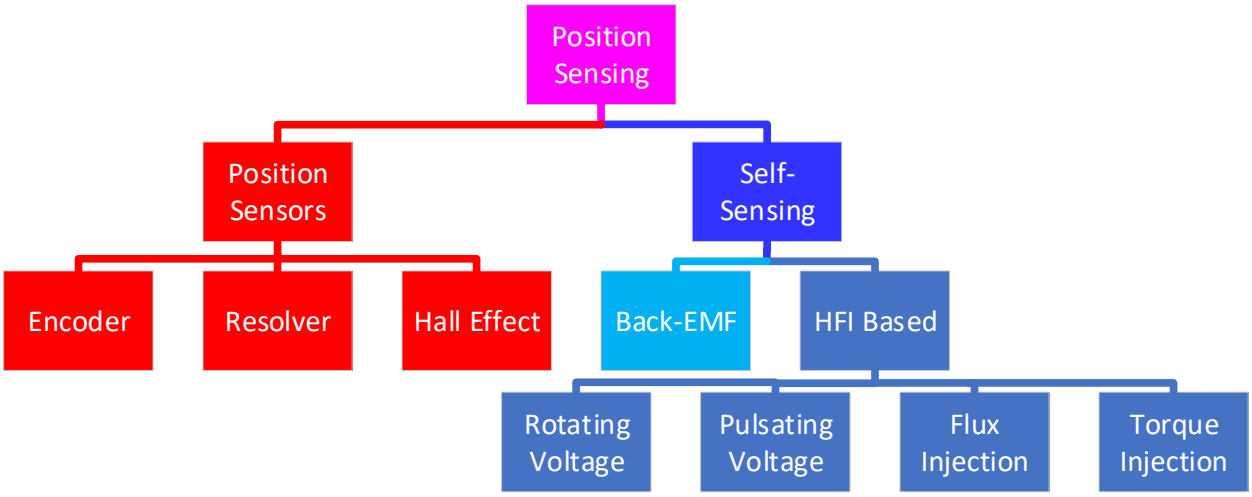

Figure 1.1 – Position sensing methods overview.

These technologies are well known and have been reviewed elsewhere [1-6]. This section will give a high-level overview to highlight the research opportunities available in the field. Detailed derivations of implemented methods based on the state of the art literature have been developed in 6.3Appendix A.

1.1 Position Sensors

1.1.1 Common Sensing Methods

a) 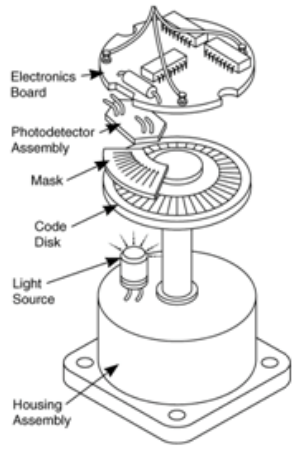

b) 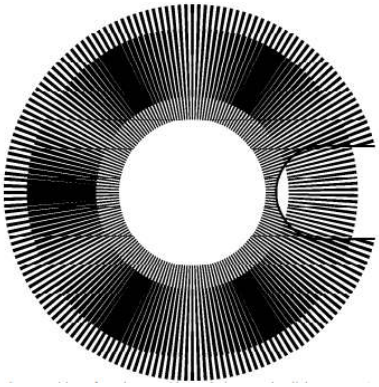

Figure 1.2 – Optical encoder, a) schematic [7], b) Moiré pattern created from interaction of disk and mask [8].

The optical encoder operates by generating a Moiré pattern and turns that pattern into a position. A light is shown through two specially slotted disks and the light intensity which passes through the disks is measured using a pair of photodetectors. One disk is attached to, and rotates with, the encoder shaft. The second disk is stationary in between the light source and the photodetectors, but mounted eccentrically from the rotating disk so that a Moiré pattern is formed resulting in a sinusoidally changing light intensity. This assembly is shown in Figure 1.2 a). An example of a Moiré pattern created between two full disks is shown in Figure 1.2 b). The position of the photodetectors is such that there is a 90° shift in the sinusoidal intensity measured between them and will form the signals A and B. The number of sinusoidal periods in a mechanical revolution equals the number of lines, N, on the code disk.

The output signals produced by an optical encoder can be either analog or digital. Analog signals are less common but will show the quadrature sinusoidal signals captured by the photodetectors as shown in Figure 1.3 and represented as a rotating vector in (1.1). More common is a digital incremental encoder which will convert the continuous sinusoidal signals

into discrete steps. Typically, this is further simplified to provide just a count of the number of steps the encoder moved either forward or backward by tracking the edges of the digital signals. This has the advantage of being easy to use, but limits the resolution to four times the number of lines on the code disk. If the analog signals are provided, vector tracking, as described in section [2, 4], can be applied with an increase in accuracy.

In Figure 1.3 the top signals are the quadrature signals A (blue) and B (red) as received by the photodetectors. The signals at the bottom are the discretized A (blue) and B (red). A single encoder line is shown, which represents 360/N° mechanical and can be decoded into an incremental count.

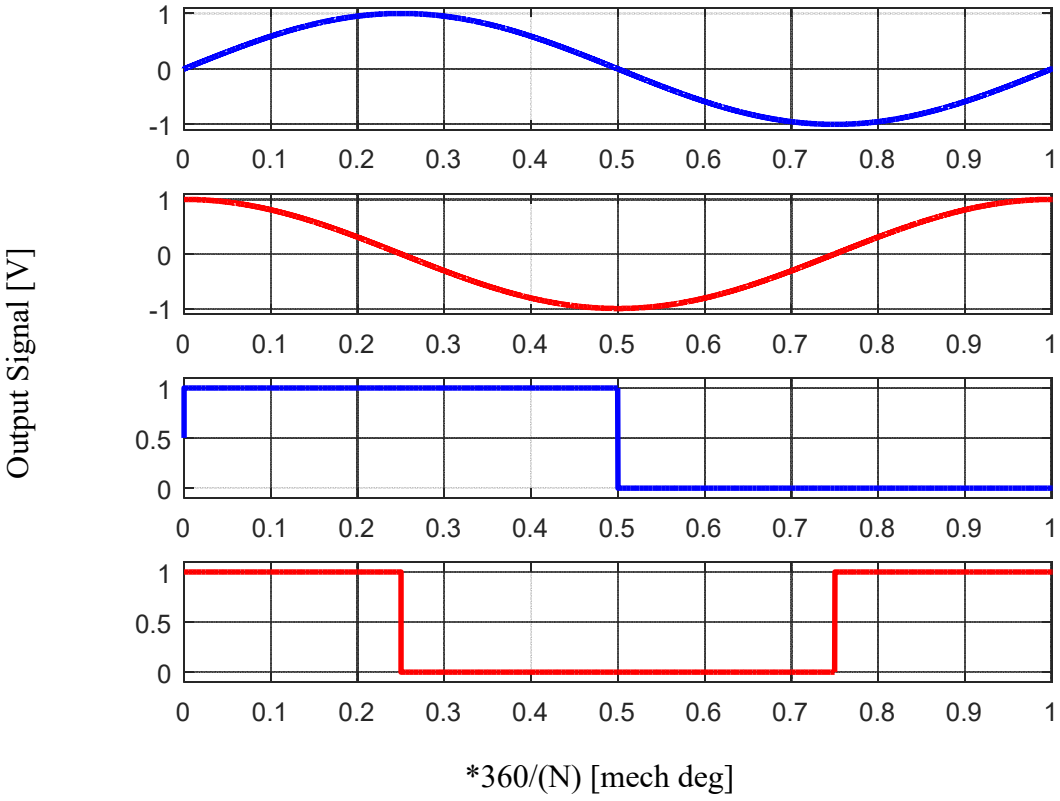

Figure 1.3 – Example analog and discretized signals in an optical encoder.

To decode a set of digital signals into an incremental count, the transitions at each edge must be considered [2]. The smallest increment which can be detected is described in (1.2) as

360° divided by four times the number of lines, due to the fact that each quadrant of a line can be detected. [9]

$$E_{\alpha\beta} = \cos(N\theta_{rm}) - j*\sin(N\theta_{rm}) \quad (1.1)$$

$$\theta_{inc} = \frac{360°}{(4*N)} \quad (1.2)$$

Resolvers operate on the same principle as electric machines. Namely the coupling of electromagnetic fields between sets of coils on the rotor and stator. Figure 1.4 shows a photo of a resolver a) and a diagram of a two-pole resolver with sin and cosine coils set in quadrature on the stator, and an excitation coil on the rotor which can be a commutated coil or magnetically coupled with the stator.

a)

b)

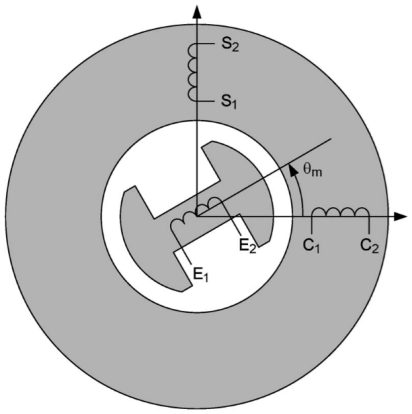

Figure 1.4 – Optical encoder, a) representative encoder and resolver sizing [10], b) resolver electrical diagram demonstrating quadrature sets of coils[11].

$$V_e = V_o\cos(\omega_c t) \quad (1.3)$$

$$V_c = V_o\cos(\omega_c t)\cos(\omega_{rm} t) \quad (1.4)$$

$$V_s = V_o\cos(\omega_c t)\sin(\omega_{rm} t) \quad (1.5)$$

$$V_{c2} = V_o\cos^2(\omega_c t)\cos(\omega_{rm} t) \quad (1.6)$$

$$V_{s2} = V_o\cos^2(\omega_c t)\sin(\omega_{rm} t) \quad (1.7)$$

If the rotor coil has an excitation signal of the form of (1.3), then the measured quadrature coupled voltages can be shown to be of the form of (1.4) and (1.5) with the assumption that the excitation frequency is significantly higher than the rotor frequency [12]. The goal is to isolate the position information from these measurements. Two of the most common methods for extracting this information are synchronous demodulation and convolution plus filtering. In synchronous demodulation, only the peaks of the waveform are sampled and as such the carrier cosine term is considered equal to one and drops out leaving just the rotor position dependent sine and cosine terms. Using a convolution-based method multiplies (1.4) and (1.5) by the carrier sinusoid again, resulting in (1.6) and (1.7) respectively. [12-17]

This process is shown in Figure 1.5 and is perhaps easiest understood in the frequency domain as shown in the right column. In Figure 1.5 a) the carrier signal with frequency 10 Hz is shown and has a peak in the frequency domain at the expected 10 Hz. The ideal quadrature signals with a rotor frequency of one Hz are shown in Figure 1.5 b). In Figure 1.5 c) the carrier and ideal signals are multiplied together in the time-domain and the corresponding convolution in the frequency domain is evident. Note that the envelope of the quadrature signals is still visible in the time-domain. In the case of synchronous demodulation, only the peaks are sampled which results in a sampled version of b). In Figure 1.5 d) the modulated signal from c) is again multiplied by the carrier frequency. The envelope is again plainly visible in the time-domain, and the convolved signals are shown in the frequency domain. It is also clear that the desired position signals have reappeared at the rotor frequency. The high frequency components will be at two times the carrier frequency and returning to our assumption that the carrier is significantly higher than the rotor speed, these signals can be separated. The most common way

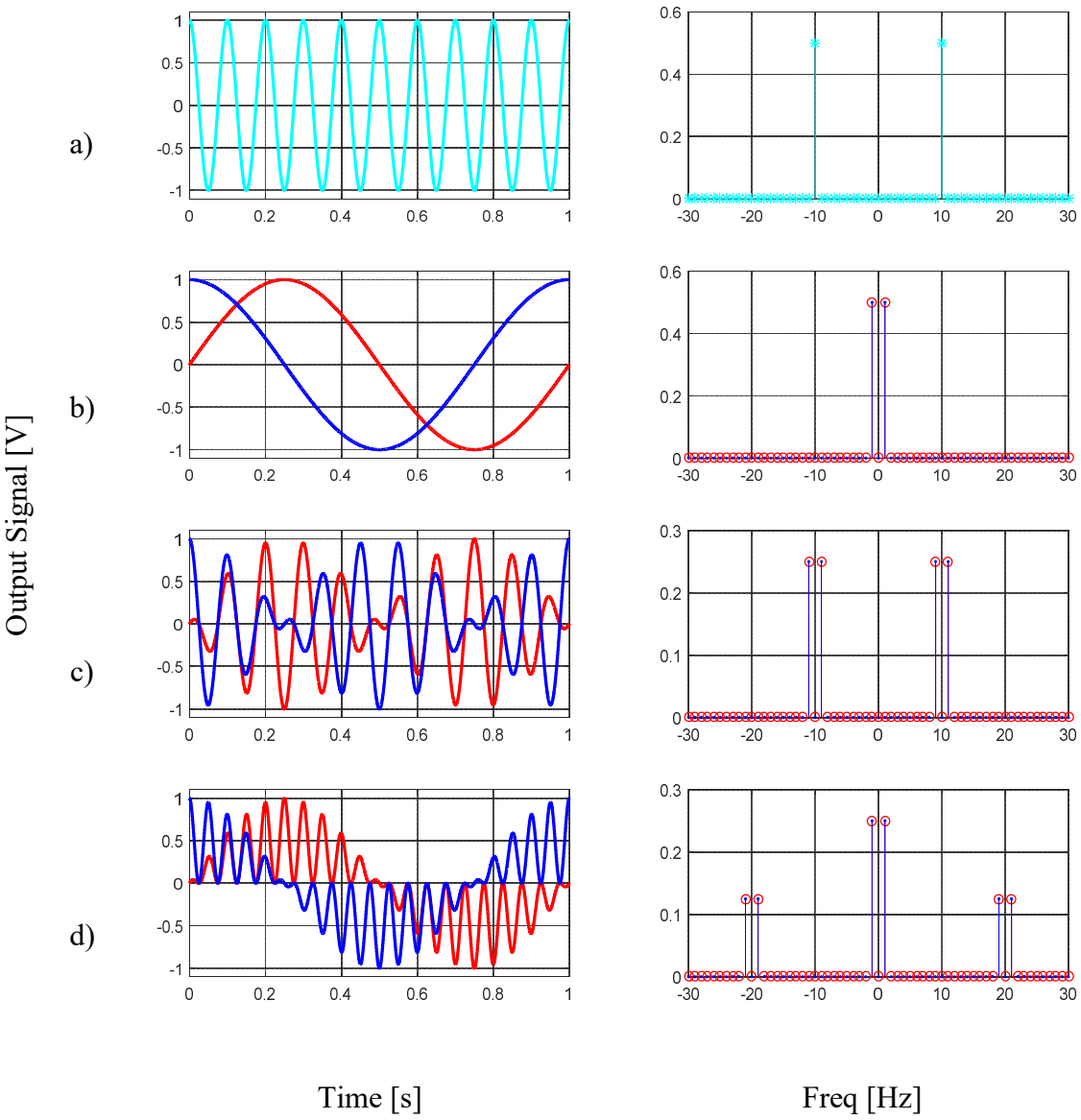

Figure 1.5 – Resolver modulation and demodulation signals in time and frequency domains.

to remove the undesired high frequency components is to create a low-pass filter with a break frequency below the carrier frequency. These higher frequency components are only a function of the carrier and should be well known, as such they can be directly decoupled. Once the sine and cosine terms are obtained by whatever method, vector tracking can be applied as described in [2] to determine the rotor position.

a) b)

Figure 1.6 – a) Shaft-end mounting allows for absolute angular measurement, b) Circumferential mounting allows for incremental angular measurement [18].

Anisotropic Magneto-Resistive (AMR) sensing takes advantage of the magneto-resistive properties of thin film permalloys. These AMRs are physically separated by 90 electrical degrees (quadrature) and placed into Wheatstone bridge configuration as discussed in [19].

Two magnetic configurations are applicable for rotary applications, one makes use of a shaft-end magnet attached as in Figure 1.6 a) and allows for absolute position measurement. The other configurations make use of magnets mounted to the circumference of a shaft and allow for incremental position as in Figure 1.6 b).

$$V_c = \cos(2\alpha) \quad (1.8)$$

$$V_s = \sin(2\alpha) \quad (1.9)$$

The outputs of the quadrature sensors will rotate at twice the rotor speed as in (1.8) and (1.9) which can be tracked using a vector tracking observer as described in [2, 4].

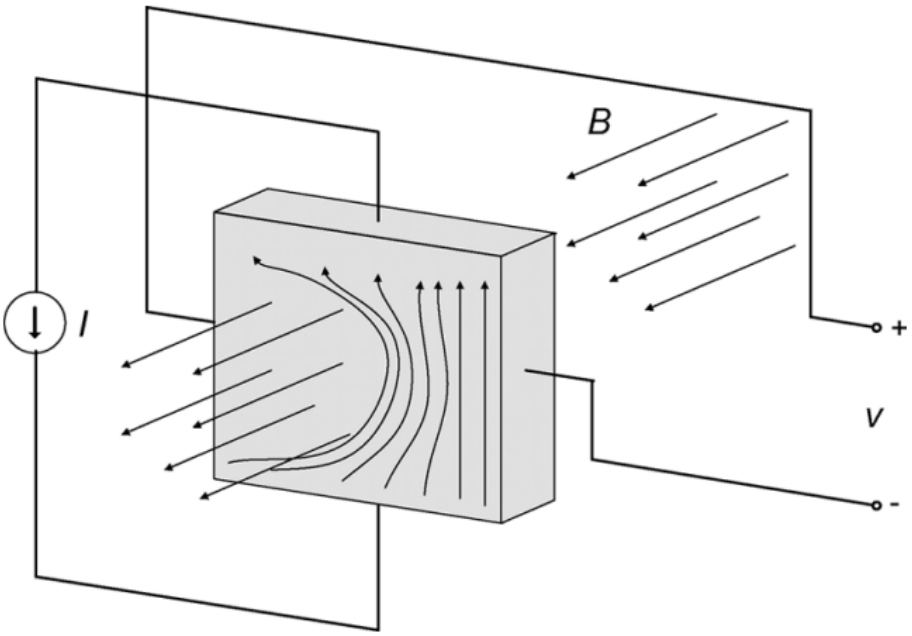

Figure 1.7 – A current flowing through a thin conductive material experiences a Lorentz force if an external magnetic field B is applied [20].

When a current I flows through a thin sheet of thickness d of conductive material, in a magnetic field with flux density B, a voltage V is generated perpendicular to the field and current as illustrated in (1.10) where R_H is a material dependent Hall coefficient described in (1.11). In (1.11), n is the carrier density and q is the charge of the current carrier and is valid for materials with either positive or negative charge carriers. In semiconductors the relationship is more complicated and simply defined by R_H [20].

$$V_H = \frac{I \times B}{nqd} = R_H \frac{I \times B}{d} \quad (1.10)$$

$$R_H = nq \quad (1.11)$$

A diagram of this process is shown in Figure 1.7. For position sensing, two sensors are placed in quadrature, over a magnetic pole pitch. This leads to the familiar situation where the analog signals produced from the two sensors are a sine and cosine signal which can be interpreted as a rotating vector and tracked using the vector tracking described in [21]. If digital signals are produced they lead to the same situation as with an incremental encoder and can be decoded in the same manner [2, 4, 20, 22-25].

1.1.2 Sensing Method Drawbacks

Table 1.1 shows commercially available devices with maximum accuracy and cost range at the time of this publication. It is clear that with commercially available devices accuracy of <0.002° can be achieved, however this accuracy comes with increased price and cheaper sensors universally provide lower accuracy. In many commercial devices cost is one of the largest driving factors and so being able to maintain an acceptable accuracy while decreasing cost is desirable. In many applications such as fans and pumps this is especially true where the machine is to supply a torque and the shaft position is only a concern in the control of the machine, not explicitly in the application itself. Other applications such as servo motors tend to demand higher accuracy, but in this case the position of a tool or joint is the variable directly under control and so position as well as torque are of concern.

Table 1.1 – Sensor Accuracy and Cost Comparison [26]

	Accuracy [Mech °]	Cost [$US March 2020]
Optical Encoder	0.0018-90	9 - 3700
Absolute Encoder	0.0014-10	41 - 2700
Resolver	0.09-15	200 - 700
Magnetic Encoder	0.022-90	35 - 300
Magnetoresistive	0.03-15	1.5-350
Hall Effect	0.9-15	1.5 - 350

A secondary concern is the bulk and mass associated with the sensors themselves. These parameters tend to be similar across sensing methods, but scale with application, particularly shaft size. This is a driving factor in many applications where additional mass must be transported and can reduce the overall system efficiency. The consideration of bulk is application dependent. Some applications, particularly high-speed applications, are particularly concerned with additional bulk as it means longer shafts and can impact the vibration modes of the product.

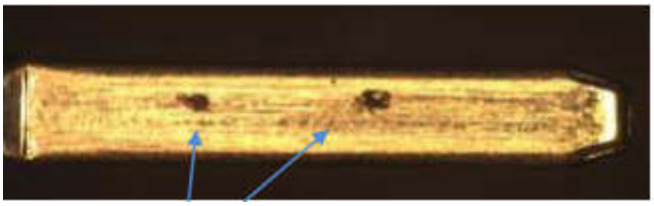

Figure 1.8 – Axial vibration induced fretting in blade connector [27].

In many applications the failure modes are a large concern. Particularly in drilling and manufacturing applications where a damage encoder may mean the loss of substantial operating costs while the sensor fault is diagnosed and replaced. These failure modes tend to involve the electrical connectors, which are a well-known failure source [28-33]. In high vibration environments the connectors tend to develop fretting as in Figure 1.8. This can change the impedance of the connector and in extreme cases can result in open or short circuits. Similarly, the connector housing can be damage and fail. This is a common concern regardless of sensing technology.

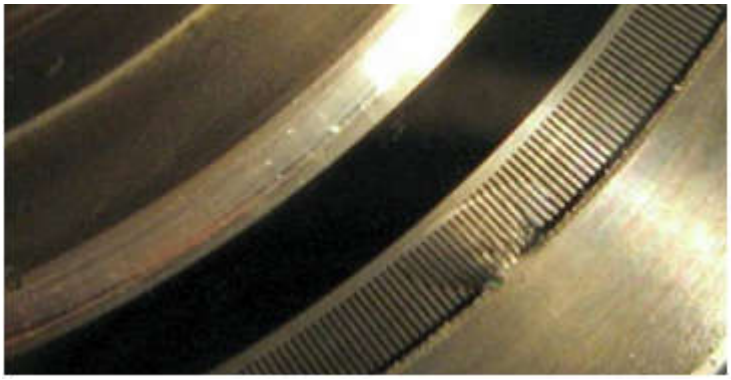

Figure 1.9 – Damaged glass optical encoder disk [34].

The use of rotating glass disks in close proximity results in optical encoders being sensitive to high vibration environments. Figure 1.9 shows the damage that can result to the optical disk. This sort of damage can decrease the accuracy near the damage, or if severe enough may prevent the device from working altogether.

Optical encoders tend to have additional sensitivities when compared to other sensing methods. Any infiltration of dust, oil, or other contaminants can decrease the accuracy or cause an outright failure [34].

1.2 Self-Sensing at High Speed

Self-sensing at high speed, relies on the back-EMF of the machine [23, 35-40]. Viewing the SPMSM machine equations in the stationary reference frame in (1.12) and (1.13) and modeling only the resistive and inductive loads, the back-EMF clearly rotates locked to the position of the rotor. By estimating the back-EMF as a disturbance voltage, a back-EMF state filter can be created as in Figure 1.10. The rotating voltage can then be tracked using a vector tracking method. [2, 4]

$$V_{\alpha\beta} = L_{\alpha\beta} I_{\alpha\beta} \frac{d}{dt} + R_s I_{\alpha\beta} + j\omega_e \lambda_{pm} e^{j\theta e} \tag{1.12}$$

$$E_{\alpha\beta} = \omega_e \lambda_{pm} \begin{bmatrix} \cos\theta_e \\ -\sin\theta_e \end{bmatrix} \tag{1.13}$$

Back-EMF tracking faces several known challenges. The most obvious can be observed from (1.13), namely that the back-EMF scales proportionally with speed. At higher speeds, the back-EMF is a relatively large signal, with a high signal to noise ratio, making it easy to measure and track. At low speeds, the back-EMF tends to be lost in system and sensor noise [36, 37]. Numerous secondary effects have been neglected in (1.12) which can degrade the position estimation. The effects of back-EMF harmonics was evaluated in [36, 37] and a vector tracking method including the harmonic tracking is shown in the full system back-EMF tracking diagram in Figure 1.10.

Additionally, cross-coupling due to latching and reference frame effects is often neglected in first approximations. These effects are proportional to speed and have been evaluated in [41].

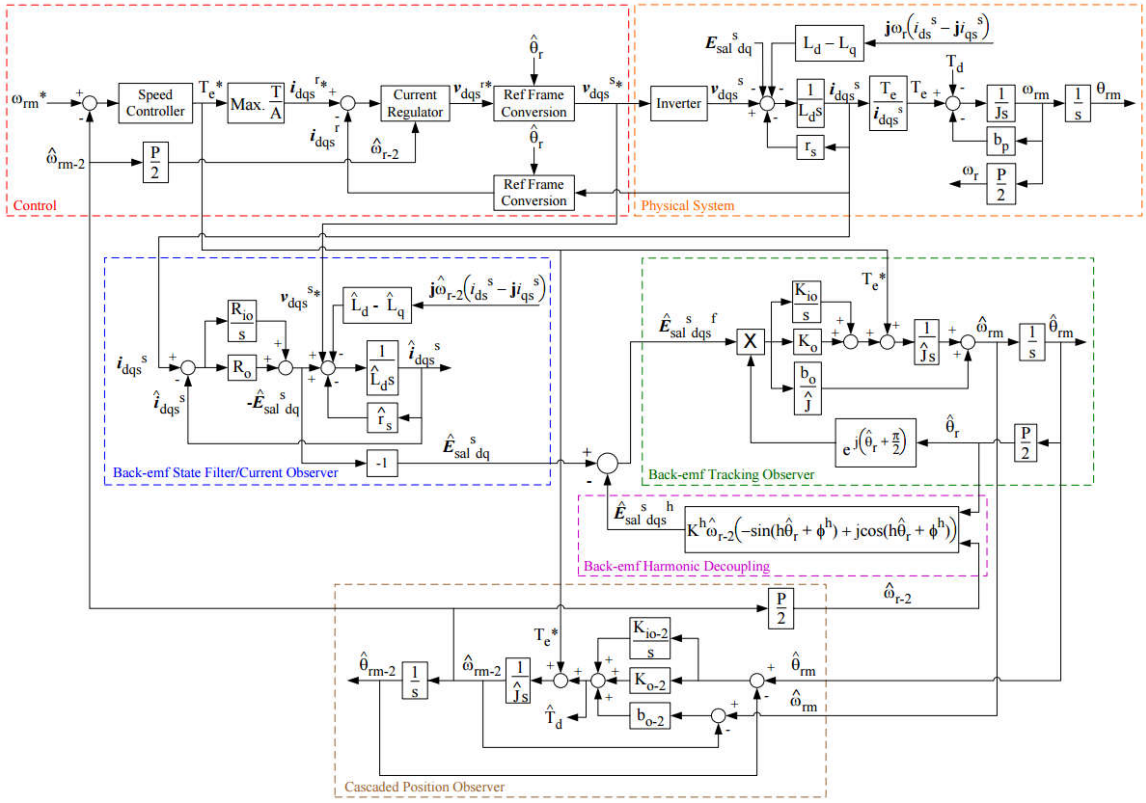

Figure 1.10 – State-block diagram of the implementation of harmonic decoupling with motion controller, physical system, and cascaded position observer shown from [37].

1.3 Self-Sensing at Low Speed

Back-EMF tracking tends to be robust at medium-to-high speed where the signal is large enough to be discerned from the sources of noise. However, at low speeds it suffers from poor signal-to-noise ratios and so other methods have been explored. The most common methods rely on exciting a position-dependent feature of the machine, such as a resistance or inductance variation (also called a saliency or anisotropy) [1, 5, 42, 43]. The most common methods inject either a rotating voltage into the stationary reference frame, or a pulsating voltage into the estimated synchronous reference frame. Numerous variations and extensions of these methods have been explored including increasing the injection frequency to half of the switching frequency as in square-wave injection [44], formulating the injection as a flux, as in flux injection [45-50], and more exotic forms combining features of both, such as pulsing injection

[51]. Additional methods rely on injection of an oscillating torque to generate a large enough back-EMF to track while tolerating system vibrations [52-55].

The major variations of stationary frame rotating voltage injection and estimated synchronous frame pulsating voltage injection will be briefly reviewed to demonstrate their operating principles, strengths and weaknesses. Full derivations of the operating methods and implementations can be found in 6.3Appendix A.

1.3.1 Stationary Frame Rotating Voltage Injection

Rotating vector injection makes use of an injection into the stator reference frame. This injection rotates with respect to the stator and collects information about the entire rotor over a single injection cycle. Typically, this injection frequency is high enough to capture variations in inductance [42], however, at lower frequencies, variations in resistance can be used to generate a trackable signal [1, 56, 57]. This system is shown in Figure 1.11 with the high frequency injection being combined with the fundamental to form a reference voltage for the voltage source inverter. Note that the resulting high frequency current has both positive and negative rotating vectors, but that only the negative rotating vector contains rotor position information as in (1.14). A full derivation is given in section 6.3A.12 . The positive high frequency portion is removed, typically with a very high bandwidth negative carrier reference frame low-pass filter so as to minimize dynamic impact.

$$I_{\alpha\beta} = \frac{V_c}{\omega_c(\Sigma L^2 - \Delta L^2)} \left(\Sigma L \begin{bmatrix} \cos(\omega_c t) \\ -\sin(\omega_c t) \end{bmatrix} + \Delta L \begin{bmatrix} -\cos(2\theta - \omega_c t) \\ \sin(2\theta - \omega_c t) \end{bmatrix} \right) \tag{1.14}$$

The negative sequence then forms a rotating vector which can be tracked via a vector tracking method [2, 4]. Figure 1.12 shows the modified vector tracking demodulation process specifically for the high frequency rotating vector injection self-sensing method. The drawback

with this method is that the injection in the stationary reference frame periodically aligns with the q-axis, which generates torque and results in high frequency vibration and audible noise.

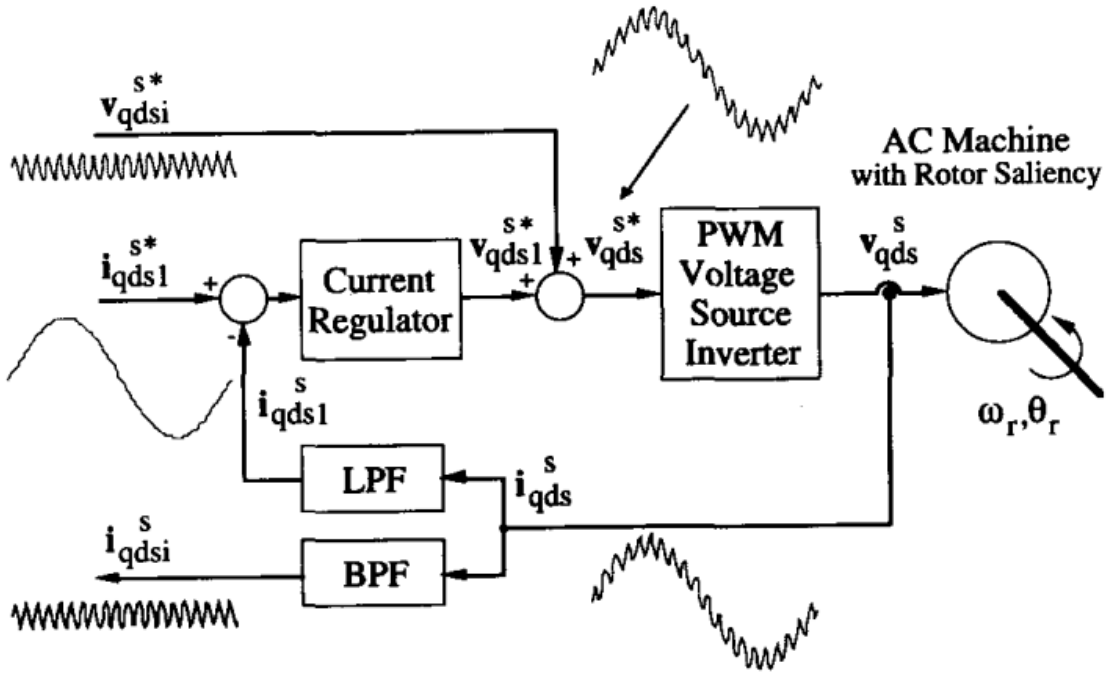

Figure 1.11 – High frequency signal injection into the stationary reference frame combined with the fundamental excitation and a simple filtering current separation scheme [42].

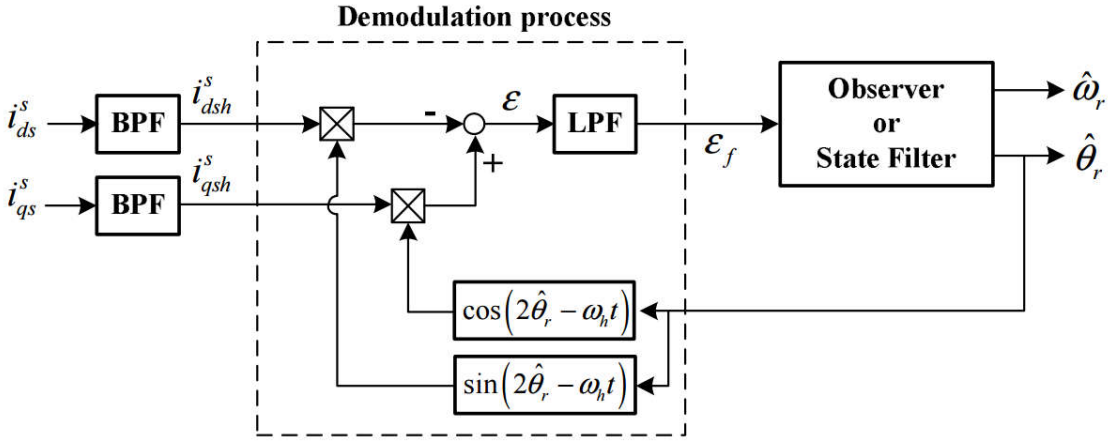

Figure 1.12 – Block diagram of the heterodyning demodulation process for rotating vector injection [1].

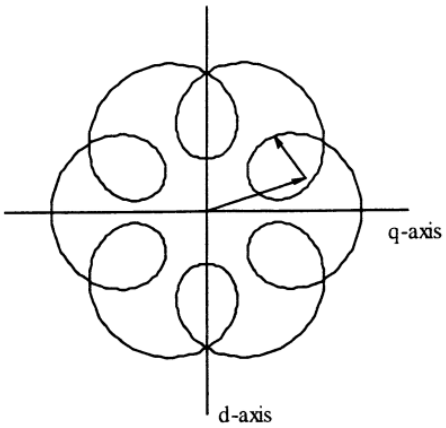

Figure 1.13 – Negative sequence components of the carrier current response, plotted in the negative carrier reference frame from [58].

Filtering the positive carrier component from (1.14), and transforming the signal to a reference frame which is synchronous with the negative carrier results in polar plots similar to Figure 1.13. In [58-60] this form is analyzed as relative to the harmonics present in the inductance which is unique to a machine at a given load level, and presents additional information which can be tracked.

1.3.2 Estimated Synchronous Frame Pulsating Voltage Injection

Pulsating vector injection is done by realizing that in the ideal case an injection along an axis should only return a response along that axis. However, if there is position estimation error then the injection will be partially along the quadrature axis. By measuring and driving the quadrature magnitude to 0, the angle can be reliably tracked. This is shown graphically in Figure 1.14. The choice of injection axis is left to the system designer, however injection along the q-axis will generate a pulsating torque which is typically undesirable. To minimize this, d-axis injection is often selected [1, 43, 57].

A system block diagram is shown in Figure 1.15. The pulsating vector injection in the estimated synchronous reference frame is shown in (1.15) with magnitude V_{inj} and carrier

angular velocity ω_c and the response in the synchronous reference frame can be shown to be (1.16). A full derivation of the pulsating response and associated states and variables is given in section 6.3A.10 . It should be noted that if the resistive portion of the impedance is being tracked, that the current response is phase shifted by 90°. It is also instructive to view the injection in the stator reference frame as (1.17). In this form, it is clear to see that the voltage injection is identical to two counter-rotating vectors, and can be related directly to rotating vector HFI [57].

$$V_{dq}^{\hat{e}} = V_c \begin{bmatrix} 0 \\ \cos(\omega_c t) \end{bmatrix} \tag{1.15}$$

$$I_q^{\hat{e}} = \frac{\Delta L \, V_c}{\omega_c(\Sigma L^2 - \Delta L^2)} \sin(2\tilde{\theta}) \sin(\omega_c t) \tag{1.16}$$

$$v_{dqs}^{s} = -j\frac{V_{inj}}{2}\left(e^{j(\omega_c t + \hat{\theta}_{err})} + e^{j(-\omega_c t + \hat{\theta})}\right) \tag{1.17}$$

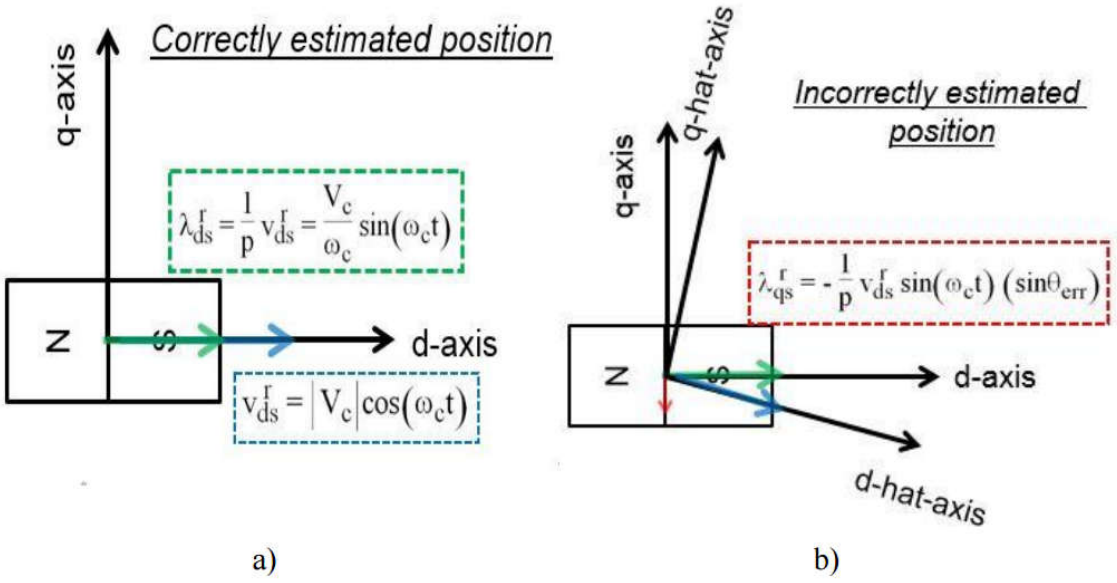

Figure 1.14 – Flux response to a high frequency voltage injection in a) the actual axis b) an axis with a small position estimation error [52].

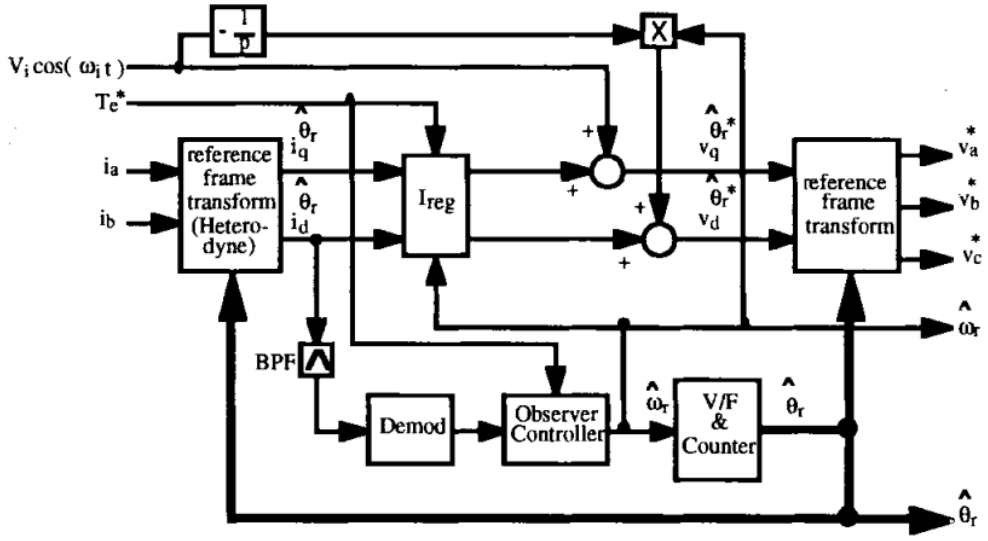

Figure 1.15 – System block diagram of pulsating injection in the estimated synchronous reference frame.[43]

A heterodyning demodulation process can be applied to I_{qh} the high frequency current from (1.17). A block diagram of the process is shown in Figure 1.16 with the I_{qh} being multiplied by a sinusoid to form ε, a noisy error term. The result of this is low-pass filtered, and then fed into an ELSO of the form described in [43]. It has been shown that the low-pass filter bandwidth used in the demodulation process limits the bandwidth of both the ELSO and the motion controller [1, 57, 61].

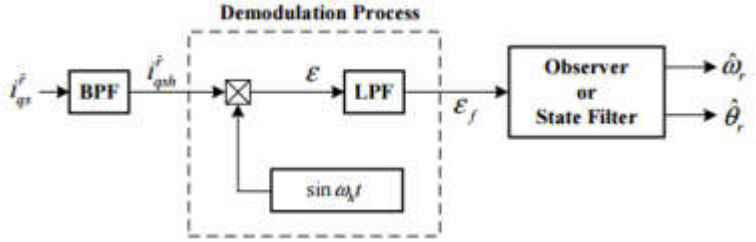

Figure 1.16 – Heterodyning demodulation for inductive-based pulsating HFI self-sensing [1].

1.4 Non-Ideal Effects on Low Speed Methods

The ideal model used for high frequency injection assumes a continuous time model, with a perfectly sinusoidal inductance in the stationary frame mapping directly to L_d and L_q, with negligible resistance at high frequencies, perfectly separated high frequency and fundamental current signals and no inverter effects [1, 42, 43]. For many applications these assumptions are reasonable, particularly those which spend minimal time in the low speed region and only suffer a small efficiency drop while in that region. For applications which deal with position and hold and require high accuracy in their position estimates the small errors from each of these assumptions leads to intolerable errors. This is often the case in servo applications.

A version of this base model is developed in 6.3A.2.2 . The impact of the assumptions above depends on the machine, inverter, and controller selected for a particular application. As such, the relative impact of each will vary significantly and must be evaluated per application.

1.4.1 Current Separation

Ideal modeling assumes that the high frequency model does not see any effects from the torque regulator. In practice, torque regulators may be pushed to significantly high bandwidths such that the current regulator response to the high frequency injection may not be negligible. This acts as a secondary injection at the same frequency as the carrier but attenuated and phase shifted and will result in a phase error in the demodulated current signal. Initially, it was proposed to separate the signals with a low-pass filter for the fundamental signal, and a bandpass filter for the carrier [42]. Later, it was observed that the filters introduce lagging effects, and the current regulator continues to respond even at frequencies beyond the frequency of the filters and current regulator [59]. The proposed solution uses a number of high-pass filters, implemented in a reference frame synchronous with the positive and negative sequence components, along with a recombination of the fundamental and error terms which can be used for current regulator feedback as shown in Figure 1.17. This was further expanded in [62] using carrier observers as

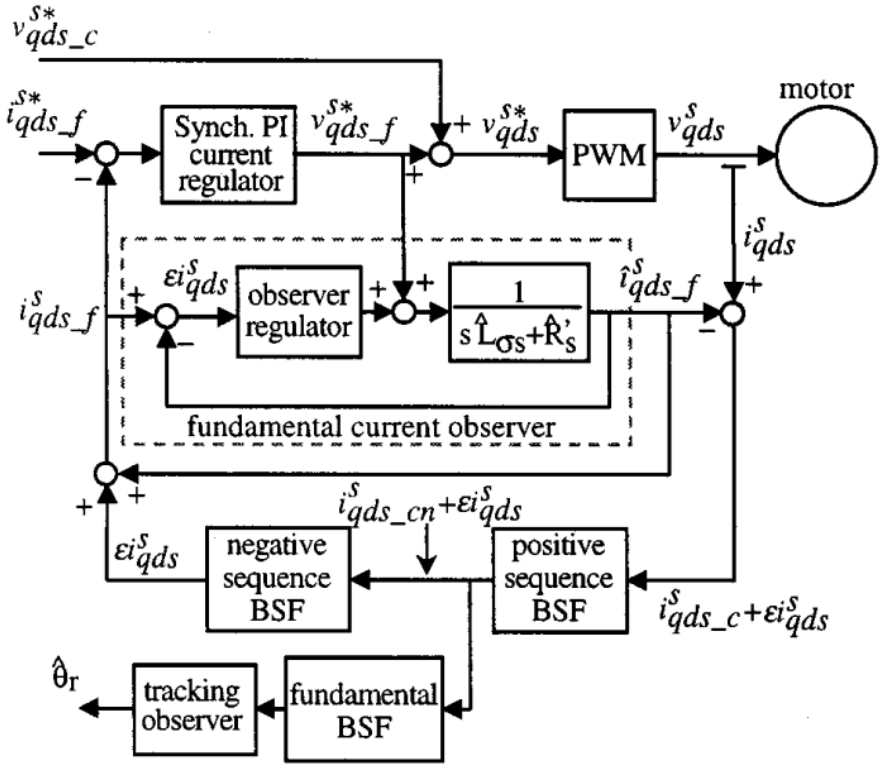

Figure 1.17 – State block diagram of an observer based method of reducing high frequency content reaching the current regulator based on the structures presented in [59].

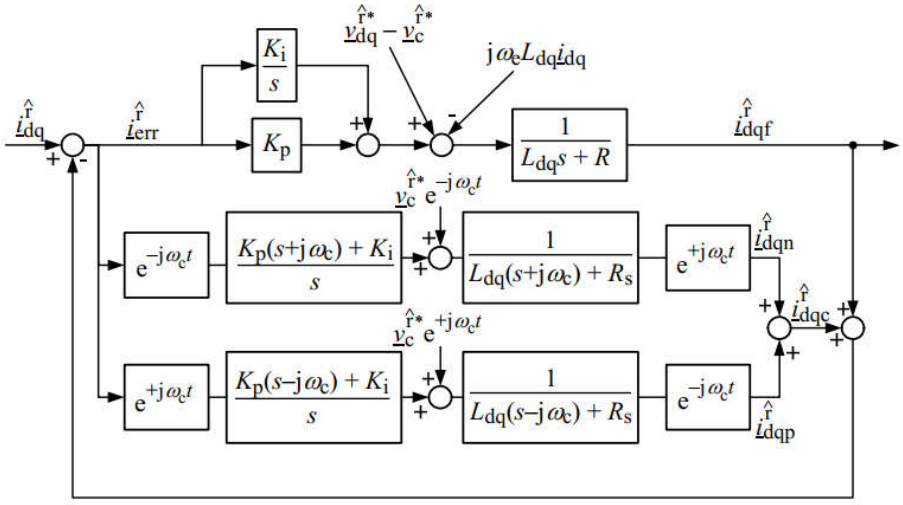

Figure 1.18 – State block diagram of an observer based method of reducing high frequency content reaching the current regulator based on the structures presented in [62].

shown in Figure 1.18 to further reduce the high frequency signals reaching the current regulator and allowed higher achievable system bandwidth.

1.4.2 Effects of Non-Ideal Inductance

In most electric machines, the dq-axes are not perfectly isolated, and cross-saturation effects show up. As opposed to an inductance matrix which has only L_d and L_q, to model cross-saturation the off-axis terms contain an L_{dq} term as shown in (1.18). A full derivation of the current response to a rotating voltage injection is derived in 6.3A.12.2 and for a pulsating voltage injection in 6.3A.10.2 . The effects of cross-saturation show up as a phase shift in the error term as in (1.19) and can be measured and decoupled with either a lookup table, or using adaptive methods [63].

$$L=\begin{bmatrix} L_q & L_{qd} \\ L_{qd} & L_d \end{bmatrix} \tag{1.18}$$

$$\theta_{err} = \arctan\left(\frac{L_{qd}}{\Delta L}\right) \tag{1.19}$$

In general, the inductance of the machine is not purely sinusoidally distributed but is position dependent and can be modeled as a Fourier series as shown in (1.20), with a full derivation of the states and variables provided for a rotating voltage injection is shown in 6.3A.12.2 and for a pulsating voltage injection is shown in 6.3A.10.2 . The effects of cross-saturation can be included in this generalized model as a modification of the magnitude and phase at the harmonic h=0. The effects have been studied and shown to result in harmonics on the estimated position with methods for decoupling or tracking them presented in [58, 60]. These harmonics present an additional source of position dependent information as shown in Figure 1.13.

$$L = \Sigma L\begin{bmatrix} 1 & 0 \\ 0 & 1 \end{bmatrix} + \sum_h \Delta L_h \begin{bmatrix} \cos(h\theta+\phi_h) & -\sin(h\theta+\phi_h) \\ -\sin(h\theta+\phi_h) & -\cos(h\theta+\phi_h) \end{bmatrix} \tag{1.20}$$

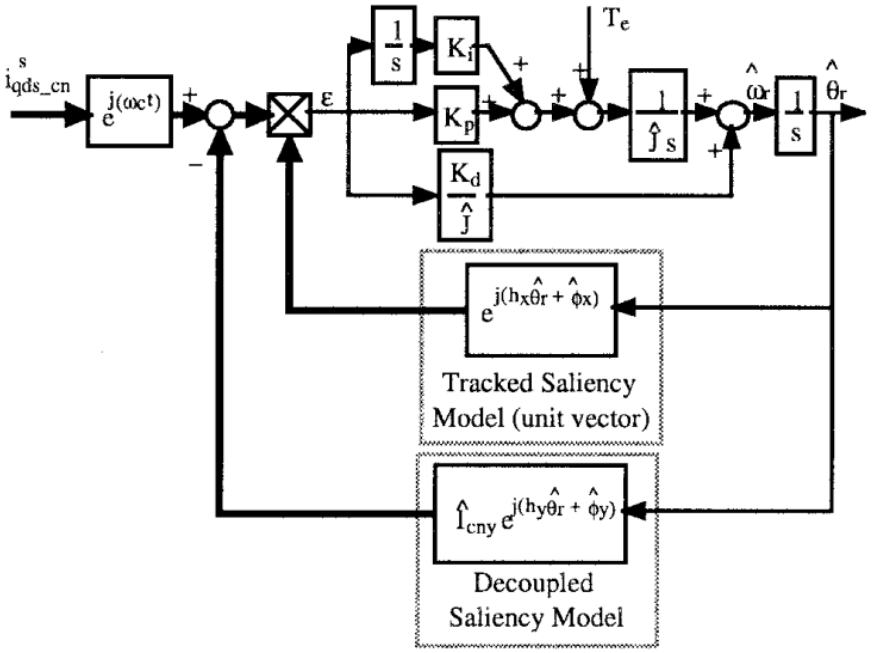

Figure 1.19 – Demodulation scheme to decouple and track known multiple saliencies presented in [60].

1.4.3 Resistance Effects

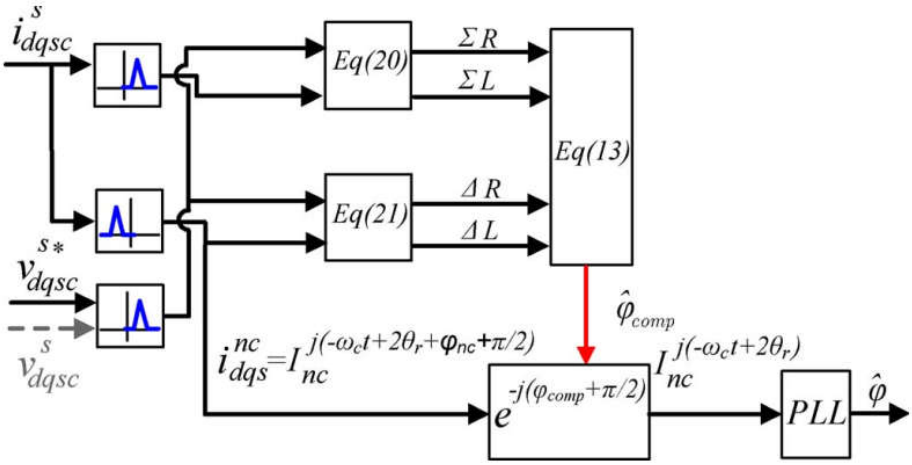

Figure 1.20 – Demodulation scheme to decouple the effects of resistance [64].

The effects of resistance are typically very small because at high frequency, the machine appears as an inductor. In cases where the machine's time constant is relatively small, or the injection frequency is relatively small, resistance can have a significant impact on the position

estimation. These effects appear as a constant position error offset relative to the resistance of the machine and can be decoupled using the method shown in Figure 1.20. However, measuring the resistance of a machine can be challenging as it varies with machine temperature. To overcome this, [64] proposed a scheme not only to decouple a known resistance effect, but additionally to adaptively decouple the effects in real-time.

1.4.4 Inverter Effects

In [65-69] the effects of non-ideal inverters are considered. The sources of these effects can be dead-time [66, 67, 70-72], zero-current clamping [66, 68, 69, 71], switch turn-on and turn-off times [66], and parasitics [66, 71, 72]. These effects show up as harmonic distortion, typically near the positive and negative sequence, and can cause substantial position estimation errors up to tens of mechanical degrees. Compensation methods have been developed in [36, 37, 73] which, at high current levels, add the dead-time back into the command to compensate, but at lower loads, use approximations or lookup tables to compensate the current dependent effects as shown in Figure 1.21

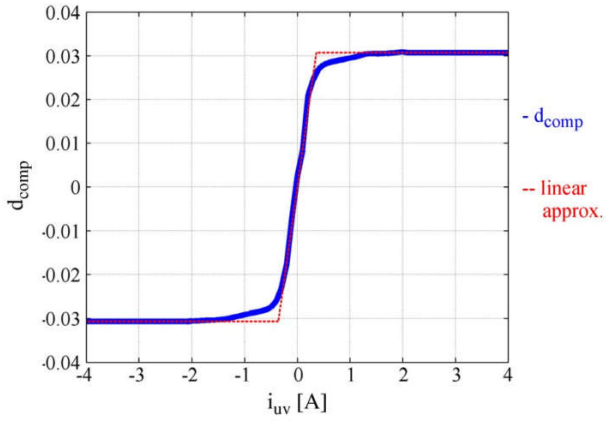

Figure 1.21 – Current dependent compensation of inverter effects developed in [36].

1.4.5 Speed-dependent effects from reference frame and latch modeling

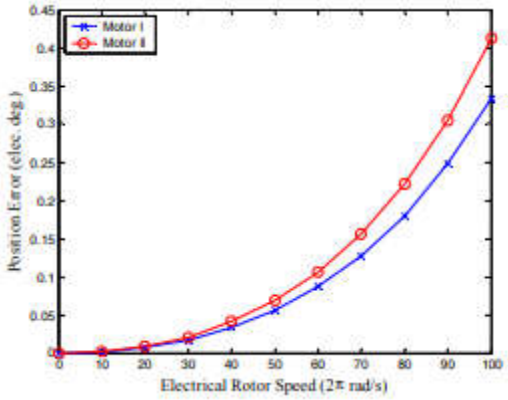

Figure 1.22 – Increasing estimation error with speed as identified and neglected in [74]

Several authors have noted the presence of speed dependent estimation error [65, 74-76] one of these is shown in Figure 1.22. The source of the error is typically neglected if It is even noted. Compensation methods note that the voltage applied to the machine is not the ideal expected and propose the use of voltage sensors to measure and correct for the source of the error. For pulsating voltage injection methods the entire model is in the estimated synchronous reference frame. However, discrete time modeling and, in particular, the effects of the stationary frame latch have not been explored. Similarly, for rotating voltage injection methods the injected voltage is assumed to be perfect with no cross-coupling due to the stationary frame voltage latch.

1.5 Image Registration

The field of image processing is closely related to both pattern matching and signal processing in multiple dimensions [77, 78]. One of the main areas of research is the topic of image registration, i.e. finding the transformation that aligns two images best. An example of this is shown in Figure 1.23. An image of a face is cross-correlated (1.21) with a search space, and the maximum of the correlogram is found to identify the location of the best match.

$$Rft(y) = \sum_{x} f^*(x)t(x-y) \tag{1.21}$$

(a) (b)

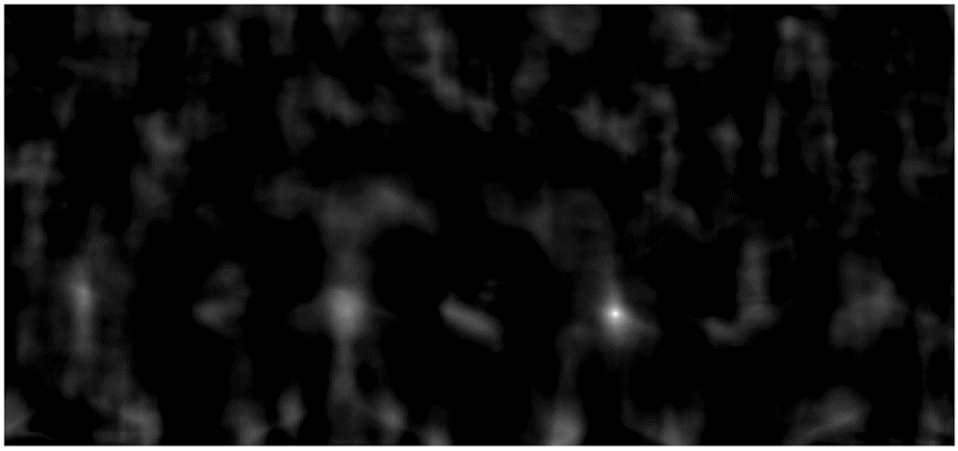

(c)

Figure 1.23 – A template and search space pair of images, with the resulting cross-correlation map [21].

The cross-correlation process is very computationally intensive, especially when considering multiple parameters such as translated location, rotation and scaling. A method of linearizing the process was shown in [79] to improve processing. Further optimization using

identities of cross-correlation and the Fourier transform were explored in [80-82] to reduce the computational time from polynomial time to n*log(n) time and to be more noise tolerant.

In the late 1990's and early 2000's, a family of algorithms appeared which focused on the identification of key points which are invariant to noise and scaling, and then to use features of each key point to find matches between two images. The most famous of these are SIFT [83] and SURF [84] which extended the idea by relaxing the affine transform constraints. These methods are much faster and can be more easily parallelized to make use of modern hardware.

1.5.1 Image Registration with Stationary Frame Voltage Injection

Several works have focused on the use of a rotating voltage in the stationary reference frame as the source of excitation and have replaced the demodulation scheme with image registration methods. Many have focused on the current response in the stationary reference frame with demodulation methods including cross-correlation [2, 21, 57], Recursive Least Squares [85], Neural Networks [86], and Principle Component Analysis [87]. Of these, all these methods used offline processing of current data as the computational load for the method was significant enough to preclude use in real-time controls. The exception [85] spent considerable effort to reduce the computation of the pattern matching approach to be suitable for application in real-time.

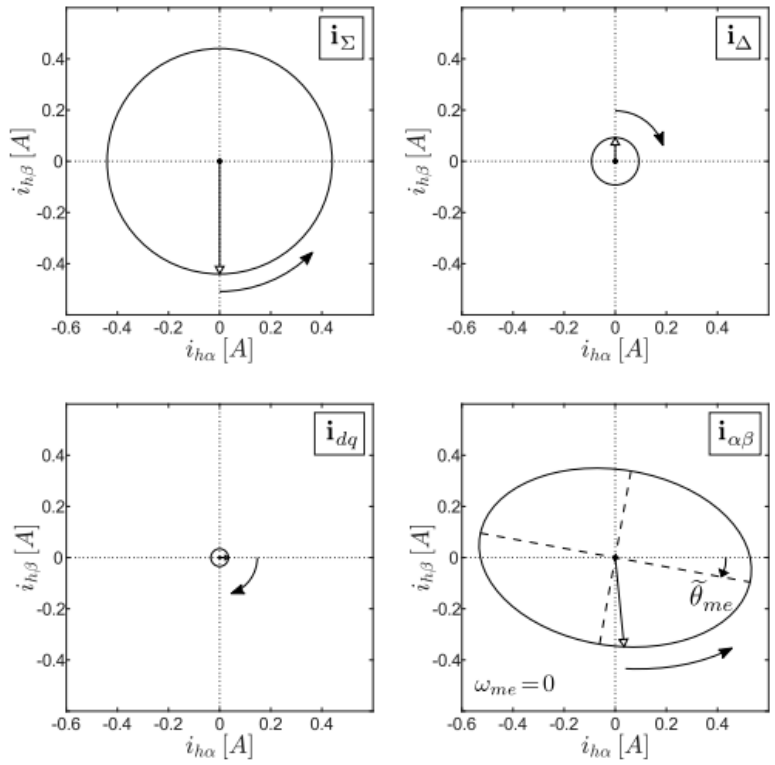

Figure 1.24 – Diagram showing the movement of the current components in different reference frames from [85]

In principle, all of the methods us the current response shown in (1.14) which represents the full high frequency current response as a rotating ellipse in the stationary reference frame as shown in Figure 1.24. Each method uses a different method to estimate the relative rotation of the ellipse and uses this as an estimate of the rotor position. These methods can be very effective; in offline tests show accuracy greater than those achieved using traditional heterodyning demodulation techniques as shown in Figure 1.25. However, some non-ideal conditions can cause larger errors. In [85] the effects of cross-saturation were explored and show up the same as in traditional heterodyning demodulation, namely as a load dependent position offset which must be compensated. Additionally, in [21, 57] it was realized that multiple saliencies cause harmonics similar to heterodyning demodulation. These harmonics in the movement of the ellipse are challenging to compensate for as they cause the ellipse to wobble back and forth even in smooth constant speed conditions. This leads to a situation where pattern

matching with the ellipse is no longer a one-to-one function, meaning that multiple rotor positions can map to the same ellipse orientation.

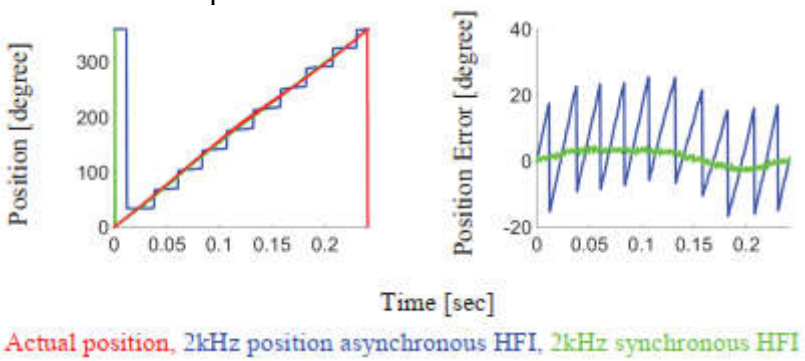

Figure 1.25 – Offline estimation accuracy demonstrating a less than 0.75° mechanical position error using cross-correlation [2].

1.5.2 Image Registration with Estimated Synchronous Frame Voltage Injection

One method of using a pulsating voltage in the estimated synchronous reference frame was attempted [3]. In this work the current response is shown to be ideally a line, but practically an ellipse when considering sensor noise with major axis related to the position error as shown in Figure 1.26.

As the method is based on position error, which tends to be influenced by sensor noise and non-ideal effects, the method was only able to show a tradeoff between improved accuracy of position error with a larger number of points with a cost of a reduced system response time. This is due to the fact that the collection of multiple samples functions similarly to a moving average filter with an frequency response shown in Figure 1.27. By increasing the number of points, it decreases the bandwidth of the filter underpinning the tradeoff between improved accuracy and lower dynamic response. This method was tested online to show this tradeoff.

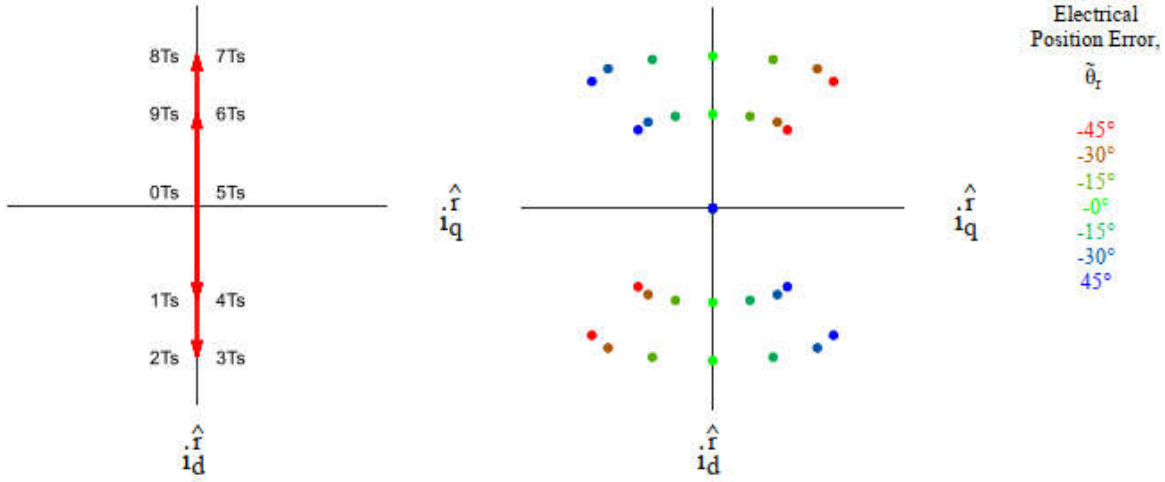

Figure 1.26 – Current response over an injection cycle at different electrical position errors to show relation [3].

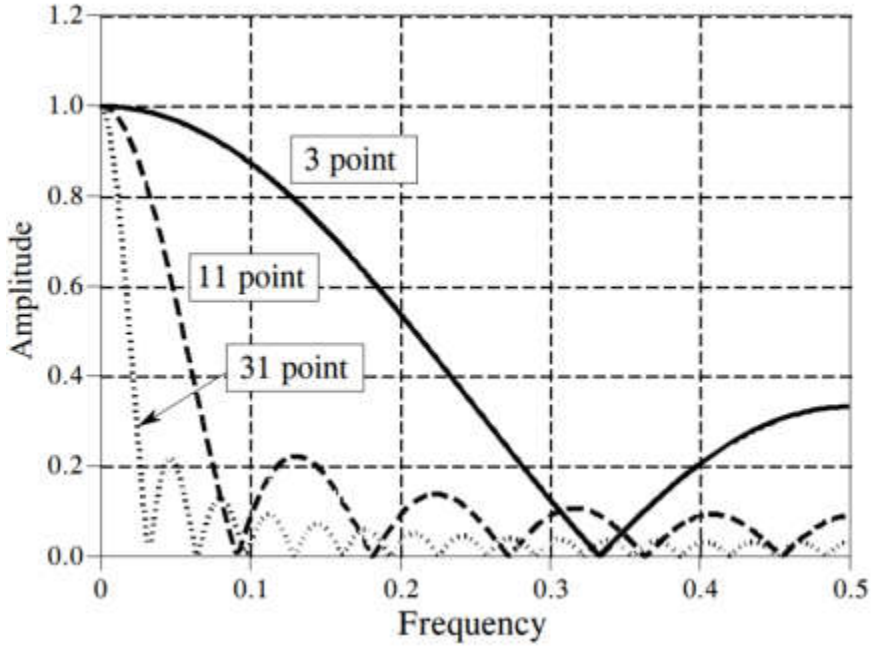

Figure 1.27 – Moving average filter varying the number of samples used [88].

1.6 Summary of Research Opportunities Identified

Based on the state-of-the-art review in this chapter, the key identified research opportunities are:

Negative Sequence Image Tracking

- Image tracking solutions applied to rotating voltage injection-based systems have not utilized the negative carrier frame to focus attention on the position information contained within the negative sequence response.

Stationary Frame Voltage Latch Effects on Self-Sensing

- Estimation error speed dependences have been noted in the literature, however the voltage latch in the stationary frame has not been investigated as a source of this error.
- Development of a model of the cross-coupling caused by the stationary frame latch, analysis and quantification of the self-sensing error the latch generates has not been performed.
- Methods of mitigation and compensation have not been developed.

Online Image Tracking Implementation

- Existing image tracking self-sensing methods have focused on offline estimation accuracy and have not analyzed the resulting closed-loop dynamics.
- A full closed-loop online implementation has not been developed, or the limitations of these implementations evaluated.

Chapter 2 Stationary Frame Voltage Latch Analysis of Effects on Self-Sensing and Compensation Methods

This chapter documents the presence of a heretofore unidentified position error based on a neglected cross-coupling between the axes due to the voltage being latched in the stationary reference frame and position assumed to be constant within a switching period. In reality, the rotor continues to spin causing a speed dependent cross-coupling of the applied voltage. This cross-coupling generates a high frequency current response which ultimately demodulates into a speed dependent estimation error. This effect is identified, a method of modeling it is developed utilizing a full order current observer which considers discretization effects, finally a compensation method is proposed.

2.1 Identification of Effects of the Stationary Frame Voltage Latch on Self-Sensing Estimation Error

During the development of the simulation to analyze state-of-the-art self-sensing methods, as well as the image tracking methods, the speed dependent estimation error effects of the stationary frame voltage latch were realized. Figure 2.1 shows the system overview and the model of the electrical plant. In the system overview particular attention should be paid to the generation of the pulsating voltage injection as both the output from the current regulator and the high frequency d-axis injection are added together in the synchronous reference frame. After this, the command is converted to the 3-phase stationary reference frame. In the electrical plant, the details are shown starting with the 3-phase stationary reference frame latch, the inverter, and the reference frame transformations back into the synchronous reference frame. The inconsistency comes from the fact that the discrete system uses a position estimate which is

generated every sample period and latched for the duration, conversely the electrical system is continuous and so the position used for reference frames is continuously changing.

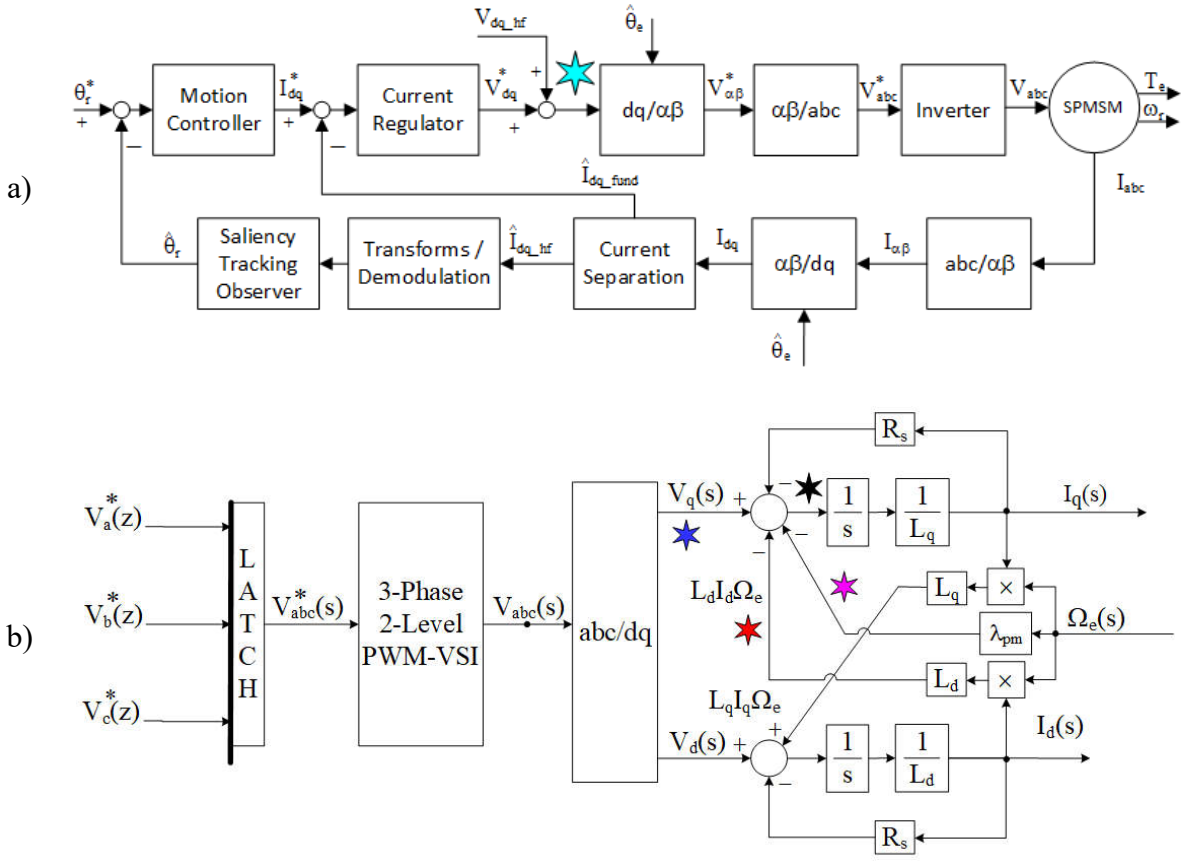

a) Self-sensing system overview for an IPMSM
b) IPMSM electrical plant

Figure 2.1 – Annotated system with voltages highlighted to match those shown in Figure 2.2.

An example of these signals are shown in Figure 2.2 tracing the voltage along the q-axis through this path. The injected voltage is a 1V pulsating voltage injection along the d-axis and theoretically should provide only the q-axis voltage required to compensate for the back-EMF voltage and the cross-coupling. Here the discrete command as well as the commanded voltage supplied by the inverter are shown in cyan and blue respectively. The problem is already visible as the discrete voltage command appears as a discrete signal comprised of the component parts.

However, the blue signal showing the voltage delivered in the q-axis of the continuous electrical plant shows a ramping feature. Also shown is the cross-coupling component which is compensated for by the method presented in 6.3A.3 and the back-EMF component which is compensated for in the complex vector current regulator presented in 6.3A.3 . Finally, the effective voltage applied to the machine is shown in black. This voltage has 2 features which should be noted. At the beginning of each switching period the effective voltage is zero, showing that the compensation for cross-coupling and back-EMF is calculated correctly and working as intended. However, within a switching period the voltage appears to be a ramp. Since the simulation is using a constant rotor speed, this makes sense as the axes are coupled linearly in steady-state. The other major feature is that the size of the ramp changes each switching period. This is also consistent as the high frequency voltage injection for pulsating voltage self-sensing is a sinusoidal voltage along the d-axis. The cross-coupling combines these features as dependent on the speed of the rotor, and the q-axis voltage and assuming a constant speed over the switching period can be modeled as in (2.1).

$$\begin{bmatrix} V_q^e \\ V_d^e \end{bmatrix} = \begin{bmatrix} 1 & \omega_e t \\ \omega_e t & 1 \end{bmatrix} \begin{bmatrix} \hat{V}_q^e \\ \hat{V}_d^e \end{bmatrix} = \begin{bmatrix} \hat{V}_q^e & \hat{V}_d^e \omega_e t \\ \hat{V}_q^e \omega_e t & \hat{V}_d^e \end{bmatrix} \tag{2.1}$$

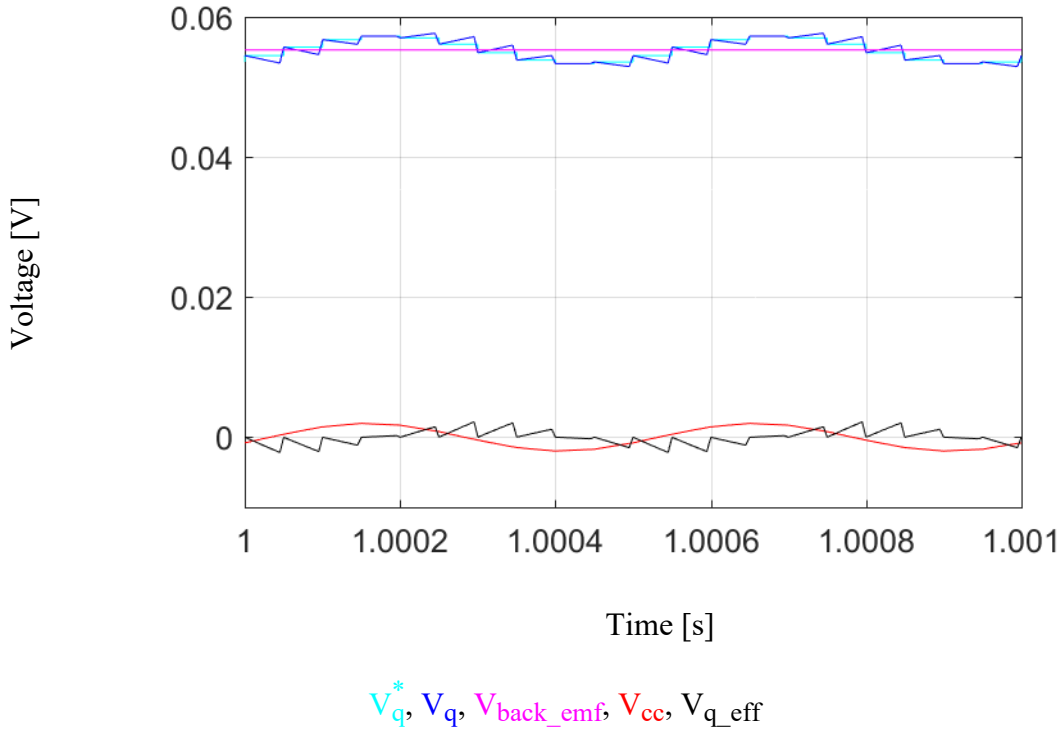

Figure 2.2 – Simulated q-axis voltage along the path from the discrete controller, through the latch, and what is effectively applied to the machine.

Isolating just the effective voltage applied to the q-axis is shown in Figure 2.3 at different operating speeds. This again illustrates the voltage within a switching period is dependent on the d-axis voltage, and the speed of the machine.

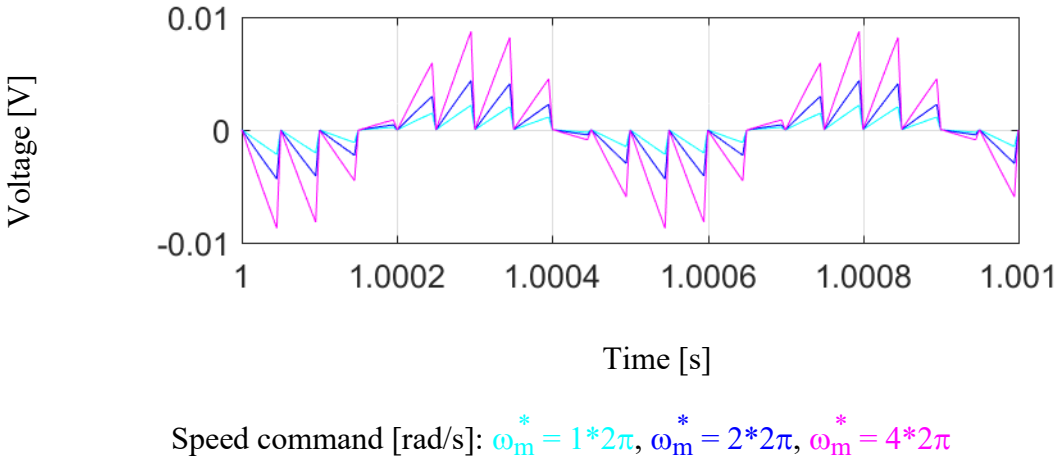

Figure 2.3 – Simulated q-axis effective voltage at different speed operating points showing speed dependence.

The effective voltage applied to the machine generates a small current which is also speed dependent as shown in Figure 2.4. This current is the result of the voltage applied to the L-R electrical plant, which at high frequencies is dominated by the inductance, and shows an almost 90° lag as is expected. This current is sampled, multiplied by the pulsating demodulation local oscillator using the process described in 6.3A.10 . The resulting error term is plotted and shows a speed dependent small position estimation error. While this may be small, for precision motion control, this error represents a substantial contribution to the error shown in Figure 2.4.

The average value of the estimation error shown in Figure 2.4 can be measured at a given operating point and subtracted from the demodulated signal to remove the average effect but is dependent on the machine parameters and operating speed requiring careful calibration to remove.

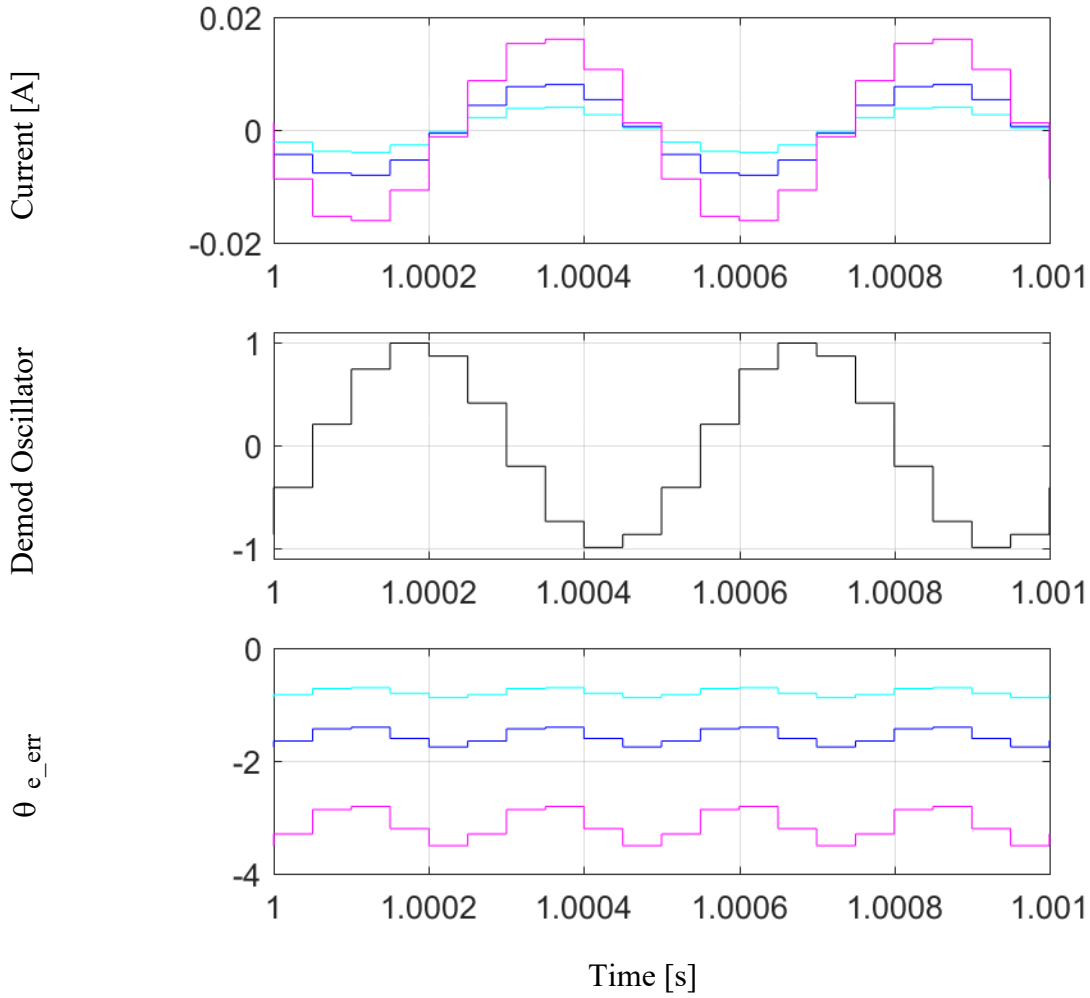

Figure 2.4 – Simulated sampled current, local oscillator, and estimated position error at varied speed operating points showing dependence of estimated error on speed.

2.2 Full Order Modeling of Discrete System Effects and Simulated Evaluation

A full order system including proper discretization of the stationary frame latch interface, the plant cross-coupling, the plant salient inductance and resistance effects was developed in [89]. In Figure 2.5 a) the form of the plant used in traditional high frequency self-sensing is

shown. This neglects resistance, cross-coupling, reference frame, and latch effects on the final solution. For many applications this is able to meet the specifications required of the self-sensing. In other particular instances some of these effects are compensated for independently. A description of these methods are discussed in 6.3A.10.2 and 6.3A.12.2 . In Figure 2.5 b) the form of the full order model is considered. This model captures cross-coupling, resistance,

a)

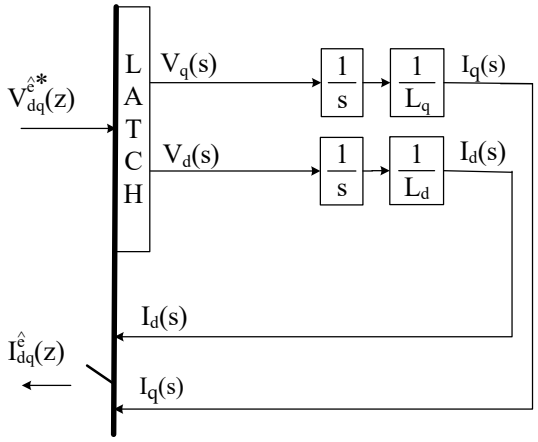

b)

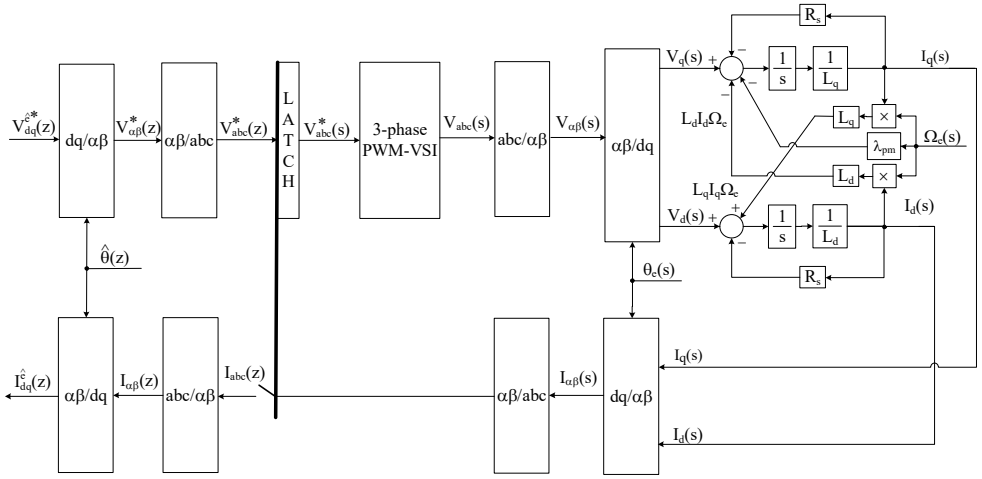

Figure 2.5 – Comparison of typical high frequency injection based self-sensing modeling as shown in state block diagram form in a) with a full order modeling considering the full plant, stationary frame latch, and relevant reference frame transforms as shown in state block diagram form in b).

salient inductance, as well as the addition of reference frame, latch, and discretization effects on the sampled current.

The final model in current observer form is shown in (2.2) with associated conventions and definitions shown in (2.3) through (2.7). There are several important factors to note about the development of this model. Because the inductance matrix L_{dq} contains a saliency, it cannot be simplified to a scalar for use with complex vector notation and as such requires the rest of the modeling to be done using vectors and matrices. In this derivation vectors are underlined, and matrices are bolded. Additionally, when the inverse Laplace transform is taken it results in the exponential matrices shown in (2.2). These conceptually function as exponents and are used to capture the dynamics of the system.

$$\underline{I}_{dq}[k+1] = \mathbf{L}_{dq}^{-1}\boldsymbol{\tau}e^{-\mathbf{J}\omega_e T_s}(\mathbf{I} - e^{-\boldsymbol{\tau}^{-1}T_s})\underline{v}_{dq}[k] + \mathbf{L}_{dq}^{-1}e^{-\boldsymbol{\tau}_{\boldsymbol{\omega}}^{-1}T_s}\mathbf{L}_{dq}\underline{I}_{dq}[k] + \mathbf{L}_{dq}^{-1}\left(e^{-\boldsymbol{\tau}_{\boldsymbol{\omega}}^{-1}T_s} + \boldsymbol{\tau}_{\boldsymbol{\omega}}(\mathbf{I} - e^{-\boldsymbol{\tau}_{\boldsymbol{\omega}}^{-1}T_s})\boldsymbol{\tau}^{-1} - \mathbf{I}\right)\underline{\lambda}_{pm} \quad (2.2)$$

$$\underline{V}_{dq} = \begin{bmatrix} F_d \\ F_q \end{bmatrix} = F_d + jF_q \quad (2.3)$$

$$\mathbf{I} = \begin{bmatrix} 1 & 0 \\ 0 & 1 \end{bmatrix} \quad (2.4)$$

$$\mathbf{J} = \begin{bmatrix} 0 & -1 \\ 1 & 0 \end{bmatrix} \quad (2.5)$$

$$\boldsymbol{\tau}_{\boldsymbol{\omega}} = (R_s\mathbf{L}_{dq}^{-1} + \mathbf{J}w_e)^{-1} \quad (2.6)$$

$$\boldsymbol{\tau} = \mathbf{L}_{dq} / R_s \quad (2.7)$$

To evaluate the model, a simplified simulation was created based on the state block diagram shown in Figure 2.5 b) with the ability to control a fixed speed, and to inject a signal at an arbitrary angle, a block diagram is shown in Figure 2.6. This allows for the model to be evaluated in the synchronous reference frame, and with an applied error, the effects in the estimated synchronous reference frame.

To verify the model properly estimates the current, even considering the cross-coupling and reference frame effects, the current observer was evaluated at varied speeds. Since the model is in the form of a current observer, it estimates a single time step ahead. In Figure 2.7 a)

the model is evaluated in the synchronous reference frame. It is shown that the model properly estimates a time step ahead.

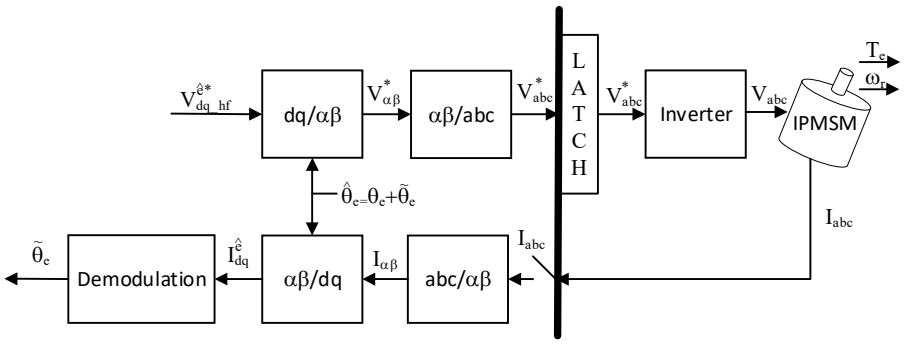

Figure 2.6 – Simplified system model, with a method for imposing artificial reference frame error and fixed speed, for evaluating the current model and demodulation.

Further evaluation of the model takes places with an estimated synchronous reference frame formulation. To evaluate the effects of speed, the same test was applied with varied speed in Figure 2.7 b) and again the model is shown to estimate the current a time step ahead. Finally, the model was held at constant speed but with varying the estimated synchronous reference frame to show that the model properly estimates even when the reference frame has error in its position. This test was performed in Figure 2.7 c) and again the model properly estimates regardless of position error applied to the reference frame.

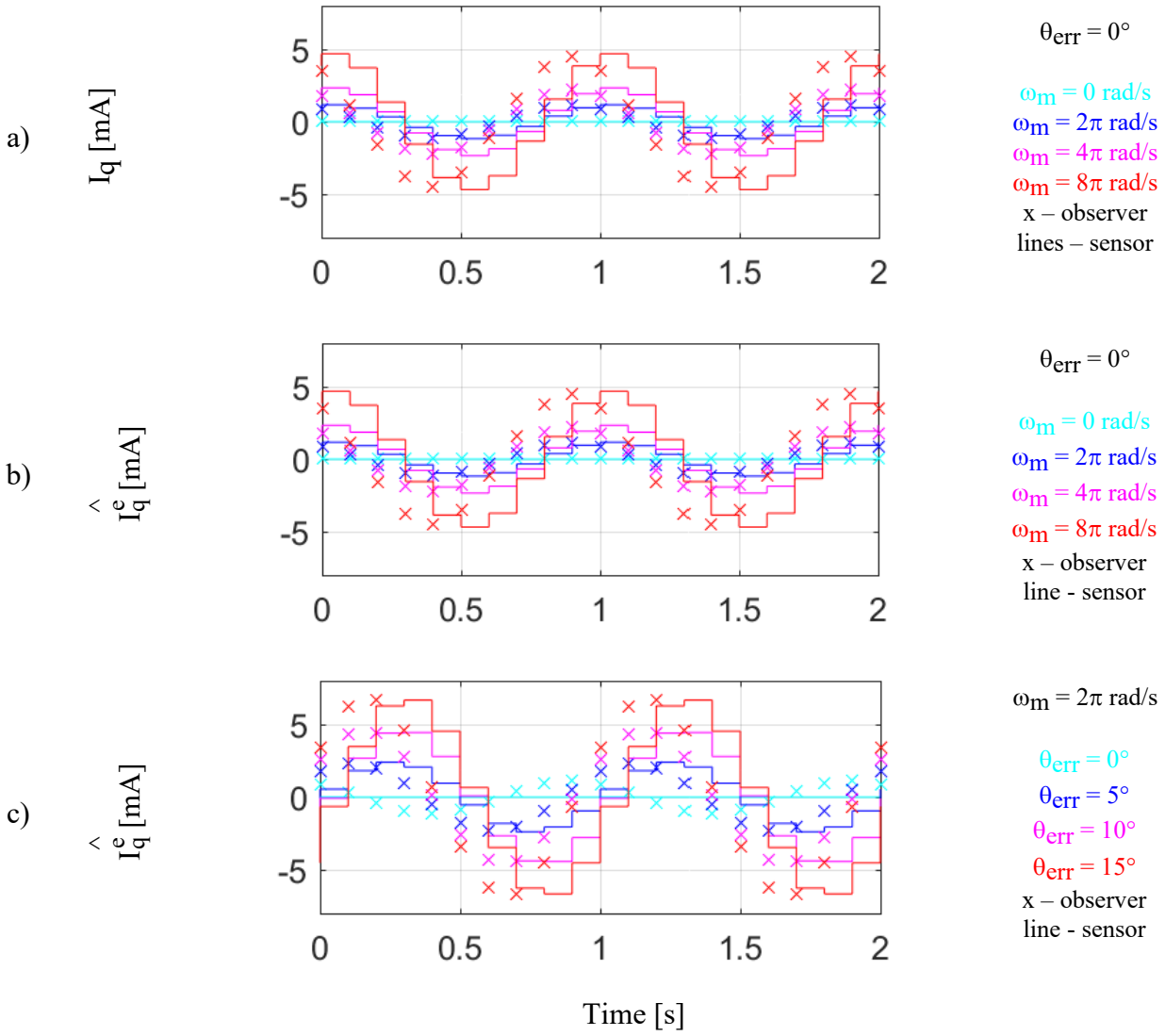

Figure 2.7 – Time-domain current observer estimation to a high frequency voltage injection Vc = 1V, fc = 2kHz. a) current observer in synchronous reference frame at varied speeds, b) current observer in estimated synchronous reference frame at varied speeds, c) current observer in estimated synchronous reference frame at fixed speed with varied reference frame error.

2.3 Analytical Effects of Full Order Model on Self-Sensing and Proposed Compensation Method

The full order model presented in [89] provides the starting point for the analysis of the estimation error which develops due to neglecting these secondary effects. Starting with the full order current observer in (2.2) several steps will be taken. First the back-EMF will be neglected as It is a slowly changing variable and can easily be filtered or decoupled from a high frequency response. Next, the observer model will be delayed a time step so that it predicts the current value based on previous values. Finally, the current will be rearranged as in (2.8) to form an effective change in current. It should be noted that this is not simply the change in current between time instances but also depends on the machine parameters and current speed to generate ΔI_{dq}. The right side of (2.8) remains as a much simpler equation dependent on the voltage injection, the machine parameters, and the rotor speed.

For pulsating voltage injection, the voltage is injected into the estimated synchronous reference frame, but the previous development through (2.8) was done in the actual synchronous reference frame. Therefore, (2.8) is transformed into the estimated synchronous reference frame as shown in (2.9). Next, the pulsating voltage is shown in the estimated synchronous frame in (2.10) and applied to the change in current from (2.9), and furthermore the q-axis is isolated as we're only interested in the portion which is projected onto the q-axis which results in (2.13). Equations (2.11) and (2.12) define an average and differential response. This is analogous to the average and differential inductance from classical derivations as presented in 6.3A.10 . These terms also capture the effects of the resistance and will similarly modify the magnitude of the current response with the saliency as in classical pulsating voltage self-sensing.

$$\Delta \underline{I}_{dq}[k] = \underline{I}_{dq}[k] - \mathbf{L}_{\tilde{dq}}^{-1} e^{-\boldsymbol{\tau}\boldsymbol{\omega}^{-1}T_s} \mathbf{L}_{dq} \underline{I}_{dq}[k-1] = \mathbf{L}_{\tilde{dq}}^{-1} \boldsymbol{\tau} e^{-\mathbf{J}\omega_e T_s} (\mathbf{I} - e^{-\boldsymbol{\tau}^{-1}T_s}) \underline{v}_{dq}[k-1] \tag{2.8}$$

$$\Delta\hat{\underline{I}}^{e}_{dq}[k] = \mathbf{R}(\theta[k])\mathbf{L}_{dq}^{-1}\boldsymbol{\tau}e^{-\mathbf{J}\omega_e T_s}(\mathbf{I} - e^{-\boldsymbol{\tau}^{-1}T_s})\mathbf{R}(\theta[k])^{-1}\hat{\underline{v}}^{e}_{dq}[k-1] \tag{2.9}$$

$$\hat{\underline{v}}^{e}_{dq}[k-1] = V_c\begin{bmatrix}\cos(w_c k T_s)\\ 0\end{bmatrix} \tag{2.10}$$

$$\Delta\rho = \frac{1}{2}\left(e^{-R_s T_s/L_d} - e^{-R_s T_s/L_q}\right) \tag{2.11}$$

$$\Sigma\rho = \frac{1}{2}\left(e^{-R_s T_s/L_d} + e^{-R_s T_s/L_q}\right) \tag{2.12}$$

$$\Delta\hat{\underline{I}}^{e}_{q}[k] = \frac{V_c}{R_s}\Big(-\sin(\omega_e * T_s) - \Delta\rho\cos(\omega_e T_s)\sin(2\theta[k]) + \Delta\rho\sin(\omega_e T_s)\cos(2\theta[k]) + \Sigma\rho\sin(\omega_e T_s)\Big)\cos(\omega_c K T_s) \tag{2.13}$$

Equation (2.13) provides the basis for the self-sensing method as it contains the position error term which must be extracted to estimate the current position. This is done similarly to the classical pulsating demodulation. The first step is to multiply by a cosine term as in (2.14). By realizing this generates two terms one at DC and one at twice the carrier frequency content as defined in (2.15), and applying a low-pass filter significantly lower than twice the carrier, (2.14) can be simplified as (2.16). As this method is for low speeds and T_s will be very small, a small angle approximation can be applied to the sinusoidal terms depending on speed. Similarly, the angle error should be small or controlled operation will not be possible and so a small angle approximation can be applied to the sinusoidal terms depending on position error. This simplifies (2.16) into (2.17). Rearranging (2.17) to isolate the position error term results in (2.18). This final form shows that there is a speed dependent portion of the error term which is entirely neglected in classical demodulation and accounts for the error previously identified.

$$\text{demod} = \Delta\hat{\underline{I}}^{e}_{q}[k]\cos(\omega_c k T_s) = \text{demod} = \Delta\hat{\underline{I}}^{e}_{q}[k]\cos(\omega_c K T_s) = \frac{V_c}{R_s}\Big(-\sin(\omega_e T_s) - \Delta\rho\cos(\omega_e T_s)\sin(2\tilde{\theta}[k]) + \Delta\rho\sin(\omega_e T_s)\cos(2\tilde{\theta}[k]) + \Sigma\rho\sin(\omega_e T_s)\Big)\cos^2(\omega_c k T_s) \tag{2.14}$$

$$\cos^2(\omega_c k T_s) = \frac{1}{2}\left(\cos(2\omega_c k T_s) + 1\right) \tag{2.15}$$

$$\text{demod\_lpf} = \frac{V_c}{2R_s}\Big(-\sin(\omega_e T_s) - \Delta\rho\cos(\omega_e T_s)\sin(2\theta[k]) + \Delta\rho\sin(\omega_e T_s)\cos(2\theta[k]) + \Sigma\rho\sin(\omega_e T_s)\Big) \tag{2.16}$$

$$\text{demod\_lpf} = \frac{V_c}{2R_s}\left(-\omega_e T_s - \Delta\rho\, 2\theta[k] + \Delta\rho\, \omega_e T_s + \Sigma\rho\, \omega_e T_s\right) \tag{2.17}$$

$$\tilde{\theta}[k] = \frac{-R_s}{\Delta\rho V_c}\text{demod\_lpf} - \frac{\omega_e T_s}{2\Delta\rho}(1 - \Delta\rho - \Sigma\rho) \tag{2.18}$$

a)

b)

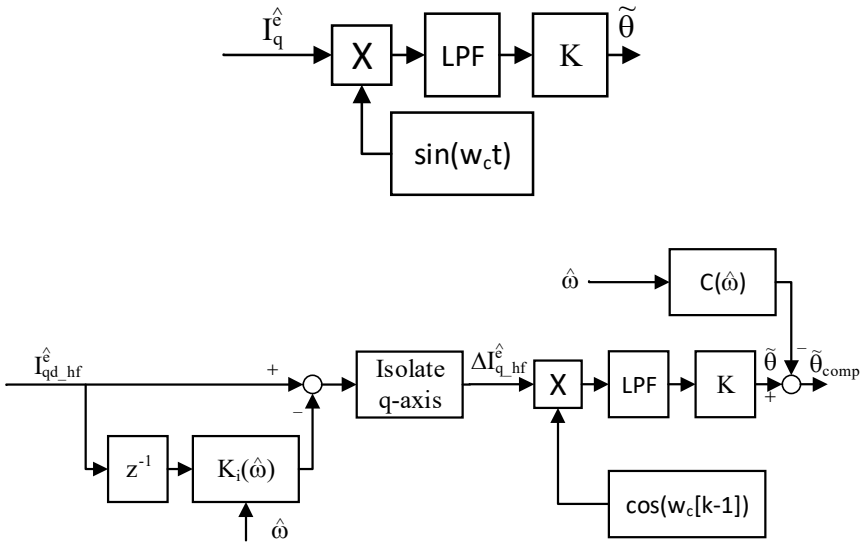

Figure 2.8 – Comparison of demodulation methods for pulsating voltage high frequency injection to extra position error. a) classical demodulation, b) proposed demodulation

The equation form of the demodulation is shown in (2.18) and repeated in state block diagram form in Figure 2.8 b) with constants and functions of speed defined in (2.19)-(2.21). Classical demodulation is also shown in Figure 2.8 a) for ease of comparison. It is clear that the proposed method is significantly more complicated involving a method to extract the change in q-axis current, as well as a speed dependent method for compensating the position error term.

$$\text{Ki} = \mathbf{L}_{dq}^{-1} e^{-\boldsymbol{\tau}_{\boldsymbol{\omega}}^{-1} T_s} \mathbf{L}_{dq} \tag{2.19}$$

$$K = \frac{-R_s}{\Delta\rho V_c} \tag{2.20}$$

$$C = \frac{\omega_e T_s}{2\Delta\rho}(1 - \Delta\rho - \Sigma\rho) \tag{2.21}$$

2.4 Simulated Evaluation of Compensation Method

The simulation developed to analyze the current model, described in Figure 2.6 was used with the machine parameters for the prototype machine developed in [46, 47]. The results are compared with the reference frame held constant and a varied speed as in Figure 2.9 a). Here it is shown that the proposed method does not contain error in the demodulation estimated position error, while the classical pulsating demodulation method has increasing estimation error with increased speed. This makes sense as the classical method doesn't consider the reference frame cross-coupling, and to a lesser extent the other non-ideal effects of the plant such as cross-coupling and resistance, while the proposed method accounts for all of these effects. To show that the proposed method can accurately estimate error, the same test was performed with a constant speed held at 2π rad/s. The imposed reference frame error was increased from 0° to 15°. In all cases the proposed method correctly estimates the reference frame error. The classical demodulation shows the expected sinusoidal error, but also has increased offset and error amplitude as the reference frame gets further away from the 0° error.

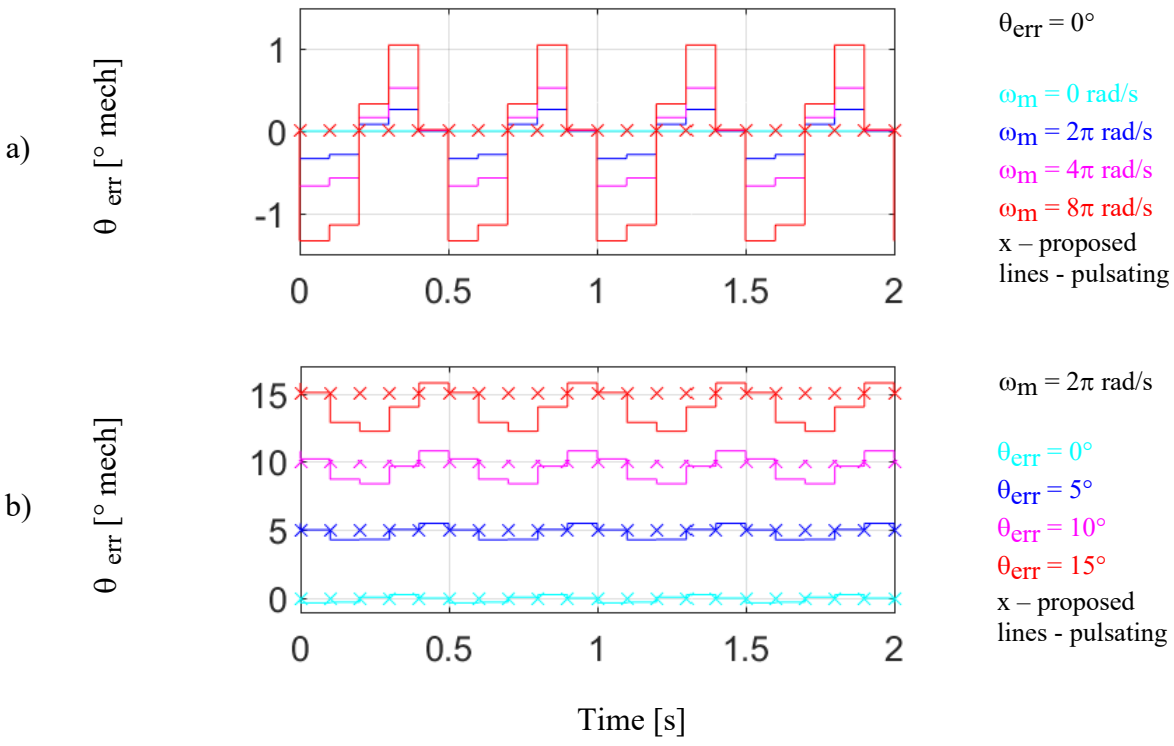

Figure 2.9 – Time-domain estimation error with a voltage injection V_c = 1V, f_c = 2kHz. a) reference frame error held constant at 0°, comparison with increasing speed, b) speed held constant at 2π rad/s, comparison with increasing reference frame error.

2.5 Summary

This chapter documented the presence of a previously unidentified cross-coupling between axes in high frequency injection methods due to the voltage being latched in the stationary reference frame. An advanced cross-coupled current observer was used and extended to provide estimates of the estimated synchronous reference frame currents and verified in simulation. The model was further extended to provide position estimates including resistance and cross-coupling effects from reference frame transforms. A demodulation method was developed to account for these variations and was validated in simulation.

Chapter 3 Negative Sequence Image Tracking: Method and Analytical Results

This chapter documents the development and analytically evaluates a new self-sensing method which utilizes a high frequency rotating voltage injection. The collection of a time series of current responses to form a current image enables the use of image processing techniques to generate a position estimate. The image formulation and position estimation methodology are documented. The limitations, particularly computational complexity, cost, and arc length variation with speed, are discussed and methods of mitigating these limitations are proposed.

3.1 Sensor Replacement Overview

The goal of image tracking is to create a sensor replacement technology. Using a voltage injection and the measured current response it is desired to have a high accuracy, high bandwidth position estimate. The general overview of this type of system is shown in Figure 3.1 where the demodulation process of rotating voltage injection described in 6.3A.12 is entirely replaced with a stand-alone position estimation process. In Figure 3.1 b) this design is shown with the optional cascaded position observer included to provide zero-lag filtering.

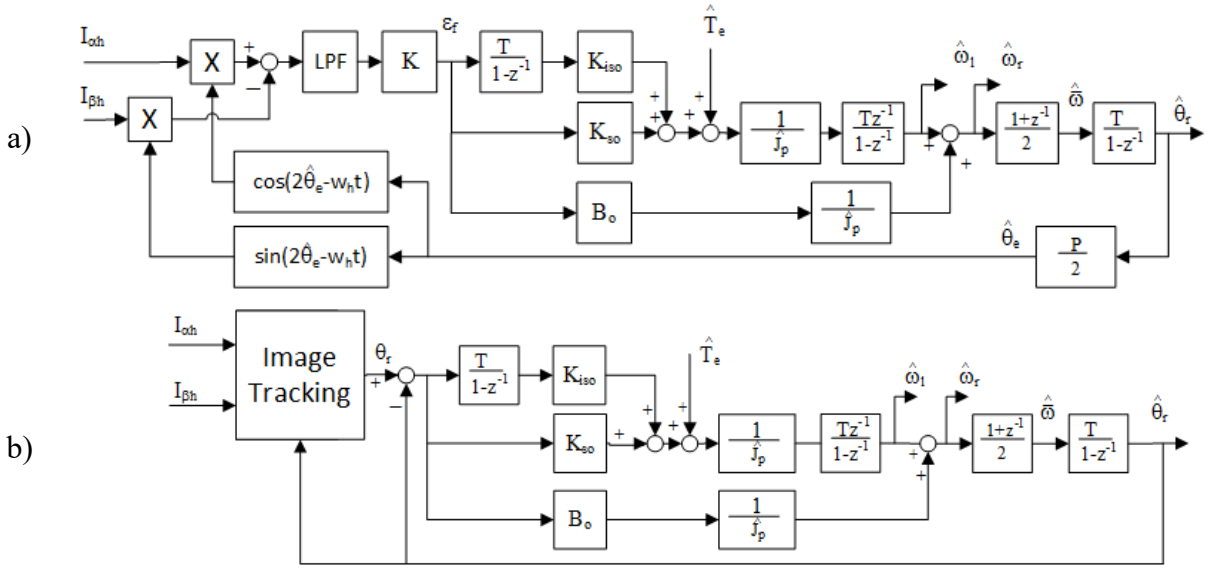

a) Heterodyning demodulation with cascaded saliency tracking observer
b) Negative sequence image tracking method with cascaded saliency tracking observer

Figure 3.1 – Contrasting state block diagrams of position estimation methods of state-of-the-art heterodyning demodulation and negative sequence image tracking.

3.2 Negative Sequence Image Formulation

The first crucial step in performing image tracking is to form the image. The name may suggest a camera or optical sensor, but in this work the image will be formed by the creation of a time series current response to a high frequency voltage. In section 6.3A.12 rotating voltage injection-based self-sensing is discussed in detail. The current response to a rotating voltage injection, considering only an ideal saliency with no secondary effects is shown in (0.125) and restated here for convenience as (3.1). This response forms a rotating ellipse in the stationary reference frame and in previous work has been the subject of image processing techniques to estimate position [2, 21, 85-87]. Parsing this equation though there is a component at the positive carrier frequency, and a component in the negative sequence near the negative carrier. Only the negative sequence component contains position information. Noting that the signals are separated from each other by nearly two times the carrier frequency and are nearly a full carrier

frequency separation from the fundamental at low speeds provides an opportunity to isolate these components with either filters or observers. In this work a high-pass filter is applied in a reference frame synchronous with the positive carrier frequency to remove it from the current response resulting in (0.126), restated here as (3.2) for convenience.

$$I_{\alpha\beta} = \frac{V_c}{\omega_c(\Sigma L^2 - \Delta L^2)}\left(\Sigma L\begin{bmatrix}\cos(\omega_c t)\\ -\sin(\omega_c t)\end{bmatrix} + \Delta L\begin{bmatrix}-\cos(2\theta-\omega_c t)\\ \sin(2\theta-\omega_c t)\end{bmatrix}\right) \tag{3.1}$$

$$I_{\alpha\beta\_nc} = \frac{\Delta L\, V_c}{\omega_c(\Sigma L^2 - \Delta L^2)}\begin{bmatrix}-\cos(2\theta-\omega_c t)\\ \sin(2\theta-\omega_c t)\end{bmatrix} \tag{3.2}$$

$$I^{nc}_{dq\_nc} = \frac{\Delta L\, V_c}{\omega_c(\Sigma L^2 - \Delta L^2)}\begin{bmatrix}-\cos(-2\theta)\\ -\sin(2\theta)\end{bmatrix} \tag{3.3}$$

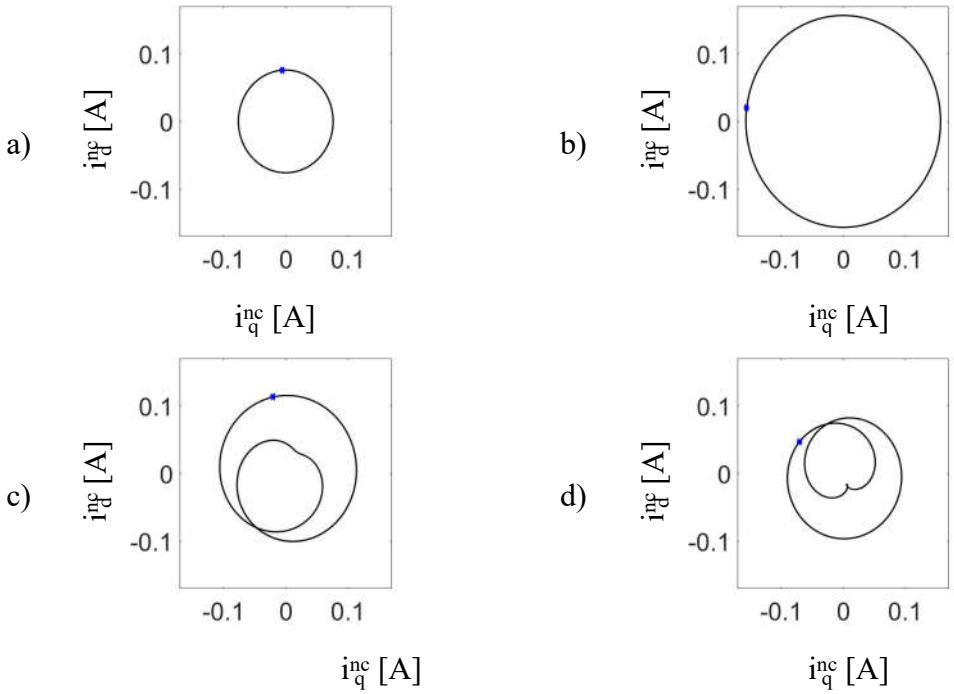

Figure 3.2 – Negative sequence current images in the negative carrier reference frame with current when θ_e=0 marked.

a) ideal current response, b) current response containing cross saturation with L_{dq} = 0.1*ΣL, c) current response with inductance harmonic h_1 = 2 and a multiple harmonic h_2 = 3 with I_{cn1} / I_{cn2} = 2, d) current response containing effects from both b) and c).

Next, the carrier frequency is well known and so transforming the current response into a reference frame which is synchronous with the negative carrier frequency is easily accomplished. This removes the carrier dependence seen in (3.2) and results in simply (3.3). This response is plotted in the complex plane over a full electrical cycle, it results in a circle traced on top of itself twice as shown in (3.2) with the current response when the rotor position iszeroshown as a blue dot for reference. Therefore, each rotor position maps directly onto this circle, albeit with a second mapping offset by 180°. This is analogous to the ellipse in the stationary reference frame being identical to itself when rotated 180° and appears as a problem for heterodyning demodulation as well as other forms of image tracking.

$$L = \Sigma L\begin{bmatrix} 1 & 0 \\ 0 & 1 \end{bmatrix} + \sum_{h} \Delta L_h \begin{bmatrix} \cos(h\theta+\phi_h) & -\sin(h\theta+\phi_h) \\ -\sin(h\theta+\phi_h) & -\cos(h\theta+\phi_h) \end{bmatrix} \tag{3.4}$$

$$I_{\alpha\beta h} = \frac{V_c}{\omega_c\left(\Sigma L^2 - (\sum_{h} \Delta L_h)^2\right)}\left(\Sigma L\begin{bmatrix} \cos(\omega_c t) \\ -\sin(\omega_c t) \end{bmatrix} + \sum_{h} \Delta L_h \begin{bmatrix} -\cos(h\theta-\omega_c t+\phi_h) \\ \sin(h\theta-\omega_c t+\phi_h) \end{bmatrix}\right) \tag{3.5}$$

$$I_{dqh}^{nc} = \frac{V_c}{\omega_c\left(\Sigma L^2 - (\sum_{h} \Delta L_h)^2\right)}\left(\sum_{h} \Delta L_h \begin{bmatrix} -\cos(h\theta+\phi_h) \\ \sin(h\theta+\phi_h) \end{bmatrix}\right) \tag{3.6}$$

The current response can be calculated when both cross-saturation and multiple inductance saliencies are considered into the inductance matrix as shown in (3.4). This results in a full stationary frame current response as in (3.5). Again, note the positive carrier which contains no information, and the portion near the negative sequence which contains many harmonics all of which are position dependent. Applying a high-pass filter in the carrier synchronous reference frame removes the positive carrier component, and transforming the response to the negative carrier reference frame results in (3.6). The current responses with cross-saturation and multiple saliencies are shown in Figure 3.2 b-d. It should be noted that a

simple cross-saturation only changes the phase and magnitude of the current response as shown in Figure 3.2b and the same problems, namely symmetry at 180°, are still present. However, the inclusion of multiple saliencies as shown in Figure 3.2c-d demonstrates uniqueness of the current response at varied rotor position. Of course there are points where the figure crosses over itself and which will present ambiguity if a full image is considered, however it is not the pure overlap of the full cycle at 180° offset as in the other methods and so disambiguation is possible if the rotor is moving or not near one of those few cross-over points.

To form an image, several samples are captured and aggregated to form a time series. When plotted in the polar plane it represents an arc portion of the full electrical cycle with length dependent on the speed.

3.3 Image Tracking Methodology

Using the analysis outlined in section 3.2, the current response considering non-ideal inductances can be used to determine the position. This process is outlined in flow chart form in Figure 3.3, each step will be outlined in the Figure 3.4 through Figure 3.7. In essence it uses a known current response with associated positions, and a small current sample captured in real-time, to match the two currents and use the template's position as a position estimate.

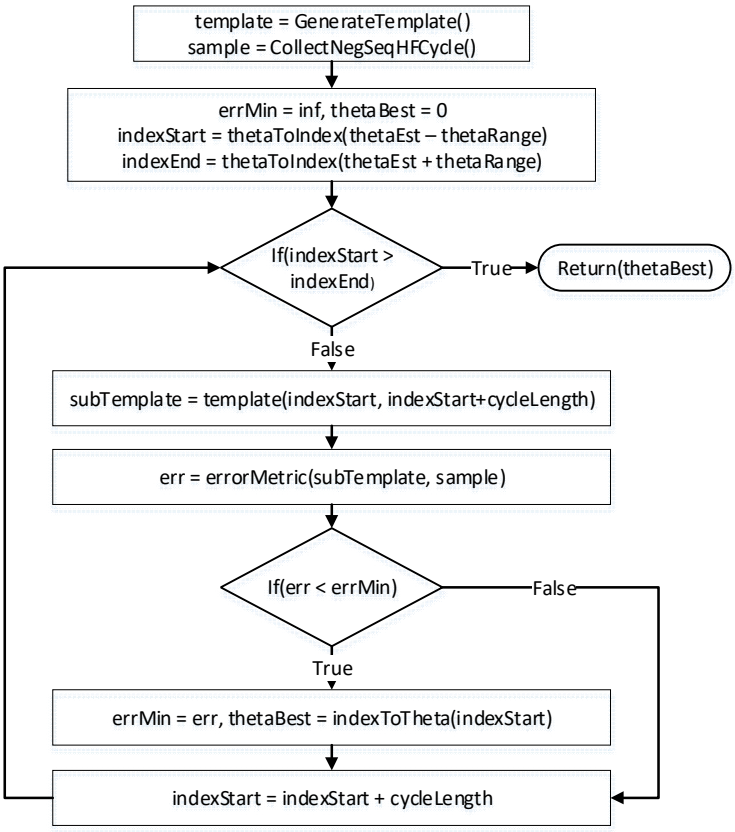

Figure 3.3 – Rotor position estimation using image registration of a negative sequence template and the negative sequence of a full injection cycle.

To begin, a commissioning process is required where the current response to a rotating high frequency voltage injection is captured along with the position. This process can also be accomplished using FEA and simulation if the models accurately predict the current response of the machine. In this work a method using an encoder to commission the machine was performed experimentally. If the template is captured experimentally the full system configuration should be set including inverter, cabling, and controller so that secondary effects are properly captured. A representative template plotted across a full electrical cycle is shown in Figure 3.4a. A zoomed in version is shown in Figure 3.4b with the array indices and associated positions are annotated near the beginning of the electrical cycle.

In real-time operation, a set of current samples is collected. This is shown in Figure 3.4c where N=10 samples are collected and aggregated into a time series. Each of the ten samples is stored in an array with indices shown in Figure 3.4c. N is left to the controls engineer to determine as a larger N will increase the number of switching periods between position estimates thereby potentially increasing lag, where a smaller N will result in a poorer match and a smaller signal-to-noise ratio.

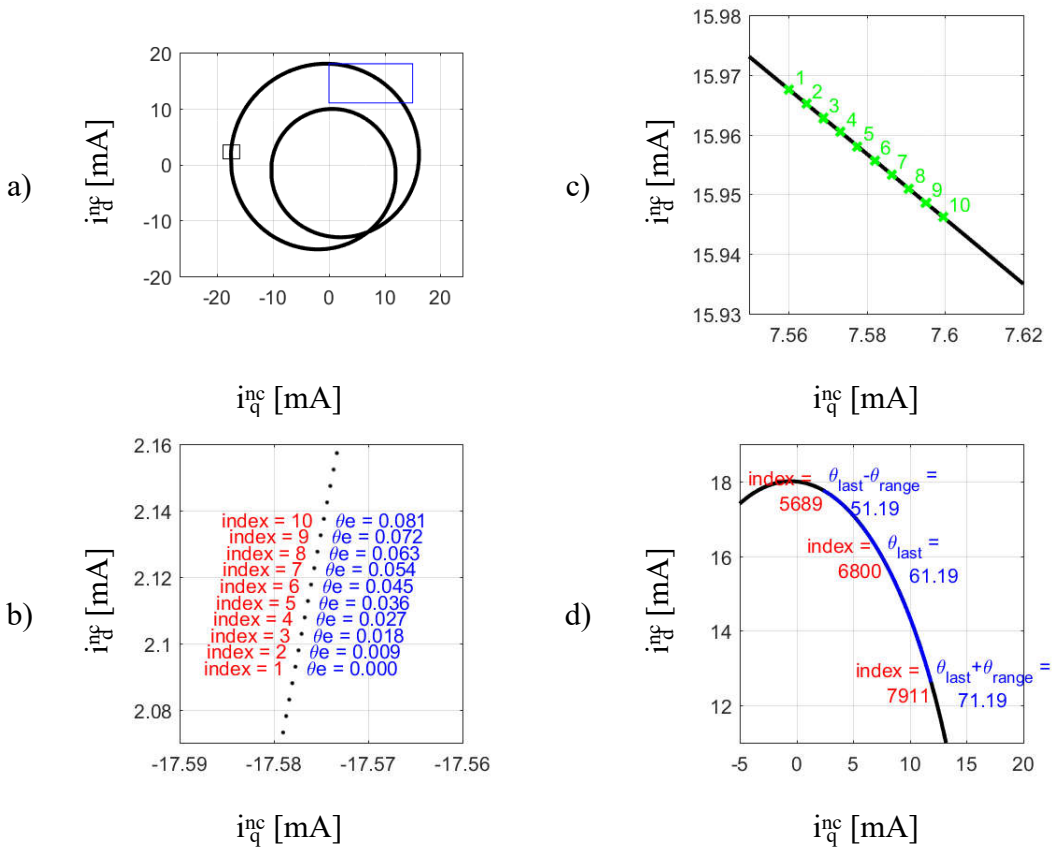

Figure 3.4 – a) template across a full electrical cycle with parameters L_d and L_q from Table 1, and ΔL_1 to be 0.3*ΔL for demonstration, b) template zoomed into black box in 3a showing the start of the electrical cycle with indices and corresponding electrical angles annotated. c) Time sampled current shown with order of the collection shown, overlaid on the template for reference from the blue box area in a), d) 10° range limited template with indices and angles in electrical degrees shown.

To limit the processing required, only a portion of the template is used to determine the position. This process takes the last position estimate as the center of the template arc, and adds and subtracts θ_{range} to obtain the range limited template arc which will be used to find the position. This process is annotated in Figure 3.4d with indices and positions shown for reference.

To find the best match between the sample and the range limited template, portions of size N are selected from the range limited template for comparison with the sample. This is shown in Figure 3.5 where the portion is shown, and a zoomed in version is shown with indices numbered for reference.

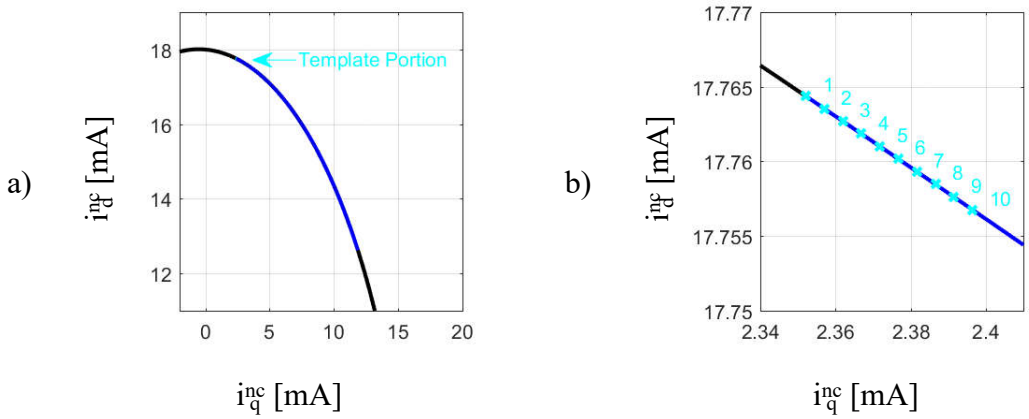

Figure 3.5 – a) Template portion overlaid with range limited template and full template overlaid for reference, b) zoomed in template portion with indices numbered.

$$xcorr(s, t) = \Sigma_n[(t_d(t)\, s_d(t+n) + (t_q(t)\, s_q(t+n)] \quad (3.7)$$

$$error(s, t) = \sqrt{\Sigma_n[(t_{dn} - s_{dn})^2 + (t_{qn} - s_{qn})^2]} \quad (3.8)$$

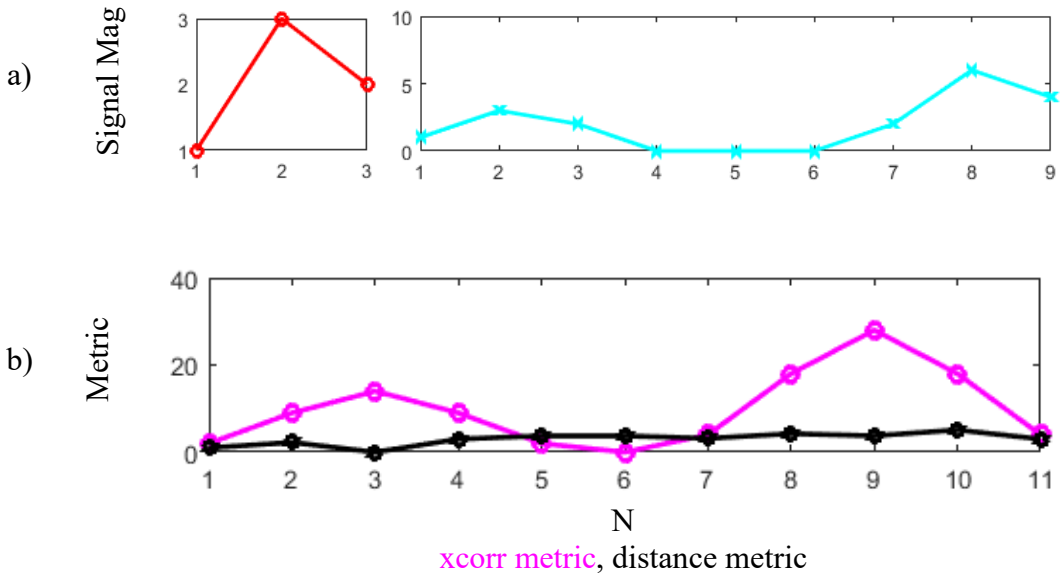

Figure 3.6 – Graphical comparison of error metrics with simple 1-D signals. a) sample signal and template, b) results of applying each metric to the sample and template in a)

Next the arcs must be compared to generate an error metric. In previous work a cross-correlation metric as shown in (3.7) was used. In its most basic form, the cross-correlation has problems with amplitude variation and can match similar shaped patterns between two signals even if the patterns have differing amplitudes. This source of error is shown in Figure 3.6 when the cross-correation between the template and sample are calculated. A peak in the cross-correlation is seen at index 8 which generates the global maximum, when index 2 in the template is the correct match. This is due to the cross-correlation being a multiplication between the sample and template which is sensitive to changes in magnitude in both signals. The correct match will be a local maximum in this case, but is not necessarily the global maximum. There are known ways to handle these errors [90] with cross-correlation. Alternately a different metric can be used such as the two-dimensional Euclidean distance (3.8). Using the same sample and template, the distance is minimized at the second index in Figure 3.6a.

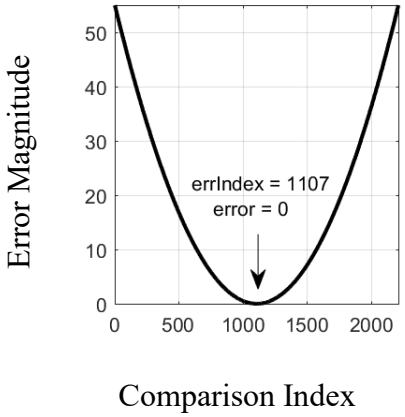

Figure 3.7 – Error metric shown with index of minimum error, and minimum error shown. In simulation the error is zero as all conditions are ideal, in practice it will be a small positive value.

This process is extended into 2-dimensional time series for use with the sampled current and the N-size portion of the range limited template. It is then repeated by incrementing the starting index of the N-size portion of the range limited template and repeating the process. This has the effect of comparing the sample to a slide N-size portion of the template. At each of these slides, the error between the sample and the N-size portion of the template is calculated. After this is completed the observation that the global minimum is the best match can be used to determine the index of the best match as shown in Figure 3.7. Since the template was captured at known positions, finding the best match determines the estimated position. This position estimate can then be used in control algorithms directly or can be fed into a position tracking observer if zero-lag filtering, or additional state estimates are required.

3.4 Arc Length Variation with Speed

The amount of the electrical cycle arc which is captured within N samples is dependent on the speed of the rotor. These effects are shown in Figure 3.8 where an arc captured at four

times higher speed traces out a four-times-longer length of current arc. This results in an error based on speed if the sample and template are captured at differing speeds.

The error metric described in section 3.3 matches each current sample within the sampled arc to the same index within the template portion. The effect of this is that if the arc length of the sampled arc is of a different size than the template portion, the error metric will align the centers of the two arcs as is shown in Figure 3.8. The length of an arc is 360° divided by the number of samples per electrical cycle as shown in (3.9) where N is the number of samples per image or arc, f_e is the electrical frequency and f_s is the system sampling frequency.

As the two arcs are matched at their centers, the error caused by the speed is then the lengths of the template portion and the sample subtracted from each other, divided by two as shown in (3.10) where ft is the electrical frequency at which the template was captured. To analyze the impact this may have, a few example numbers are chosen with N = 10 as is typically used in this work, f_t = 1Hz, f_e = 1Hz, and f_s = 10kHz numbers representative of the situation shown in Figure 3.8 which results in a 0.54° electrical error.

$$\tilde{\theta}_e = 360° \left(\frac{N}{f_s / f_e} \right) \tag{3.9}$$

$$\tilde{\theta}_e = 360° \left(\frac{N}{2} \right) \left(\frac{f_t - f_e}{f_s} \right) \tag{3.10}$$

a)

b)

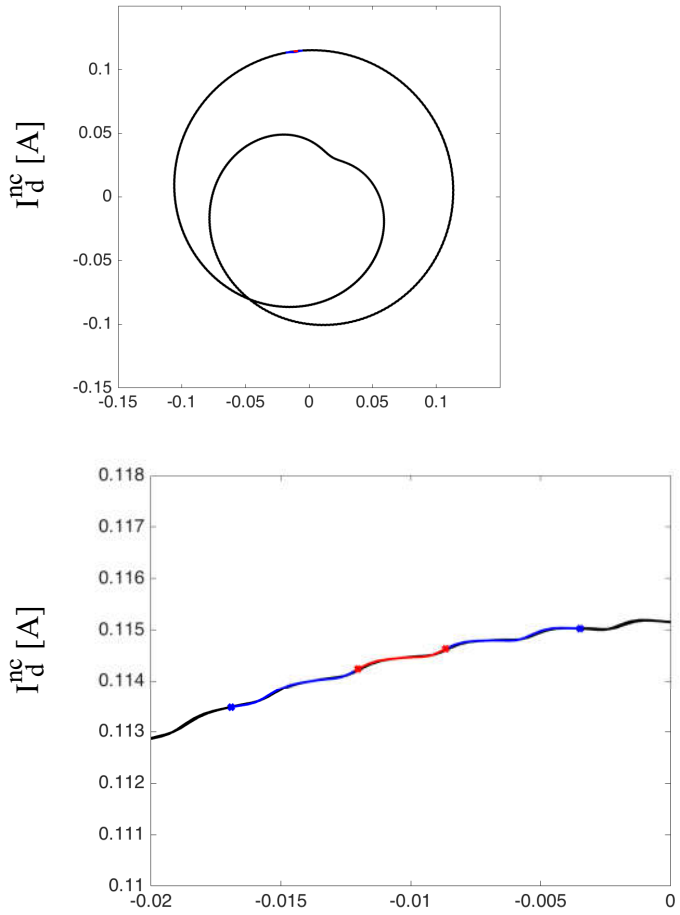

Figure 3.8 – a) Effects of speed on the captured sample arc, b) zoomed in arc portion.

This error is small, but for some applications may be substantial. To compensate for this error, the template should be captured at multiple speed operating points and the correct template selected for that speed. Alternately, if the template is characterized using a tool such as a Fourier series, it could be dynamically resampled at the cost of additional computation power required at runtime.

3.5 Computational Load

Analysis of the computational complexity begins by looking at the program flow outlined in Figure 3.3. The core computations create loop which slides the sampled current response across a portion of the template. In this implementation the operating speed is assumed to be at or near the speed at which the template was collected. This means that the current samples have the same angular spacing between them as the template does which makes calculating the computation required simpler. Additionally, the electrical cycles are all assumed to be identical which reduces the size of the template required.

When the algorithm is designed, the controls engineer selects a thetaRange which is suited for the operation. This is a design variable which impacts the amount computation required as well as the maximum amount of position error which can be accounted for between position estimates. To determine the number of discrete current samples, the resolution of the position sensor used in commissioning is divided by the number of pole pairs as in (3.11). Next the indexRange is found by taking the specified thetaRange in degrees and scaling it by the templateLength divided by electrical degrees in a full cycle as in (3.12). This specifies the angular range to either side of the current estimate which is included in the part of the template which will be compared. The full arc length is given as in (3.13). To determine the number of times the sampled current must be slide across this template arc, the sampled image size is subtracted from the template arc length plus one for the initial comparison as is given in (3.14).

$$\text{templateLength} = \text{encCount} * \frac{2}{\text{P}} \tag{3.11}$$

$$\text{indexRange} = \text{round}\left(\text{thetaRange} * \frac{\text{templateLength}}{360^\circ}\right) \tag{3.12}$$

$$\text{templateArcLength} = 2*\text{indexRange} + 1 \tag{3.13}$$

$$\text{numSlides} = \text{templateArcLength} - \text{imageSize} + 1 \tag{3.14}$$

To compare the current sample with the template, each current sample in the image of imageSize must be compared. To compare each individual sample with the current along the

template, six assignments, four subtractions, two additions, two multiplies, and a comparison are required. If the comparison is true, two additional assignments are required. To calculate the total number of cycles to perform a comparison on the AIX, the number of cycles per instruction were found experimentally and relevant portions are shown in Table 3.1. The total time to compare two individual current samples is calculated as 31 cycles. To find the computations per slide, these 31 cycles must be done for imageSize current samples, which in this work is ten. In total requiring 310 cycles per slide.

Table 3.1 – Cycles Per Instruction

Instruction	Cycles Per Instruction	Number Used Per Comparison	Cycles Per Comparison by Instruction
=	6	2	12
+	2	2	4
-	2	2	4
*	2	2	4
<	7	1	7
Total Cycles Used Per Comparison			31

In Table 3.2 the variables required to calculate the computation time as they were used in this work are given. Multiplying the number of slides by the cycles per slides gives a total execution time per position estimate of 65720 cycles. Given that the AIX operates at 100 MHz, and this work uses a 20 kHz switching frequency, that gives 5000 cycles per control loop. In this work, the cycles to perform normal sensing, control, safety and output functions takes roughly 3500 cycles depending on the settings used, and the branches taken during execution. Obviously the 65720 cycles required by this algorithm cannot be executed within the remaining 1500 cycles so additional hardware must be utilized.

Table 3.2 – Negative Sequence Tracking Settings	
Variable	Value Used
thetaRange	8°
encCount	20000
imageSize	10
numSlides	212
Cycles per Slide	310

3.6 Cost Analysis

To analyze the tradeoff in computation power and monetary costs, several factors must be considered. The main purpose of self-sensing in general is to remove the cost of the encoder from the system while maintaining acceptable resolution and accuracy of the position estimate for the application. Several encoders are considered which were used in this project and are representative of servo grade encoders as shown in Table 3.3. These are characterized particularly on their lines which is a measure of resolution, and their cost. Note that price and resolution are correlated and as one increases the other increases. Throughout this section minimum order quantity is given to capture any effects of higher volume discounts.

Table 3.3 – Encoder specifications.

Manufacturer	Model	Lines	Unit Cost [USD]	Minimum Order Quantity
Tamagawa	TS5208N530	1024	125	1
Heidenhain	ROC 426	10000	425	1
SICK	DFS20A-A2BAC005000	5000	400	1

Next several current sensors are characterized, specifically ones used within this project. Several aspects are of interest. First note that either two or three current sensors can be used, two can be used to perform the reference frame transforms assuming there is no zero-sequence

component to the current. However, to add noise tolerance and fault tolerance to the system three current sensors are considered for this implementation and cost evaluation.

Aspects of the current sensors which must be considered when choosing them for an application are the current range which will be sensed, this is typically determined by the rating of the inverter, motor, and wiring of the system. The current range sensed can be modified by adding additional turns which has the effect of increasing accuracy by the turns ratio but decreasing the maximum current by the turns ratio. The number of turns should be maximized to allow the machine to operating over its entire operating space plus a margin of error, this will allow the full range of the sensor to be utilized and give the controller the highest accuracy measurements possible.

With regards to self-sensing, for a rotating voltage injection, the current response is given in (0.126) and is dependent on the machine saliency, voltage injection magnitude, and voltage injection frequency. The rating of the current sensor, times its accuracy, should be smaller than the magnitude of (0.126) to achieve high quality results. If this is violated, the system should be tested to verify the sensors accuracy by ensuring repeatable measurements compared to another high range, high accuracy current sensor such as a current probe.

The current range, accuracy, and cost are shown in Table 3.4. Note that as current range and accuracy increase, the cost also increases.

Table 3.4 – Current sensor specifications.

Manufacturer	Model	Current Range [A]	Accuracy [%]	Cost [USD]	Minimum Order Quantity
Delta Electronics	C2000	25	1.3	8	20
LEM	LA 55-P	50	0.65	20	25
LEM	HAIS 100-P	100	1	17	25

Finally, the processing requirements are considered. Three processors are considered which are used in aspects of this project and are suitable for real-time control systems. While many characteristics of the chip determine the execution time of the real-time code, clock speed is a good predictor of execution time and is shown for each chip along with its cost in Table 3.5. Note that in general faster clock speeds tend to cost more. The ADSP-21161NKCA is more expensive at the time of writing as it is no longer in production and so the cost has increased.

Table 3.5 – Controller processor specifications.

Manufacturer	Model	Clock Speed [MHz]	Cost [USD]	Minimum Order Quantity
Infineon	TC1782	180	15	1
Analog Devices	ADSP-21161NKCA	100	50	1
NPC	QorIQ PS5021	2000	280	1

Combining all of these into representative systems and assuming that the associated inverters, ADC circuitry, and other signal routing and condition circuitry is roughly comparable in cost and can therefore be neglected results in the systems shown in Table 3.6.

Configuration 1 represents a high-resolution encoder on a low power system, while configuration 2 represents the same system without an encoder. These systems form the basis for the analysis provided in Chapter 4 and 6.3Appendix A and are suitable for traditional demodulation schemes and offline image tracking evaluation.

Next 3 and 4 represent commercial systems using a moderate and high-resolution encoder respectively, with system costs increasing with higher resolution. Configuration 5 shows the same system configured with a higher accuracy current sensor, and more powerful processor, but without the encoder. These systems form the basis for the analysis provided in Chapter 5 and 6.3Appendix B are suitable for traditional as well as image tracking demodulation schemes.

Table 3.6 – Representative system configurations.

Configuration Number	Processor	Encoder	Current Sensor (3)	System Cost
1	ADSP-21161NKCA	DFS20A-A2BAC005000	HAIS 100-P	525
2	ADSP-21161NKCA	-	HAIS 100-P	125
3	TC1782	TS5208N530	C2000	165
4	TC1782	ROC 426	C2000	465
5	QorIQ PS5021	-	LA 55-P	340

Overall, the cost analysis shows that self-sensing systems can remove the cost of the encoder but may require an increase in cost in the current sensors. This comes with the tradeoff of lower accuracy, which in some applications such as servo motors, may be unacceptable. To regain some of this accuracy, an image tracking solution could be applied. This comes with the additional tradeoff that the increase in accuracy is paired with an increase in the cost of the processing power. In applications where high accuracy is still required while the cost of the encoder would preferably be removed, image tracking becomes an attractive option. Furthermore, image tracking is suitable for a dedicated implementation in either FPGA or ASIC which would increase development costs but decrease manufacturing costs further.

3.7 Summary

The current response to a high frequency rotating voltage injection can be formulated in the negative sequence to isolate and highlight the position dependent component. The negative sequence can be accumulated into a time series image and with the use of a template generated a priori can be used to estimate the rotor position. The error metric used for matching has a large impact on the quality of the match, a distance metric is suitable for the two-dimensional data used in the negative sequence image. Arc length variation is a minor concern as at low speeds this will be a small fraction of an electrical degree. For extremely high precision, template

resampling can be instituted to generate variable length templates in real-time, at the cost of additional computational power. Computational power in general is a concern with this method and effectively trades off increased computational power for increased accuracy. This tradeoff will increase price but for some high precision application at low speed the tradeoff may be worth the effort.

Chapter 4 Negative Sequence Image Tracking Evaluation on a 13 Watt Low Saliency Ratio SPMSM

4.1 Overview

The methods presented in Chapter 3 are evaluated in simulation and offline experiments on a low saliency ratio SPMSM developed in [91]. This machine's parameters are specified in Table A.1 and tuning is specified in Table A.2. These parameters and tuning are used throughout this chapter for simulation evaluation of the image tracking methodology. The controller integrated into this test bench is based on an ADSP-21161NKCA-100 processor which is a 100 MHz processor. Operating at 20 kHz, this proved to be too low of processing power for an online implementation to validate the experiments. However, the initial offline evaluation is provided in 4.4.

4.2 Simulated Ideal Response on a Low Saliency SPMSM

To begin with, the negative sequence image tracking method was implemented and directly replaced the heterodyning demodulation from the state-of-the-art rotating demodulation. The command tracking and closed-loop estimation accuracy are shown in Figure 4.1. Performance here shows significant error with periodic segments of oscillation. The current at startup is shown in Figure 4.2 with the template overlaid for reference. Note that the sampled current is two orders of magnitude larger than the current expected in the template. This effect results from the closed-loop properties when using the speed estimate from the cascaded position observer to decouple back-EMF effects from the current. The oscillations and quick change in

position error result in large speed errors. This erroneous speed is used to decouple the back-EMF from the current and introduces large high frequency content into the current spectrum. This results in a current image which deviates largely from the expected current and generates poor position estimates. This cycle feeds back to drive the phenomena shown in Figure 4.1 and Figure 4.2.

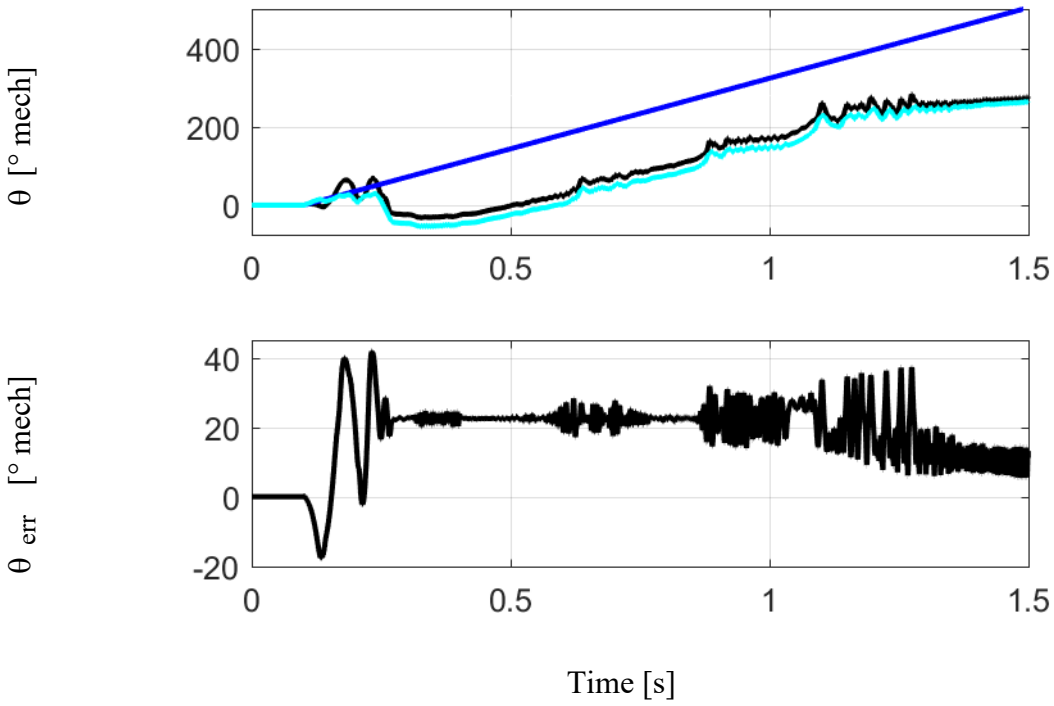

θ , θ^*, $\hat{\theta}_{nst}$

ω_m^* = 1 Hz, 15/3/0.6 Hz MC

Figure 4.1 – Simulated time-domain estimation accuracy and command tracking using closed-loop self-sensing feedback at startup with only a position cascaded observer.

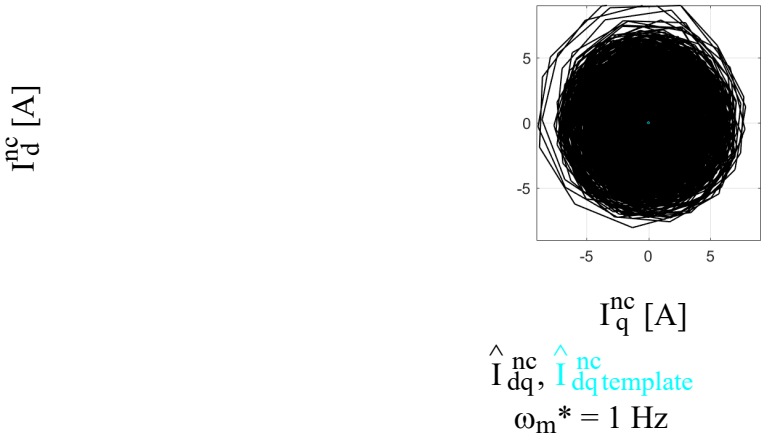

Figure 4.2 – Experimental negative sequence response for at startup with only a cascaded position observer.

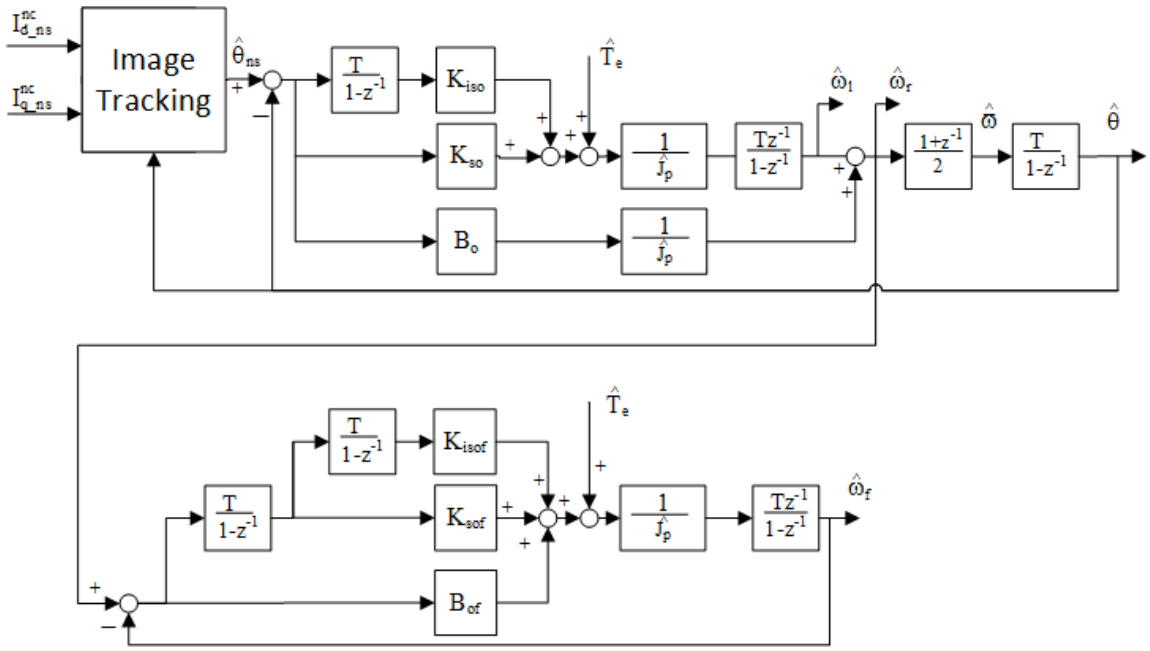

Figure 4.3 – State block diagram of Negative Sequence Image Tracking with a cascaded saliency tracking observer to generate position estimates, with a cascaded speed observer to provide a zero-lag filtered speed estimate.

S cascaded speed observer was added to the negative sequence image tracking solution to mitigate errors caused by small steps in position estimation causing large speed estimation errors, and the feedback loop of speed-based back-EMF decoupling errors leading to additional position

estimation errors and propagating into unstable or oscillatory states. This is a truncated version of the position estimation observer, with a similar tuning process as outlined in section 6.3A.5 . In this section, the cascaded speed observer was tuned to a bandwidth of 5Hz, and for a fair comparison it was also added to the state-of-the-art rotating voltage solution which is also able to take advantage of the cleaner back-EMF decoupling to achieve higher bandwidths than those presented in section 6.3A.12 . An alternate solution, albeit with a performance decrease, is to neglect the back-EMF decoupling and cross-coupling decoupling in the low speed region by setting the ω_{fb} to 0. This solution is a reasonable approximation in many applications as ω_m is small and so these cross-coupling terms are likewise small.

To evaluate the estimation accuracy, the motion control feedback was set to the motion observer, and the saliency tracking observer command feed-forward was disconnected to show the estimation properties of both rotating voltage demodulation and negative sequence image tracking without the effects of torque command feed-forward tracking. The estimation accuracy in the frequency domain is shown in Figure 4.4 comparing both rotating voltage demodulation and negative sequence image tracking each with the highest achievable bandwidth. The effects of the higher achievable negative sequence image tracking system bandwidths are clear. The rotating voltage demodulation is tuned to a motion controller bandwidth of 15Hz and a saliency tracking observer bandwidth of 30Hz. These tunings agree with the results presented in the estimation accuracy FRF with an achieved bandwidth of 34Hz according to the magnitude criteria, and 25Hz according to the phase criteria. The negative sequence image tracking system is tuned to a motion controller bandwidth of 50Hz, and a saliency tracking observer bandwidth of 100Hz. These tunings are confirmed with an achieved bandwidth of 100Hz according to the magnitude criteria and 66Hz according to the phase criteria. This confirms the improved performance of the higher achievable stable system bandwidths under negative sequence image tracking.

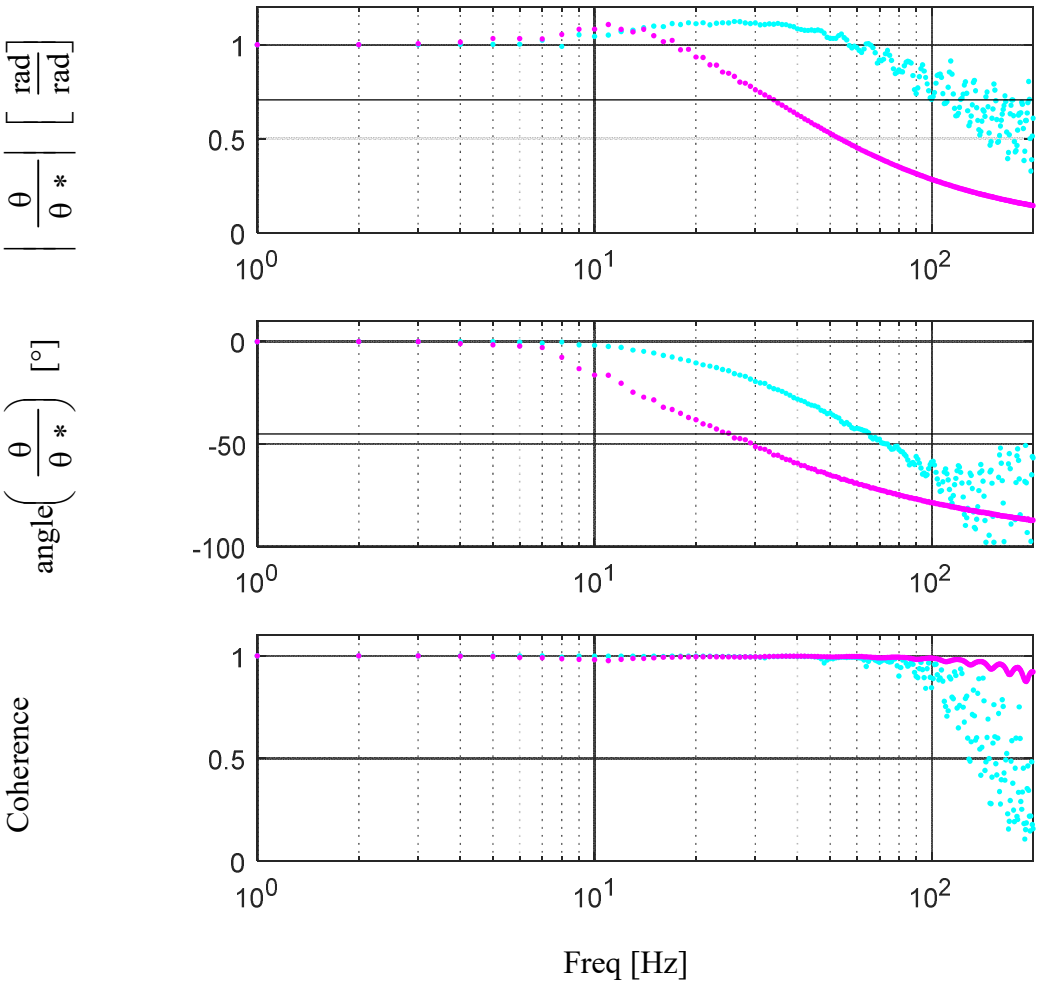

Rotating FRF 15/3/0.6 Hz MC, NSIT FRF 50/10/2 Hz MC, BW References
ω_m* = chirp with f_0 = 1Hz, f_1 = 200Hz, T = 5s, magnitude = 1Hz, DC offset = 1Hz

Figure 4.4 – Estimation accuracy comparison of the self-sensing methods when T_{cff} was removed from the cascaded saliency tracking observers.

The improved estimation accuracy of negative sequence image tracking is also shown in the time-domain estimation accuracy results presented in Figure 4.5 and Figure 4.6. In Figure 4.5 the comparison is shown between a rotating voltage demodulation system tuned with a motion controller tuned to 15Hz and saliency tracking observer tuned to 30Hz is compared to negative sequence image tracking systems tuned with system bandwidths of 15Hz and 50Hz for fair comparisons. In steady-state, the error of the rotating voltage system is 0.2 degrees, while

the maximum error of the 50Hz bandwidth negative sequence image tracking system is 0.1 degrees, and the maximum error of the 15Hz bandwidth negative sequence image tracking system is 0.04 degrees. The error present in the rotating voltage demodulation is identified as due to the effects of the stationary frame voltage latch, which are assumed to be negligible in the state-of-the-art, and are shown to be very small in this figure. However, in both negative sequence image tracking solutions the estimation accuracy is significantly improved, and the achievable bandwidth is additionally improved. The higher bandwidth solution performs slightly worse as the entire system more aggressively tracks the small estimation errors resulting from imperfect pattern matching. In Figure 4.6 the same steady-state is shown zoomed in on individual time steps.

The effects of the stationary frame voltage latch are magnified here as the rotating demodulation saliency tracking observer is 0.2 degrees off, which equates to about ten time steps lagging, where the observer should ideally be 1 time step ahead. The negative sequence image tracking on the other hand performs as expected and estimates with a very small degree of error and is 1 time step ahead. It is also visible that position estimates are generated every time step at 20 kHz, while the negative sequence image tracking is generating position estimates at 2 kHz. This is due to the negative sequence image tracking position estimate being fed into the saliency tracking observer, but the observer itself runs at 20 kHz using the open loop model and the command feed-forward to provide accuracy position estimates at every controller switching period.

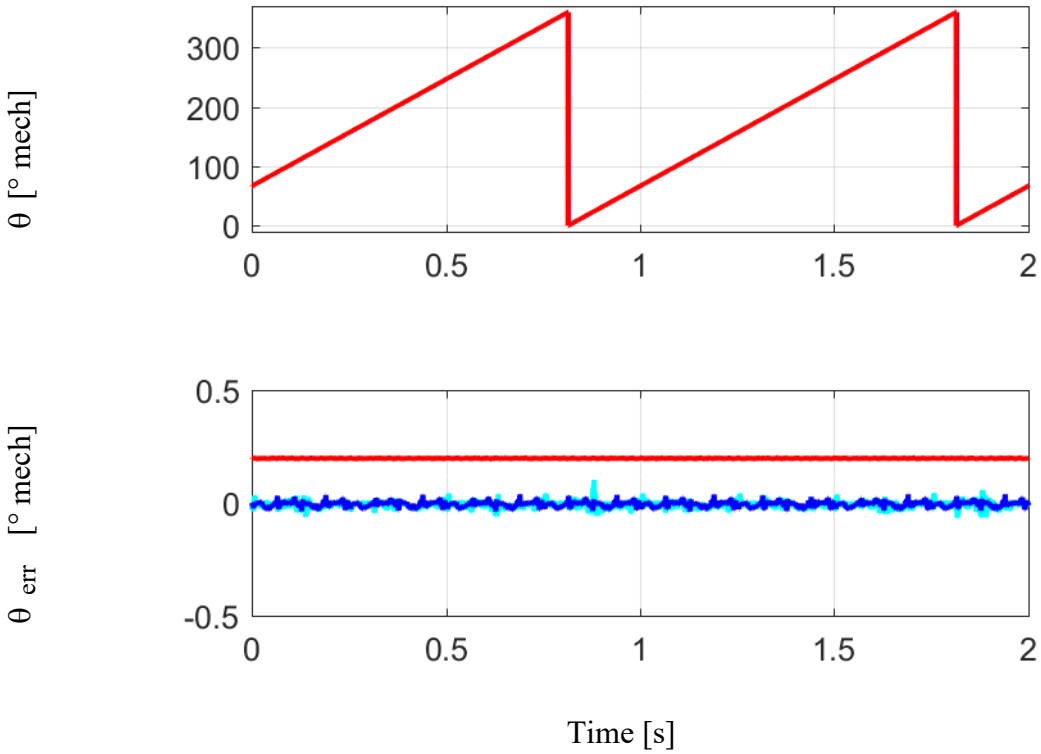

Rotating 15/3/0.6 Hz MC, NSIT 15/3/0.6 Hz MC, NSIT 50/10/2 Hz MC

$\omega_m^* = 1$Hz

Figure 4.5 – Simulated time-domain estimation accuracy using closed-loop self-sensing feedback with a motion controller tuned to the highest achievable stable bandwidth.

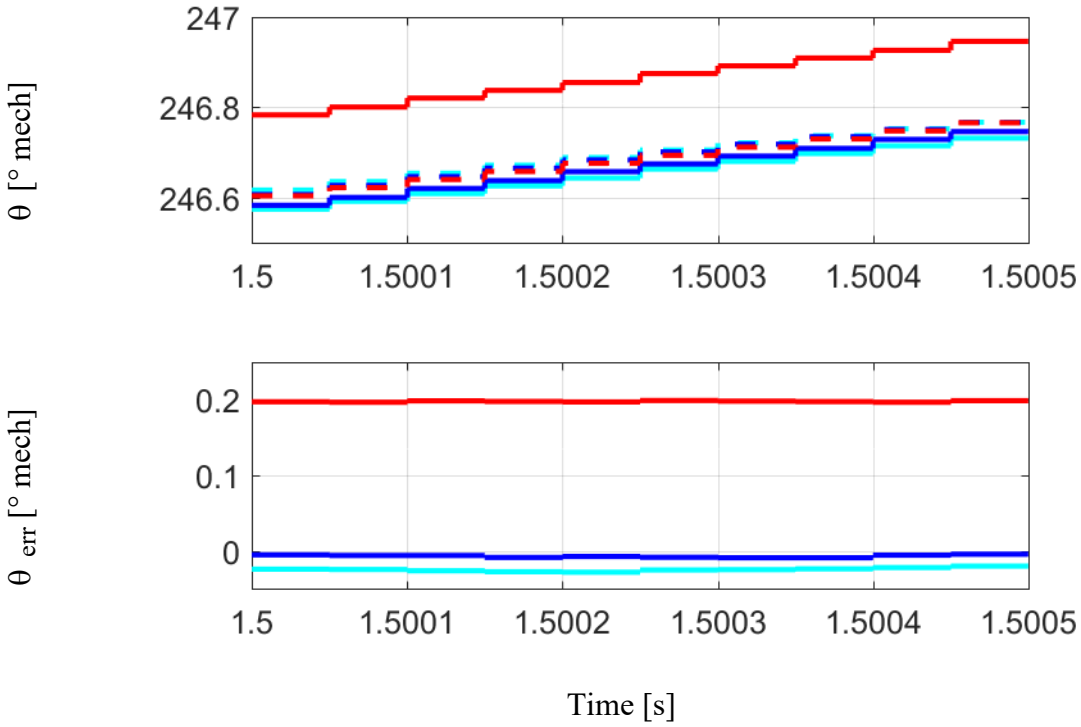

Rotating 15/3/0.6 Hz MC, NSIT 15/3/0.6 Hz MC, NSIT 50/10/2 Hz MC
Solid Line – Encoder Position, Dashed Line – Estimated Position
ω_m^* = 1Hz

Figure 4.6 – Simulated time-domain estimation accuracy with closed-loop self-sensing feedback with a motion controller tuned to the highest achievable stable bandwidth.

Figure 4.7 shows the comparison of the startup response of each system at startup. In each system, there is an initial transient when the machine applies a torque to accelerate to the steady-state speed command. This torque generates a small change in the negative sequence current

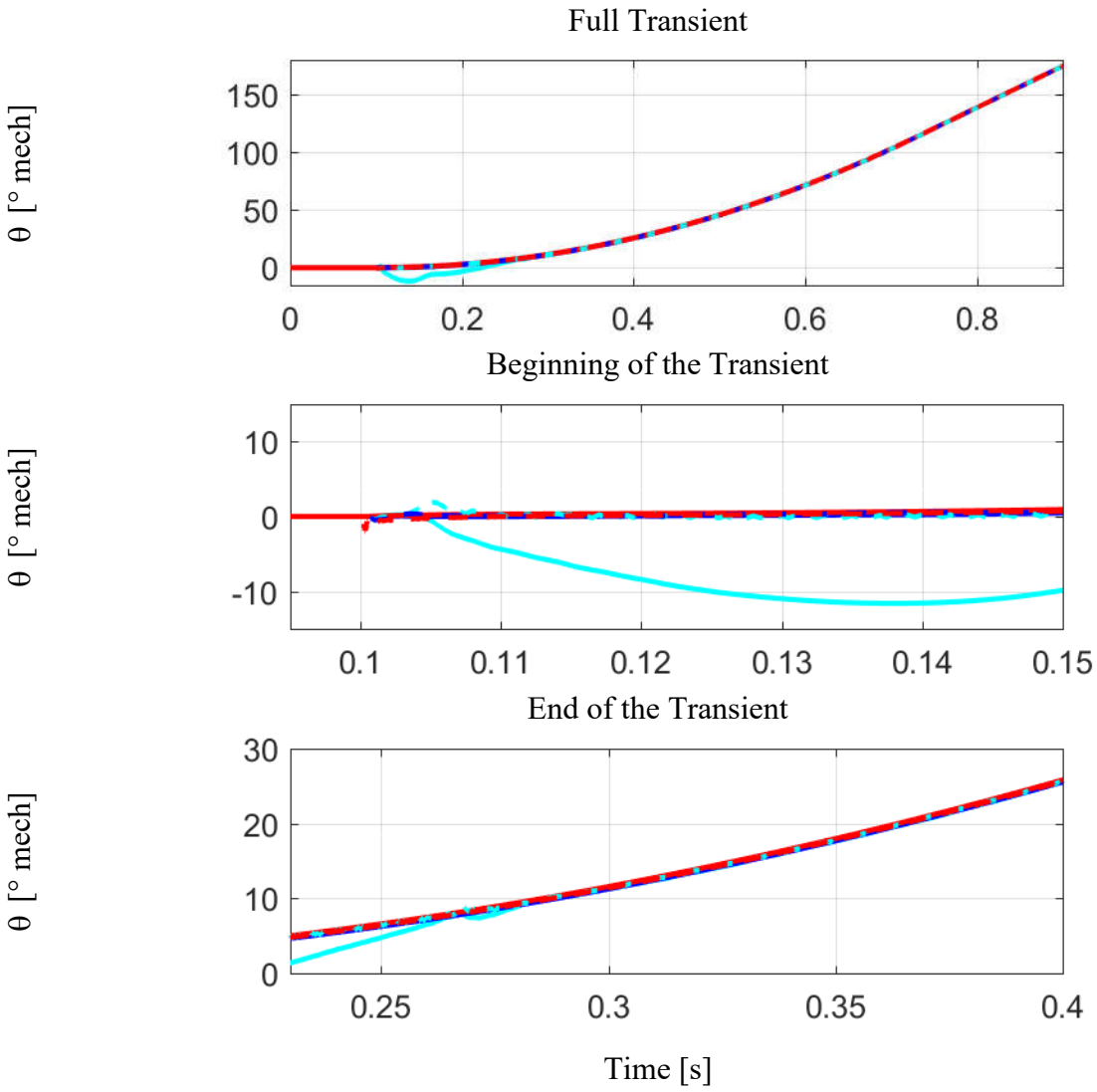

Rotating 15/3/0.6 Hz MC, NSIT 15/3/0.6 Hz MC, NSIT 50/10/2 Hz MC
Solid Line – Encoder Position, Dashed Line – Estimated Position
$\omega_m^* = 1$Hz

Figure 4.7 – Simulated closed-loop self-sensing feedback with a motion controller tuned to the highest achievable stable bandwidth as noted, zoomed to beginning and end of the startup transient.

response and in each system, there is some initial position estimation error. In each system, within 0.2s after the initial command is given, the system has settled back into a low error estimate of position and is tracking correctly. The system with the highest bandwidth has the

largest error as any errors in the position estimate due to disturbances in the negative sequence are most aggressively tracked. In Figure 4.8, the maximum error is shown to be in the high bandwidth negative sequence image tracking solution of -12° compared to 2° for rotating voltage demodulation and 0.5° for the low bandwidth negative sequence image tracking system. This situation presents an interesting design tradeoff as a higher system bandwidth will more aggressively track

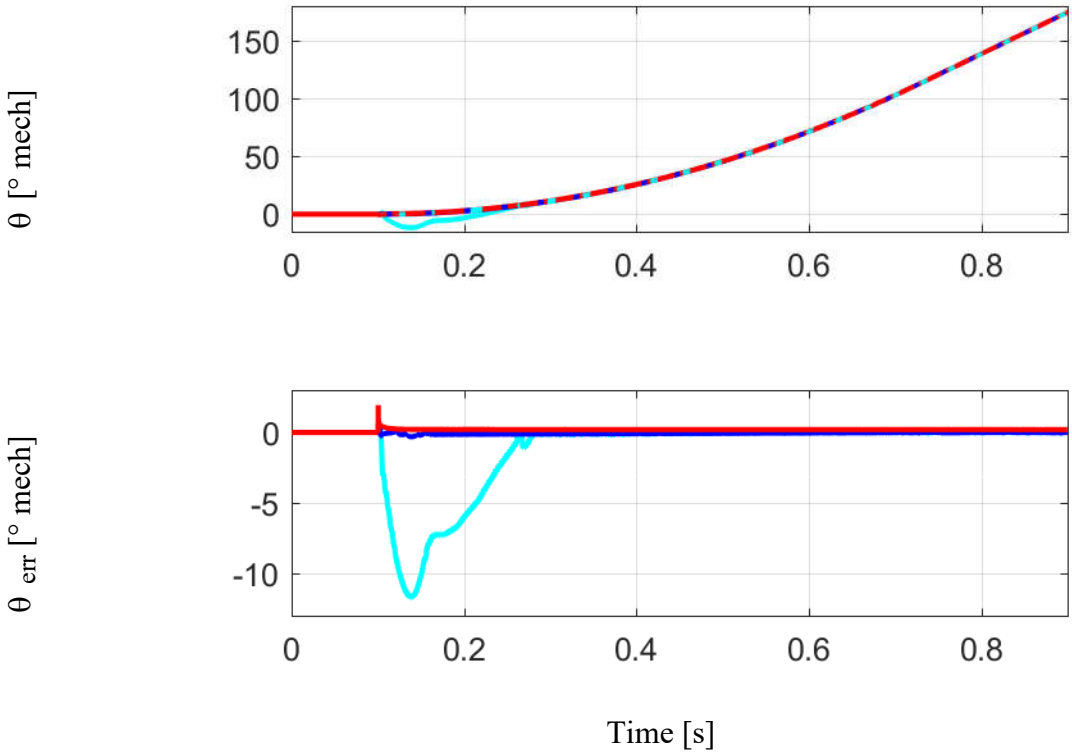

Rotating 15/3/0.6 Hz MC, NSIT 15/3/0.6 Hz MC, NSIT 50/10/2 Hz MC
Solid Line – Encoder Position, Dashed Line – Estimated Position
$\omega_m^* = 1$Hz

Figure 4.8 – Simulated closed-loop self-sensing feedback with a motion controller tuned to the highest achievable stable bandwidth as noted, with a ω_m^* of 1Hz at steady-state.

errors in the negative sequence causing substantial position errors during transients. However, comparison of a rotating voltage demodulation system with a negative sequence image tracking

system of the same bandwidth shows an increased estimation for the negative sequence image tracking during the transient. This leaves the choice of higher system bandwidth and the associated benefits at the loss of some accuracy during transients, or lower system bandwidth for higher accuracy during transients than state-of-the-art rotating demodulation.

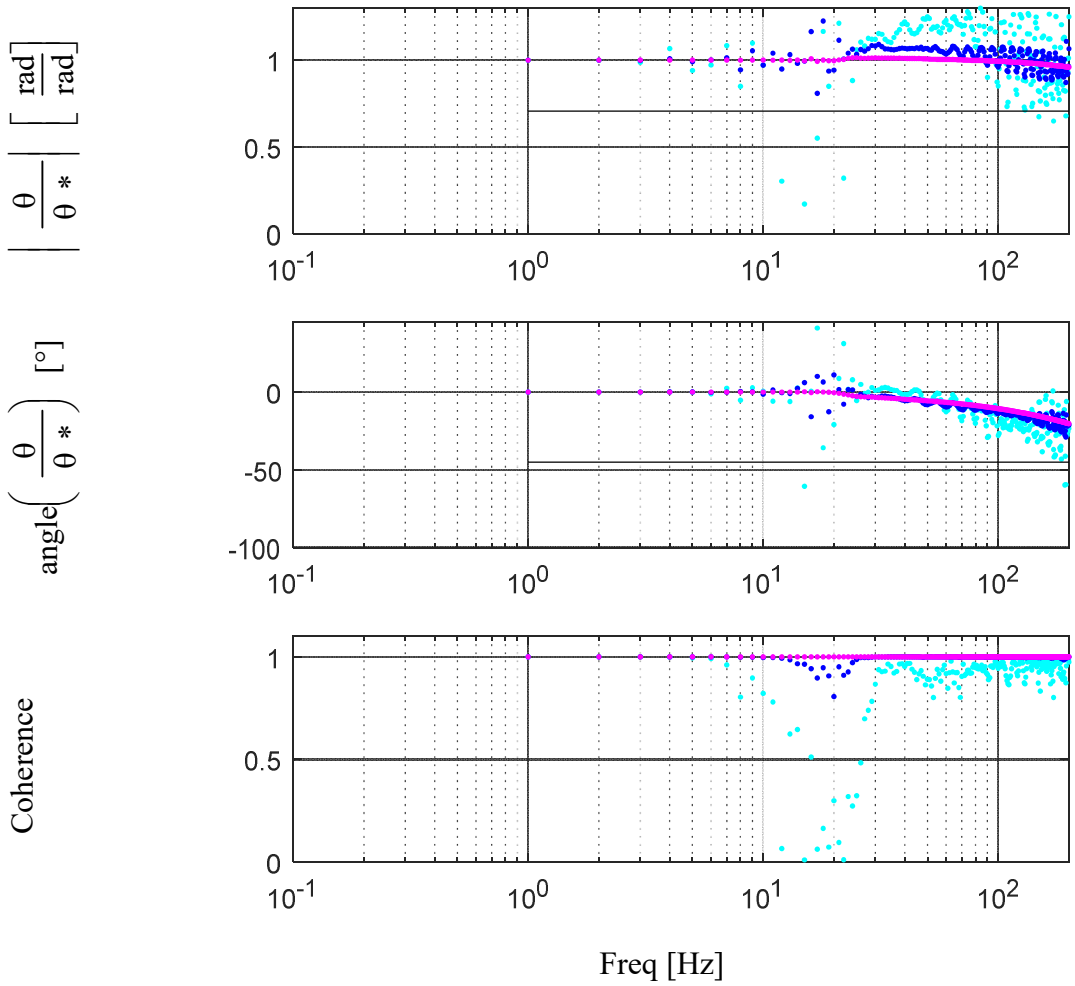

Rotating FRF 15/3/0.6 Hz MC, NSIT FRF 15/3/0.6 Hz MC, NSIT FRF 50/10/2 Hz MC
ω_c* = chirp with f_0 = 1Hz, f_1 = 200Hz, T = 5s, magnitude = 1Hz, DC offset = 1Hz

Figure 4.9 – System command tracking comparison of the self-sensing methods.

System command tracking performance in Figure 4.8 is similar between the three combinations of tuning and position estimations. The system includes command feed-forward for the motion controller and so shows similar magnitude and phase between all three configurations. The system begins to degrade at higher frequencies in both magnitude and phase due to the limitations of the motion command state filter which is tuned to 200Hz.

The simulated dynamic stiffness comparison between state-of-the-art rotating demodulation and negative sequence image tracking is shown in Figure 4.10. Here the effects of the increased system bandwidths are more clearly seen as the dynamic stiffness of the negative

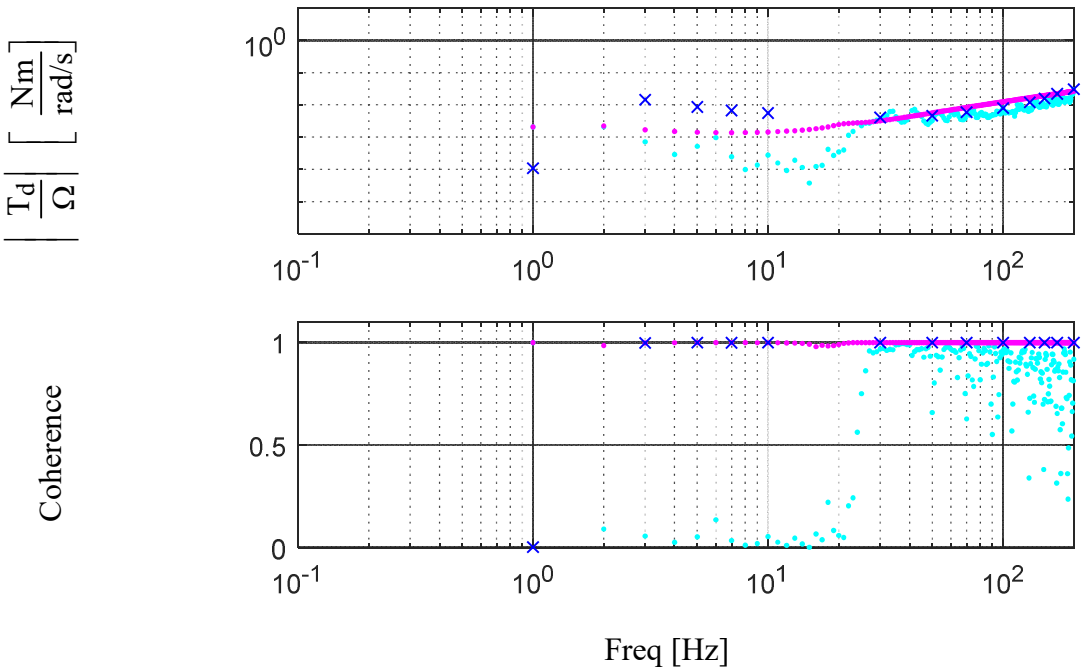

NSIT Dynamic Stiffness with MC tuned to 50Hz from: Chirp FRF, Single Sine Test
Rot Dynamic Stiffness with MC tuned to 15Hz from: Chirp FRF
T_d* chirp with f_0 = 1Hz, f_1 = 200Hz, T = 0.5s, magnitude 0.1pu

Figure 4.10 – Simulated dynamic stiffness FRF comparing rotating demodulation with negative sequence image tracking feedback.

sequence image tracking demonstrates the 50Hz motion controller tuning and increased lower frequency dynamic stiffness when compared to state-of-the-art rotating demodulation with motion controller tuned to 15Hz.

4.3 Simulated Non-Ideal Inductance Response on a Low Saliency SPMSM

In section 6.3A.12.2 , the effects of non-ideal properties are discussed with their effect on the current response to a rotating high frequency voltage injection. These same effects will show up in the negative sequence image according to the same equations. In Figure 4.11, the effects of cross-saturation and a single multiple saliency are shown. Additionally, a reference point representing the current response with the rotor position is at $\theta=0°$ is noted to show the effects on the image phase. In Figure 4.11a, the simulated image with ideal properties is shown. In Figure 4.11b, the image with a cross-saturation is shown. Note that the shape is the same, but the magnitude and phase change according to the current response including cross-saturation effects as denoted in (0.133). In Figure 4.11c, the effects of a single multiple saliency are shown. Here the image has more harmonic content and loses the symmetry the ideal case has when $\theta_e=180°$ as governed by the current response in (0.136). Finally, in Figure 4.11d, the effects of both cross-saturation and multiple saliencies are shown. The image is similar to Figure 4.11c, but with a noticeable rotation due to the cross-saturation, and a modulation of the amplitude.

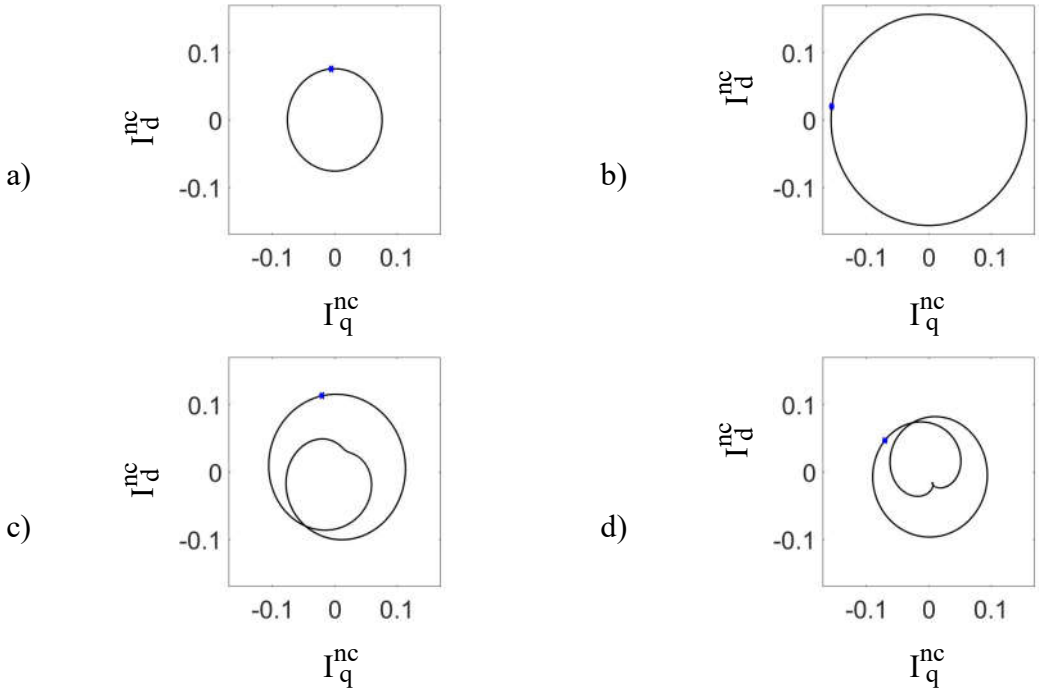

a) Ideal current response
b) Cross-saturation current response with $L_{dq} = 0.1\Sigma L$
c) Multiple saliency response with $h_1 = 2$, $h_2=3$ with $I_{cn1} / I_{cn2} = 2$
d) Current response with cross-saturation from b) and multiple saliency from c)

Figure 4.11 – Negative sequence current images in the negative carrier reference frame when $\theta_e=0$ highlighted to show relative phase

If the template and sample data are from the same model, then matching will produce the correct result. However, machine properties change with operating point. This machine was specifically designed to have zig-zag leakage flux which causes the saliency [91], but also has saturation effects in the current due to load as shown in [2, 57, 91]. So, while the collection of experimental templates at known operating points will allow matching at those operating points, if the operating point drifts, the machine properties will change and the sampled arc will not perfectly match against the template arc.

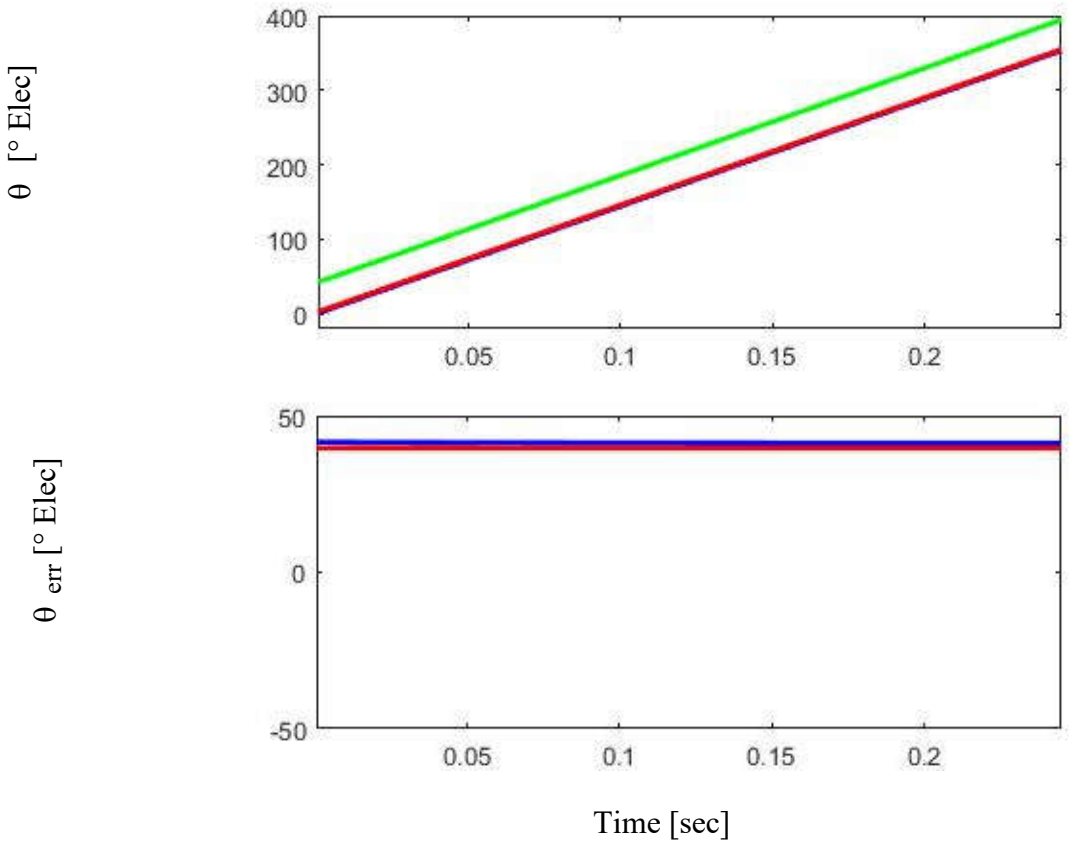

Figure 4.12 – Simulation results comparing estimation accuracy of self-sensing methods with cross-saturation that is not decoupled or included in the negative sequence image tracking template.

To analyze these effects, a simulation was performed using negative sequence image tracking with an ideal template, but with the effects of non-ideal inductance properties to allow analysis of how the algorithm will perform in these unknown conditions. For comparison, the simulation was also performed with rotating demodulation using a normal demodulation process with no cross-saturation or multiple saliency compensation was analyzed. In Figure 4.12 an exaggerated cross-saturation was applied. The results show that this uncompensated for cross-

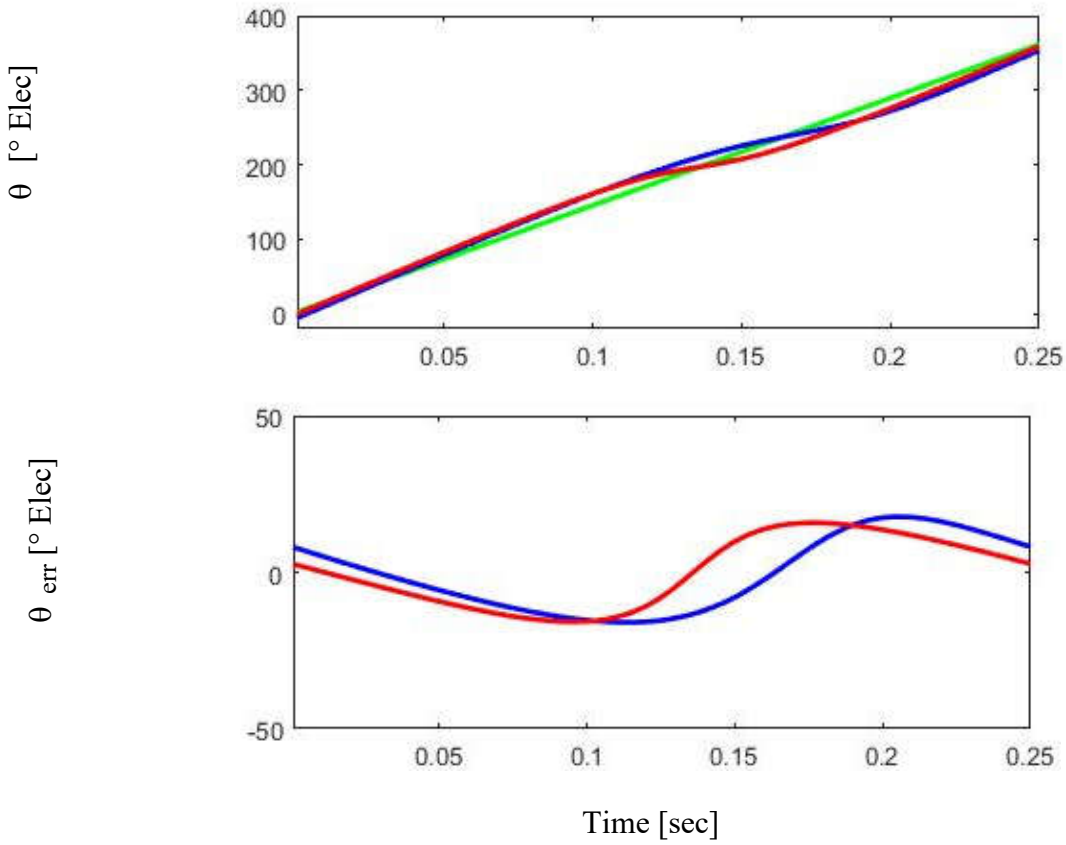

Actual Position, Rotating Point-Tracking, Neg. Seq. Image Registration
Multiple saliency: h_2=3 and I_{cn1}/I_{cn2} = 2

Figure 4.13 – Simulation results comparing estimation accuracy of self-sensing methods with a secondary inductance harmonic that is not decoupled or included in the negative sequence image tracking template.

saturation has the same effect on both rotating and negative sequence image tracking. Furthermore, in Figure 4.13, a similar test was performed using an ideal template for negative sequence image tracking, and an ideal demodulation with no multiple saliency compensation for the rotating self-sensing. Here the results are similar with the same magnitude error using both demodulations, but with a phase shift due to the pattern matching of negative sequence.

4.4 Offline Estimation Accuracy Evaluation on a Low Saliency SPMSM

Further analysis was performed experimentally. While the algorithm is complex and cannot be run in real-time on the AIX controller, a rotating voltage was applied with filtering as described in [2, 57]. The negative sequence image was then plotted over four electrical cycles. This shows that there are small variations in each electrical cycle, likely due to small manufacturing defects. For reference, an injection arc in shown to show the size of the segment traced out when the rotor is spinning at 1Hz mechanical.

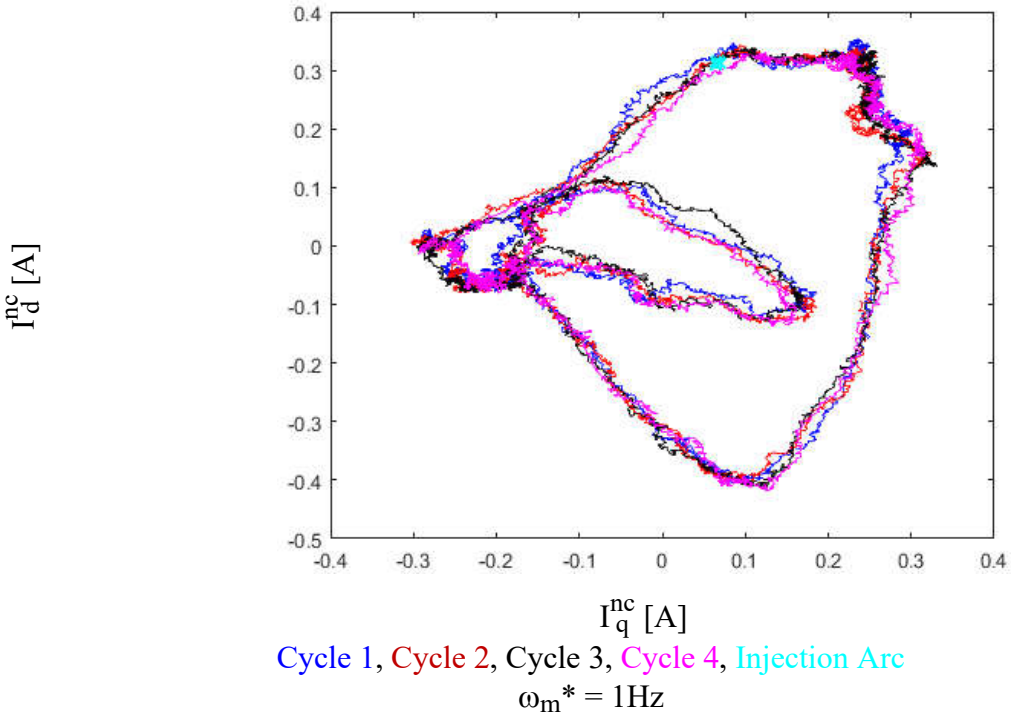

Figure 4.14 – Experimental negative sequence response for four consecutive electrical cycles comprising a full mechanical cycle with an injection cycle included for reference.

One of these cycles was used as a template, while the others were used as sample data and processed according to the negative sequence image tracking method presented in Figure

3.3. The data was processed offline to generate the offline position estimation accuracy as shown in Figure 4.15. This is plotted against the rotating vector demodulation for the same set of data. It is clear that the error is significantly reduced. The underlying reason is that the template captures the non-ideal effects which rotating demodulation does not compensate for and so it is able to provide a more accurate position estimate than rotating demodulation.

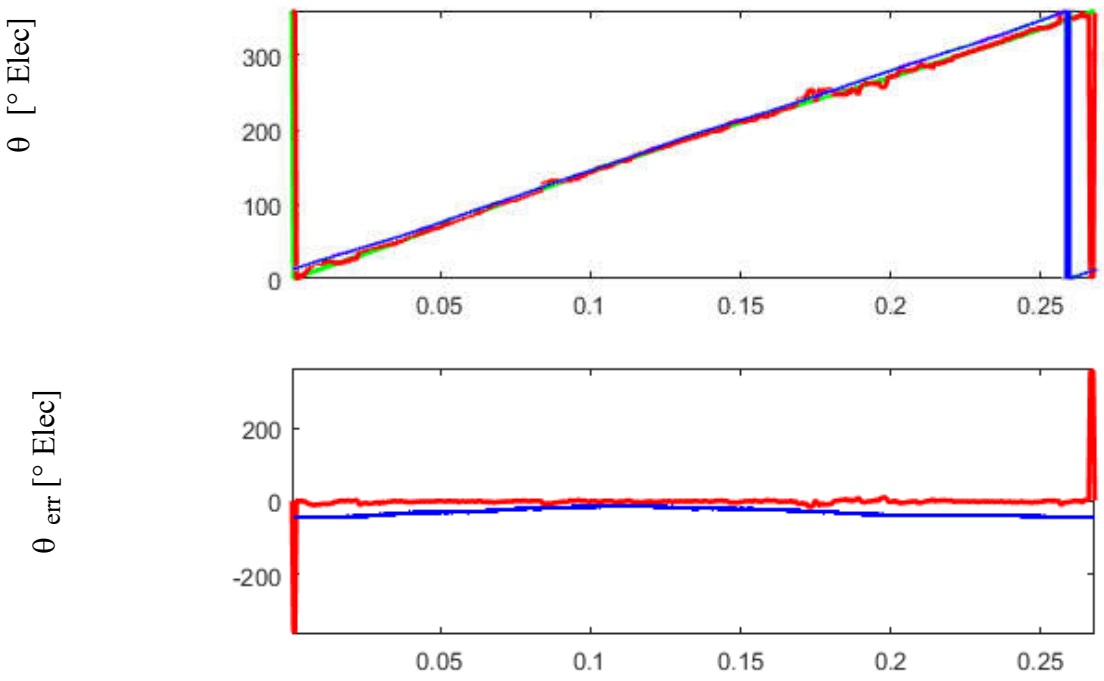

Figure 4.15 – Experimental estimation accuracy calculated offline with experimental data comparing position estimates from rotating demodulation and negative sequence image tracking.

4.5 Summary

This chapter demonstrates by both simulation and experimental results the practical challenges to implementing NSIT, as well as other self-sensing algorithms, during transients. Also shown is how to formulate the speed feedback so that tracking can be maintained. Furthermore, simulated results show an improvement in achievable steady-state accuracy by 50% and an improvement in achievable system bandwidths by 3.3x. Additionally, a design tradeoff was demonstrated showing that during transients the improved bandwidth can increase estimation error temporarily, but that at comparable tuning between heterodyning demodulation and image tracking, the image tracking method shows improved accuracy even during the transients. Finally, the offline estimation accuracy shows an improvement over heterodyning demodulation demonstrating by 30% the viability of the method if computation power is available.

Chapter 5 Negative Sequence Image Tracking Evaluation on a 3.7 kW Low Saliency Ratio SPMSM

5.1 Overview

The methods presented in Chapter 3 are evaluated in simulation and online experiments on a low saliency ratio SPMSM developed in [46, 47]. This machine's parameters are specified in Table B.1 and Table B.2 and tuning is specified in Table 5.2 and Table 5.3. These are used throughout this chapter for simulation and experimental evaluation of the image tracking methodology. The controller integrated into this test bench is a dSpace MicroLabBox based on a dual core, 2GHz DSP.

5.2 Simulated Ideal

A simulation was created to implement the control structures shown in Figure 3.1 and Figure 3.3. The parameters for the simulation are the same as for the experimental machine and are given in Table B.1 and Table B.2 while the bandwidths used for the various control structures is given in Table 5.1. For demonstration purposes a rotating voltage injection with heterodyning demodulation implementation was created for use as a reference point.

Table 5.1 – Simulated Control Structure Tuning

Control Structure	Bandwidth [Hz]
Current Regulator	500
Fundamental Current Observer	100
Current Observer Carrier HPF	200
Motion State Filter	200
Motion Controller	X
Saliency Tracking Observer	2X
Demodulation LPF	6X
*X specified in corresponding tests, ratios constant between methods.	

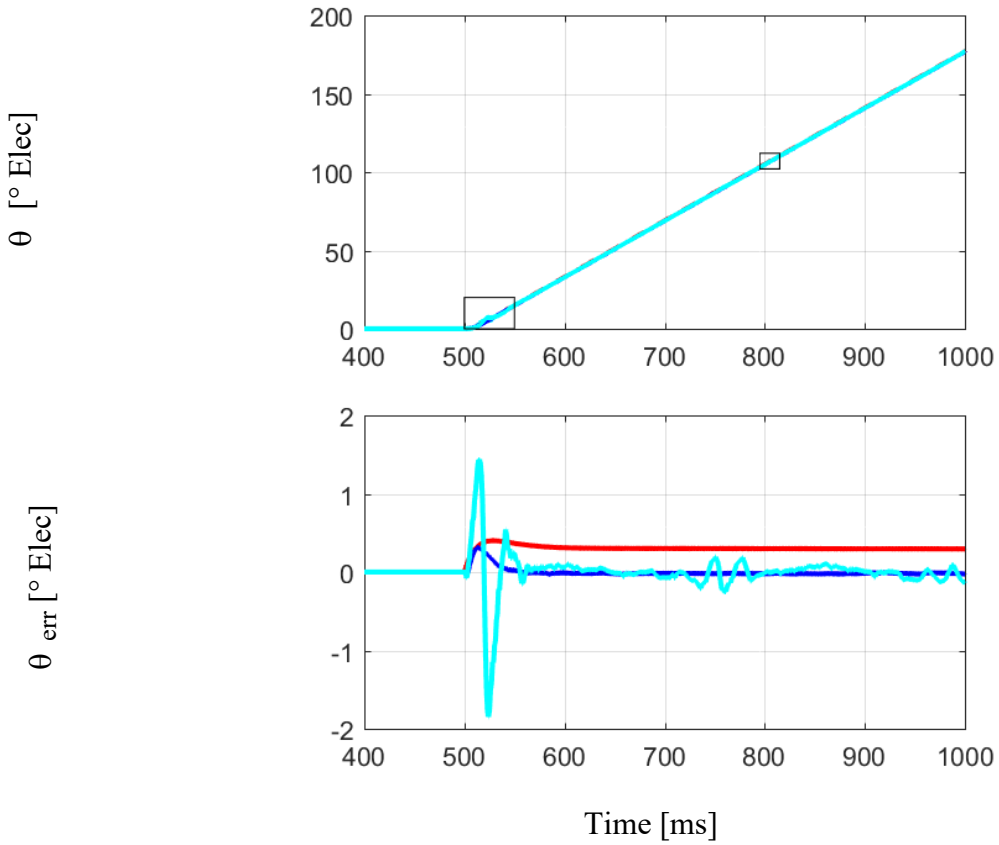

ω_m* = 1Hz, Heterodyning Demodulation 5Hz MC, NSIT 5Hz MC, NSIT 10Hz MC

Figure 5.1 – Simulated closed-loop self-sensing feedback with tuning as noted

To evaluate the image tracking method, two sets of bandwidths were tested. One set for both heterodyning demodulation and negative sequence image tracking tuned to 5Hz, and a second for negative sequence image tracking tuned to 10Hz, both sets representing the highest

achievable stable bandwidth on the respective systems during initial transients of an acceleration from standstill to 1Hz mechanical frequency. The lower bandwidth image tracking solution is used to provide a fair comparison. The system was commanded to start up from zero speed to 1Hz mechanical frequency with the results shown in Figure 5.1. The boxed portions are zoomed in on and shown in subsequent figures to demonstrate the transient, in Figure 5.2, and steady-state properties in Figure 5.3.

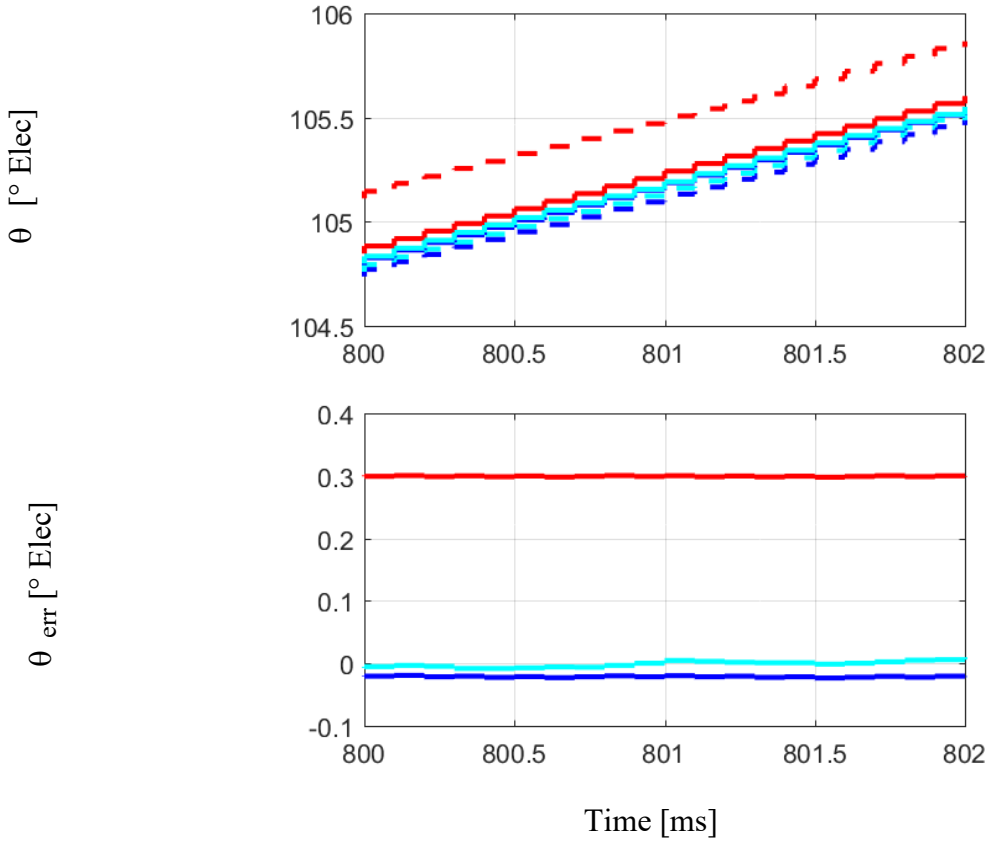

Heterodyning Demodulation 5Hz MC, NSIT 5Hz MC, NSIT 10Hz MC

ω_m* = 1Hz, Vc = 50V, fc = 1000 kHz, Tuning described in Table 5.1

Figure 5.2 – Simulated closed-loop self-sensing feedback with tuning as noted, zoomed in steady-state shown in Figure 5.1.

Several interesting details emerge. In the steady-state analysis, in Figure 5.2 both of the image tracking observers estimate at a single time step ahead of the actual value as is predicted

from the observer control theory, this results in very little error in either case. However, the heterodyning demodulation has a 0.3° electrical error as a constant offset. The heterodyning demodulation compensates for resistance and cross-coupling of the electrical plant, as described in 6.3A.12.2 . The remaining error is largely due to the inexact nature of the high-frequency injection analytical derivation, assuming a continuous implementation and neglecting the cross-coupling effects of the stationary frame latch. It should be noted, that since the negative sequence image tracking solution captures the template experimentally, these effects are captured in the template, as well as in the sampled data and accounts for them in the position estimate.

In Figure 5.3, the initial transient is observed, and the effects of the system bandwidths become more apparent. The lower bandwidth solutions both show lower tracking error than the higher bandwidth negative sequence image tracking. Heterodyning demodulation and the experimentally obtained template both assume steady-state, during transients the constant speed assumption used in steady-state is broken and the current response differs significantly from the expected current, resulting in position errors. The higher bandwidth system more aggressively tracks this unmodeled behavior and results in the larger error observed in Figure 5.3.

This provides an interesting tradeoff for the design of the control systems. At equal tuning, negative sequence image tracking solutions provide a higher accuracy position estimate. Additionally, higher tuning is possible but results in a larger position estimation error during transients.

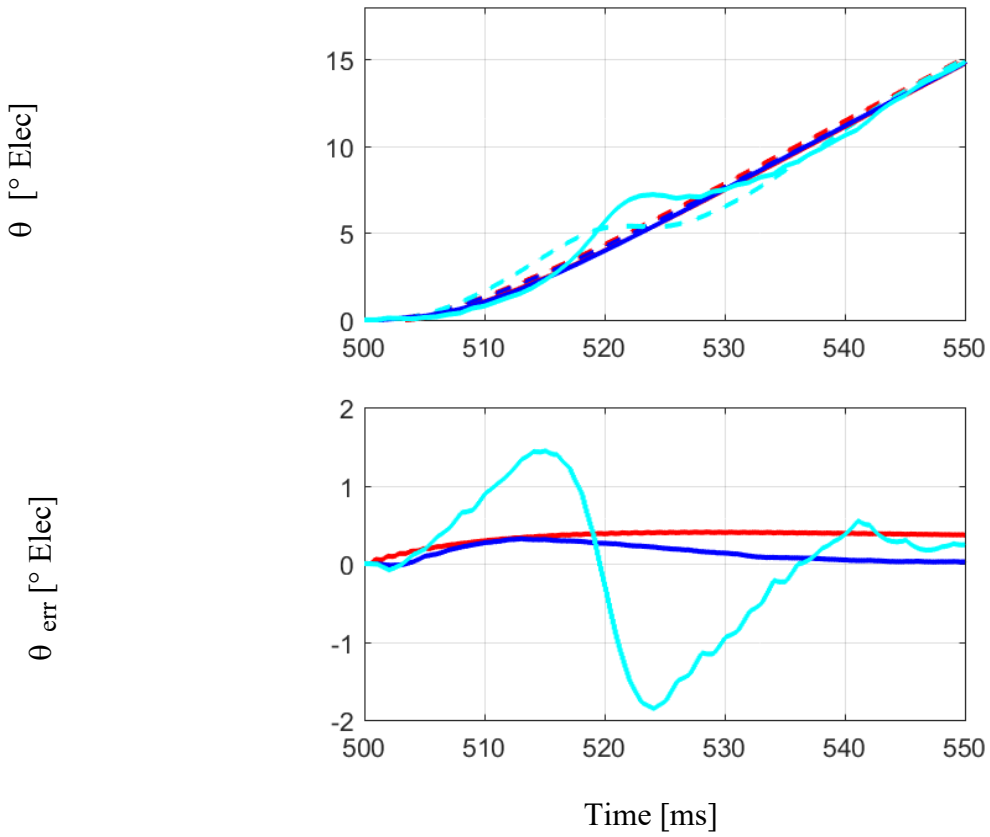

Heterodyning Demodulation 5Hz MC, NSIT 5Hz MC, NSIT 10Hz MC

ω_m* = 1Hz, Vc = 50V, fc = 1000 kHz, Tuning described in Table 5.1

Figure 5.3 – Simulated closed-loop self-sensing feedback with tuning as noted, zoomed in initial transient shown in Figure 5.1.

To confirm the additional achieved bandwidth of the negative sequence image tracking solution, the dynamic stiffness was captured and shown in Figure 5.4. Here the eigenvalues are estimated with the heterodyning demodulation showing the lower tuning of 5Hz as is expected, and the image tracking solutions provides 10Hz of bandwidth again as is expected, confirming the tuning and achievable system bandwidths.

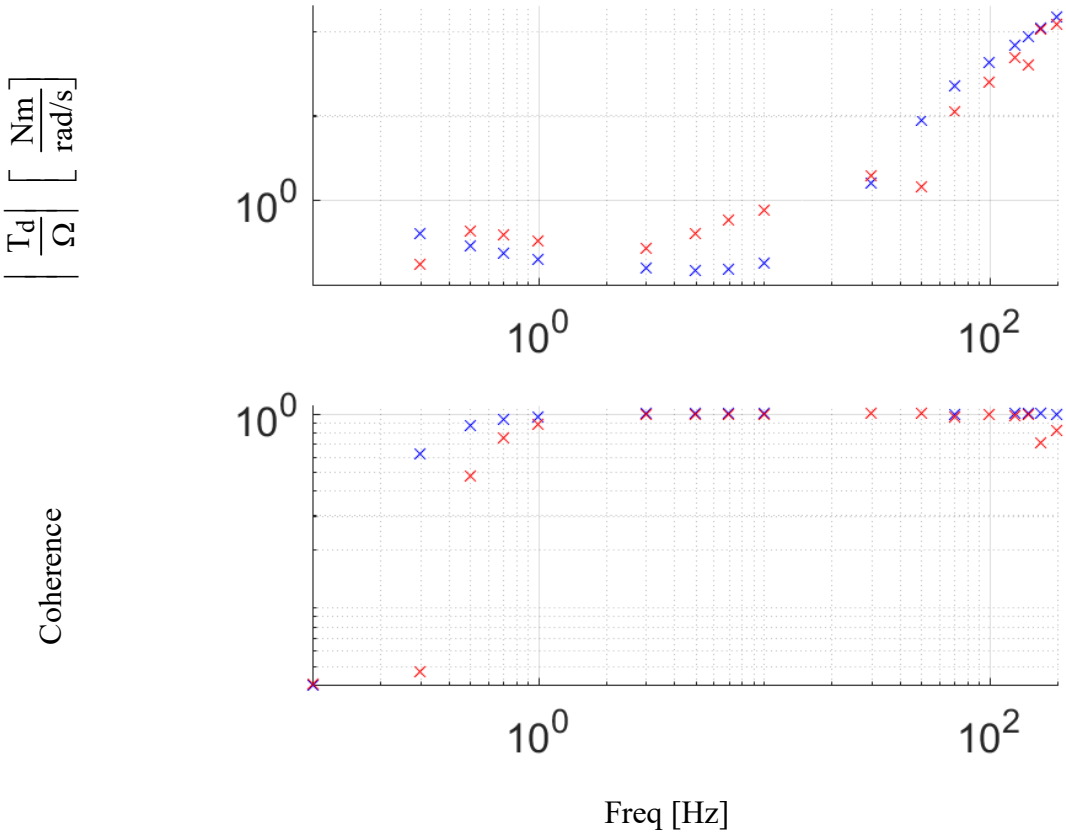

Heterodyning Demodulation 5Hz MC, NSIT 10Hz MC
T_d* sine wave at each frequency, magnitude 0.01P.U.

Figure 5.4 – Simulated dynamic stiffness FRF comparing feedback from heterodyning demodulation with negative sequence image tracking.

5.3 Load Dependent Evaluation of Template Variation

As outlined in section 3.3, the first step to performing image tracking is to obtain a template of the machine's current response at known positions. This can be done through FEA if it matches the test bench accurately, but this work is done by experimentally capturing the template. The changes in the template are predicted to be load sensitive due to saturation of the machine. In [46, 47] the machine was designed specifically to have a small but relatively

constant saliency with load changes. Even so, a single electrical cycle was captured and plotted in Figure 5.5a-c at varied loads. Additionally, FFTs of the negative sequence current responses are shown in Figure 5.5a-c. These shown that as load changes from 0P.U. to 1P.U. the harmonics present in the current response and subsequently, the shapes of the current image vary.

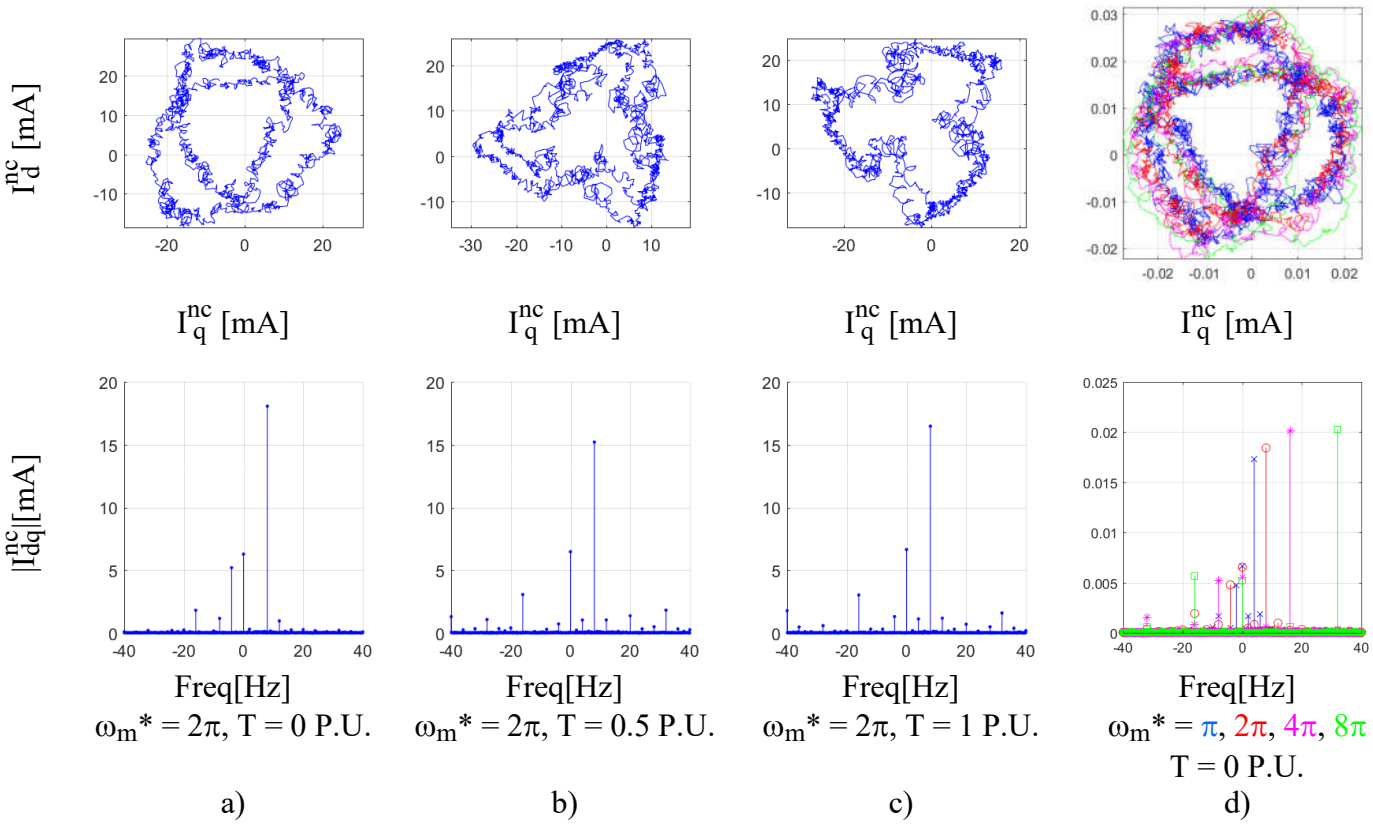

Figure 5.5 – Experimentally captured current response image showing the effects of different operating points. a-c show the effects of changing load on a single electrical cycle at a constant speed while d shows the effects of different speeds at no load.

From 6.3A.12 the ideal current response should contain 2nd harmonic content, i.e. the current image will rotate twice per electrical cycle and should be a circular response with the angle equal to the position plus a possible offset due to cross-saturation. Here, there are significant -4th, -1st, 0th, 2nd harmonics present at no load, and with the 0th and 2nd harmonics

remaining relatively constant with load. This shows a primary saliency, with a secondary inductance likely due to an eccentricity of the rotor.

In Figure 5.5d the effects of speed are shown. The frequency of the current response obviously changes with the speed operating point as is predicted from the current response equations. However, the magnitude of the response at each harmonic stays relatively constant over the operating range, also as is expected.

In summary, loading conditions change the template significantly and if multiple operating points are expected to be used each will need to be captured in a template and in real time the templates should be selected based on load. Otherwise, errors related to unmodeled inductance characteristics will appear as discussed in section 4.3. Speed effects show minimal variation on the template. For best performance templates could be captured at each speed operating point and selected based on operating condition. However, as changes in magnitude are minimal but arc length is speed dependent as discussed in section 3.4 a simpler solution of resampling the template based on estimated speed is recommended.

5.4 Template Generation via Spatial Synchronous Averaging

From Figure 5.5, it can be seen that there is significant noise on the measurements. This is expected as the signals are only a few tens of mA, which is 0.0003P.U., which are very small signals to measure. In the template matching step there will be a template and a sampled current with possibly both being noisy as a result of the small signals and system noise. The sampled data will have this noise on it and that cannot be avoided. This section explores how the template may be prepared in a manner to suppress the noise while maintaining the integrity of the template.

a)

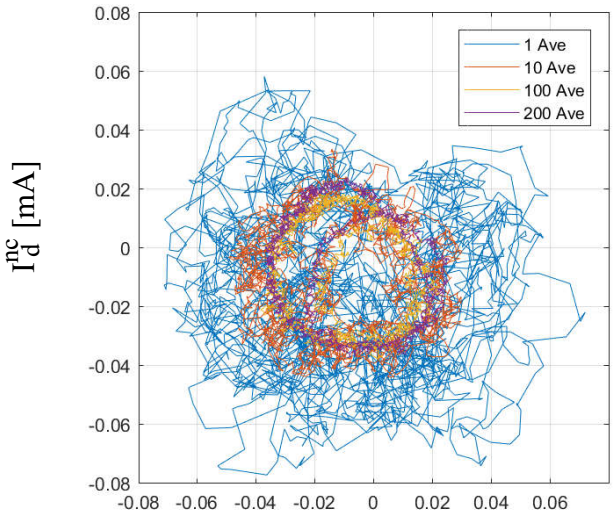

b)

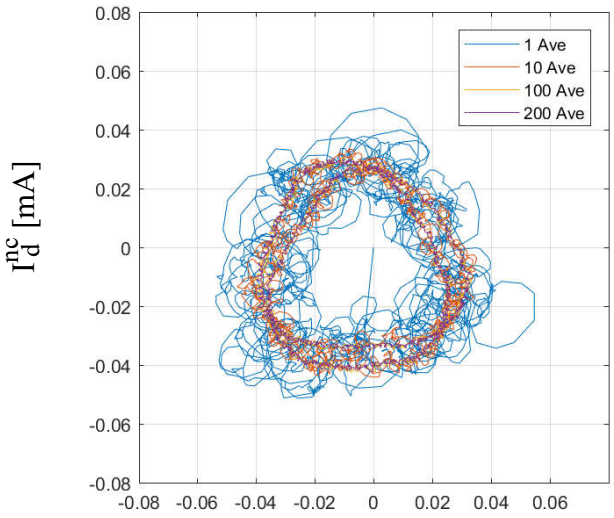

I_q^{nc} [A]

$\omega_m^* = 2\pi$ [rad/s]

Figure 5.6 – Current image template collected using encoder feedback, with varied numbers of time averages. a) 5Hz Motion Controller, b) 25Hz Motion Controller

A first attempt at creating a template using varied time averages is shown in Figure 5.6 collected using encoder feedback at two different motion controller bandwidths. If the machine is assumed to be at constant speed of ω_m = 1Hz as commanded, and with a switching frequency of 10kHz, with four pole pairs, then one electrical cycle happens every 2500 samples. Ideally,

every 2500th sample would align in position and they could be averaged together over numerous cycles to create a template that suppresses noise. The results of increasing numbers of averages is shown in Figure 5.6 where a single cycle has significant variance, and as the number of averages increases, the image becomes somewhat clearer. However, it should be noted that the template at differently tuned bandwidths generates different templates if a time averaging is applied. This is not a physics issue as the spatial inductances are not changing. It is a problem caused by time averaging and the assumption that every 2500th sample lines up at the same spatial position. With a lower bandwidth motion controller, any torque disturbance will cause the speed the deviate from the commanded significantly more than a higher bandwidth controller.

Clearly the problem is that time averaging is the wrong domain to approach this problem in. The template is fundamentally the current response as a function of position, so the current samples should be averaged spatially instead of temporally. One method to do this, is to spatial synchronously average the data [4, 92]. This method is outlined in Figure 5.7 with a block diagram of the process as well as a sample data structure used to perform the averaging. The method takes a large number of samples of current and position and segments the electrical cycle by the number of encoder counts per cycle into bins. Every sample is then accumulated in the bin based on its position, and the count of that bin is incremented. When all of the samples have been accumulated, the total accumulated is divided by the number of samples added to that bin, and the average is obtained. This resulting average is the current as a function of position with any noise, which is not spatially synchronous removed.

a)

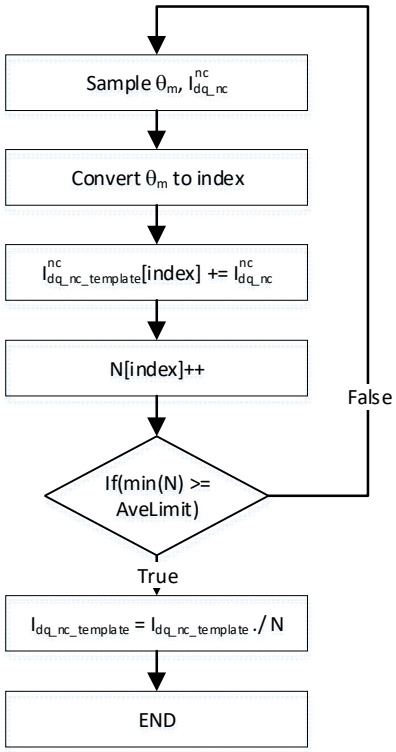

b)

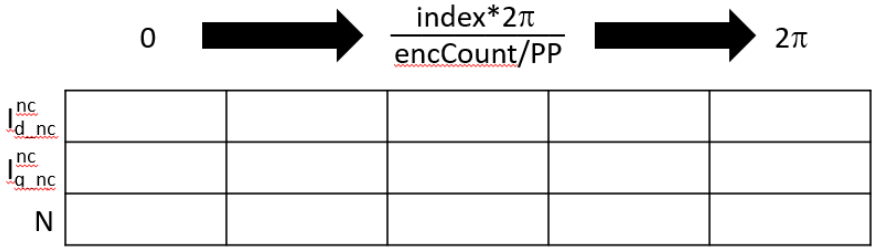

a) Algorithm for spatial synchronous averaging
b) Data structure used for accumulating spatial data

Figure 5.7 – Block diagram of spatial synchronous algorithm with data structure used to accumulate spatial data.

This data can be formed into a lookup table and used at the template itself. In this work, further processing is applied to gain a more versatile analytical result. Data was captured with a 25Hz bandwidth motion controller using encoder feedback, and with a 50V rotating voltage

injection applied as is done in the associated experiments in section 5.5. Spatial synchronous averaging was applied to the machine spinning with a mechanical frequency of 1Hz. This allows for 240 averages of the electrical cycle to be performed to remove non-spatially synchronous noise. In Figure 5.8 the spatial FFT of the data is shown using the q-axis as the 0° reference point. The dominant harmonics are selected as the -4th, -1st, 0th, 2nd, 5th as shown in Table 5.2 and are used with a Fourier Series as in (5.1) to recreate the template.

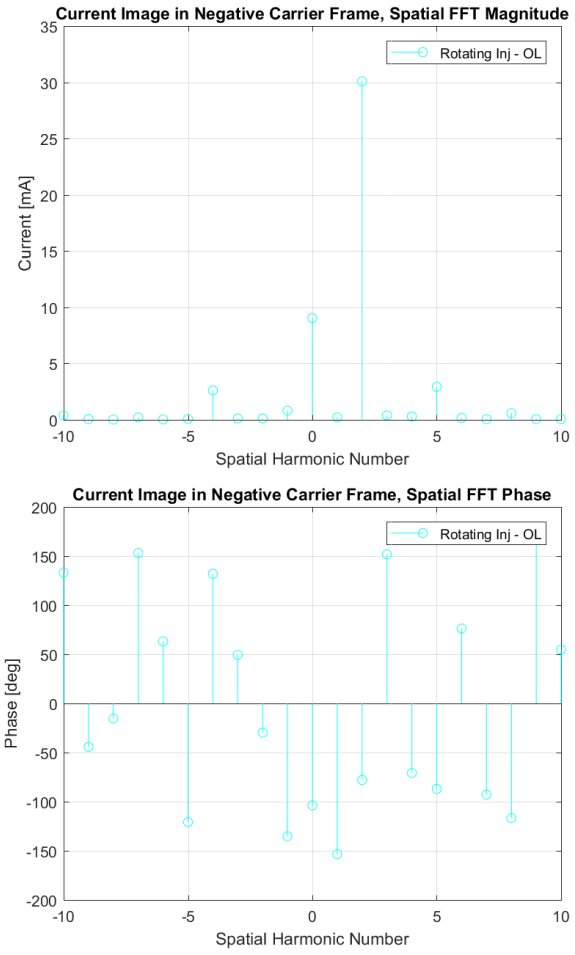

$\omega_m^* = 2\pi$ rad/s, $V_c = 50$V, $f_c = 1$ kHz, $I_q^* = 0$A

Figure 5.8 – FFT of the spatial synchronous averaged current.

$$\hat{I}_{dq}(\theta_e) = \sum_h A_h e^{jh\theta_e + \phi_h} \tag{5.1}$$

Table 5.2 – Template harmonic components		
h	A_h [mA]	ϕ_h [rad]
-4	2.6	2.30
-1	0.815	-2.36
0	9.04	-1.81
2	30.1	-1.36
5	2.92	-1.52

With the analytical characterization of the template several uses can be devised. In this work the dominant harmonics are selected, the operating speed of 1Hz mechanical is selected, and a 10 kHz sampling frequency is selected all to match the conditions on the bench. Then using (5.1) and the parameters in Table 5.2 a template was reconstructed and saved relating d- and q-axis components to the specified positions. The reconstructed template using 1Hz mechanical frequency, and 10 kHz sampling is overlaid with the spatial synchronously averaged data in FFT and polar plot in Figure 5.9. These show good agreement.

As opposed to simply using the spatial synchronously averaged data as a template, the Fourier Series representation can be resampled at different speeds. This can be done offline and saved as a lookup table similarly to what was done in this work. Additionally, it leaves the controls engineer an option to resample the template in real-time based on the estimated speed of the machine. A mismatched template speed compared to the actual speed with result in small estimation errors as discussed in section 3.4.

a)

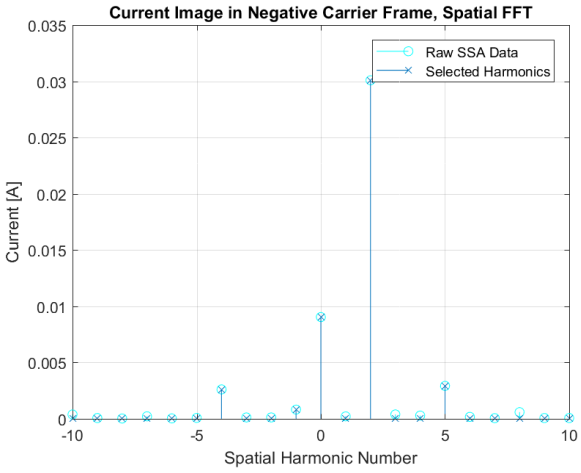

b)

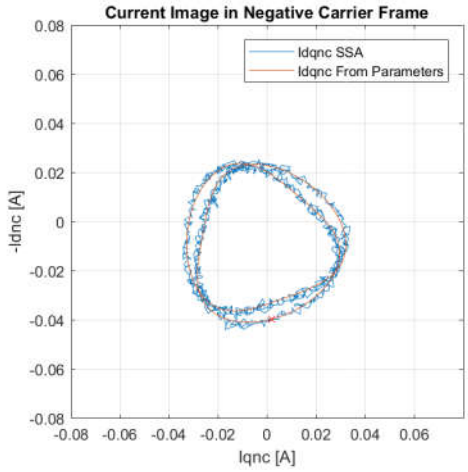

$\omega_m^* = \pi$ [rad/s]

Figure 5.9 – FFT of spatial synchronously averaged data with overlaid harmonics selected for parameterization. a) FFT of current and parameterized current, b) polar image from spatial synchronously averaged data and parameterized current.

An additional use of the spatial synchronous averaging is another way to analyze the effects of speed variation and torque disturbances. If the rotor is regularly slowing down at a specific position, the number of times that position is sampled with increase. This can readily be seen by plotting the number of counts of each position bin and is shown in Figure 5.10 with a low and high bandwidth motion controller. The higher bandwidth motion controller is better at rejecting disturbances and so maintains a more constant speed, while the low bandwidth motion controller shows a regular slow down around 300° electrical, which shows up as around the 850

encoder count. Discussion of the torque disturbances which cause this speed error is given in section 6.3B.7 .

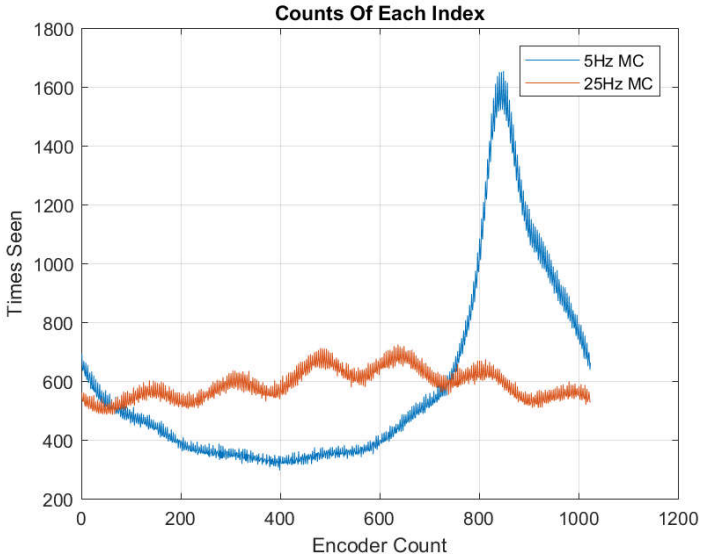

Figure 5.10 – Plot of the count of the spatial bins used in spatial synchronous averaging.

5.5 Experimental Results

The system described in previous sections was implemented on a dSPACE MicroLabBox controller using MATLAB Simulink auto code generation. The template created in 5.4 was used to do the negative sequence image tracking self-sensing. Additionally, two forms of heterodyning demodulation were applied. The first was rotating heterodyning demodulation is the classical method of vector tracking described in 6.3A.12.1 . The second method which will be called multiple saliency decoupling (MSDC) is based upon heterodyning demodulation but decouples the effects of multiple saliencies identified the Fourier series characterization in section 5.4 and described in section 6.3A.12.2 . The tuning for each method was identical with values listed in Table 5.3. Note, the evaluation provided in this section is done with a standalone

motor disconnected from the dynamometer for a number of reasons which are documented in section 6.3B.7 .

Table 5.3 – Experimental Control Structure Tuning

Control Structure	Bandwidth [Hz]
Current Regulator	200
Fundamental Current Observer	2X
Current Observer Carrier HPF	25X
Motion State Filter	2X
Motion Controller	X
Saliency Tracking Observer	2X
Demodulation LPF	10X
*X specified in corresponding tests, ratios constant between methods.	

To evaluate the performance of the different methods, a time-domain estimation accuracy was collected using the encoder for feedback while applying a high-frequency voltage injection of 1kHz with magnitude 50V. The position estimate from each method was collected and is shown in Figure 5.11. The heterodyning demodulation method shows large harmonic errors with 20° magnitude and at twice the frequency of the rotor. While the 2^{nd} harmonic in the current response contains the main saliency position information, the 0^{th} harmonic observed in the previous section presents as a 2^{nd} harmonic on the position estimate and is expected if no compensation method is applied. Using a heterodyning demodulation with multiple saliency decoupling improves this to a 10° amplitude ripple, with the 2^{nd} harmonic removed leaving non-spatially synchronous torque disturbances as the source of error. Finally, the negative sequence image tracking improves the estimate to 6° maximum error for a 40% reduction in error over state-of-the-art methods applied to this bench.

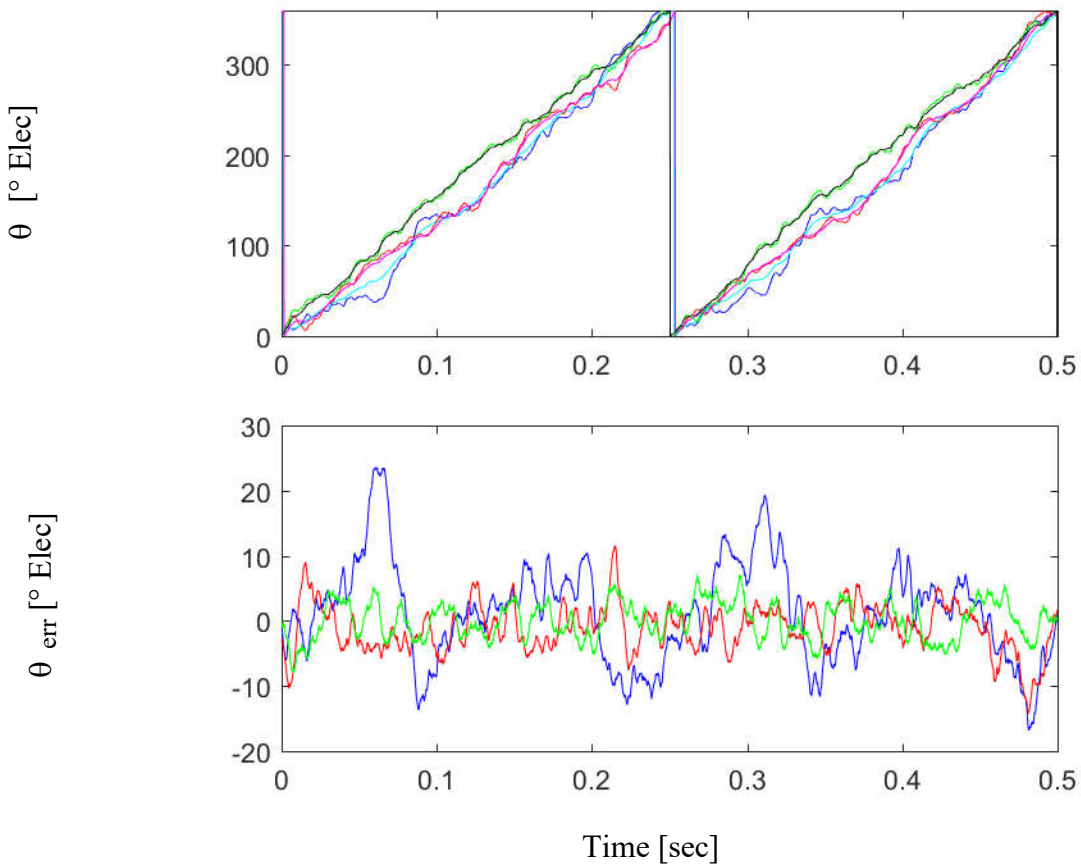

Figure 5.11 – Experimental estimation accuracy at steady-state using encoder feedback to evaluate performance of two forms of heterodyning demodulation and negative sequence image tracking.

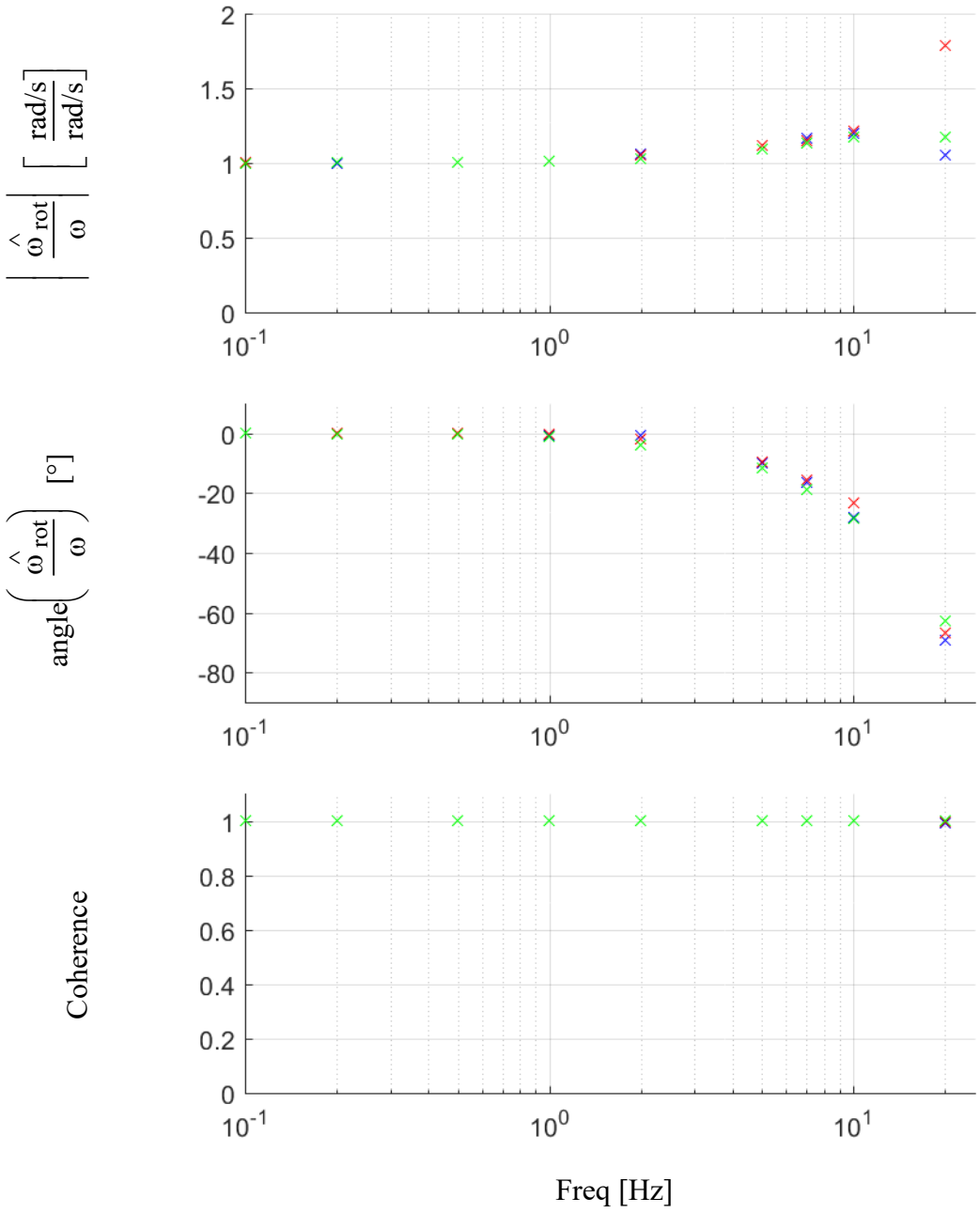

Heterodyning Demodulation 15Hz MC,
Heterodyning Demodulation w/ Decoupling 15Hz MC, NSIT 15Hz MC
ω_c* = sine wave at each frequency, magnitude = 1Hz, DC offset = 1Hz

Figure 5.12 – Self-sensing estimation accuracy using encoder feedback comparing two forms of heterodyning demodulation with image tracking.

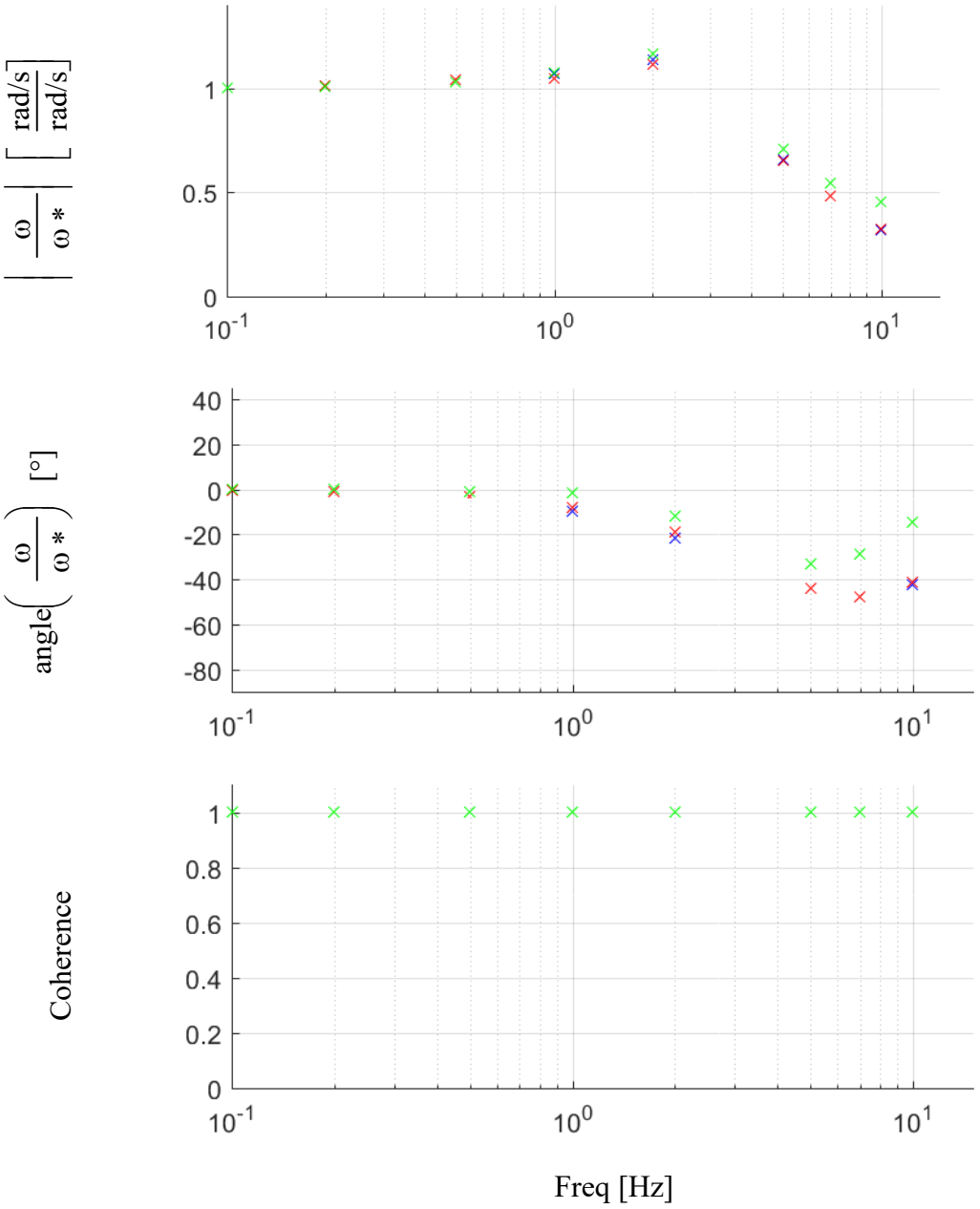

Heterodyning Demodulation 15Hz MC,
Heterodyning Demodulation w/ Decoupling 15Hz MC, NSIT 25Hz MC
ω_c* = sine wave at each frequency, magnitude = 1Hz, DC offset = 1Hz

Figure 5.13 – System command tracking using feedback from two forms of heterodyning demodulation compared to image tracking.

Next, a frequency domain estimation accuracy was collected using the encoder for feedback while injecting a high-frequency voltage. A sinusoidal command was applied to observer the ability of each estimate to track the position as shown in Figure 5.12. As the system is using command feed-forward and comparable system bandwidths, the response is similar between all three methods.

The frequency domain command tracking was collected as shown in Figure 5.13 by having each method's motion information be used as feedback for the motion controller and injecting single sine wave commands at each plotted point.. The negative sequence image tracking was able to be tuned to a higher stable value and shows a slightly higher bandwidth in the command tracking plots, however, the effects are limited as each method is using command feed-forward in the motion controller.

A sample of the command tracking at steady-state is shown in Figure 5.14. This plot shows that heterodyning demodulation has significant ripple content at twice the electrical frequency. It also shows that the NSDC method reduces but does not perfectly remove this 2^{nd} harmonic content. The NSIT removes the 2^{nd} harmonic content as it is now tracked in the template, however there is significant error as the higher bandwidth system more aggressively tracks errors.

Finally, each estimate was used as the feedback for the controller while applying a sinusoidal commanded torque disturbance with results shown in Figure 5.15. Here we can clearly see the effects of the higher bandwidth tuning of the negative sequence image tracking as it has a larger dynamic stiffness across much of the range compared to the heterodyning demodulation and NSDC methods. Around 20Hz the methods begin to converge to a level lower than the value expected by the system inertia. This is a result of an interaction with the current observer as frequency separation of the current observer, current regulator, and current filters is not perfect and results in interaction in the mid-range frequencies.

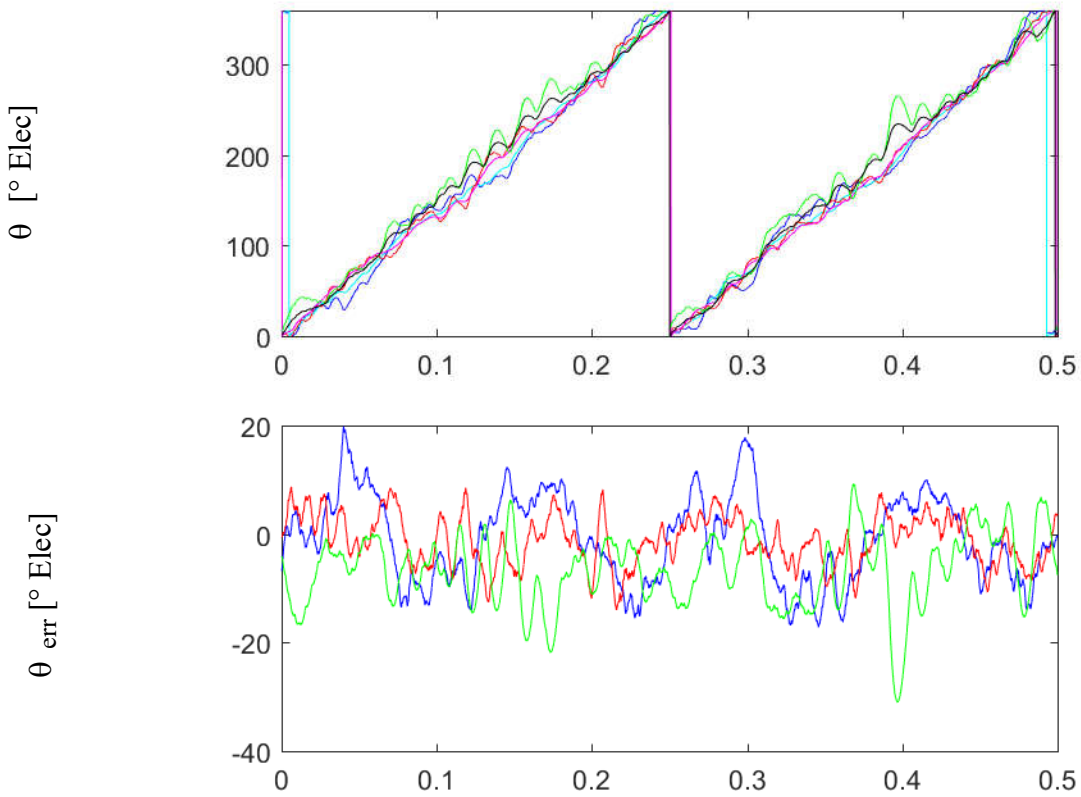

θ_{enc_rot}, $\hat{\theta}_{rot}$, θ_{enc_nsdc}, $\hat{\theta}_{nsdc}$, θ_{enc_nsit}, $\hat{\theta}_{nsit}$

$\omega_m^* = 1Hz$

Figure 5.14 – Experimental command tracking at steady-state using self-sensing feedback to evaluate performance of two forms of heterodyning demodulation and negative sequence image tracking.

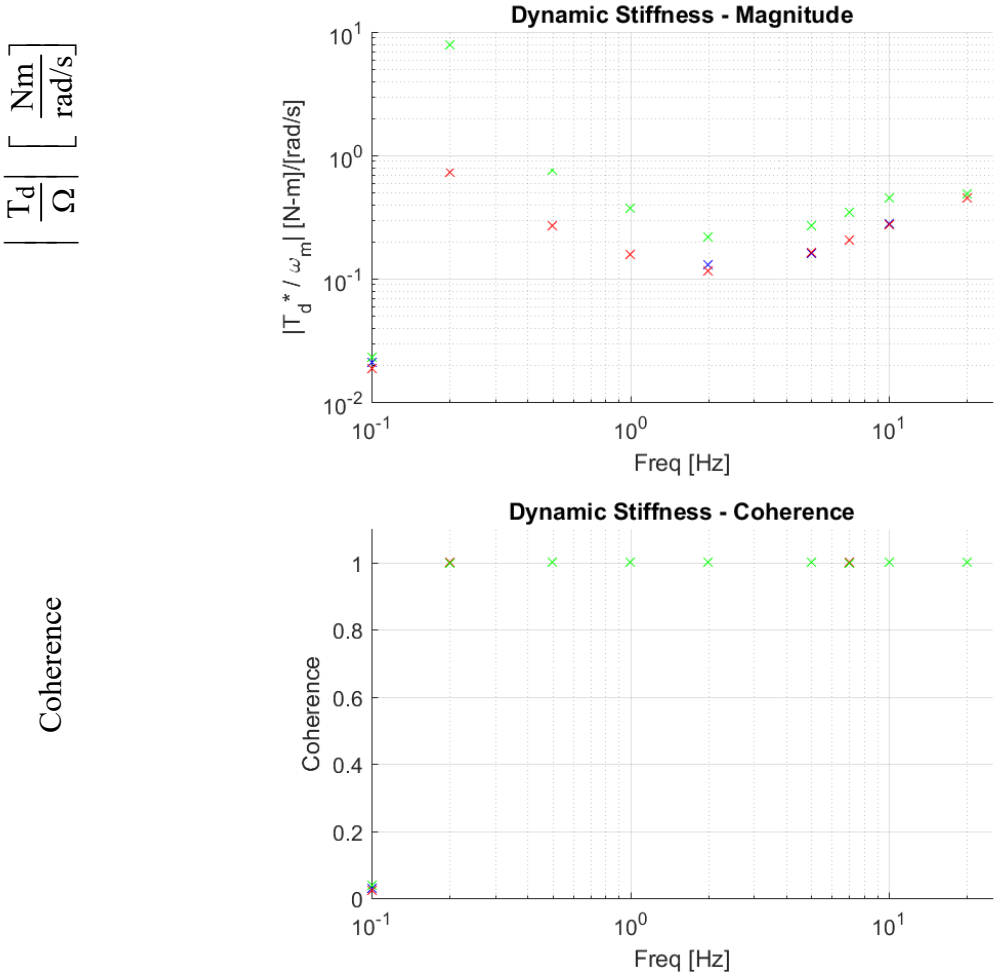

Heterodyning Demodulation 15Hz MC,
Heterodyning Demodulation w/ Decoupling 15Hz MC, NSIT 25Hz MC
T_d^* = sine wave at each frequency, magnitude = 0.03P.U., ω_m^* offset = 1Hz

Figure 5.15 – Experimental dynamic stiffness comparing two forms of heterodyning demodulation with negative sequence image tracking.

5.6 Summary

Simulated and experimental results for a 3.7kW SPMSM test bench are provided showing an improvement in both achievable accuracy to nearly perfect results and higher achievable bandwidth by 2x. The challenges of template creation are addressed considering the

variation of the saliencies with load, and the challenge noise presents when creating a template. A method based on spatial synchronous averaging is applied to create a template with reduced noise, and a method to convert it into a parameterized function suitable for resampling at various speeds is presented. Experimental results are shown demonstrating a 1.65x improvement to bandwidth, as well as a reduction in estimation accuracy error by 70% over heterodyning demodulation and a 40% over state-of-the-art compensation methods. Experimental results show valid improvements but lesser magnitude improvements than simulation. This is largely due to a combination of current sensor resolution and accuracy limitations and significant experimental torque disturbances.

Chapter 6 Conclusions, Contributions, Planned Remaining Work

6.1 Research Conclusions

The following list summarizes the key conclusions offered by this research.

6.1.1 Conclusions from the State-Of-The-Art Review

- Image tracking methodologies have not been developed for pulsating voltage injection-based self-sensing systems.
- Image tracking methodologies have not been developed in a form which is compatible with DB-DTFC.
- Image tracking solutions utilizing rotating voltage injection have not utilized the negative carrier reference frame to isolate the position-dependent information.
- Estimation error speed dependencies have been noted, but the voltage latch in the stationary frame has not been identified as a cause nor its effects analyzed.
- Image tracking solutions have not been implemented online in a closed-loop feedback system to evaluate achievable system performance.

6.1.2 Conclusions from Stationary Frame Voltage Latch Effects on Self-Sensing

- The stationary frame voltage latch couples the d- and q-axes which creates a coupling of the injection and results in a speed-dependent current response.
- The current response, when demodulated, results in a speed dependent error in the position estimate in state-of-the-art demodulation techniques when latch effects are neglected.

- Modeling of the stationary frame latch as a rotating latch in the synchronous frame allows for accurate current estimation.
- Applying a high frequency voltage injection to the properly modeled system allows for the speed effects on estimation error to accurately modeled.
- Analytically identifying the latch speed dependent terms allows for them to be accurately decoupled, removing the speed dependence

6.1.3 Conclusions from Negative Sequence Image Tracking Self-Sensing

- The negative sequence current response to a rotating voltage injection forms a unique fingerprint of the machine properties and manufacturing defects at steady-state.
- Collecting the negative sequence over an injection cycle traces a speed dependent arc that can be compared to a template image to estimate rotor position.
- By obtaining the template experimentally, all non-ideal effects present in the system are included in the template and improve accuracy without decoupling.
- If the template arc length speed dependency is neglected, the template matching will have inherent error as the template is inconsistently sampled relative to the template.
- The image arc length speed dependency presents an opportunity that with proper template resampling will provide an additional means to estimate rotor speed.
- Negative sequence image tracking provides a 40% increase compared to state-of-the-art rotating self-sensing in offline estimation accuracy.
- Negative sequence image tracking requires a cascaded speed observer to provide additional filtering of the speed to increase closed-loop bandwidth in simulation.
- A cascaded speed observer prevents small steps in position estimation from generating large erroneous speed estimates by reducing the step's impact on other system state estimates which are dependent on speed feedback for decoupling.

- Small steps in position estimation result in large speed estimates due to the derivative relationship, further causing back-EMF and cross-coupling decoupling to be noisy and degrade the resulting current images.
- A cascaded speed observer allows for filtered speed estimates to accurately decouple the back-EMF, retain high quality current images, and result in high estimation accuracy.
- Negative Sequence Image Tracking provides a 2x improvement over state-of-the-art rotating self-sensing in closed-loop simulation.
- Achievable closed-looped bandwidth of negative sequence image tracking in simulation is 3x larger than achievable bandwidths demodulation-based methods.
- Spatial synchronous averaging can be used to improve the quality of the negative sequence current response image used as a template.
- Negative sequence image tracking experimental bandwidth can be increased by 1.65x over existing heterodyning demodulation-based methods.
- Negative sequence image tracking experimental estimation accuracy can be improved by 70% over heterodyning demodulation, and 40% over state-of-the-art decoupling methods.

6.2 Contributions

The following list summarizes the key contributions made by this research.

- Developed methods to estimate rotor position by performing pattern matching between a sampled current response image and an experimentally captured template.
- Developed a negative carrier reference frame model of the current response image to a rotating voltage in the stationary reference frame including non-ideal inductance effects.
- Developed methodologies of extracting the steady-state current response of a PMSM to a high frequency voltage injected into the stationary reference frame.
- Developed a generalized analytical, multiple saliency current model of a high-frequency pulsating voltage injected into the estimated synchronous reference frame.

- Developed current response image models to a high frequency pulsating voltage injected into the estimated synchronous reference frame.
- Developed a method of filtering the speed estimate specifically to generate a high quality back-EMF decoupling and resulting current response image.
- Developed a method of capturing and processing the negative sequence current image into a high-quality parametrized method suitable for use as a lookup table, or real-time resampling.
- Developed a method for analyzing the speed-dependent effects the unmodeled stationary frame latch has on high-frequency injection self-sensing.
- Developed a method for compensating for speed-dependent effects from the unmodeled stationary frame latch.

6.3 Recommended Future Work

- **Explore Better Matching of Current Response with Current Sensors.**

  In all self-sensing methods, current sensors take the place of position sensors. Torque production is machine dependent, but typically large values and set the minimum max current rating of the sensor. Self-sensing is typically designed to generate the least current response possible to minimize losses, acoustic noise, and to preserve voltage bus space for torque production. This implies that current sensors must sense both large signals and small signals simultaneously, which requires very high accuracy sensors. To better evaluate the design options of self-sensing, the torque and self-sensing signals should both be well within the accuracy of the current sensors.

- **Experimental Analysis of Arc Length Changes and Implementation of Compensation Schemes.**

  In section 3.4 a method for accounting for speed dependent arc length variation was presented. In section 5.4, a method of template generation which is suitable for the resampling method described in 3.4 was presented. These methods should be combined and

evaluated experimentally. It is expected that the accuracy will improve, but that dynamics may become a significant factor. This is due to the template resampling being dependent on estimated speed, in the event that speed estimates are incorrect, the goodness of the position match will be impacted and will likely need to dynamic degradation. Solutions to this problem should be investigated and their limits explored.

- **Development of an Optimal Method to Select and Change Between Image Templates Based on Load.**

  As was shown in section 5.3, the saturation effects caused by different loads have an impact on the current image. This leads to degradation of position estimate if the load differs significantly from the load the template was collected at. For a full production level implementation of negative sequence image tracking, the templates should vary with load level. This may be as simple as a look-up table of template based on load. However, it will need to be verified that the polar plane location of the current response at a given position does not jump between selected templates. This jumping will cause a jump in position estimation and it will need to be evaluated against the application requirements. If the jump is too large, finer resolution templates will need to be created, or a method of interpolating between the templates will need to be developed.

- **Expand the Method to Handle Super Sampling of Current.**

  NSIT requires a time series to be collected to compare against the template. If the current were sampled faster, and the processing power were available, position sampling could be achieved faster. This would also reduce the error in speed estimation which was shown to cause numerous difficulties in the image creation process.

- **Experimental Verification of Stationary Frame Voltage Latch Compensation**

  In Chapter 2 the modeling of the effects of the stationary frame voltage latch on the current response to a high frequency voltage injection and subsequently on the position estimate was

performed. Furthermore a compensation method was proposed. Due to the non-ideal torque and saliency properties of the test bench evaluated in appendix B.6

References

[1] Kim, S., and Sul, S. K., "Sensorless control of AC motor — Where are we now?," Proc. Electrical Machines and Systems (ICEMS), 2011 International Conference on, pp. 1-6.
[2] T. Slininger, Y. H. X., R.D. Lorenz, 2016, "Enhancing Estimation Accuracy by Applying Cross-Correlation Image Tracking to Self-Sensing Including Evaluation on a Low Saliency Ratio Machine," IEEE Energy Conversion Congress and ExpoMilwaukee, WI.
[3] Rush, E., 2018, "Self-Sensing Estimation Using Image Tracking-Based Pulsating High Frequency Injection on a Low Saliency Machine," MS, University of Wisconsin - Madison.
[4] Secrest, C., 2015, "General Methodologies for Improving Motor Drive Precision in Order to Utilize It as an Embedded Application Sensor," PhD, University of Wisconsin - Madison, Madison, WI.
[5] Hinkkanen, M., 2019, "Sensorless Plug-and-Play Control of Industrial Drives," Proc. International Symposium on Sensorless Control for Electric Drives (SLED).
[6] Ghule, A., 2019, "Torque Modulation and Self-Sensing for Separately Excited Synchronous Electrostatic MAchines," Doctor of Philosophy, University of Wisconsin - Madison.
[7] Automation, A., 2016, "Encoder Guide."
[8] Gabrielyan, E., 2007, "Fast optical Indicator created with multi-ring moiré Patterns," Switzernet research reports, 4.
[9] R.D.Lorenz, 2013, "ME 547 - Physics-Based Modeling for Computer Control,"University of Wisconsin - Madison.
[10] Attaianese, C., and Tomasso, G., 2007, "Position Measurement in Industrial Drives by Means of Low-Cost Resolver-to-Digital Converter," IEEE Trans. Instrum. Meas., 56(6), pp. 2155-2159.
[11] Bergas-Jané, J., Ferrater-Simón, C., Gross, G., Ramírez-Pisco, R., Galceran-Arellano, S., and Rull-Duran, J., 2012, "High-Accuracy All-Digital Resolver-to-Digital Conversion," IEEE Transactions on Industrial Electronics, 59(1), pp. 326-333.
[12] Bergas-Jan, J., Ferrater-Sim, C., Gross, G., Ram, R., rez, P., Galceran-Arellano, S., and Rull-Duran, J., 2012, "High-Accuracy All-Digital Resolver-to-Digital Conversion," IEEE Transactions on Industrial Electronics, 59(1), pp. 326-333.
[13] Boyes, G. S., 1980, Synchro and resolver conversion, Memory devices.
[14] Hanselman, D., "Resolver signal requirements for high accuracy resolver-to-digital conversion," Proc. Industrial Electronics Society, 1989. IECON '89., 15th Annual Conference of IEEE, pp. 486-493 vol.482.
[15] Hanselman, D. C., 1991, "Techniques for improving resolver-to-digital conversion accuracy," IEEE Transactions on Industrial Electronics, 38(6), pp. 501-504.
[16] Sarma, S., Agrawal, V. K., and Udupa, S., 2008, "Software-Based Resolver-to-Digital Conversion Using a DSP," IEEE Transactions on Industrial Electronics, 55(1), pp. 371-379.
[17] R.D.Lorenz, 2013, "ME 746 - Dynamics of Controlled Systems,"University of Wisconsin - Madison.
[18] GmbH, S., 2016, "Magnetoresistive Sensors for angular and linear position sensing applications,"

http://www.sensitec.com/upload/SENSITEC/PDF_Downloads/Informationsmaterial/4Seiter_AA700.pdf.
[19] Semiconductors, N., 2010, "KMZ41 Magnetic Field Sensor - Product Data Sheet," http://www.nxp.com/documents/data_sheet/KMZ41.pdf.
[20] Ziegler, S., Woodward, R. C., Iu, H. H. C., and Borle, L. J., 2009, "Current Sensing Techniques: A Review," IEEE Sensors Journal, 9(4), pp. 354-376.
[21] Slininger, T. S., 2018, "Enhancing Self-Sensing Estimation Accuracy Through the Use of Cross-Correlation Image Tracking," Master of Science, University of Wisconsin - Madison.
[22] Capponi, F. G., Donato, G. D., Ferraro, L. D., Honorati, O., Harke, M. C., and Lorenz, R. D., 2006, "AC brushless drive with low-resolution Hall-effect sensors for surface-mounted PM Machines," IEEE Transactions on Industry Applications, 42(2), pp. 526-535.
[23] Harke, M. C., Donato, G. D., Capponi, F. G., Tesch, T. R., and Lorenz, R. D., 2008, "Implementation Issues and Performance Evaluation of Sinusoidal, Surface-Mounted PM Machine Drives With Hall-Effect Position Sensors and a Vector-Tracking Observer," IEEE Transactions on Industry Applications, 44(1), pp. 161-173.
[24] Scelba, G., Scarcella, G., Donato, G. D., Capponi, F. G., and Bonaccorso, F., "Fault tolerant rotor position and velocity estimation using binary Hall-effect sensors for low cost vector control drives," Proc. 2013 IEEE Energy Conversion Congress and Exposition, pp. 2123-2130.
[25] Tesch, T. R., 2005, "Dynamic Torque Estimation in a Sensor Limited Environment," PhD, University of Wisconsin - Madison.
[26] 2020, https://www.digikey.com/.
[27] Yang, H., and Flowers, G., 2015, "Fretting in Electrical Connectors Induced by Axial Vibration," IEEE Transactions on Components, Packaging and Manufacturing Technology, 5(3), pp. 328-336.
[28] Antler, M., 1985, "Survey of Contact Fretting in Electrical Connectors," IEEE Transactions on Components, Hybrids, and Manufacturing Technology, 8(1), pp. 87-104.
[29] Antler, M., 1981, "Sliding Wear of Metallic Contacts," IEEE Transactions on Components, Hybrids, and Manufacturing Technology, 4(1), pp. 15-29.
[30] Fricke, W. G., and Rawlins, C. B., 1968, "Importance of Fretting in Vibration Failures of Stranded Conductors," IEEE Transactions on Power Apparatus and Systems, PAS-87(6), pp. 1381-1384.
[31] Shearer, J. F., 1964, "Modes of Failure of Electrical Connectors," IEEE Transactions on Aerospace, 2(2), pp. 558-562.
[32] Irving, D. B., 1945, "Cable terminations," Journal of the Institution of Electrical Engineers - Part II: Power Engineering, 92(26), pp. 73-84.
[33] Pecht, M., and Ramappan, V., 1992, "Are components still the major problem: a review of electronic system and device field failure returns," IEEE Transactions on Components, Hybrids, and Manufacturing Technology, 15(6), pp. 1160-1164.
[34] Winter, B. W., "Ending Encoder-Related Downtime in Oil & Gas Drilling Applications," Nidec Avtron Automation.
[35] Tamai, S., Sugimoto, H., and Yano, M., "Speed sensorless vector control of induction motor applied model reference adaptive system," Proc. Conf. Record IEEE/MS Annual Meeting, pp. 613-620.

[36] Hejny, R. W., and Lorenz, R. D., 2011, "Evaluating the Practical Low-Speed Limits for Back-EMF Tracking-Based Sensorless Speed Control Using Drive Stiffness as a Key Metric," IEEE Transactions on Industry Applications, 47(3), pp. 1337-1343.
[37] Hejny, R. W., 2008, "Degradation of Dynamic Stiffness at Low Speeds When Using Back-emf Tracking for Closed Loop Speed Control," MS, University of Wisconsin - Madison.
[38] Harke, M. C., Ribeiro, L. A. d. S., and Lorenz, R. D., "Disturbance rejection limitations of back-emf based sensorless PM drives," Proc. Power Electronics and Applications, 2007 European Conference on, pp. 1-10.
[39] Ribeiro, L. A. D. S., Harke, M. C., and Lorenz, R. D., "Dynamic Properties of Back-emf Based Sensorless Drives," Proc. Conference Record of the 2006 IEEE Industry Applications Conference Forty-First IAS Annual Meeting, pp. 2026-2033.
[40] Harke, M. C., 2006, "Fundamental Sensing Issues In Motor Control," PhD, University of Wisconsin - Madison.
[41] Tuovinen, T., Awan, H. A. A., Saarakkala, S. E., and Hinkkanen, M., "Discrete-time observer design for sensorless synchronous motor drives," Proc. 2015 IEEE Energy Conversion Congress and Exposition (ECCE), pp. 867-874.
[42] Jansen, P. L., and Lorenz, R. D., 1995, "Transducerless position and velocity estimation in induction and salient AC machines," IEEE Transactions on Industry Applications, 31(2), pp. 240-247.
[43] Corley, M. J., and Lorenz, R. D., 1998, "Rotor position and velocity estimation for a salient-pole permanent magnet synchronous machine at standstill and high speeds," IEEE Transactions on Industry Applications, 34(4), pp. 784-789.
[44] Hwang, C., Lee, Y., and Sul, S., "Analysis on the position estimation error in position-sensorless operation using pulsating square wave signal injection," Proc. 2017 IEEE Energy Conversion Congress and Exposition (ECCE), pp. 844-850.
[45] Lee, J. S., 2013, "Voltage- and Current- Limited Operation of Deadbeat-Direct Torque and Flux Control for Interior Permanent Magnet Synchronous Machines," PhD, University of Wisconsin - Madison.
[46] Huthaifa Flieh, T. S., Shao-Chuan Chien, Li-Hsing Ku and Robert Lorenz, 2019, "Flux Weakening Surface Mounted Permanent Magnet Servo Motors Design with Enhanced Self-Sensing Properties," IEEE Energy Conversion Congress and ExpoBaltimore, MD, USA.
[47] Huthaifa Flieh, T. S., Shao-Chuan Chien, Li-Hsing Ku and Robert Lorenz, 2019, "Self-Sensing and Power Conversion Comparison for Flux Weakening Surface Mounted Permanent Magnet Servo Motors Designed using Symmetric and Asymmetric Rotors," IEEE Energy Conversion Congress and ExpoBaltimore, MD, USA.
[48] H. Flieh, T. S., R.D. Lorenz, E. Totoki, 2018, "Self-Sensing via Flux Injection with Servo Dynamics including a Smooth Transition to Back-EMF Tracking," 2018 IEEE Energy Conversion Congress and Exposition (ECCE), IEEE, Portland, OR.
[49] Flieh, H. M., 2014, "Self-Sensing Deadbeat Direct Torque and Flux Control for Surface Mount Permanent Magnet Synchronous Machine," MS, Universidad de Oviedo.
[50] Bouxsein, C., 2015, "Injection-Based Self-Sensing with Deadbeat-Direct Torque and Flux Control for Surface-Mounted PM Synchronous Machines," MS, University of Wisconsin - Madison.

[51] Belie, F. D., and Melkebeek, J., "Seamless integration of a low-speed position estimator for IPMSM in a current-controlled voltage-source inverter," Proc. 2010 First Symposium on Sensorless Control for Electrical Drives, pp. 50-55.
[52] Graf, T. F., 2014, "Implementaion and Evaluations of Non-Injection Based Flux Tracking Self-Sensing for SPMSMs from Zero to High Speeds Using a Voltage Sensors," MS, University of Wisconsin - Madison.
[53] Zhou, R., 2016, "Investigation of back-EMF based Self-Sensing for Surface-Mounted Permanent Magnet Synchronous Motors at Zero-to-low Speed," MS, University of Wisconsin - Madison.
[54] Blank, M., Löhdefink, P., Reinhardt, B., and Dietz, A., "Evaluation of a new microcontroller based solution for sensorless control of electrical drives," Proc. 2014 6th European Embedded Design in Education and Research Conference (EDERC), pp. 132-136.
[55] Instruments, T., 2013, InstaSPIN-FOC and InstaSPIN-MOTION.
[56] Yang, S. C., and Lorenz, R. D., 2012, "Surface permanent magnet synchronous machine position estimation at low speed using eddy-current-reflected asymmetric resistance," IEEE Transactions on Power Electronics, 27(5), pp. 2595-2604.
[57] Xu, Y. H., 2016, "Implementation, Evaluation and Improvement of High Frequency Injection (HFI) Self-Sensing Techniques on SPMSM with Slight Saliency," MS, University of Wisconsin - Madison.
[58] Degner, M., 1998, "Flux, Position, and Velocity Estimation in AC Machines Using Carrier Signal Injection," PhD, University of Wisconsin - Madison.
[59] Briz, F., Diez, A., and Degner, M. W., "Dynamic operation of carrier signal injection based sensorless, direct field oriented AC drives," Proc. Conference Record of the 1999 IEEE Industry Applications Conference. Thirty-Forth IAS Annual Meeting (Cat. No.99CH36370), pp. 2313-2320 vol.2314.
[60] Degner, M. W., and Lorenz, R. D., 1998, "Using multiple saliencies for the estimation of flux, position, and velocity in AC machines," IEEE Transactions on Industry Applications, 34(5), pp. 1097-1104.
[61] Petit, M., 2015, "Implementation of Self-Sensing on Interior Permanent Magnet Synchronous Machine Drives using Deadbeat-Direct Torque and Flux Control," MS, RWTH Aachen University.
[62] Petit, M. S., Sarlioglu, B., Lorenz, R. D., and Broeck, C. H. v. d., "Carrier Separation Techniques for Improved Disturbance Rejection of Injection-Based Self-Sensing Control," Proc. 2019 IEEE 10th International Symposium on Sensorless Control for Electrical Drives (SLED), pp. 1-6.
[63] Reigosa, D. D., Garcia, P., Raca, D., Briz, F., and Lorenz, R. D., 2008, "Measurement and Adaptive Decoupling of Cross-Saturation Effects and Secondary Saliencies in Sensorless Controlled IPM Synchronous Machines," IEEE Transactions on Industry Applications, 44(6), pp. 1758-1767.
[64] Reigosa, D. D., Garcia, P., Briz, F., Raca, D., and Lorenz, R. D., 2010, "Modeling and Adaptive Decoupling of High-Frequency Resistance and Temperature Effects in Carrier-Based Sensorless Control of PM Synchronous Machines," IEEE Transactions on Industry Applications, 46(1), pp. 139-149.

[65] Garcia, P., Briz, F., Degner, M. W., and Diaz-Reigosa, D., 2007, "Accuracy, Bandwidth, and Stability Limits of Carrier-Signal-Injection-Based Sensorless Control Methods," IEEE Transactions on Industry Applications, 43(4), pp. 990-1000.
[66] Guerrero, J. M., Leetmaa, M., Briz, F., Zamarron, A., and Lorenz, R. D., 2005, "Inverter nonlinearity effects in high-frequency signal-injection-based sensorless control methods," IEEE Transactions on Industry Applications, 41(2), pp. 618-626.
[67] Silva, C., Asher, G. M., and Sumner, M., "Influence of dead-time compensation on rotor position estimation in surface mounted PM machines using HF voltage injection," Proc. Proceedings of the Power Conversion Conference-Osaka 2002 (Cat. No.02TH8579), pp. 1279-1284 vol.1273.
[68] Jong-Woo, C., and Seung-Ki, S., 1995, "A new compensation strategy reducing voltage/current distortion in PWM VSI systems operating with low output voltages," IEEE Transactions on Industry Applications, 31(5), pp. 1001-1008.
[69] Choi, C. H., and Seok, J. K., 2007, "Compensation of Zero-Current Clamping Effects in High-Frequency-Signal-Injection-Based Sensorless PM Motor Drives," IEEE Transactions on Industry Applications, 43(5), pp. 1258-1265.
[70] Lee, Y., Kwon, Y. C., Sul, S. K., Baloch, N. A., and Morimoto, S., "Compensation of position estimation error for precise position-sensorless control of IPMSM based on high-frequency pulsating voltage injection," Proc. 2017 IEEE Energy Conversion Congress and Exposition (ECCE), pp. 859-864.
[71] Wiedmann, K., Wallrapp, F., and Mertens, A., "Analysis of inverter nonlinearity effects on sensorless control for permanent magnet machine drives based on High-Frequency Signal Injection," Proc. 2009 13th European Conference on Power Electronics and Applications, pp. 1-10.
[72] Gong, L. M., and Zhu, Z. Q., 2011, "A Novel Method for Compensating Inverter Nonlinearity Effects in Carrier Signal Injection-Based Sensorless Control From Positive-Sequence Carrier Current Distortion," IEEE Transactions on Industry Applications, 47(3), pp. 1283-1292.
[73] Jong-Woo, C., and Seung-Ki, S., 1996, "Inverter output voltage synthesis using novel dead time compensation," IEEE Transactions on Power Electronics, 11(2), pp. 221-227.
[74] Wang, J., and Gao, J., "Influence of speed EMF on position estimation error in carrier signal injection based sensorless control of PMSM," Proc. 2012 15th International Conference on Electrical Machines and Systems (ICEMS), pp. 1-6.
[75] Gunawan, R., and Yusivar, F., "Reducing estimation error due to digitizing problem in a speed sensorless control of induction motor," Proc. 31st Annual Conference of IEEE Industrial Electronics Society, 2005. IECON 2005., p. 6 pp.
[76] Gabriel, F., Belie, F. D., and Neyt, X., "Inductance-based position self-sensing of a brushless DC-machine using high-frequency signal injection," Proc. IECON 2012 - 38th Annual Conference on IEEE Industrial Electronics Society, pp. 3682-3687.
[77] Dana H. Ballard, C. M. B., 1982, Computer Vision, Prentice-Hall, Inc, Englewood Cliffs, New Jersey.
[78] Rafael C. Gonzalez, R. E. W., 2008, Digital Image Processing, Pearson Education, Inc., Upper Saddle River, NJ.

[79] Keren, D., Peleg, S., and Brada, R., "Image sequence enhancement using sub-pixel displacements," Proc. Computer Vision and Pattern Recognition, 1988. Proceedings CVPR '88., Computer Society Conference on, pp. 742-746.
[80] Reddy, B. S., and Chatterji, B. N., 1996, "An FFT-based technique for translation, rotation, and scale-invariant image registration," IEEE Transactions on Image Processing, 5(8), pp. 1266-1271.
[81] Balci, M., and Foroosh, H., 2006, "Subpixel Registration Directly from the Phase Difference," EURASIP Journal on Advances in Signal Processing, 2006(1), pp. 1-11.
[82] Vandewalle, P., S, S., #252, sstrunk, and Vetterli, M., 2006, "A frequency domain approach to registration of aliased images with application to super-resolution," EURASIP J. Appl. Signal Process., 2006, pp. 233-233.
[83] Lowe, D. G., "Object recognition from local scale-invariant features," Proc. Computer Vision, 1999. The Proceedings of the Seventh IEEE International Conference on, pp. 1150-1157 vol.1152.
[84] Bay, H., Ess, A., Tuytelaars, T., and Van Gool, L., 2008, "Speeded-Up Robust Features (SURF)," Computer Vision and Image Understanding, 110(3), pp. 346-359.
[85] Berto, M., Carlet, P. G., Manzolini, V., and Alberti, L., "An Effective Ellipse Fitting Technique of the Current Response Locus to Rotating HF Voltage Injection in IPMSM for Sensorless Rotor Position Estimation," Proc. IECON 2018 - 44th Annual Conference of the IEEE Industrial Electronics Society, pp. 391-396.
[86] Urbanski, K., "Position estimation at zero speed for PMSM using probabilistic neural network," Proc. Cybernetics (CYBCONF), 2015 IEEE 2nd International Conference on, pp. 427-432.
[87] Urbanski, K., and Nowopolski, K., "Position estimation at zero speed for PMSM using the principal component analysis," Proc. 2017 22nd International Conference on Methods and Models in Automation and Robotics (MMAR), pp. 361-366.
[88] Analog Devices, I., 2018, "Analog Devices Technical Articles," https://www.analog.com/media/en/technical-documentation/dsp-book/dsp_book_Ch15.pdf.
[89] Slininger, T. S., Petit, M.S., Flieh, H., Chien, S.C., Ku, L.H., Lorenz, R.D., 2019, "Full Order Discrete-Time Modeling for Accurate and Speed Independent Pulsating Volage Injection Self-Sensing," International Symposium on Sensorless Control for Electrical DrivesTorino, Italy.
[90] Collins, R., 2007, "Lecture 7: Correspondence Matching," http://www.cse.psu.edu/~rtc12/CSE486/lecture07.pdf.
[91] Yang, S. C., 2011, "Position Sensing Of Surface Permanent Magnet Machine Using High Frequency Signal Injection," PhD, University of Wisconsin - Madison.
[92] Wolf, C. M., 2011, "Using the Motor Drive as a Sensor to Extract Spaital Domain Information," Doctor of Philosophy, University of Wisconsin - Madison.
[93] Yang, S. C., Suzuki, T., Lorenz, R. D., and Jahns, T. M., 2013, "Permanent magnet motor with stator-based saliency for position sensorless drive," Google Patents.
[94] Yang, S. C., and Lorenz, R. D., 2012, "Comparison of resistance-based and inductance-based self-sensing controls for surface permanent-magnet machines using high-frequency signal injection," IEEE Transactions on Industry Applications, 48(3), pp. 977-986.
[95] Yang, S.-C., and Lorenz, R. D., 2012, "Concurrent Designs of Surface Permanent Magnet Machines for Self-Sensing Position Estimation and Power-Conversion," IEEJ Journal of Industry Applications, 1(1), pp. 24-30.

[96] Yang, S. C., and Lorenz, R. D., 2012, "Analysis of Iron and Magnet Losses in Surface-Permanent-Magnet Machines Resulting From Injection-Based Self-Sensing Position Estimation," IEEE Transactions on Industry Applications, 48(6), pp. 1901-1910.
[97] Yang, S. C., and Lorenz, R. D., 2012, "Surface Permanent-Magnet Machine Self-Sensing at Zero and Low Speeds Using Improved Observer for Position, Velocity, and Disturbance Torque Estimation," IEEE Transactions on Industry Applications, 48(1), pp. 151-160.
[98] Yang, S. C., Suzuki, T., Lorenz, R. D., and Jahns, T. M., 2011, "Surface-Permanent-Magnet Synchronous Machine Design for Saliency-Tracking Self-Sensing Position Estimation at Zero and Low Speeds," IEEE Transactions on Industry Applications, 47(5), pp. 2103-2116.
[99] Lipo, T. A., 1996, Vector control and dynamics of AC drives, Oxford university press.
[100] R.D.Lorenz, 2013, "ME 577 - Automatic Controls Laboratory,"University of Wisconsin - Madison.
[101] Rowan, T. M., and Kerkman, R. J., 1986, "A New Synchronous Current Regulator and an Analysis of Current-Regulated PWM Inverters," IEEE Transactions on Industry Applications, IA-22(4), pp. 678-690.
[102] Briz, F., Degner, M. W., and Lorenz, R. D., 2000, "Analysis and design of current regulators using complex vectors," IEEE Transactions on Industry Applications, 36(3), pp. 817-825.
[103] Hyunbae, K., and Lorenz, R. D., "A virtual translation technique to improve current regulator for salient-pole AC machines," Proc. Power Electronics Specialists Conference, 2004. PESC 04. 2004 IEEE 35th Annual, pp. 487-493 Vol.481.
[104] Richard C. Dorf, R. H. B., 2007, Modern Control Systems, Pearson Prentice Hall, Upper Saddle River, NJ, USA.
[105] West, N. T., and Lorenz, R. D., 2009, "Digital Implementation of Stator and Rotor Flux-Linkage Observers and a Stator-Current Observer for Deadbeat Direct Torque Control of Induction Machines," IEEE Transactions on Industry Applications, 45(2), pp. 729-736.
[106] Kenny, B., 2001, "Deadbeat Direct Torque Control of Induction Machines Using Self-Sensing at Low and Zero Speed," Doctor of Philosophy, University of Wisconsin - Madison.
[107] West, N. T., 2006, "Effective Real Time Implementation of Deadbeat Direct Torque Control for AC Induction Machines," Master of Science, University of Wisconsin - Madison.
[108] Lee, J. S., Choi, C. H., Seok, J. K., and Lorenz, R. D., 2011, "Deadbeat-Direct Torque and Flux Control of Interior Permanent Magnet Synchronous Machines With Discrete Time Stator Current and Stator Flux Linkage Observer," IEEE Transactions on Industry Applications, 47(4), pp. 1749-1758.
[109] Shi, Y., 2014, "Investigation of Loss Minimizing Stator Flux Trajectories for Dynamic Load Trajectories on Induction Machine under Deadbeat-Direct Torque and Flux Control," MS, University of Wisconsin - Madison.
[110] Xu, W., 2013, "Dynamic Loss Modeling for Loss Minimizing Control of IPMSM using DB-DTFC not Operating in Voltage or Current Limits " Doctor of Philosophy, University of Wisconsin - Madison.
[111] Wang, Y., 2016, "Deadbeat - Direct Torque and Flux Control Drives for High Power Applications using Low Switching Frequency Multi-level Inverters," Doctor of Philosophy, University of Wisconsin - Madison.

[112] Wang, Y., 2013, "Investigation of Loss Manipulation in Drives via Integration of Multi-level Inverters with Deadbeat, Direct Torque and Flux Control," MS, University of Wisconsin - Madison.
[113] Kang Wang, R. D. L., Noor Baloch, 2018, "Real-time Parameter Estimation in Back-EMF Self-Sensing Mode with the Synergy of Inudction Machine Deadbeat-Direct Torque and Flux Control Drives," ECCE 2018Portland, OR, p. 10.
[114] Flieh, H., 2018, PhD Preliminary Examination, University of Wisconsin - Madison.
[115] Flieh, H., 2019, "Permanent Magnet Servo Motors Design for Dynamic Loss Minimization and Self-Sensing Control," PhD, University of Wisconsin - Madison.

Appendix A Control Structure Design and Implementation for Image Tracking

A.1 Introduction

This chapter describes the electrical and mechanical models used throughout this work as well as documents methods used for parameter estimation of the bench developed in [56, 91, 93-98]. Sections describing the control methods, their design, and their evaluation follow. The end of the chapter discusses self-sensing implementations and considerations. Each section describes the estimation and tuning methods used in this work. Where applicable, the simulation used in this work is documented and any specific considerations are documented.

Throughout this chapter some assumptions are made for the purposes of derivations. Complex variables will be represented in the form given in (0.1) where the q-axis is aligned with the real axis and the d-axis is aligned with the negative imaginary axis. The rotation matrix and its inverse are given in (0.2) and (0.3) respectively. These matrices allow reference frame transformations from stationary to synchronous as defined in (0.4) and synchronous to stationary as in (0.5).

$$F_{dq} = F_q - jF_d = \begin{bmatrix} F_q \\ F_d \end{bmatrix} \tag{0.1}$$

$$R(\theta) = \begin{bmatrix} \cos(\theta) & -\sin(\theta) \\ \sin(\theta) & \cos(\theta) \end{bmatrix} \tag{0.2}$$

$$R^{-1}(\theta) = \begin{bmatrix} \cos(\theta) & \sin(\theta) \\ -\sin(\theta) & \cos(\theta) \end{bmatrix} \tag{0.3}$$

$$R(\theta)\, F_{\alpha\beta} = F_{dq} \tag{0.4}$$

$$R^{-1}(\theta)\, F_{dq} = F_{\alpha\beta} \tag{0.5}$$

Parameters used for simulation as well as tuning of the experimental system are given in Table A.1 and are used for all calculations unless noted otherwise.

Table A.1 – Nominal Parameters

Parameter	Nominal From [21]
λ_{pm} [Wb]	0.0022
L_d [μH]	42.5
L_q [μH]	46.7
R_s [Ω]	0.117
J_p [μNs^2/rad]	60
B_p [μNs/rad]	100
T_μ [mN]	44

Bandwidths used for simulation and experimental results are summarized in Table A.2 and are used throughout this chapter unless noted otherwise.

Table A.2 – Nominal Bandwidths, Dominant Bandwidth Bolded

Controller/Filter	Simulation Bandwidth [Hz]	Experimental Bandwidth [Hz]
Current Regulator	500	500
Fundamental Current Observer	10	10
High Frequency Current Observer	10,000	10,000
Current Observer Carrier HPF	200	200
Motion State Filter	2000, **200**	2000, **200**
Motion Controller	**5**, 1, 0.2	**2**, 0.4, 0.08
Motion Observer	**100**, 20, 4	**100**, 20, 4
Saliency Tracking Observers	**10**, 2, 0.4	**3.3** , 0.7, 0.13
Rotating LPF	50	50
Pulsating LPF	25	25
Flux Observer	1000, **100**	N/A

A.2 Electric Machine Modeling and Parameter Estimation

This section outlines the electrical and mechanical models used in this work as well as their extensions. Sensor models and experimental characterization are documented. In relevant sections, methods for estimating parameters as well as the experimental results are given.

A.2.1 Ideal electrical model of a PMSM

The electric machine model used in most of the simulation, and many of the controls derivations assumes constant d-axis and q-axis inductance, a constant stator resistance, and back-EMF proportional to speed. It is based on the machine models developed in [99, 100]. This machine model is built in the synchronous frame, denoted by the subscript dq. The machine model in the stationary frame, using complex variables for a compact form, is given as (0.6). The model is converted to the synchronous frame as this results in DC quantities to control for a constant speed trajectory. This transformation is shown in (0.7). It should be noted that frame dependent cross-coupling appears due to the product-rule of differentiation when applied to the reference frame transformation and will need to be appropriately handled in the current regulator to avoid having speed dependent errors.

$$V_{\alpha\beta} = L_{\alpha\beta} I_{\alpha\beta} \frac{d}{dt} + R_s I_{\alpha\beta} + j\omega_e \lambda_{pm} \exp(\theta_e) \tag{0.6}$$

$$V_{dq} = L_{dq} I_{dq} \frac{d}{dt} + R_s I_{dq} + j\omega_e L_{dq} I_{dq} + \omega_e \lambda_{pm} \tag{0.7}$$

$$L_{dq} I_{dq} \frac{d}{dt} = V_{dq} - R_s I_{dq} - j\omega_e L_{dq} I_{dq} - \omega_e \lambda_{pm} \tag{0.8}$$

$$T_{em} = I_q \lambda_{pm} - (L_q - L_d) I_d I_q \tag{0.9}$$

The equation is rearranged to form (0.8), which will form the core of the electric machine model simulation. This equation is shown in state block diagram form in Figure A.1. Note that a simple model for the inverter is also included. This is simply a latch on the 3 phases in the stationary frame. Reference frame transformations are applied using the mechanical position from the continuous time model developed later in A.4 .

To achieve useful mechanical work, the torque equation shown in (0.9) is derived as the cross-product of flux and current. This is shown in state block diagram form in Figure A.2. All of these parts are shown together in Figure A.3 in the Simulink diagram used throughout this work.

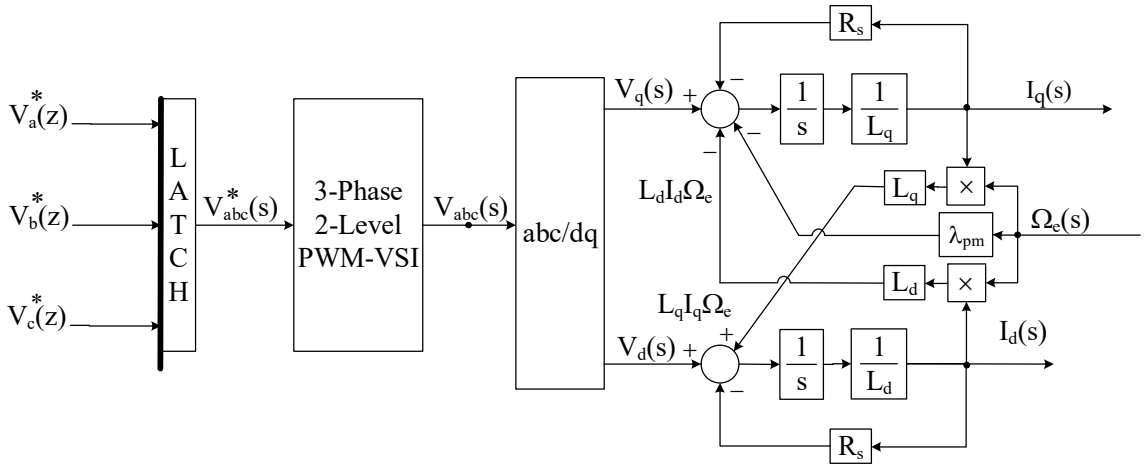

Figure A.1 – State block diagram of an IPMSM electrical model with an idealized inductance (diagonal) and constant resistance shown in the synchronous frame.

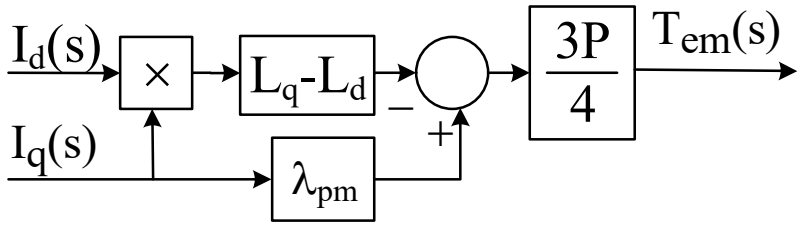

Figure A.2 – State block diagram of the air gap torque produced by an IPMSM.

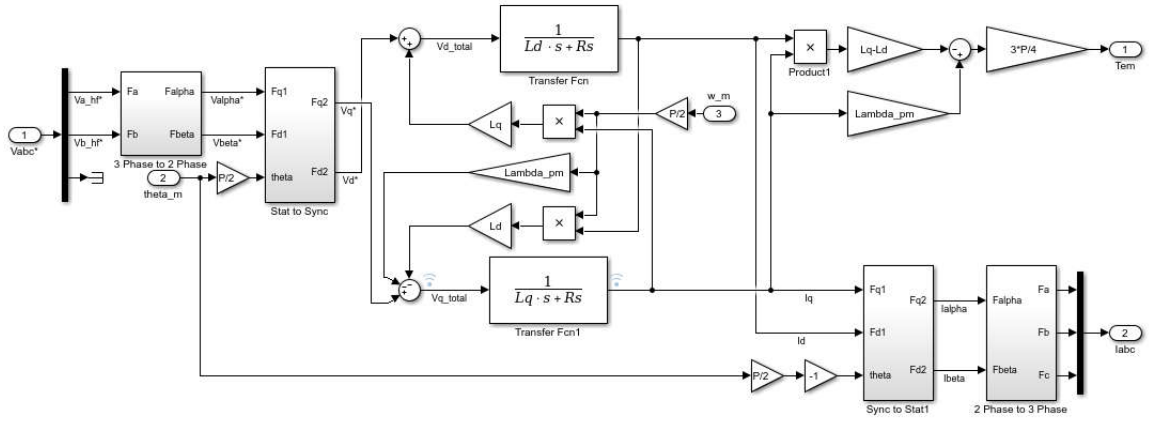

Figure A.3– Simulink implementation of the idealized electric machine model presented in this section.

A.2.2 Ideal high frequency electrical model of a PMSM

In high frequency applications, such as high frequency voltage injection self-sensing, a simpler model is used. This model assumes that the frequency of interest is significantly higher than the fundamental, and therefore content at or near the fundamental is insignificant and not included. This model removes resistance effects, back-EMF, and cross-coupling to leave just a simple inductance based model as shown in (0.10) with a salient inductance (0.12). This model is rearranged in (0.11) to be in a form more suited for simulation and one which will reappear in later high frequency injection based self-sensing which is concerned with the current resulting from the voltage injection.

In this work, this model is not used in Simulink as the full model tends to produce estimation accuracy errors which are in this case considered significant and on the order of 2-15° electrical degrees depending on parameters and injection type. This model does provide a useful starting point for analytical derivations and to gain insight into the system.

$$V_{dq} = L_{dq} I_{dq} \frac{d}{dt} \tag{0.10}$$

$$I_{dq} = L_{dq}^{-1} \int V_{dq} \tag{0.11}$$

$$L_{dq} = \begin{bmatrix} L_q & 0 \\ 0 & L_d \end{bmatrix} \tag{0.12}$$

A.2.3 Non-ideal inductance model of a PMSM

Of particular interest to this work is the current response to a high frequency voltage when the inductance matrix is more complicated than the simple salient model presented in A.2.1. To facilitate this analysis, a machine model in the stationary frame based on the flux model of a machine is presented in (0.13) and (0.14). It should be noted that the back-EMF now shows up as an explicitly position-dependent signal, and the inductance is generated as a function of position as in (0.16). Rearranging (0.14) allows for a solution for current to be obtained as in (0.15).

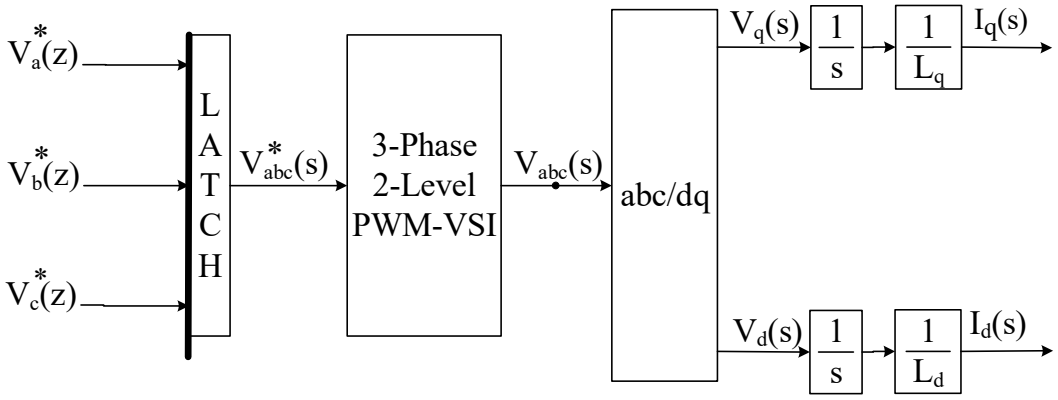

Figure A.4 – State block diagram of a high frequency electrical model suitable for simplified investigation of high frequency voltage injection based self-sensing on IPMSM machines.

$$V_{\alpha\beta} = R_S I_{\alpha\beta} + \lambda_{\alpha\beta}\frac{d}{dt} \tag{0.13}$$

$$\lambda_{\alpha\beta} = L_{\alpha\beta} I_{\alpha\beta} + \lambda_{pm}\begin{bmatrix} \sin(\theta) \\ \cos(\theta) \end{bmatrix} \tag{0.14}$$

$$I_{\alpha\beta} = L_{\alpha\beta}^{-1}\left(\lambda_{\alpha\beta} - \lambda_{pm}\begin{bmatrix} \sin(\theta) \\ \cos(\theta) \end{bmatrix}\right) \tag{0.15}$$

$$L_{\alpha\beta} = \begin{bmatrix} L_\alpha(\theta) & L_{\alpha\beta}(\theta) \\ L_{\alpha\beta}(\theta) & L_\beta(\theta) \end{bmatrix} \tag{0.16}$$

$L_{\alpha\beta}$ can be obtained from L_{dq} by using the high frequency model in (0.10). By multiplying (0.10) by the rotation matrix $R^{-1}(\theta)$ the equation can be converted to the stationary frame as in (0.17). Using the identities provided in (0.18) and (0.19) the equation can be rewritten as in (0.20) . Extracting the inductance portion results in (0.21). It should be noted that this method is slightly inaccurate as the inductance derivation neglects a portion of the response due to the resistance in the high frequency model, this is however added back in as shown in (0.13).

$$R^{-1}(\theta)V_{dq} = R^{-1}(\theta)L_{dq}I_{dq}\frac{d}{dt} \quad (0.17)$$

$$F_{\alpha\beta} = R^{-1}(\theta)\ F_{dq} \quad (0.18)$$

$$F_{dq} = R(\theta)\ F_{\alpha\beta} \quad (0.19)$$

$$V_{\alpha\beta} = R^{-1}(\theta)L_{dq}\ R(\theta)I_{\alpha\beta}\frac{d}{dt} \quad (0.20)$$

$$L_{\alpha\beta} = R^{-1}(\theta)L_{dq}\ R(\theta) \quad (0.21)$$

This form is substantially more complicated as can be seen in both the state block diagram and the Simulink diagram. The inductance and back-EMF are dependent on the rotor position, there are four inductances which need to be calculated and utilized, and the magnitude of the inverse of the inductance matrix is used to correctly scale the flux to a current.

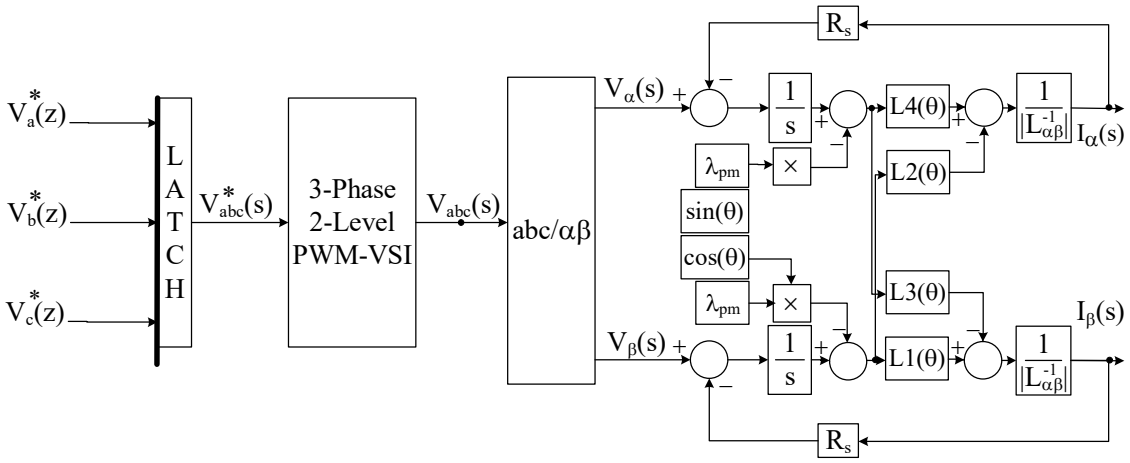

Figure A.5 – State block diagram of an IPMSM electrical model with a non-ideal inductance and constant resistance shown in the stationary frame.

A.2.4 Electrical parameter estimation

Reviewing the machine equation (0.7), there are three main parameters to estimate: inductance, resistance, and permanent magnet flux. As a starting point, nominal values are listed in [91], reproduced here in Table A.3.

Viewing equation (0.7), if current is 0, all that remains is $V_q = \omega_e\lambda_{pm}$. To perform this test, a 500hz bandwidth synchronous frame PI current regulator was used, with a current reference set to 0. The machine was then given an oscillating speed command as shown in

(0.22) with the voltage commands needed to obtain zero current plotted against the speed as in Figure A.7. This shows the expected linear relationship between speed and voltage as well as the estimated best fit line overlaid.

$$\omega^* = -24 - 16\sin(10\pi t) \quad (0.22)$$

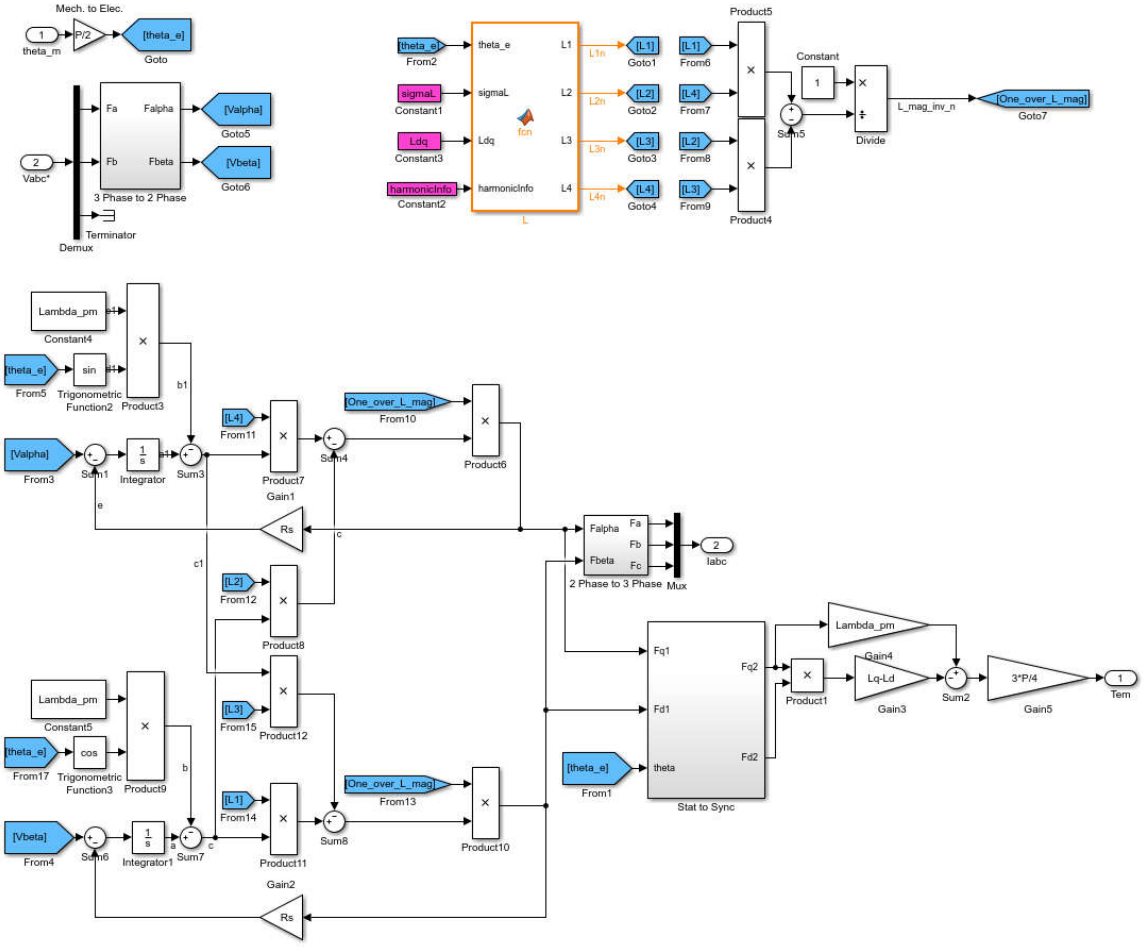

Figure A.6 – Simulink implementation of the non-ideal electric machine model presented in this section.

Viewing equation (0.7), which is rewritten here for convenience as (0.23), if ω_e is zero, the back-EMF and decoupling terms disappear. Transforming the result to the Laplace domain, (0.24) is obtained. Rearranging this into an admittance form is shown in (0.25). Several things should be noted about this form. At low frequencies, (0.25) simplifies to $1/R_s$. At high

frequencies, (0.25) is dominated by $1/(L_{dq}\, j\omega)$. This allows for estimates of the parameters by isolating asymptotes in either the low frequency region, or the high frequency region. This process is shown in Figure A.8 and Figure A.9 for the d-axis and q-axis respectively, resulting in a consistent estimate of resistance of 0.11Ω and estimates of inductance of $37\mu H$ and $41\mu H$ along the d-axis and q-axis respectively.

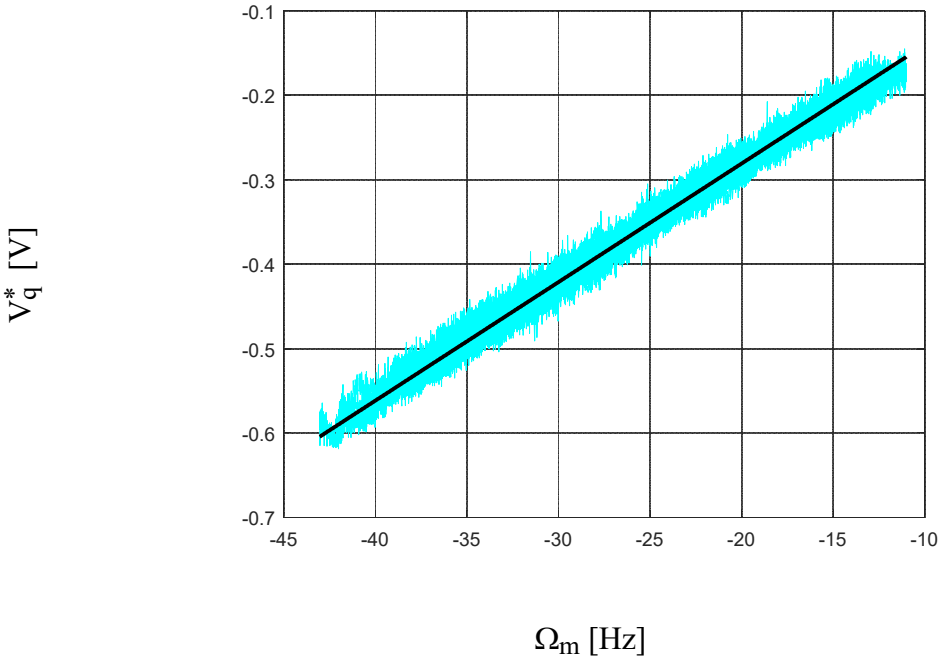

Figure A.7 – Estimation of λ_{pm} is done by relating the speed and voltage through equation (0.7) with estimated λ_{pm} of 0.0022Wb overlaid for comparison.

$$V_{dq} = L_{dq} I_{dq} \frac{d}{dt} + R_s I_{dq} + j\omega_e L_{dq} I_{dq} + \omega_e \lambda_{pm} \tag{0.23}$$

$$V_{dq}(s) = (L_{dq}\, s + R_s)\, I_{dq}(s) \tag{0.24}$$

$$\frac{I_{dq}(s)}{V_{dq}(s)} = \frac{1}{(L_{dq}\, s + R_s)} \tag{0.25}$$

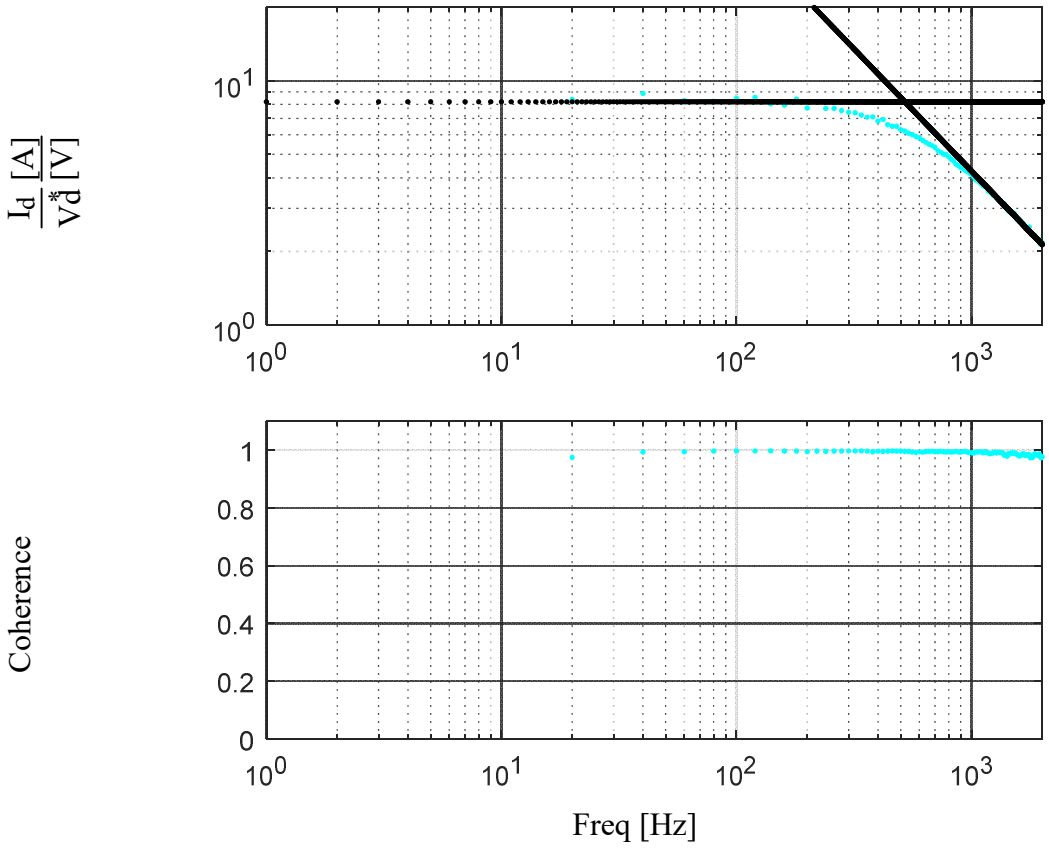

Inductance estimation FRF, Estimated Asymptotes
$\omega_m^* = 0$, V_{dq}^* chirp signal with f_0=1Hz, f_1=1kHz, T=1s, magnitude 0.3V
$R_s = 0.12\Omega$, $L_d = 37\mu H$

Figure A.8 – Estimation of d-axis parameters on test machine.

Table A.3 – Electrical Parameter Estimates

Parameter	Nominal From [21]	Obtained Experimentally
λ_{pm} [Wb]	0.0022	0.0022
L_d [μH]	42.5	37.3
L_q [μH]	46.7	41.2
R_s [Ω]	0.117	0.12

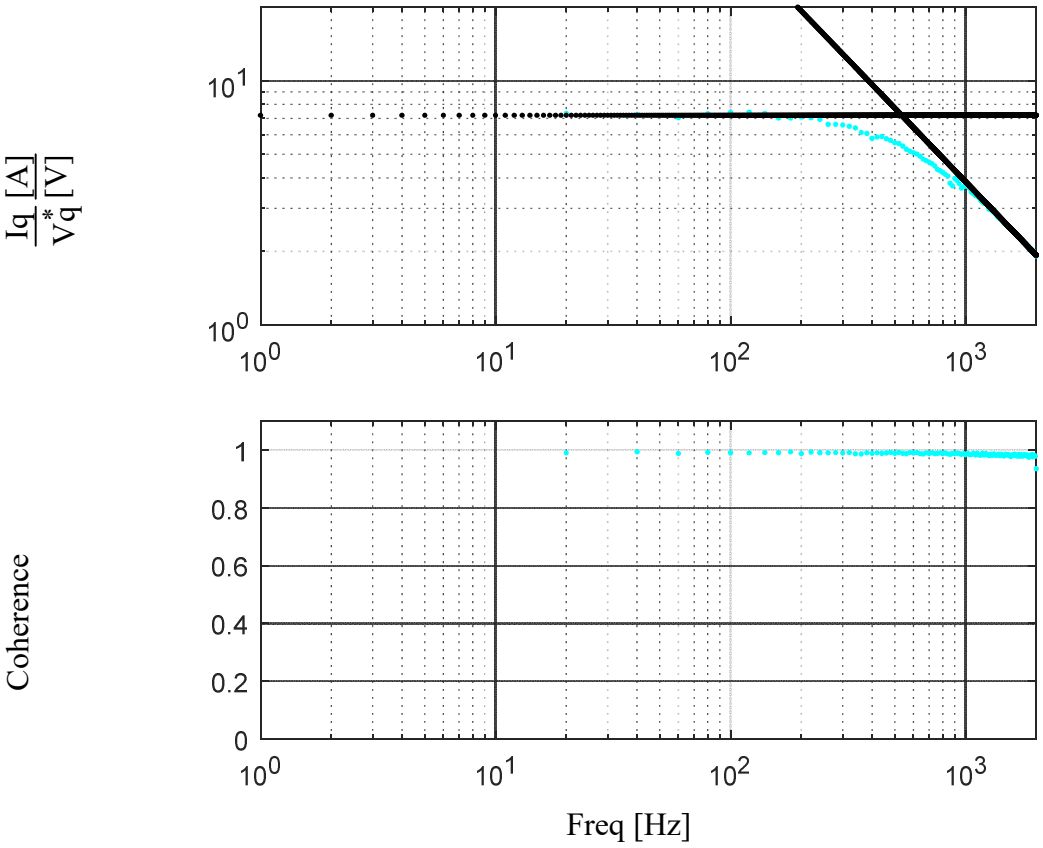

Inductance estimation FRF, Estimated Asymptotes
$\omega_m^* = 0$, V_{dq}^* chirp signal with f_0=1Hz, f_1=1kHz, T=1s, magnitude 0.3V
$R_s = 0.13\Omega$, $L_d = 41\mu H$

Figure A.9 – Estimation of q-axis parameters on test machine.

A.2.5 Modeling of rotational mechanical system

The mechanical model includes an inertial term J_p, a damping term b_p, and T_μ, which is a non-linear friction term as developed in [100]. This equation also includes the generated torque T_{em}, and any unknown disturbance torques T_d. This model is shown in state block diagram and implemented Simulink diagram in Figure A.10 and Figure A.11 respectively. It should be noted that while the friction is observed on the bench, its nonlinear nature makes analysis complicated and therefore in simulation T_μ is often set to zero to prevent numerical

problems. In bench evaluation, it is advised to also stay away from rotor speed zero-crossings to prevent this same problem.

$$\dot{\Omega}(s) = \frac{1}{J_p} * (T_{em} - b_p*\Omega - T_\mu sign(\Omega) - T_d) \quad (0.26)$$

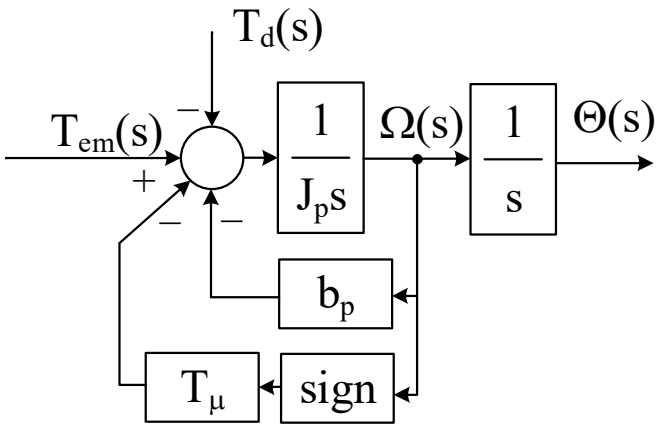

Figure A.10 – State block diagram of a rotational mechanical model with showing inertia, damping, and non-linear friction.

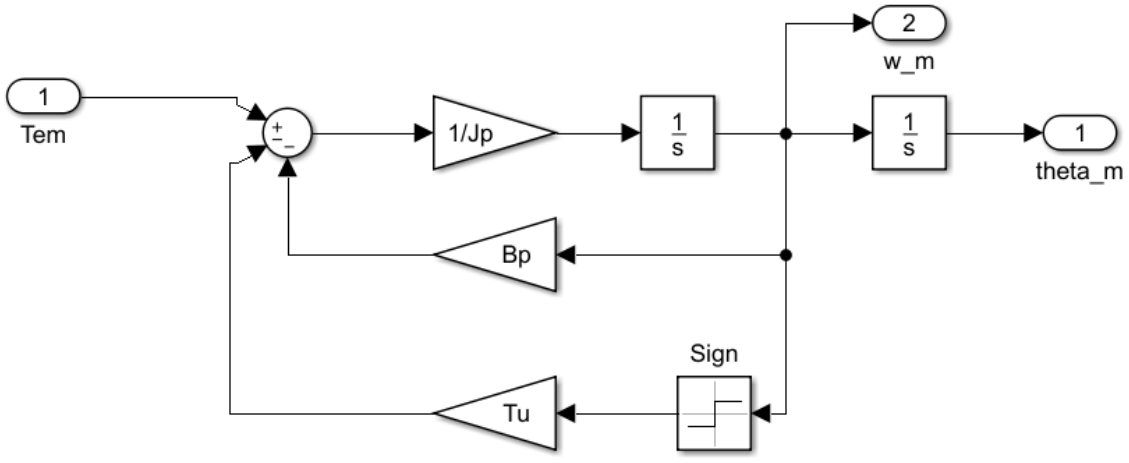

Figure A.11 – Simulink implementation of the mechanical model presented in this section.

A.2.6 Mechanical parameter estimation

To estimate the mechanical parameters, the torque is plotted against speed as in Figure A.12 and Figure A.13, known as flag plots. This gives some insight into the mechanical system when compared to equation (0.26). Noting the region near zero speed, it is clear that a non-linear phenomenon takes places, this corresponds with the reversal of static friction to oppose the direction of the motion. The relationship is shown in (0.27) and is overlaid in red.

Next, estimating the inertial portion is done by taking the derivative of the torque with respect to time and adding it to the static friction as in (0.28). This portion gives the 'flag' its width. As sine waves are used in these tests, the width is not constant and so it is slightly less accurate. For a better estimate, a triangle wave could be used. Ultimately, the inertia will be estimated from the dynamic stiffness plot later in this work. The estimated inertial torque is overlaid in black on the figures.

Finally, it is recognized that there is a definite slope to the flag. This denotes a proportional relationship between the speed and torque and corresponds to damping of the form: b_p*w(t). This is added to the static friction and inertial terms to form (0.29) and is overlaid on the figures in blue. Note that this estimate closely matches the raw experimental data. Slight variations are due to overshoot in the controller, and some lagging effects due to the filters used to remove quantization from the data.

Final parameter estimates used to generate the model overlays, and which will be used throughout this work are given in Table A.4.

$$Tem(t) = T_{\mu}sign(\omega(t)) \quad (0.27)$$

$$T_{em}(t)= J_p \dot{\Omega}(t) + T_{\mu}sign(\omega(t)) \quad (0.28)$$

$$T_{em}(t)= J_p \dot{\Omega}(t) + b_p*\omega(t) + T_{\mu}sign(\omega(t)) \quad (0.29)$$

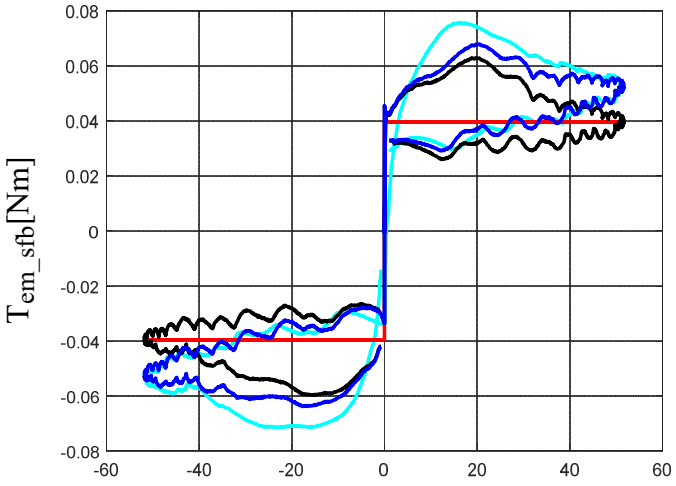

Torque from: Filtered Raw Data, Model (0.26), Model (0.27), Model (0.28)

$\omega_m^* = 8 * \sin(2\pi*0.1)$ Rad/s

Figure A.12 – Flag plot used to estimate mechanical parameters.

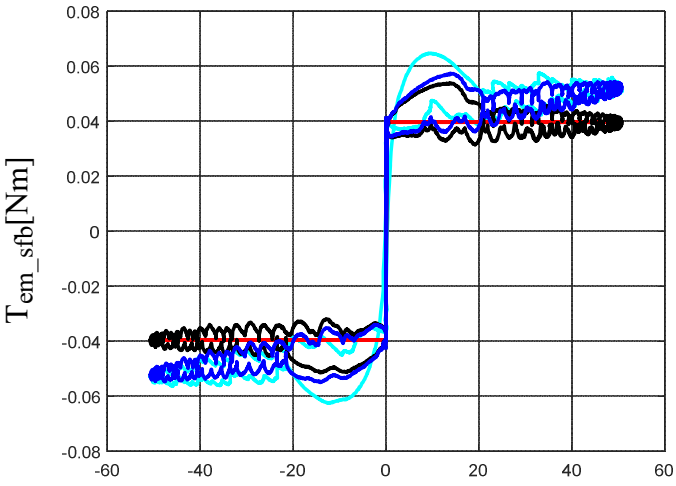

Torque from: Filtered Raw Data, Model 1, Model 2, Model 3

$\omega_m^* = 8 * \sin(2\pi*0.5)$ Hz

Figure A.13 – Flag plot used to estimate mechanical parameters.

Table A.4 – Mechanical Parameter Estimation.

	Nominal from [21]	Estimated Value
J_p [$\mu Ns^2/rad$]	60	60
B_p [$\mu Ns/rad$]	100	250
T_μ [mN]	44	39.6

A.2.7 Current sensor modeling and characterization

Current sensors have a number of characteristics which must be considered to achieve accurate current measurements including current sensor scaling, offset, and the system or current sensor noise which shows up on the measurement. In this work a set of 2 current sensors are used for each machine: LEM HAIS-100P current sensors for the speed control machine, and HAIS-50P current sensors for the load machine with the third phase estimated by assuming the zero sequence is zero.

An initial estimate of current sensor scaling can be found by checking the sensor data sheet, and the number of turns. In this work there are 2 turns for the speed control, and 3 turns for the load machine, which give a set of initial gains listed in Table A.5. This scaling factor should be approximately correct, but to verify it a sinusoidal current is applied to the machine and the sensor value is compared to a current probe. After applying this process and minimizing the error between the two sensors, the final scaling factor is found and documented in Table A.5.

Table A.5 – Current sensor characterization.

Machine/Phase	Motion/u	Motion/v	Load/u	Load/v
Gain from Spec Sheet/Turns	80	80	26.67	26.67
Tuned Gain	74.16	80	24.91	25.63
DC Offset	2.49	2.49	2.48	2.56
Noise Mean	-7.39×10^{-6}	4.69×10^{-6}	4.58×10^{-7}	1.31×10^{-6}
Noise Std Dev	0.08	0.08	0.04	0.04

Current sensors often have an offset. This offset can be compensated for at startup. Set all of the voltage commands to zero and collect the current sensor for a short period of time. In this work 0.5s are observed. At the end, the average value can be calculated and subtracted from the current sensor to provide a compensated 0. As this work compensates for the sensors each run, the offset changes slightly but values for a representative run are shown in Table A.5.

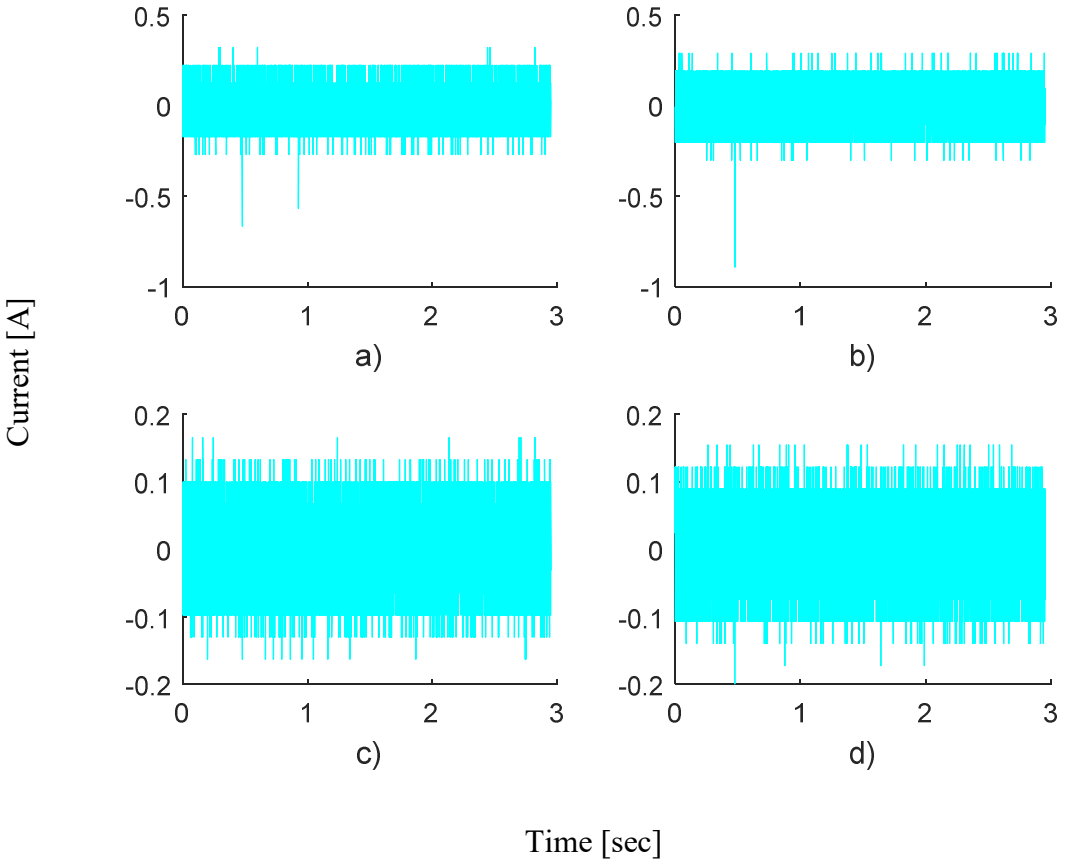

Figure A.14 – Raw current sensor output when zero voltage is commanded.

Finally, current sensors tend to have noise on them. This can be from the sensors, imperfect signal conditioning, or external equipment nearby. To characterize the sensors, set the system voltage to zero and collect the current sensor readings. This data is shown in Figure A.14 for phase machine a, phase u in a), machine a, phase v in b), machine b, phase u in c), machine b,

phase v in d). Characterization can be done in several ways. To determine if the noise is colored, an FFT can be taken as in Figure A.15. The FFT shows more of a high-pass filtering of the spectral content so a more complicated model of the noise may be a better fit to the actual sensor response.

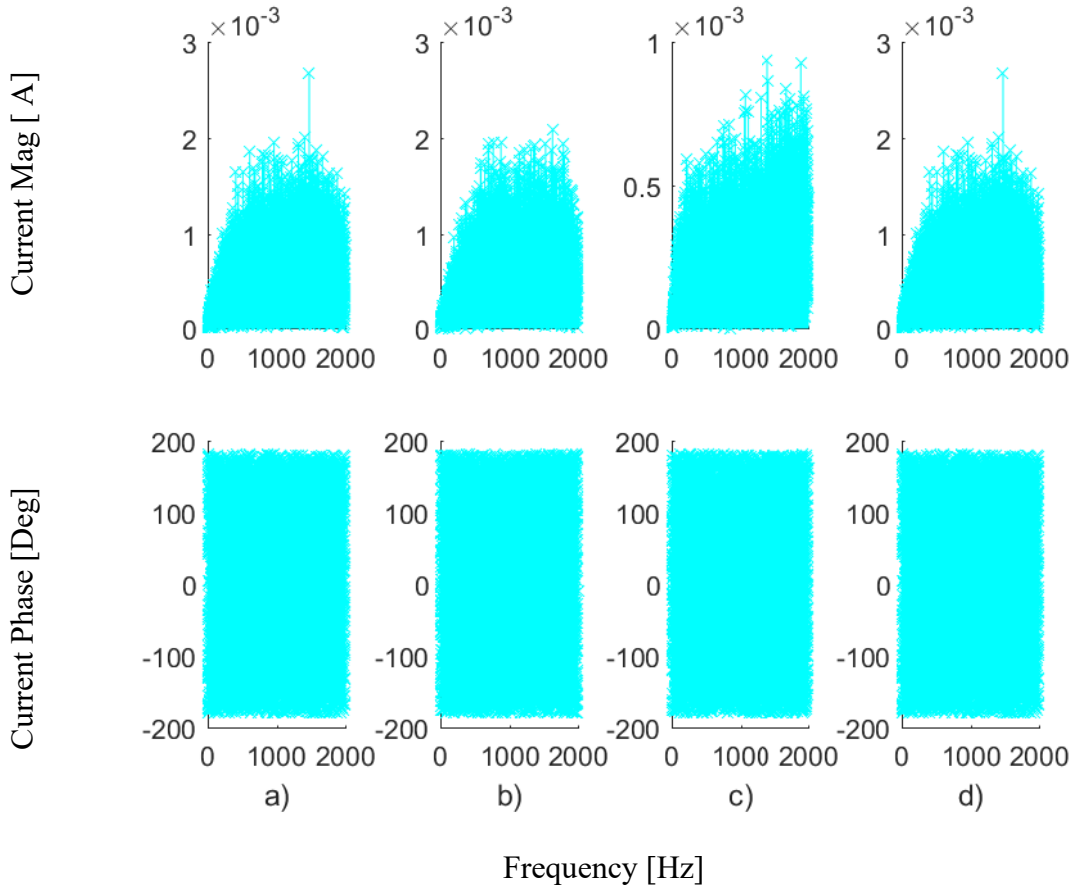

Figure A.15 – FFT of the current sensors when zero voltage is commanded.

Next, to generate a simple model, a gaussian distribution can be generated from the average and variance of the noise. In Figure A.16 a histogram is shown with a fit gaussian distribution overlaid. The average and standard deviation are listed in Table A.5. Gaussian distributions have been generated for each sensor with the experimentally obtained values and overlaid. The models match well and can be used in a simulation to observe the effect of the noise on the self-sensing performance.

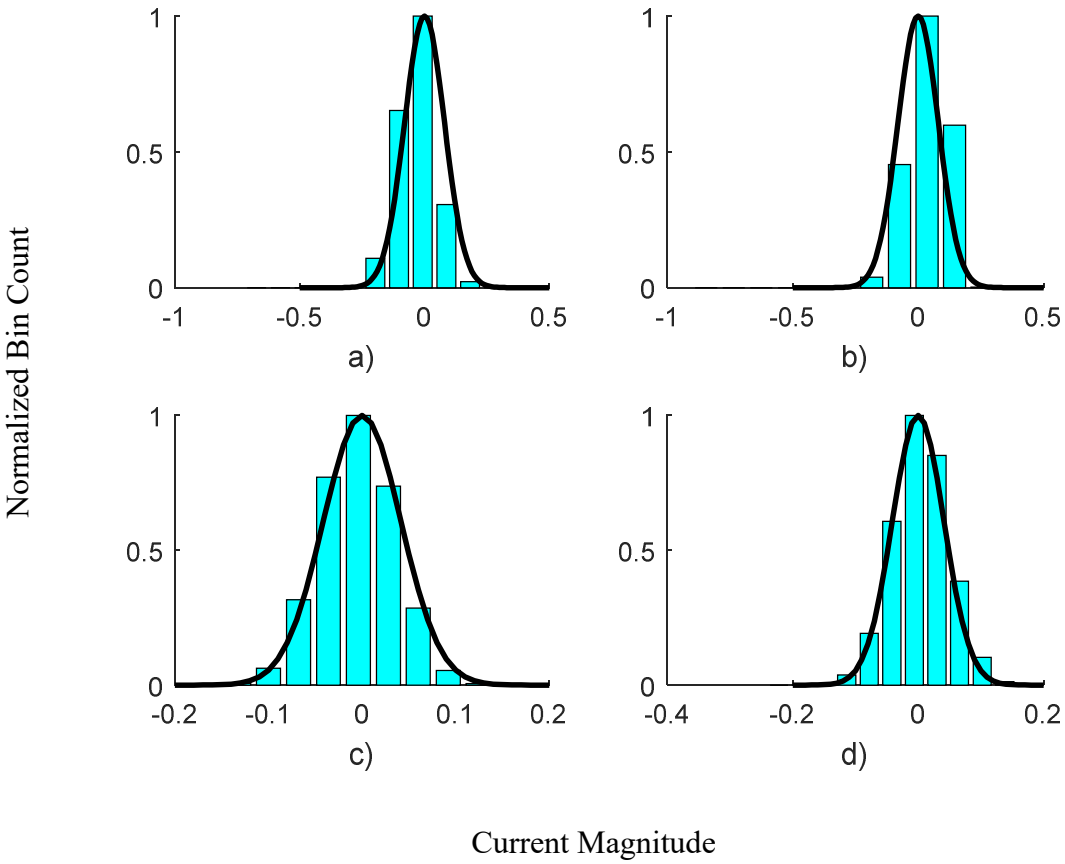

Figure A.16 – Normalized histogram of the noise of the current sensors when zero voltage is commanded with overlaid gaussian distribution probability density function generated from data average and standard deviation.

A.2.8 Encoder modeling and characterization

The encoder used in this project is a 5000-line encoder. As there are 4 counts per line, this encoder has 20,000 counts per revolution giving it a mechanical resolution of 0.018°. The AIX XCS2000 has an FPGA which handles decoding the signals from the encoder. During startup the only part which is critical is that both zero pulses have been found so that the controller can provide an absolute position. There are several ways to do this, in this project a simple rotating vector in the stationary frame is fed to a stationary frame PI current regulator.

This is not a precision control method, but it is good enough to spin the machine and allow the controller to find both zero pulses.

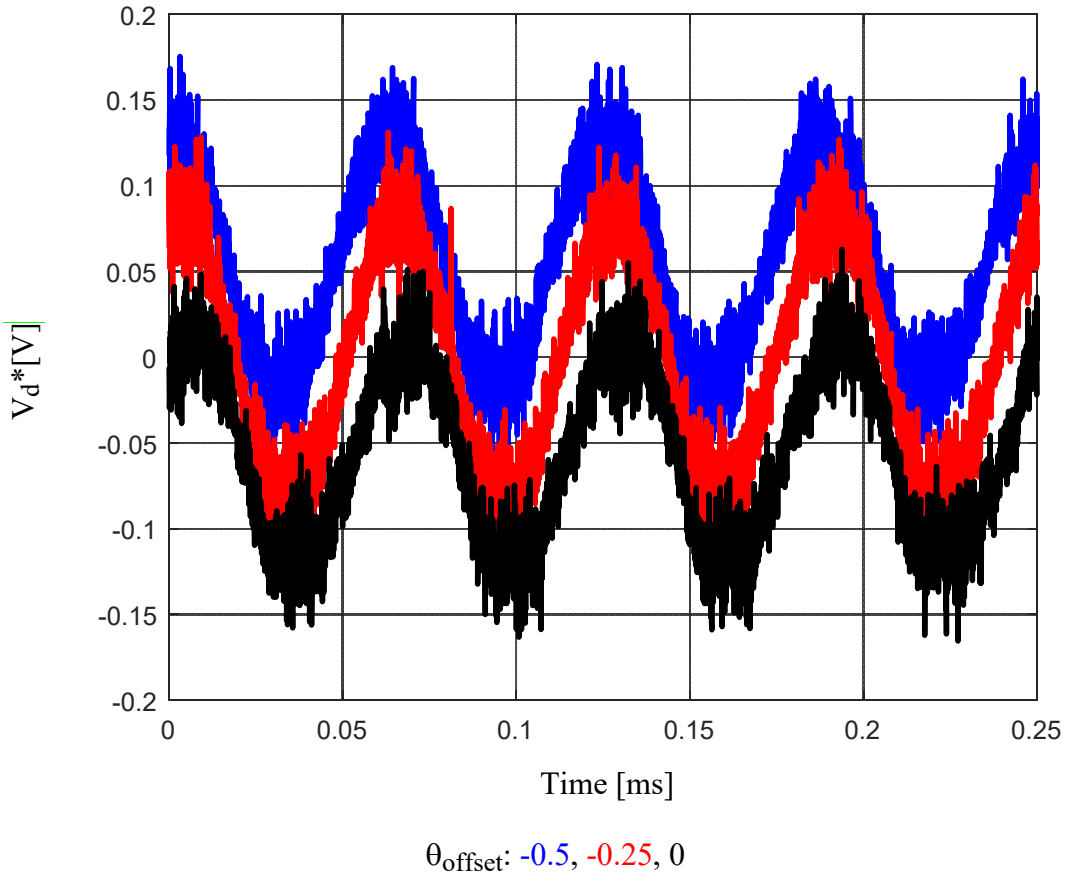

Figure A.17 – Voltage command resulting from the synchronous frame PI current regulator, when zero current is applied, and the machine is spun at a sinusoidal speed with varied encoder-to-electrical position offsets.

Once the zero pulses are found, the mechanical position is known. However, there will still be an offset between the zero-pulse and the electrical reference frame. In this work the q-axis is denoted as electrical 0°. To get a first estimate of the offset, a beta-axis pulse of current can be applied. This should align the beta-axis with the d-axis. By checking the absolute position from the encoder, the offset to one of the machine's poles is found. This method results

in a good starting estimate of the axes but should not be fully trusted as the mechanical friction and damping can slightly affect how well the beta and d-axes align.

To fine tune the position offset, spin the machine at a sinusoidal high speed to generate a back-EMF signal. Using a synchronous frame PI current regulator and setting the current command for both axes to 0, view the d-axis voltage command required to achieve zero d-axis current. The position offset can be adjusted until a zero d-axis voltage command is obtained. This results in the q-axis generating a non-zero voltage to compensate for the back-EMF. In other words, the back-EMF is purely along the q-axis as is expected.

In Figure A.17 the offset was manipulated to show the effects on the d-axis voltage command when the offset is set to values 0.25 radians to either side of the best offset. It is clear from the non-zero voltage command that there is cross-coupling due to the axes not being aligned with the physical machine.

A.3 Current Regulation

A.3.1 Complex vector current regulator

Section A.2.1 noted the frame dependent cross-coupling of the electric machine when formulated in the synchronous frame. One approach to controlling the machine is to use a synchronous frame PI regulator as in [101]. In steady-state and at low speeds this allows for very good regulation. However, as noted in [102, 103] as speed increases, the effects of the cross-coupling become significant. This is noted as an asymmetric complex pole, which is not a common feature to deal with when tuning a controller. The authors [102, 103] propose a way of handling this by placing the controller's zero asymmetrically to minimize the effects of the pole. This structure is shown in Figure A.18.

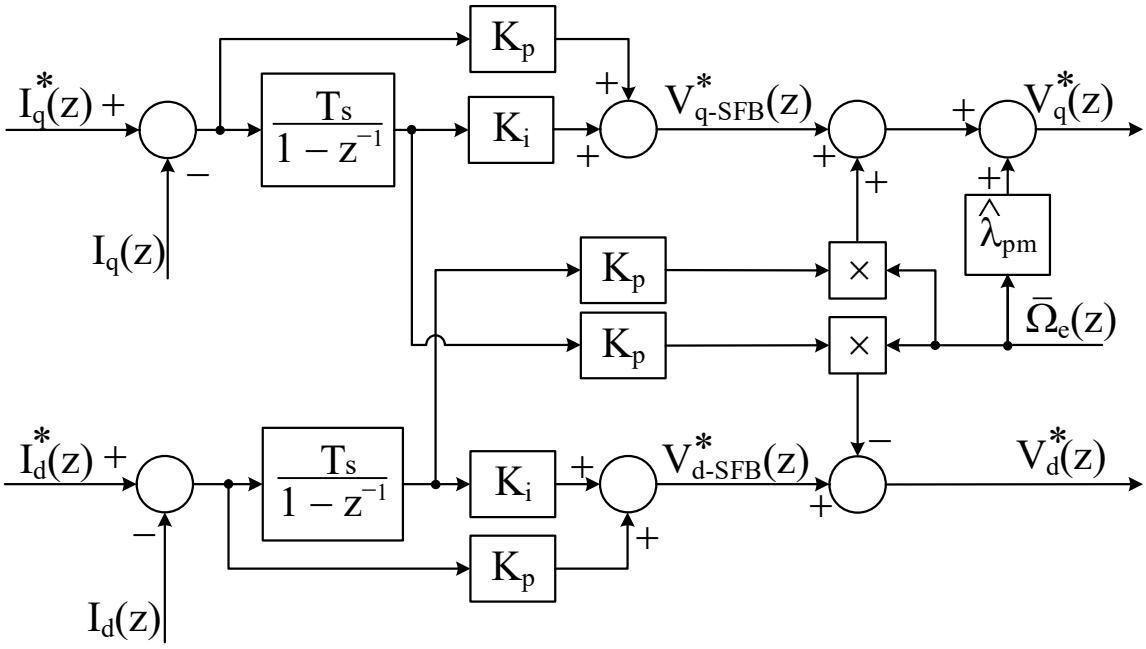

Figure A.18 – State block diagram of a complex vector current regulator as outlined in [103].

To tune this controller, the closed-loop transfer function is found as in (0.30). Next it is noted that if (0.31) holds, the equation simplifies to (0.32). Then the tuning process continues as if for a simple L/R system and K_p is found as in (0.33). A Simulink implementation of the complex vector current regulator used in this work is shown in Figure A.19.

$$\frac{V}{I} = \frac{K_p\,(s + K_i/K_p + j\omega_e)}{Ls(s + R/L + j\omega_e) + K_p\,(s + K_i/K_p + j\omega_e)} \tag{0.30}$$

$$K_i = \frac{R}{L} K_p \tag{0.31}$$

$$\frac{V}{I} = \frac{K_p}{Ls + K_p} \tag{0.32}$$

$$K_p = \omega_b L \tag{0.33}$$

A.3.2 Complex vector current regulator bench validation

To verify the performance of the current regulator, several tests were performed to verify the expected command tracking and dynamic stiffness responses. Beginning with command tracking, the response was evaluated using a rotating chirp of the form

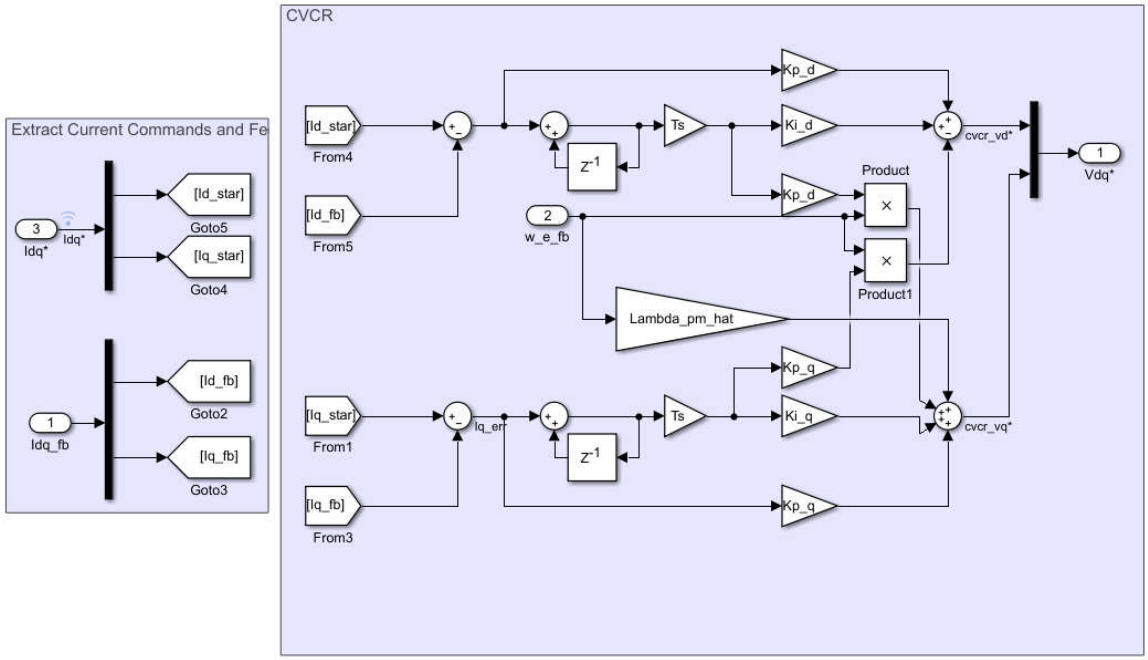

Figure A.19 – Simulink implementation of the complex vector current regulator presented in this section.

$$x(t) = \sin\left(\phi + 2\pi\left(f_o t + \frac{kt^2}{2}\right)\right) \tag{0.34}$$

(0.34) applied to the current command I_{dq}* and the current response I_{dq} was collected. Both axes are shown in Figure A.20 and Figure A.21 with overlaid lines for 0.7 magnitude and -45° phase to aid in bandwidth estimation. The test was performed at different speeds to show the effects of speed on the bandwidth. As expected, the FRFs agree at each speed. The bandwidth for both axes is estimated to be 500Hz using the magnitude, and 500Hz using the phase. This agrees with the tuning to 500Hz.

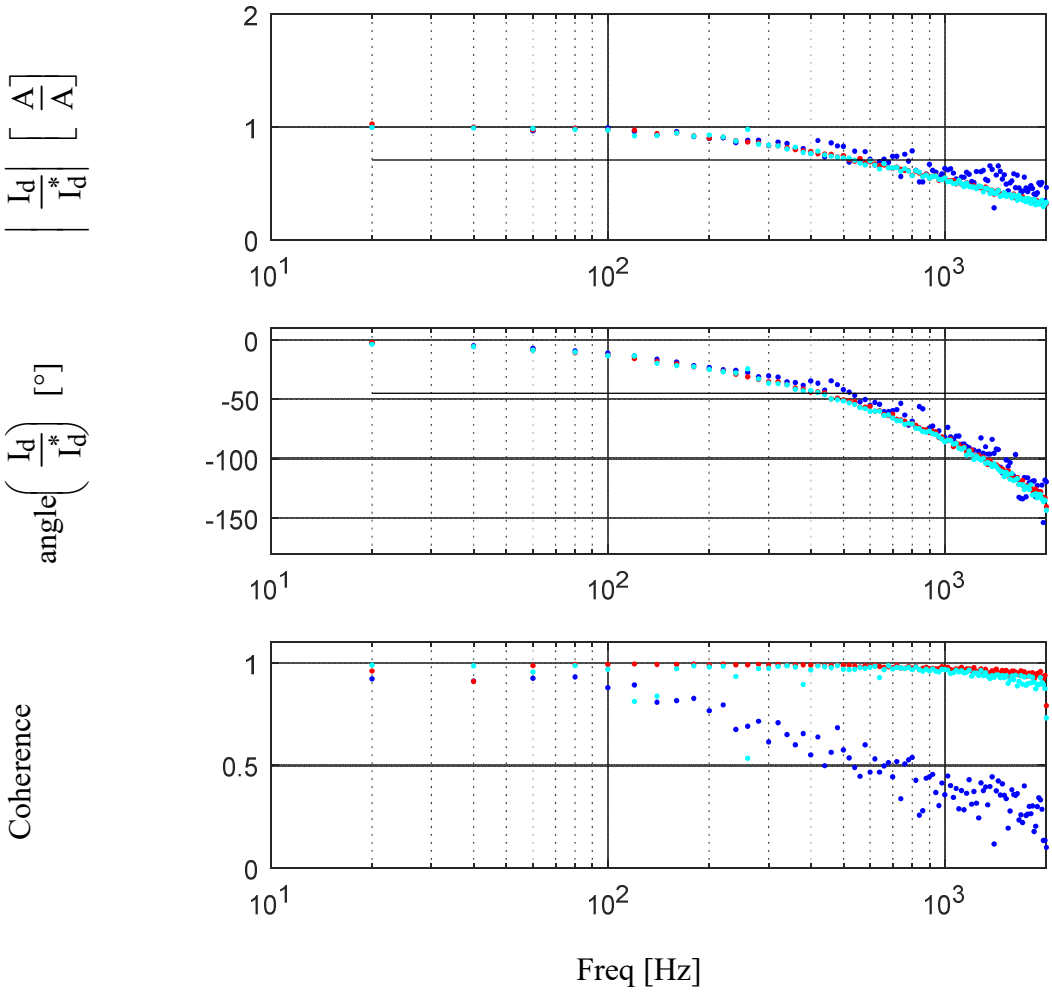

Command Tracking at ω* = 0 Hz, 8 Hz, 16 Hz
I_{dq}* chirp applied with f_0=1 Hz, f_1=2 kHz, T=1s, Magnitude = 1A

Figure A.20 – Experimental d-axis command tracking FRF.

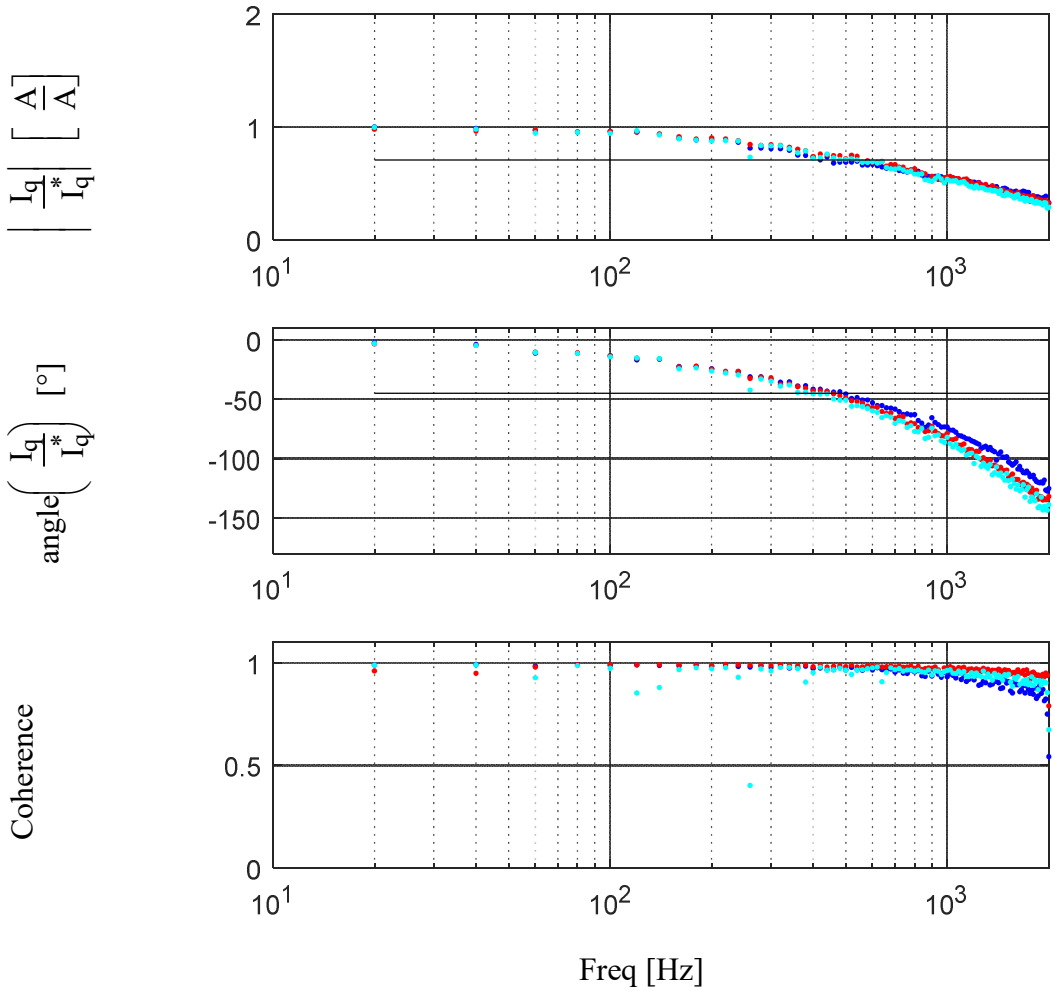

Command Tracking at ω* = 0 Hz, 8 Hz, 16 Hz
I_{dq}* chirp applied with f_0=1 Hz, f_1=2 kHz, T=1s, Magnitude = 1A

Figure A.21 – Experimental d-axis command tracking FRF.

To further verify the current regulator's performance, a dynamic stiffness FRF was obtained using a rotating chirp applied as a voltage disturbance. The resulting FRFs are shown in Figure A.22 and Figure A.23 for each axis. Asymptotes are shown estimating the L_{dq} and R portions of the FRF. The bandwidth here is estimated where the asymptotes cross. Bandwidth estimates are 1 kHz on the d-axis, and 1 kHz on the q-axis respectively. In Table A.6 parameter estimates from the asymptotes are shown next to the estimates obtained in A.2.4 .

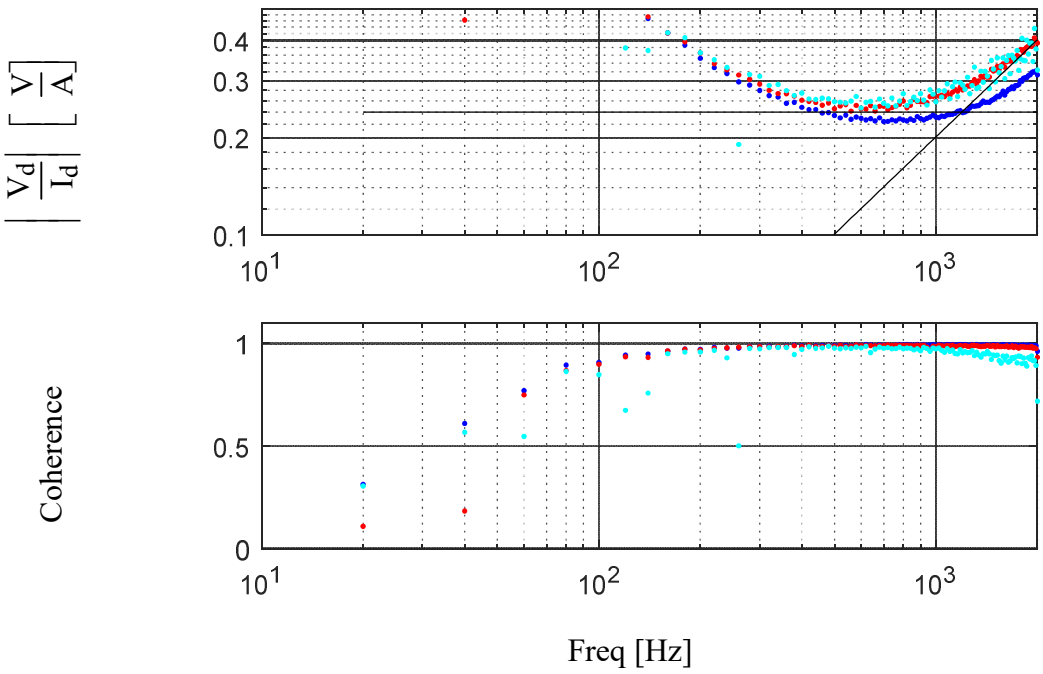

Dynamic Stiffness at ω* = 0 Hz, 8 Hz, 16 Hz
V_{dq} chirp applied with f_0=1 Hz, f_1=2 kHz, T=1s, Magnitude = 1A

Figure A.22 – Experimental d-axis dynamic stiffness FRF.

Table A.6 – Electrical Parameter Estimates

Parameter	Obtained in section A.2.4	Obtained from DS Estimate
λ_{pm} [Wb]	0.0022	0.0022
L_d [μH]	37.3	32
L_q [μH]	41.2	36
R_s [Ω]	0.12	0.12

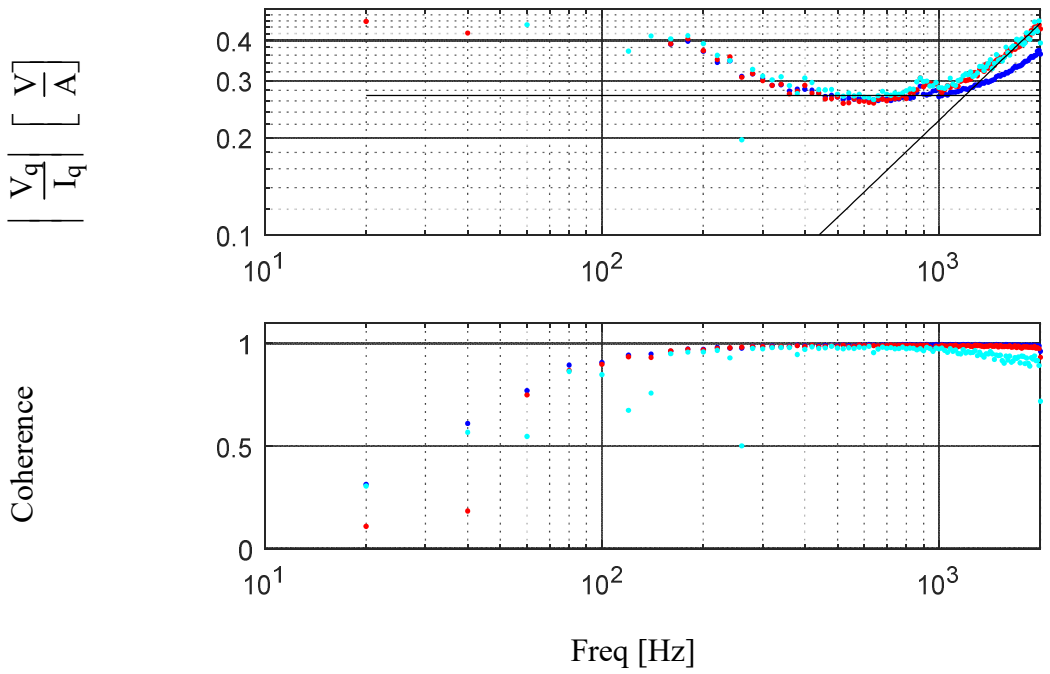

Dynamic Stiffness at ω* = 0 Hz, 8 Hz, 16 Hz
V_{dq} chirp applied with f_0=1 Hz, f_1=2 kHz, T=1s, Magnitude = 1A

Figure A.23 – Experimental q-axis dynamic stiffness FRF.

A.4 Motion Control

A.4.1 Motion state feedback controller design and validation

The physics-based motion controller utilized in this work is designed with a few assumptions to make the model simpler. First the load is assumed to be a purely inertial load. Damping can be included but makes the tuning process somewhat harder without much benefit as the damping is typically relatively small. It is advised to leave T_μ out of the model at this stage as its non-linear nature will make the system harder to tune. The second assumption used is to simplify the command and feedback model as though it is based on speed. In practice it will be formed on Δθ but this assumption greatly simplifies the tuning process.

The plant is formed using a New System Dynamics (NSD) approach [9], modeling the input to the plant as a latch and taking the z-transform as shown in (0.35). The physics-based controller takes the form of a PII but will be formed using physical unit gains to aid in the understanding of what each portion of the controller is doing. This form is shown in Figure A.24 as it will be implemented using $\Delta\theta$ for feedback, and in Figure A.25 in the Simulink implementation used in this work. The controller model is then expanded and shown in (0.36). The open loop model is formed by multiplying G_c and G_p together, the closed-loop model is then formed in the classical fashion, and the characteristic equation is extracted as shown in (0.37). Multiplying three poles together results in (0.38). By expanding (0.37), collecting terms, setting similar parts similar order parts to (0.38) equal to each other, and solving for the gains, the gain calculations are solved for as in (0.39), (0.40), and (0.41).

$$G_p(z) = NSD(z) = (1-z^{-1})Z\left(\frac{1}{\hat{J}_p s^2}\right) = \frac{T_s z^{-1}}{\hat{J}_p(1-z^{-1})} \tag{0.35}$$

$$G_c(z) = \frac{b_a(1-z^{-1})^2 + k_a T_s(1-z^{-1}) + k_{sa}T_s}{(1-z^{-1})^2} \tag{0.36}$$

$$CE(z) = \hat{J}_p(1-z^{-1})^3 + \left(b_a(1-z^{-1})^2 + k_a T_s(1-z^{-1}) + k_{sa}T_s\right) T_s z^{-1} \tag{0.37}$$

$$(z-a)(z-b)(z-c) = z^3 + z^2(-a-b-c) + z(ab+ ab + bc) - abc \tag{0.38}$$

$$b_a = \frac{\hat{J}_p}{T_s}(1-abc) \tag{0.39}$$

$$k_a = \frac{1}{T_s^2}\left(\hat{J}_p(3-ab-ac-bc) - 2b_a T_s\right) \tag{0.40}$$

$$k_{sa} = \frac{1}{T_s^3}\left(\hat{J}_p(3-a-b-c) - b_a T_s - k_a T_s^2\right) \tag{0.41}$$

To evaluate the performance of the motion controller, a command tracking FRF was obtained using a chirp input to the speed command as shown in Figure A.26. In classical controls two of the common methods of defining bandwidth use the bandwidth that the frequency response drops 3dB (0.707 magnitude) from its low frequency value, or alternately when the phase drops 45° from its zero-lag value [9, 17] [104]. Reference lines are overlaid at

0.7 magnitude and -45° to provide estimates of achieved bandwidth. Using the magnitude criteria, a bandwidth of 19Hz is achieved, using the angle criteria a bandwidth of 12Hz is achieved

Next a dynamic stiffness FRF was taken using a chirp input to the torque disturbance. Overlaid asymptotes for the physical parameters and gains are shown. Eigenvalues of the controller are where the asymptotes interact. In the tuning process, the eigenvalues are separated by 5x to achieve 0.6Hz, 3.2Hz, 16.7Hz and the dynamic stiffness plot agrees well with the overlaid asymptotes.

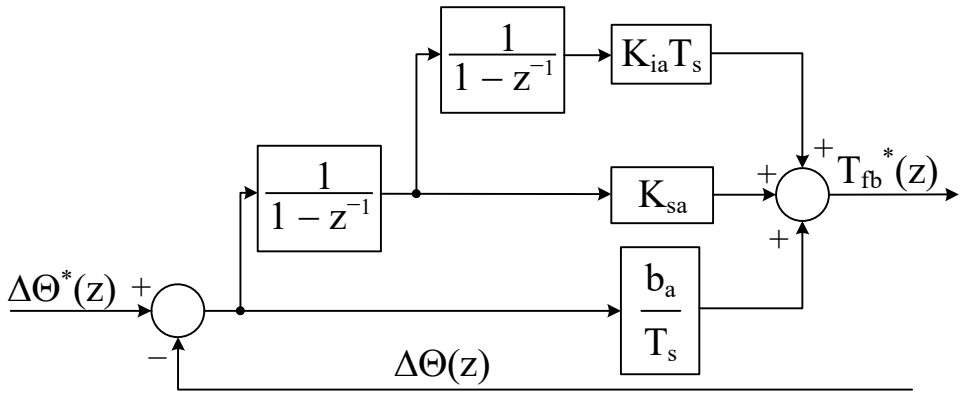

Figure A.24 – State block diagram of the physics-based motion controller.

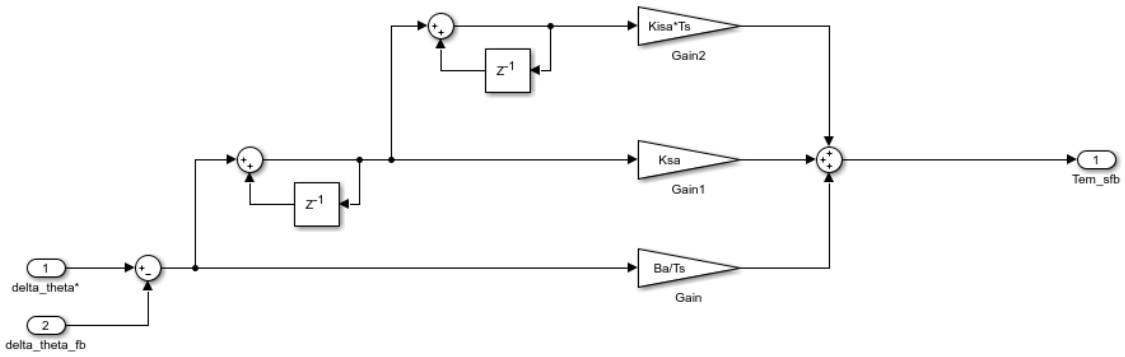

Figure A.25 – Simulink implementation of the physics-based motion controller.

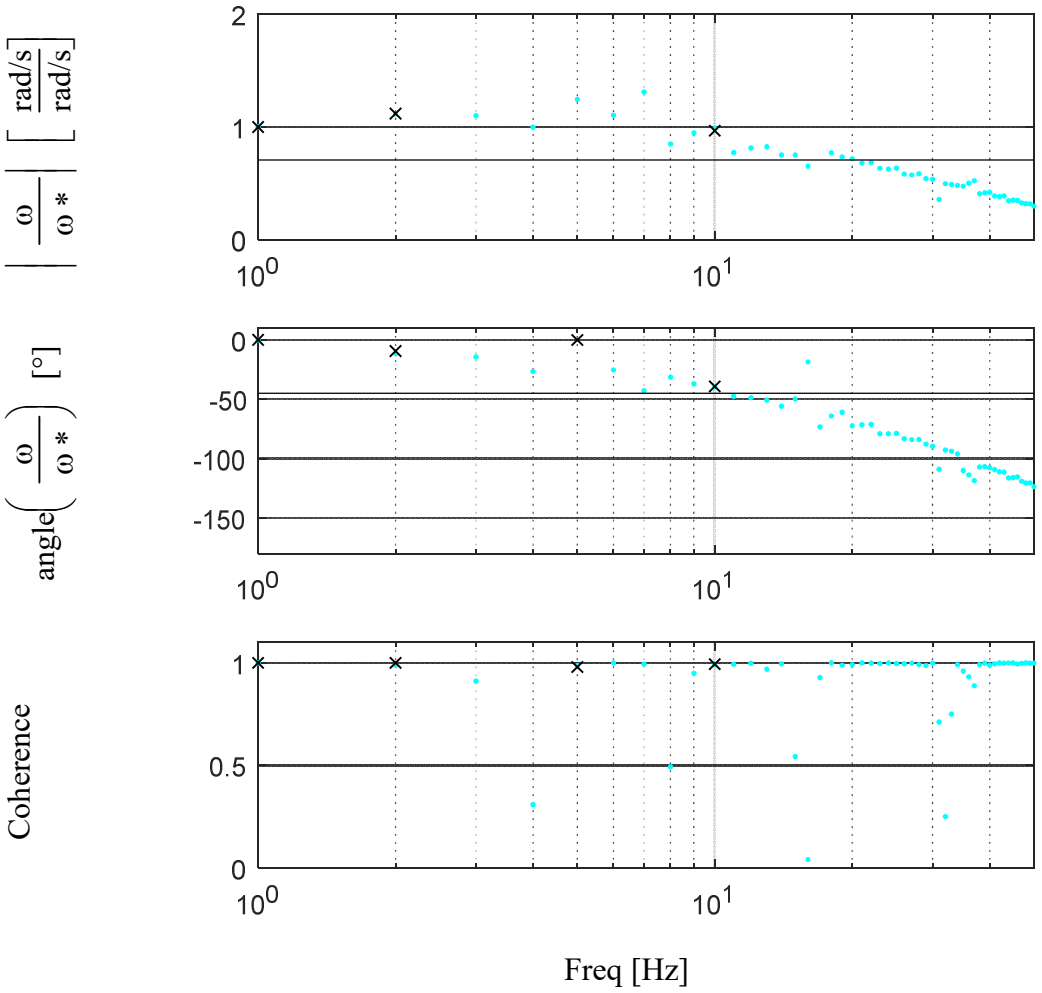

Chirp FRF, Single Sine Test

ω_m* chirp with f_0 = 1Hz, f_1= 100Hz, T=0.5s, magnitude 0.5Hz, offset 4Hz

Figure A.26 – Command tracking FRF of a motion controller tuned to 17Hz.

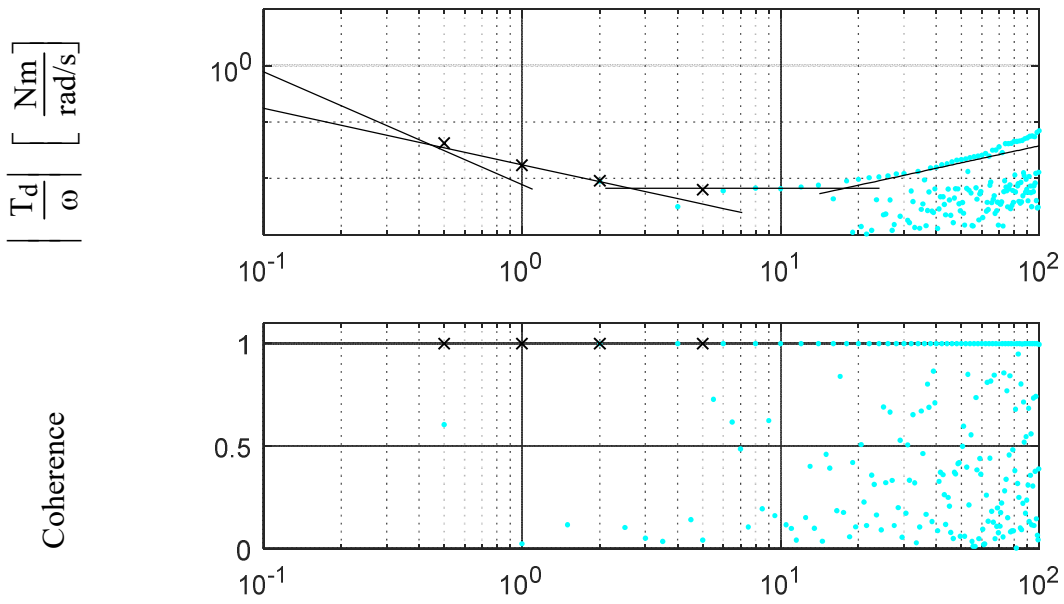

Dynamic stiffness from: Chirp FRF, Single Sine Test
T_d* chirp with f_0 = 1Hz, f_1= 100Hz, T=0.5s, magnitude 0.1PU
Overlaid asymptotes: J_p = 60 μNm, B_o+B_p = 6.6mNm/rad/s, K_a = 0.33 Nm/rad, K_{sa} = 2.71 Nms/rad

Figure A.27 – Dynamic stiffness FRF of a motion controller tuned to 17Hz

A.4.2 Motion command state filter design and validation

This project utilizes a motion state filter for two main reasons. First, the speed command may be infeasible and so by using a state filter, the bandwidth of the speed command can be controlled to a more reasonable state. Second, as will be shown in section A.4.3 a speed command, Δθ command, as well as an acceleration command are all needed to properly control the machine using a motion controller as well as a torque reference to generate a full command vector.

The state filter utilized in this project is a simple second order filter shown in Figure A.28. By recognizing that the block before $\omega_{filtered}$ is generated relates acceleration to speed,

acceleration commands can also be extracted. The Simulink block diagram is shown in Figure A.29 with several additions to generate an average speed, $\Delta\theta$ command, and θ commands.

The tuning process is similar to that of the motion controller. First the open loop model is found as in (0.42) and then the closed-loop model is calculated, and the characteristic equation is extracted as in (0.43). Next two poles are multiplied together, and similar order parts are equated to the characteristic equation. Through algebraic manipulation the gains K_1 and K_2 can be solved for as in (0.45) and (0.46). The lower of the two frequencies selected will be the limiting factor for the filter.

$$OL(z) = \frac{K_1 K_2 T_s^2}{(z-1)\,(z-1+K_2 T_s)} \tag{0.42}$$

$$CE(z) = z^2 + (K_2 T_s - 2)\,z + (1 - K_2 T_s + K_1 K_2 T_s^2) \tag{0.43}$$

$$(z-a)(z-b) = z^2 + z(-a-b) + ab \tag{0.44}$$

$$K_2 = \frac{2-a-b}{T_s} \tag{0.45}$$

$$K_1 = \frac{ab-1-K_2 T_s}{K_2 T_s^2} \tag{0.46}$$

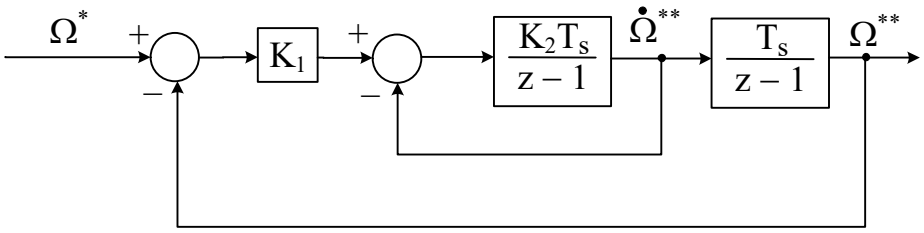

Figure A.28 – State block diagram of a motion command state filter.

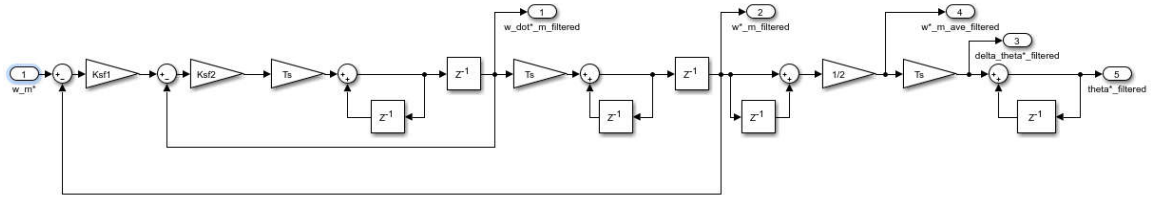

Figure A.29 – Simulink implementation of a motion command state filter.

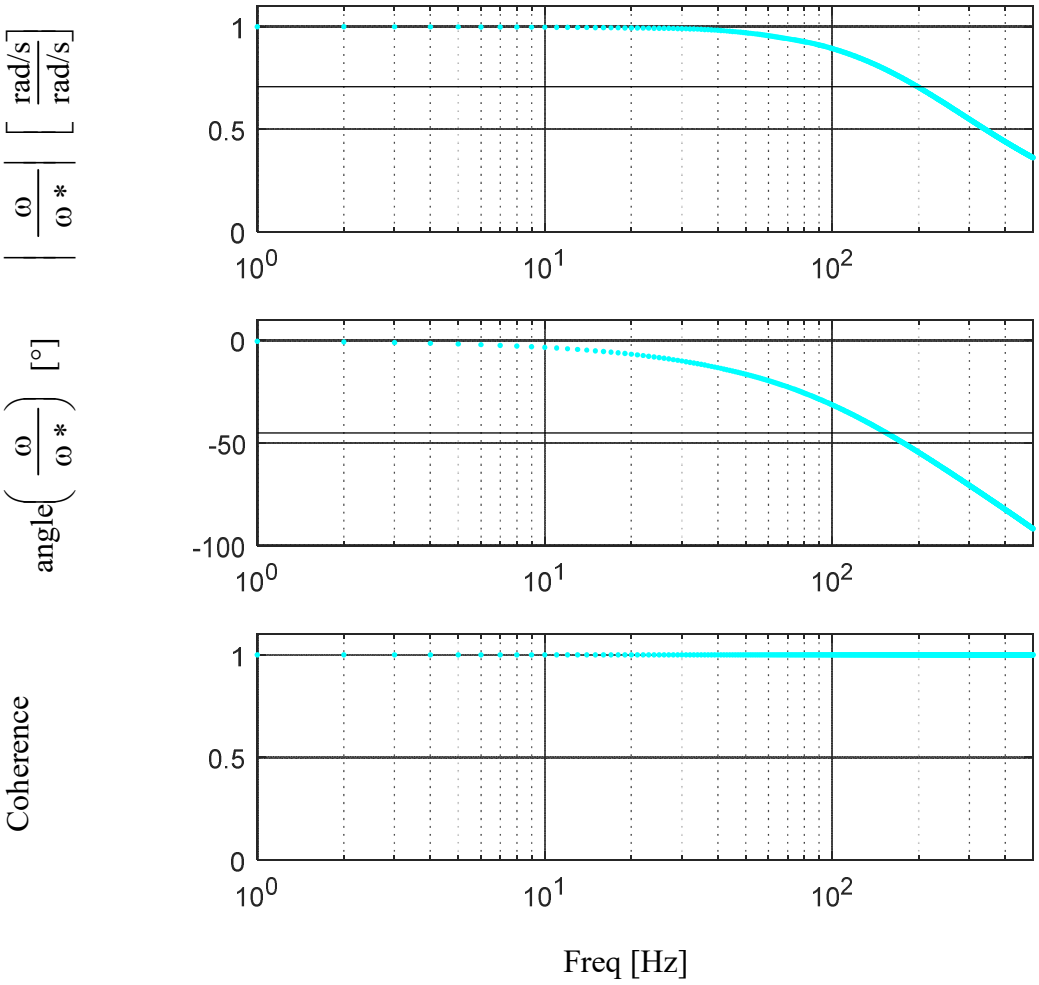

Command tracking from: Chirp FRF

ω_m* chirp applied with f_0=1 Hz, f_1=500 Hz, T=1s, Magnitude = 1Hz

Figure A.30 – Simulated command tracking of a motion state filter tuned to 200Hz. command tracking.

To verify the tuning, a command tracking FRF was taken in simulation and shown in Figure A.30. This is representative as the same code is used on the bench and there are no disturbances, just the filtering code. The filter was tuned to have a bandwidth of 200Hz using the process outlined in this section. Using the magnitude criteria, the bandwidth is between 198-

199Hz, using the phase criteria the bandwidth is 154Hz. These are reasonable and well above the expected motion controller bandwidths of around 50Hz for this project.

A.4.3 Motion command feed-forward design and validation

Rewriting equation (0.26) as in (0.47) shows what the expected torque reference for a given speed is. In the motion control presented in section A.4.1 the control law would be handled through a speed error term and subjected to the dynamics of the motion controller. By recognizing that this torque reference (and in the case of an SPMSM current) state is implicitly being set to zero with just a motion controller, an appropriate torque reference or alternately torque command feed-forward term can be generated from the speed command. By utilizing this method, the torque state feedback will be responsible for handling disturbances, or unmodeled effects of the mechanical system.

$$T_{em}(t) = J_p \dot{\Omega}(t) + b_p * \Omega(t) + T_\mu \text{sign}(\Omega(t)) \tag{0.47}$$

The state block diagram utilized to generate this current reference is shown in Figure A.31 with the Simulink implementation used in this project shown in Figure A.32. Note that this implementation uses both the speed command; and the acceleration command. Depending on the trajectory, the acceleration may not be known a priori, or it may not be easily accessible. This is the key reason for the use of the motion state filter presented in A.4.2 . Using the state filter allows for a speed command to generate filtered speed and acceleration states which can be used as in the command feed-forward.

In Figure A.33 a simulation of the effects of the command feed-forward are demonstrated. Note that when the motion controller is responsible for the entire torque reference, that the T_{sfb} term provides the entire reference. When command feed-forward is implemented, the T_{sfb} term is minimized while the T_{cff} term provides most of the torque

reference. This will also result in faster command tracking dynamics beyond the bandwidth of the controller, as even higher frequency content is captured by the command feed-forward. It should be noted that the bandwidth of the state filter, and the current limits of the machine, and the voltage limits of the inverter will be the limiting factor of the command tracking dynamics.

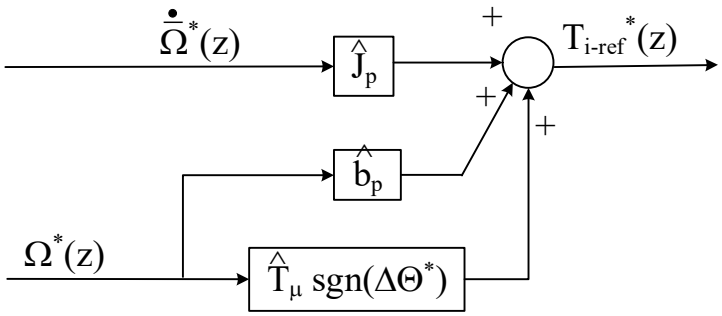

Figure A.31 – State block diagram of motion command feed-forward.

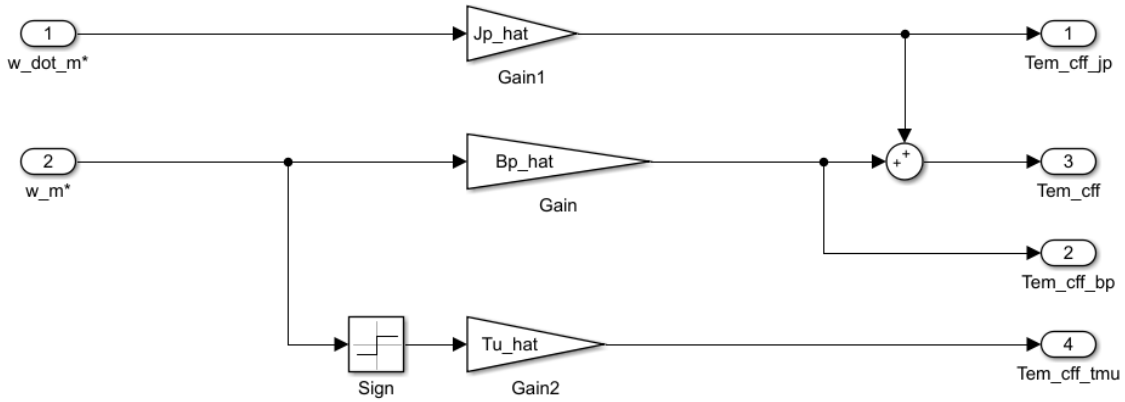

Figure A.32 – Simulink implementation of a motion command feed-forward.

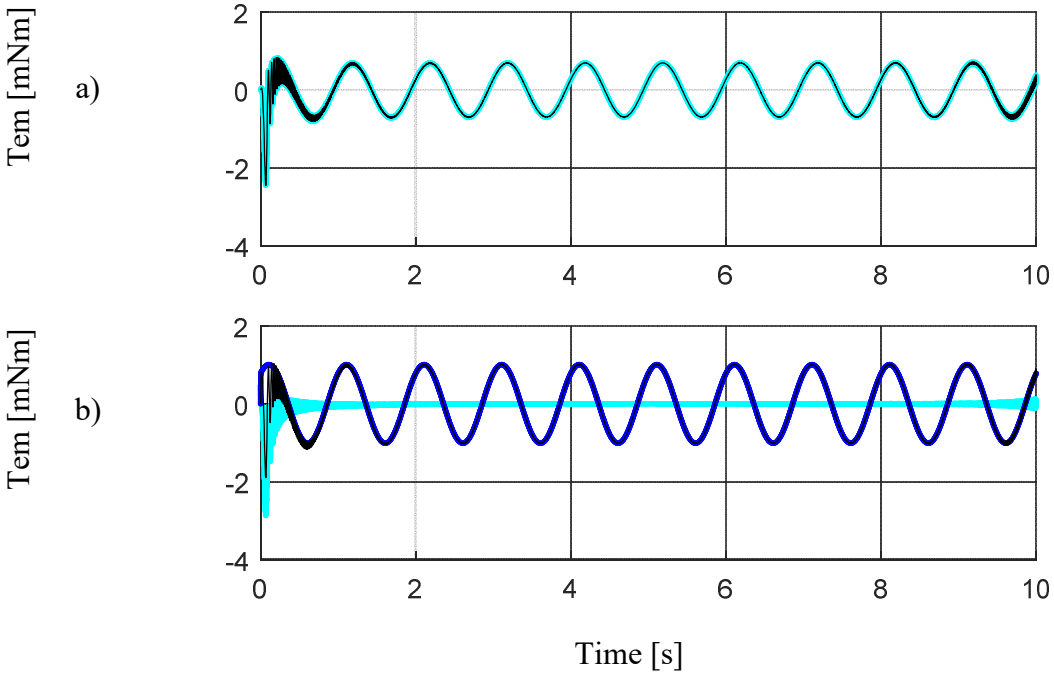

T_{em}*, T_{sfb}, T_{cff}

ω_m* = sin(2π)

a) Motion controller without command feed-forward

b) Motion controller with command feed-forward

Figure A.33 – Simulated torque commands comparing the effects of command feed-forward on the calculated torque command.

A.5 Motion Observer

As discussed in section A.2.8 the encoder position and average speed signals have significant amounts of quantization due to the resolution of the sensor. This quantization can have adverse effects as the motion controller attempts to track quantization effects. Solutions to this problem include filters and observers. Observers have several advantages over filters, namely they have zero-lag in estimation accuracy even past the bandwidth of the observer due to the command feed-forward term, this however means that disturbances will continue to have a lagging effect related to the bandwidth of the observer as the command feed-forward doesn't know about those effects. Additionally, using command feed-forward, observers can estimate

future sample period responses, this will be used where knowing the position or speed a time step ahead is required.

A motion observer modeling the plant as purely inertial is shown in Figure A.34 and the Simulink implementation used in this work is shown in Figure A.35. Attention must be paid when selecting the command feed-forward term to maintain consistency. Here the command feed-forward term is generated using T_{sfb} and T_{cff_jp}, the inertial portion of the command feed-forward used in the motion controller. If the damping and friction portions are included, they will generate an error due to the inconsistency between the feed-forward and observer plant.

The motion observer can follow the same tuning process as for the motion observer as the structures are identical.

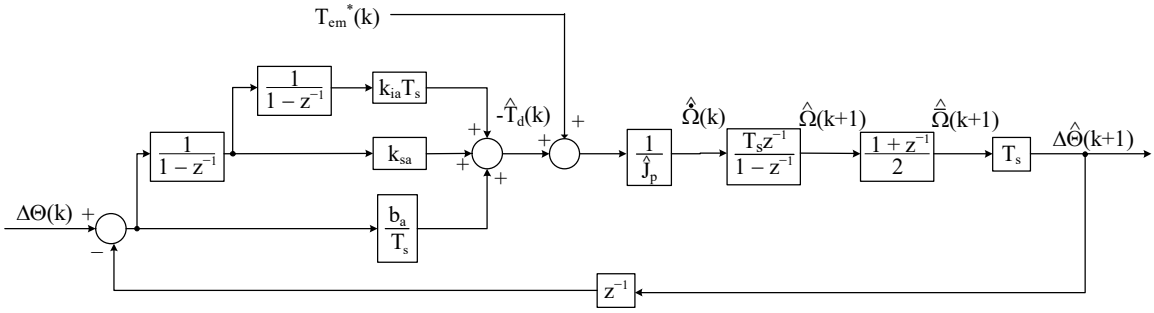

Figure A.34 – State block diagram of a motion observer.

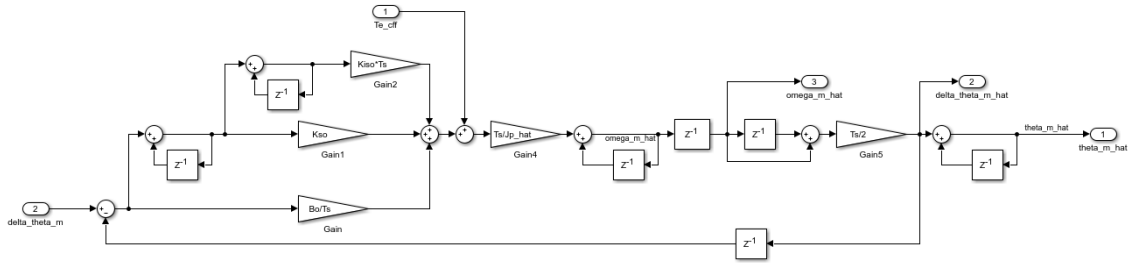

Figure A.35 – Simulink implementation of a motion observer.

To verify the tuning process and estimation properties of the system, the motion observer was intentionally detuned to 20Hz. In typical operation when used as feedback it should be tuned to at least as high of a bandwidth as the motion controller. However, as there is a motion state filter, and motion controller dynamics involved in the command feed-forward of the motion observer, the observer was detuned to remove these effects. Through the 20Hz bandwidth there is very little deviation from unity magnitude and zero phase lag. As the frequency increases, the effects of the motion state filter and the motion controller bandwidths can be seen, this is due to their filtering properties impacting the command feed-forward which provides the reference above the bandwidth of the motion observer.

A.6 Current Observer

The current observer is used for similar reasons as the motion observer. Namely, providing a zero-lag estimate, providing filtering, and being able to estimate the current a time step ahead. The structure is provided in Figure A.37 in the synchronous frame. Note that back-EMF and cross-coupling are decoupled. The observer plant model then simplifies to an L-R model. The observer controller is then modeled as a PI regulator.

To tune this structure, the open loop model is found as in (0.48). Using pole-zero cancellation, one equation for the gains can be found as in (0.50). The open loop model then simplifies to (0.51). Finding the closed-loop solution and extracting the characteristic equation results in (0.52). Setting this equal to a single pole equation and equating similar order terms results in (0.53) where a is the desired pole. Through algebraic manipulation of equations (0.50) and (0.53) the gains K_p and K_i can be solved for as in (0.54) and (0.55).

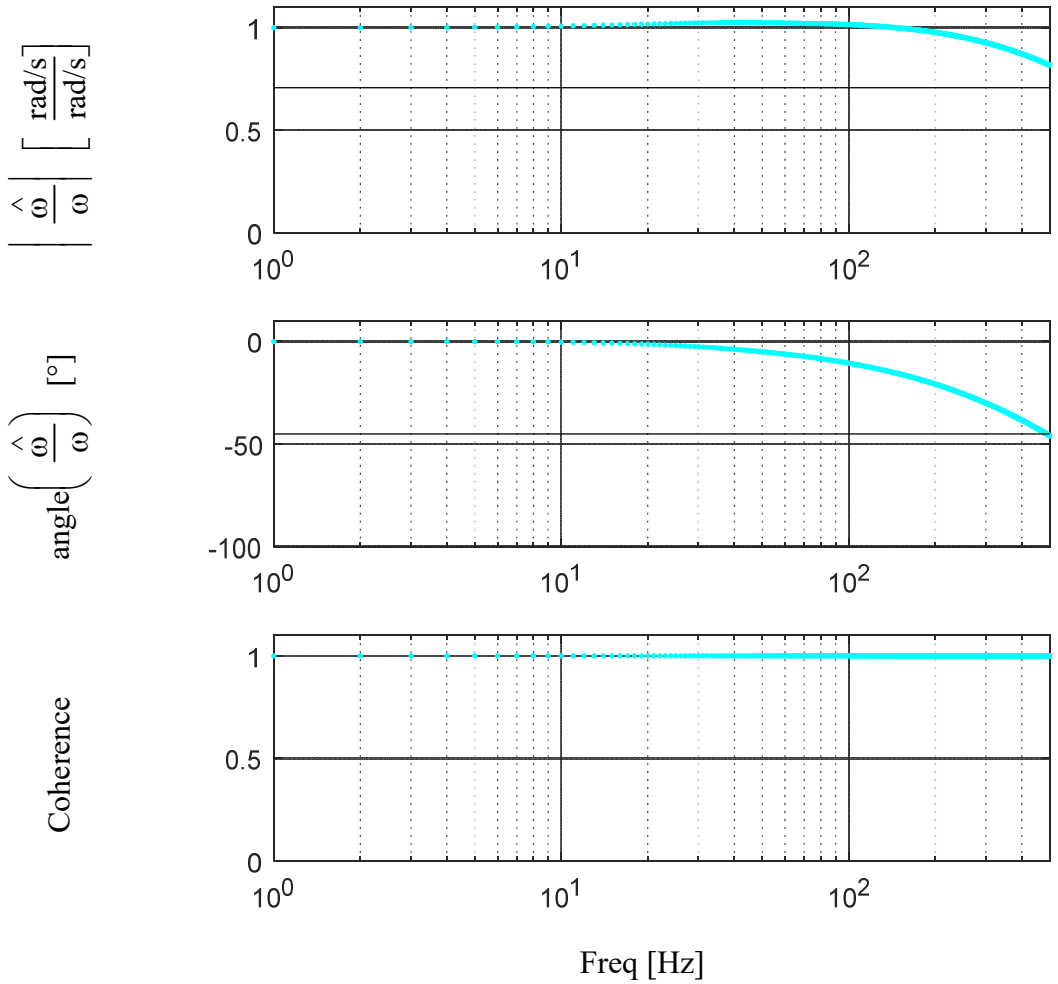

Command tracking from: Chirp FRF

$\Delta\theta^*$ chirp with $f_0 = 0.01$Hz, $f_1 = 500$Hz, T=5s, and magnitude 1Hz

Figure A.36 – Simulated estimation accuracy of a motion observer, tuned to 20Hz.

The Simulink block diagram for the synchronous frame current observer used in this work is shown in Figure A.38. This diagram includes the cross-coupling decoupling, and the back-EMF decoupling.

$$OL = \left(\frac{z - \frac{K_p}{K_p + K_i T}}{\frac{z-1}{K_p + K_i T}} \right) \left(\frac{1-b}{R_s(z-b)} \right) \tag{0.48}$$

$$b = \exp\left(\frac{-T_s}{L/R} \right) \tag{0.49}$$

$$\frac{K_p}{K_p + K_i T} = b \tag{0.50}$$

$$OL = \left(\frac{1-b}{\left(\frac{R_s(z-1)}{K_p + K_i T} \right)} \right) \tag{0.51}$$

$$CE = z - 1 + \frac{K_p + K_i T}{R_S}(1-b) \tag{0.52}$$

$$a = 1 - \frac{K_p + K_i T}{R_S}(1-b) \tag{0.53}$$

$$K_p = \frac{R_S(a-1)b}{b-1} \tag{0.54}$$

$$K_i = \frac{K_p(1-b)}{T_s b} \tag{0.55}$$

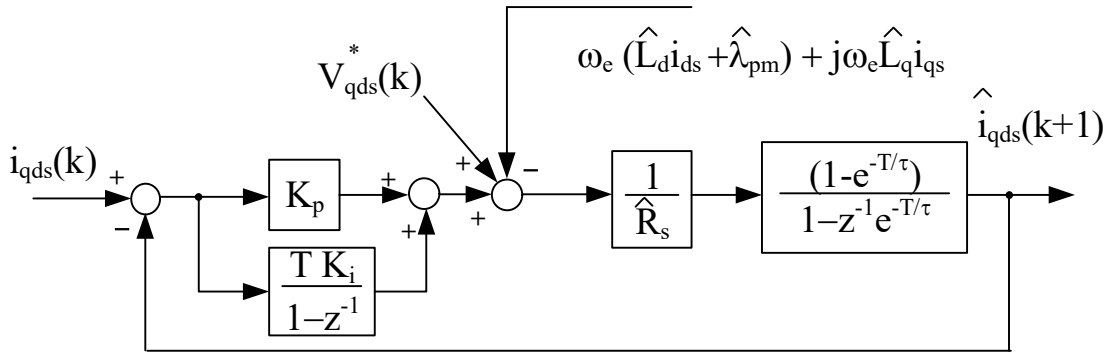

Figure A.37 – State block diagram of a discrete time synchronous frame current observer.

To verify the tuning processing, estimation accuracy FRFs of both the d- and q-axis were simulated and shown in Figure A.39 and Figure A.40. The magnitude maintains the correct amplitude throughout the entire frequency range, even beyond the bandwidth of the observer.

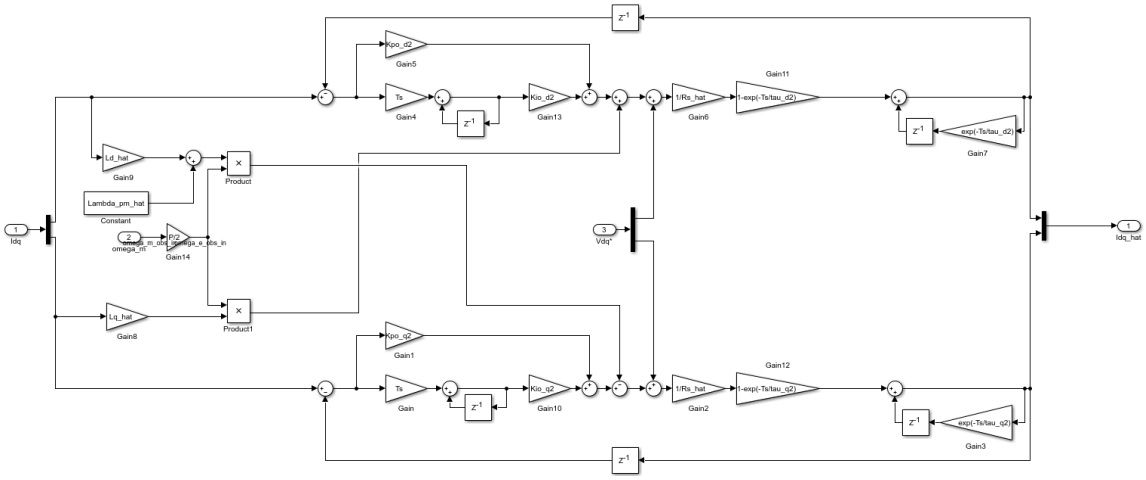

Figure A.38 – Simulink implementation of a synchronous frame current observer.

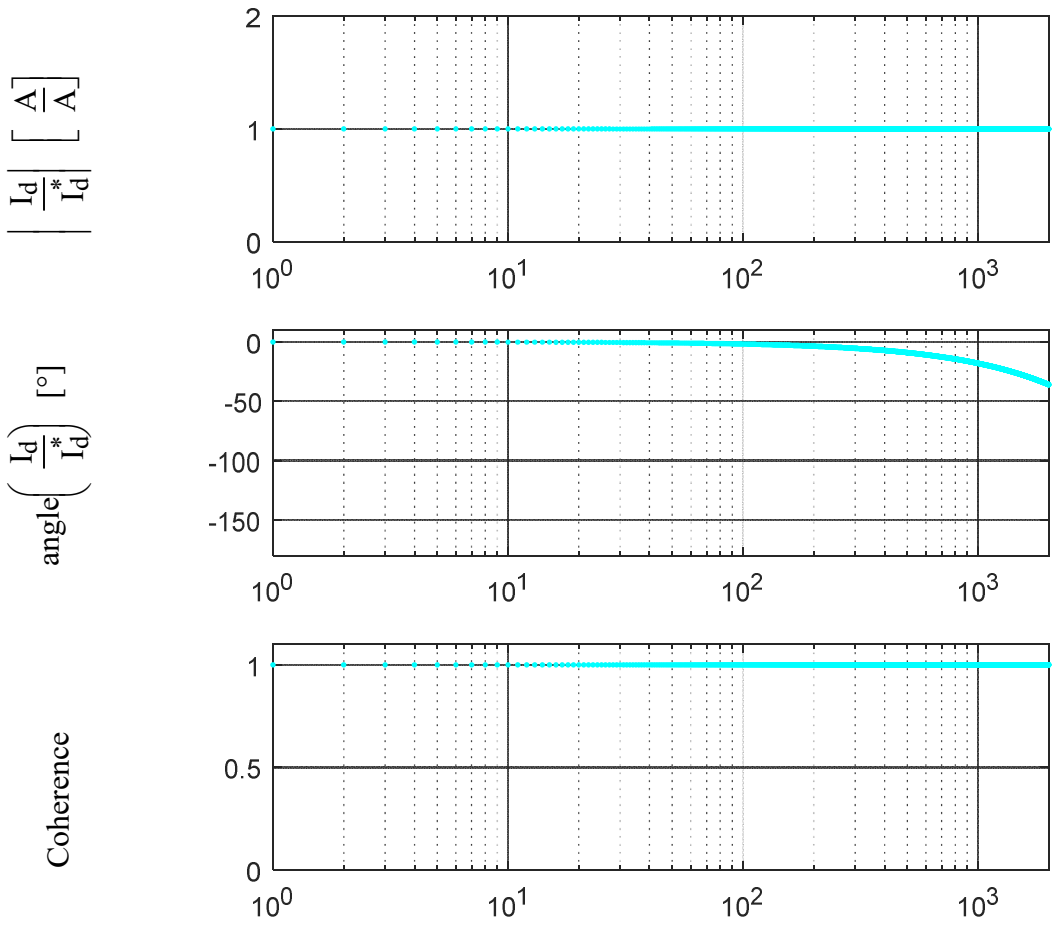

I_d* chirp applied with f_0=1 Hz, f_1=2 kHz, T=1s, Magnitude = 1A

Figure A.39 – Simulation d-axis estimation accuracy FRF of a current observer tuned to 1 kHz.

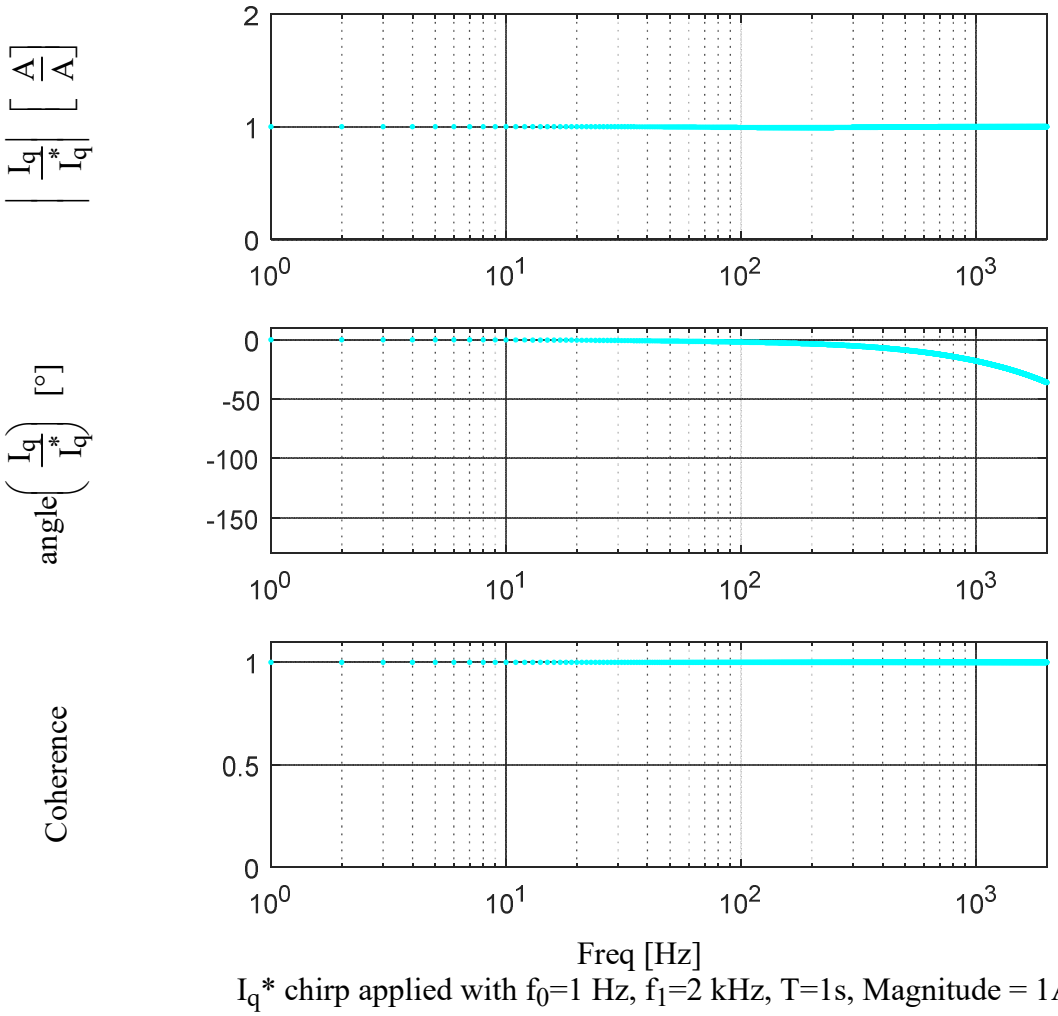

Figure A.40 – Simulation q-axis estimation accuracy FRF of a current observer tuned to 1 kHz.

A.7 Flux Observer

The flux observer presented in this section is mainly used in this work as a sensor of flux and torque for use in the DB-DTFC control algorithm presented in section A.8 . The development of the flux observer is well documented in [105] but contains two critical models that estimate flux accurately at different frequencies. The current model provides a reasonable estimate at low frequencies but is known to be parameter sensitive. The voltage model provides

a very good model at high frequencies but tends to degrade at lower frequencies. To mix these two signals a PI regulator is used as shown in Figure A.41. Below the bandwidth the current model is used, and above it the voltage model is used. It should be noted that the voltage model requires estimates of current and position one-time step ahead, and so the current and motion observers presented previously in this chapter are utilized.

To tune the flux observer the open loop model is found as in (0.56). Then the closed-loop model can be found, and the characteristic equation can be extracted as in (0.57). Multiplying out a two pole system as in (0.58), setting similar order terms equal to each other, and performing algebraic manipulation to solve for K_1 and K_2 results in (0.59) and (0.60).

$$OL = \frac{K_1 Tz + K_2 T^2 z - K_1 T}{(z-1)^2} \tag{0.56}$$

$$CE = z^2 + z(K_2 T^2 + K_1 T - 2) + (1 - K_1 T) \tag{0.57}$$

$$(z-a)(z-b) = z^2 + z(-a-b) + ab \tag{0.58}$$

$$K_1 = \frac{1-ab}{T} \tag{0.59}$$

$$K_2 = \frac{2 - K_1 T - (a+b)}{T^2} \tag{0.60}$$

The Simulink block diagram of the flux observer implemented in this project is shown in Figure A.42. Note that flux estimates are generated as from the state block diagram. Additionally, torque estimates for the current and next time instances are generated by taking the cross product of flux with current, with special attention paid to the time indices so that the results are consistent.

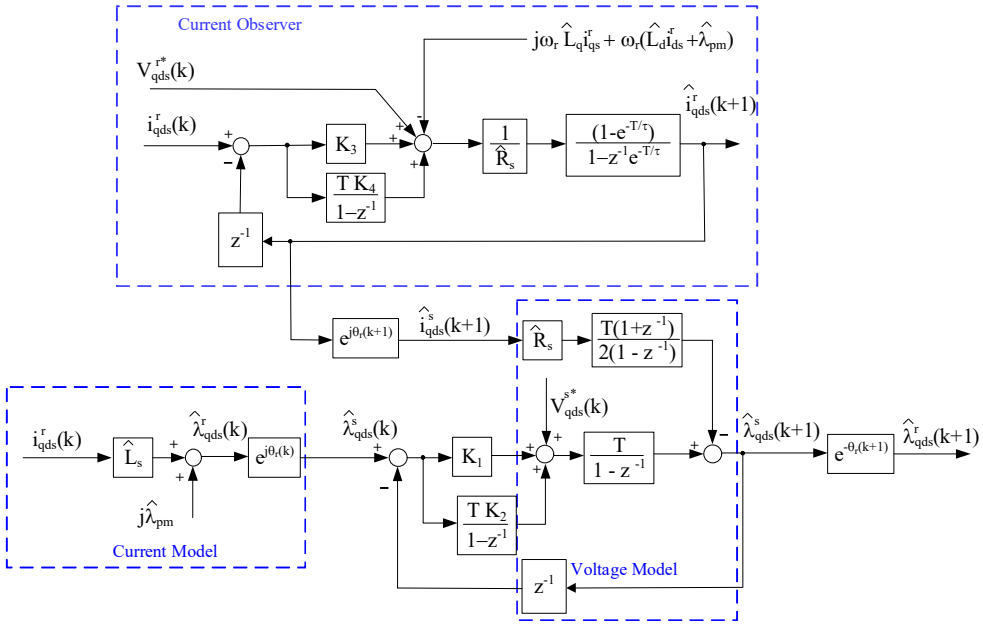

Figure A.41 – State block diagram of a discrete time flux observer.

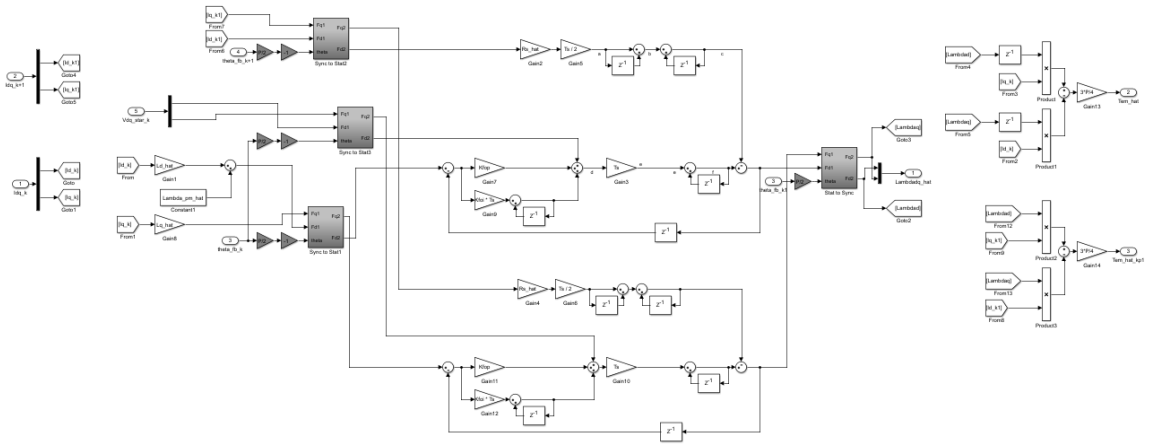

Figure A.42 – Simulink implementation of a flux observer.

A.8 Deadbeat-Direct Torque and Flux Control

Deadbeat-Direct Torque and Flux Control has been developed over the past decade initially in [106] and further refined in [45, 105, 107, 108]. This control method provides the fastest torque response possible in a discrete system by solving for the inverse solution to the electric machine equations. There have been numerous extensions to handle loss minimization

[109, 110], more precise modeling when the ratio of switching frequency relative to fundamental frequency is low [111, 112], for use with back-EMF self-sensing [111, 113], and for use with high frequency injection based self-sensing [49, 50, 61]. This work focuses on an SPMSM derivation of DB-DTFC, an IPMSM derivation for use as a flux and torque modulator discussed in this section, and implementation of a high frequency flux injection (HFFI) based self-sensing which is discussed in section A.12 .

$$V_{dq} = \lambda_{dq} \frac{d}{dt} + R_s I_{dq} \tag{0.61}$$

$$\lambda_{dq} = L_{dq} I_{dq} + j\omega_e L_{dq} I_{dq} + \omega_e \lambda_{pm} \tag{0.62}$$

$$V_{dq} = \lambda_{dq} \frac{d}{dt} \tag{0.63}$$

$$T_{em} = \frac{3P}{4}\left(\lambda_d I_q - \lambda_q I_d\right) \tag{0.64}$$

$$\dot{T}_{em} = \frac{3P}{4}\left(\dot{I}_q \lambda_d + I_q \dot{\lambda}_d - \dot{I}_d \lambda_q - I_d \dot{\lambda}_q\right) \tag{0.65}$$

$$\dot{I}_{dq} = \frac{\dot{\lambda}_{dq}}{L_{dq}} \tag{0.66}$$

$$V_{dq} = \dot{\lambda}_{dq} \tag{0.67}$$

$$V_q = MV_d + B \tag{0.68}$$

$$M = \frac{\lambda_q L_q - \lambda_q L_d}{\lambda_d L_d - \lambda_q L_q + \lambda_{pm} L_q} \tag{0.69}$$

$$B = \dot{T}_{em}\left(\frac{4}{3P}\right)\left(\frac{L_d L_q}{\lambda_d L_d - \lambda_d L_q + \lambda_{pm} L_q}\right) \tag{0.70}$$

To derive DB-DTFC for a permanent magnet machine, the machine equation presented in (0.23) is restated here as (0.61) and (0.62) for convenience. If it is assumed that the resistance, cross-coupling, and back-EMF are decoupled, the machine equation simplifies to (0.63). Next, the PM machine torque equation is stated as in (0.64), and its derivative is taken and presented in (0.65). By using the identities presented in (0.66) and (0.67), V_q can be solved for as in (0.68) with M and B defined in (0.69) and (0.70) respectively. Note that this is in the form of a classical equation for a line. This allows for the q-axis voltage command to be derived at any

time instance using the torque command, however the solution is not specific, and an entire family of solutions comprises this line.

To further specify the command an additional constraint must be placed on the system. Using a flux magnitude approach, the commanded flux magnitude is given as in (0.71). Expanding this out, substituting using (0.68), and collecting terms results in (0.72) with x, a, b, c defined in (0.73), (0.74), (0.75), and (0.76) respectively. D-axis voltage can then be solved for using the quadratic equation (0.77) resulting in (0.78).

$$\lambda^{*2} = [(\lambda_d + V_d T_s]^2 + [\lambda_q + V_q]^2 \quad (0.71)$$

$$ax^2 + bx + c = 0 \quad (0.72)$$

$$x = V_d T_s \quad (0.73)$$

$$a = (1+M^2) \quad (0.74)$$

$$b = 2\lambda_d - 2\lambda_q M - 2MBT_s \quad (0.75)$$

$$c = \lambda_d^2 + \lambda_q^2 + 2\lambda_q BT_s + B^2T_s^2 - \lambda^{*2} \quad (0.76)$$

$$x = \frac{-b \pm \sqrt{b^2-4ac}}{2a} \quad (0.77)$$

$$V_d = \frac{-b \pm \sqrt{b^2-4(1+M^2)c}}{2T_s(1+M^2)} \quad (0.78)$$

To verify the performance of the DB-DTFC algorithm, a simulation was constructed implementing the equations described in this section. The torque command was plotted against the torque estimates from the observers, as well as the torque from the simulated plant. In Figure A.43 the response is shown using the machine parameters from this chapter. Notice that while the inverse solution should generate the expected torque within a single time period, in this case it takes two time periods to settle out. This is due to the relatively high resistance in relation to the inductance of this machine, resulting in a very large electrical break frequency. Similar phenomena have been observed in [112] and are caused by broken assumptions in the derivation either in the “fast switching frequency”, the flux observer creation, or the assumption that the torque derivative is constant over a switching period.

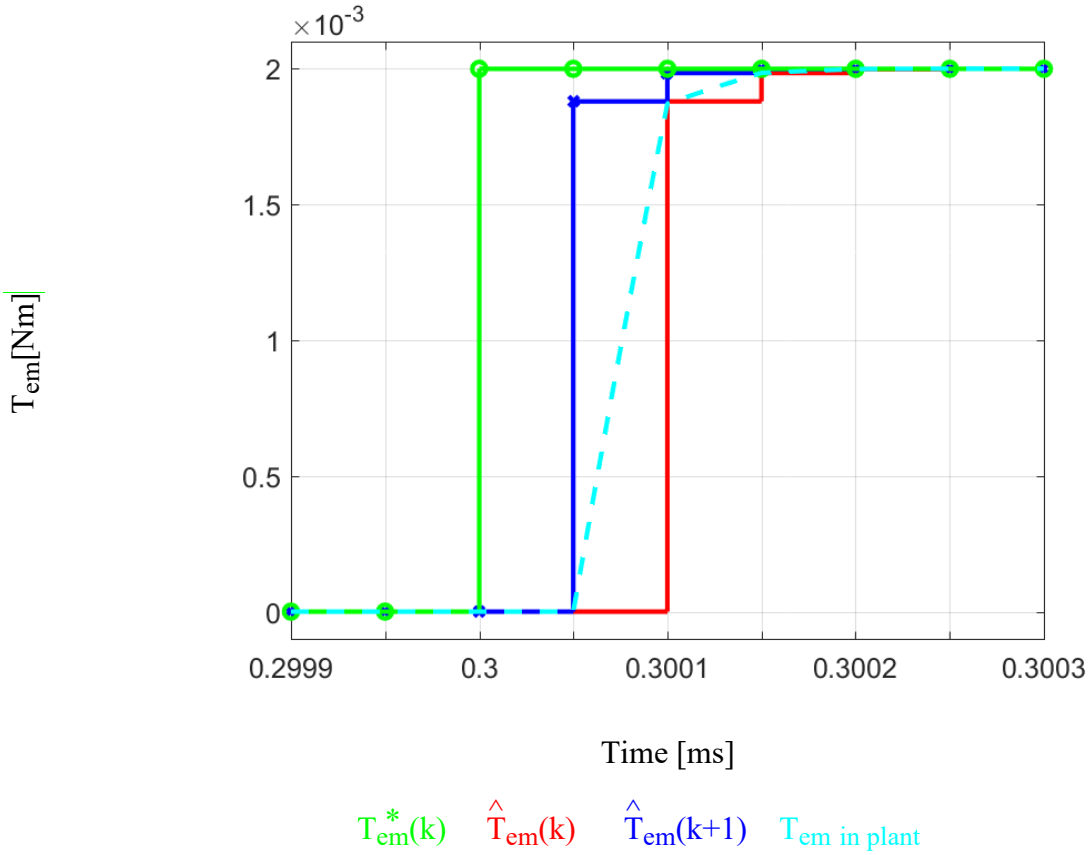

Figure A.43 – Simulated torque response using machine parameters described previously in this chapter.

To further validate this control scheme, the machine parameters for the prototype machine developed in [114] were investigated in Figure A.44. Using these parameters, the break frequency is several orders of magnitude smaller, and the torque response is now as expected.

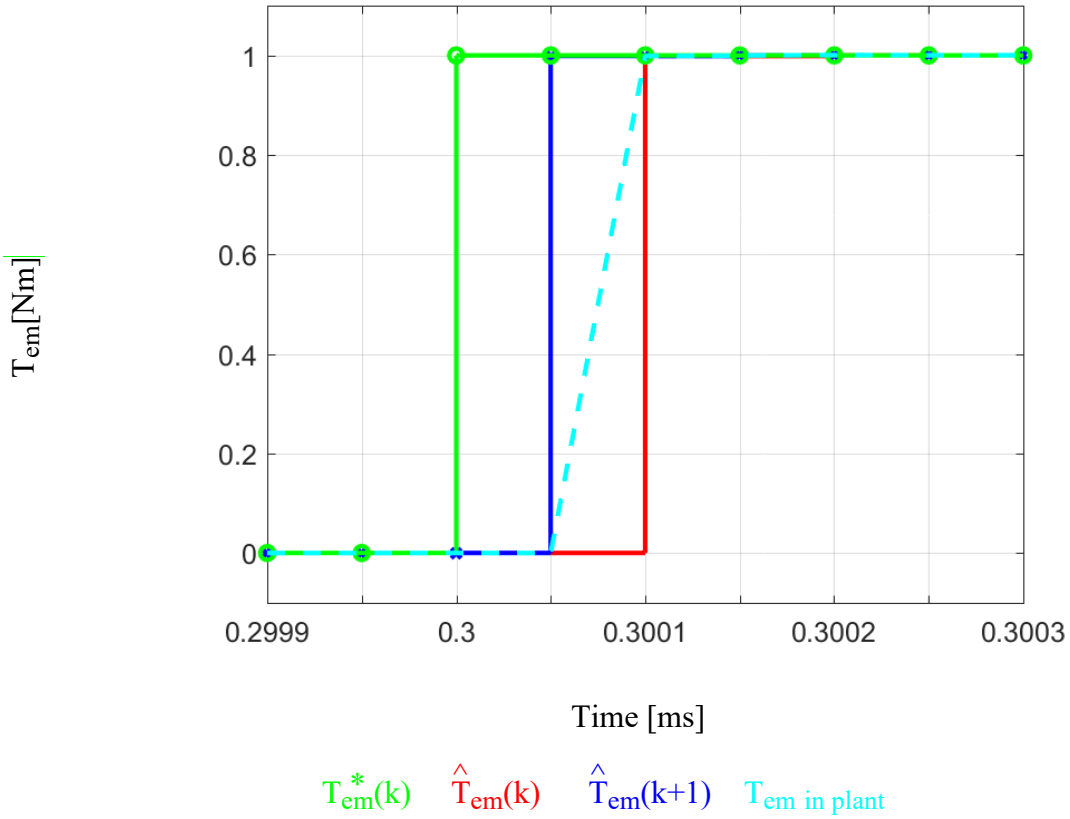

Figure A.44 – Simulated torque response using machine parameters described in [114].

A.9 Current Separation

A.9.1 Fundamental isolation via current observer

As a first step in controlling a machine via self-sensing, the current must be separated into fundamental and high frequency components. This allows the current regulator to continue functioning without trying to reject the high frequency component. If the high frequency portion is not removed, even a low bandwidth current regulator will attempt to reject the high frequency content. However, since this content is significantly above the current regulator, the response will be attenuated, and phase shifted, but will act as a secondary injection source and complicate the demodulation and position estimation process. As a first step, using a current observer as

described in section A.6 with a low bandwidth, will return simply the fundamental portion. The fundamental portion can be fed back to the current regulator.

To extract the high frequency content, the estimated fundamental current can be subtracted from the measured current which will leave only the high frequency portion remaining. This process is shown in Figure A.45 with an additional delay added between the fundamental estimation and the high frequency estimation to make sure the indices are correctly aligned. The Simulink implementation used in this work is shown in Figure A.46. It should be noted that the Simulink implementation shown here has additional feedback selection options included, this will be discussed in detail in A.9.3 for separation of the high frequency content from the fundamental content.

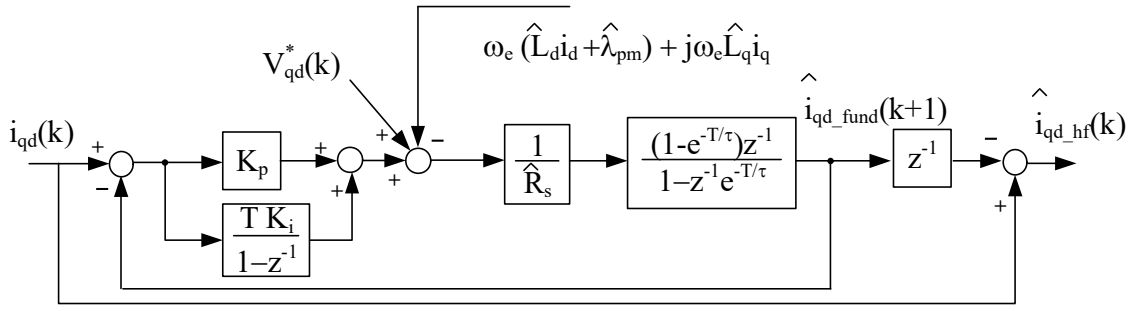

Figure A.45 – State block diagram of a synchronous frame current observer with high frequency current estimation.

To illustrate the purpose and effectiveness of this filtering, a high frequency voltage was injected as will be done for rotating self-sensing in A.12 , and the steps of the fundamental current separation are shown in Figure A.47. The black results show the current sensor and are present in all of the content. The blue appears only near the fundamental as is expected from the 10 Hz bandwidth of the current observer. The estimated high frequency current is absent near the fundamental, but correctly estimates the current near the positive and negative sequences.

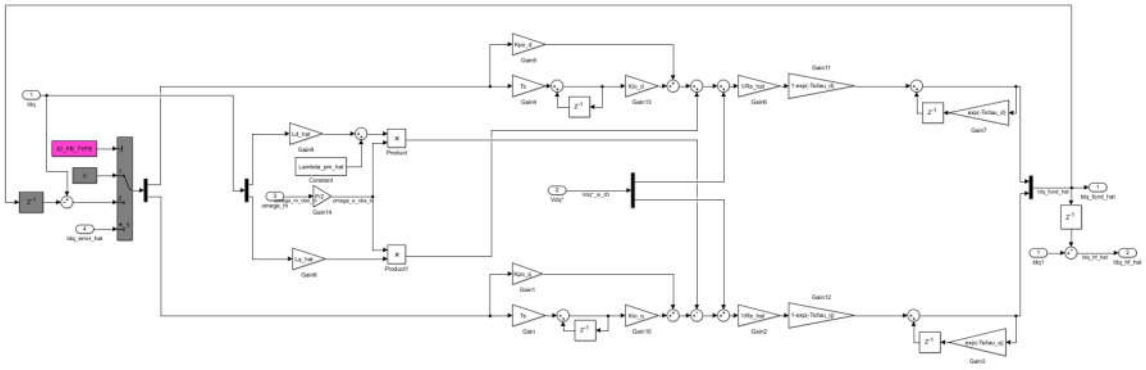

Figure A.46 – Simulink implementation of a synchronous frame current observer with current separation.

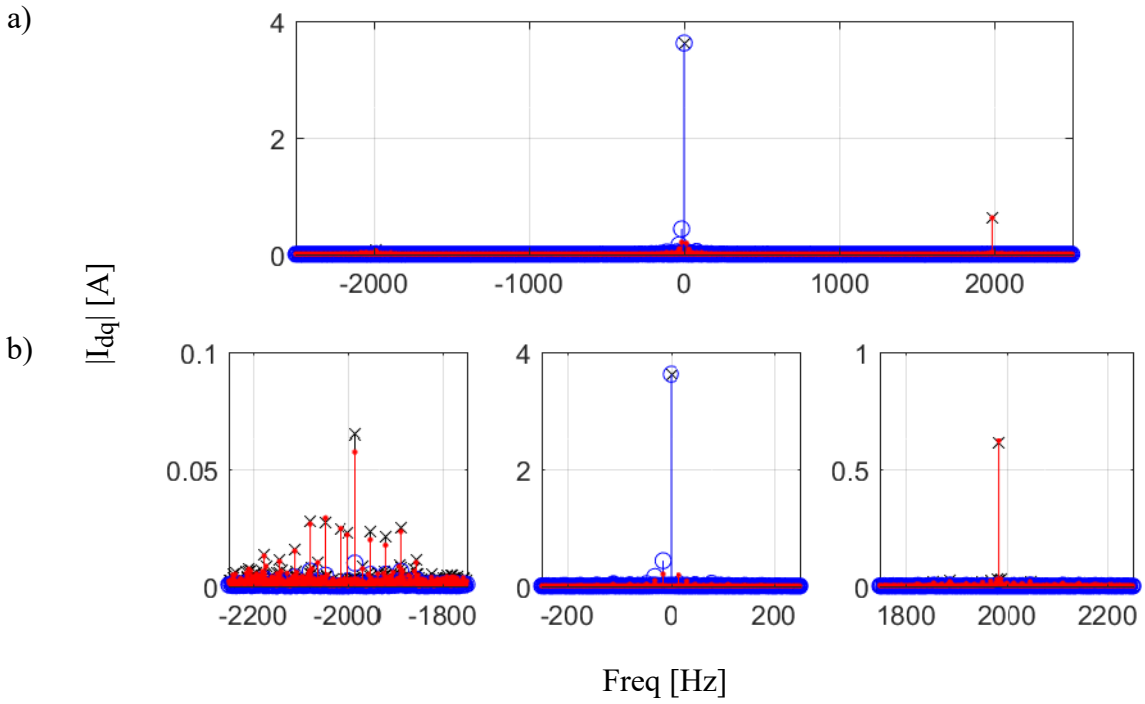

Current Spectrum: I_{dq}, I_{dq_fund}, I_{dq_hf}
MC tuned to 17Hz, CVCR tuned to 500Hz, IO tuned to 10Hz
$V_{\alpha\beta\_hf}^{*} = 0.3V * \exp(j2\pi*2000*t)$

Figure A.47 – Experimental results showing the current spectra, zoomed in an frequencies of interest for fundamental feedback and high frequency response.

A.9.2 Frequency synchronous notch filter formulation

Often times a section of frequency content needs to be filtered or extracted from the rest of the current spectra. In this work it is used to remove unwanted content near the positive carrier when applied to rotating vector injection. It can also be used to remove additional content near the fundamental if that region contains unwanted content. To perform this task a simple first-order HPF is formed as in Figure A.48. To create this structure, the NSD of a simple first-order RC circuit are found as in (0.79), (0.80), (0.81). To tune the structure, the characteristic equation is extracted and set equal to a single pole as in (0.82) and (0.83). Setting similar terms equal to each other results in a method to tune the filter as in (0.84). A Simulink block diagram of this process as used in this work is shown in Figure A.49.

$$NSD = (1-z^{-1})\, Z\left(\frac{G_p(s)}{s}\right) \tag{0.79}$$

$$Gp = \frac{s}{a+s} \tag{0.80}$$

$$NSD = \frac{z-1}{z-\exp(-aT)} \tag{0.81}$$

$$CE = z-\exp(-aT) \tag{0.82}$$

$$z-\exp(2\pi fT) = z-\exp(-aT) \tag{0.83}$$

$$a = 2\pi f \tag{0.84}$$

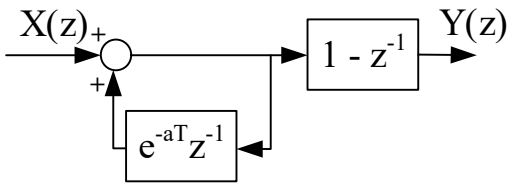

Figure A.48 – State block diagram of a high-pass filter.

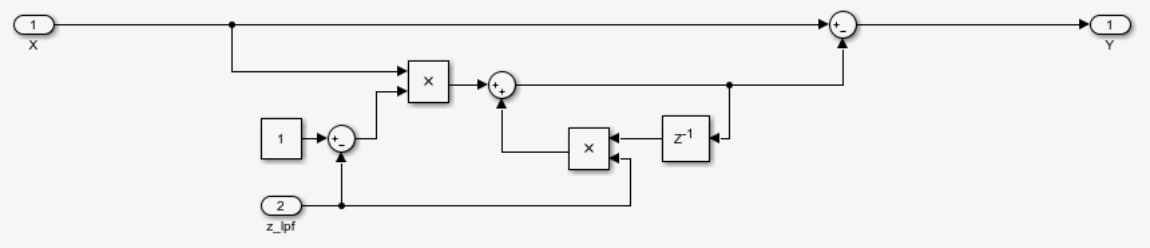

Figure A.49 – Simulink implementation of a high-pass filter

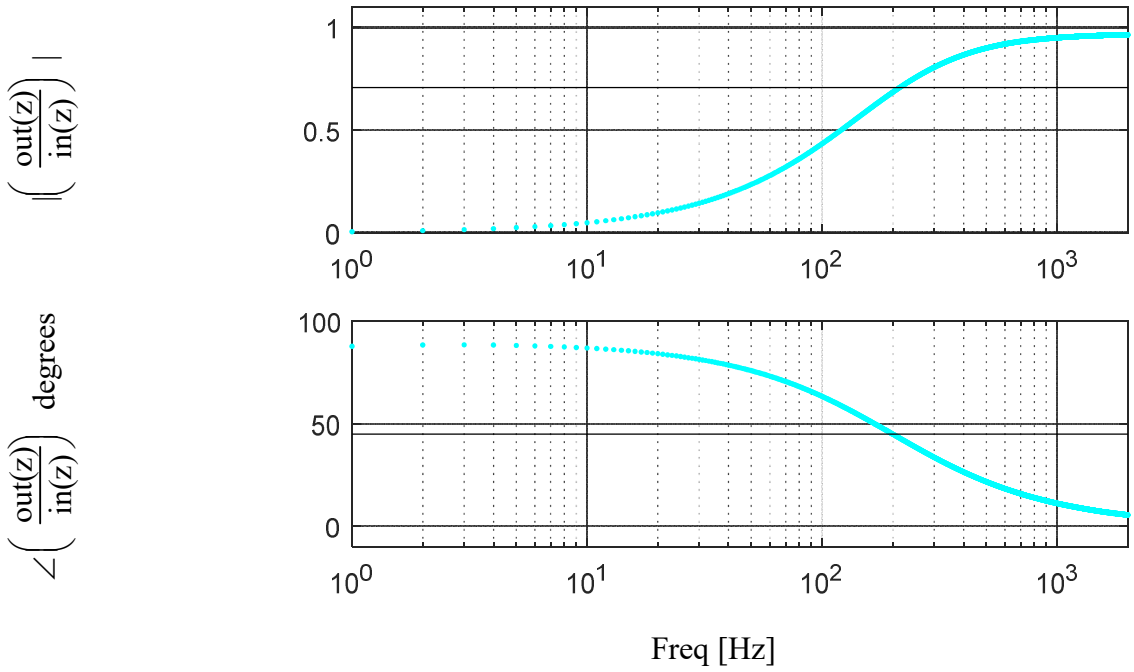

X_{in} chirp with f_0 = 1Hz, f_1 = 2 kHz, T = 5s, magnitude = 1

Figure A.50 – Simulation results showing the frequency response of the high-pass filter when it is tuned to 200Hz.

To verify the function of the high-pass filter structure, an FRF was taken using a chirp input and a tuning of 200 Hz. Using either the bandwidth or magnitude criteria the bandwidth is 200 Hz as is expected.

In this work, this filter is also used to filter specific current frequencies. To accomplish this task, the current is rotated to a frame synchronous with the content which is to be removed. The high-pass filter is applied. Finally, the current is rotated back to its original reference frame, with the desired content removed. This process is shown in block diagram form in Figure A.51.

Figure A.51 – State block diagram of a carrier synchronous high-pass filter.

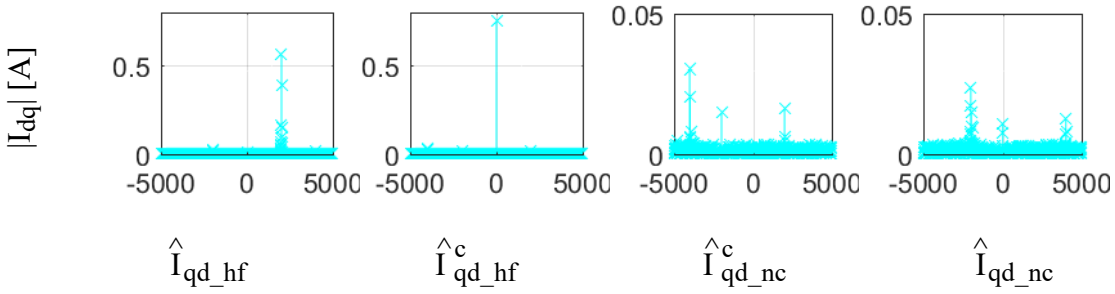

CVCR tuned to 500Hz, IO tuned to 10Hz, HPF tuned to 100Hz
V_{inj} = 0.3V, f_c = 2 kHz

Figure A.52 – Experimental current spectra at each step of the filtering process, zoomed along the y-axis.

An illustration of the carrier synchronous filtering process described in Figure A.51 with experimental data is shown in Figure A.53. Here the rotations between reference frames, and the removal of spectral content are easily viewed with the final result being that the content near the carrier is effectively removed.

A.9.3 Removal of high frequency content from current control signal

The authors of [59] noted that even with fundamental current separation as presented in section A.9.1 that the current regulator still responds slightly to the high frequency voltage injection. To further reduce the unwanted signals on the feedback signal, an enhanced separation method was developed and is shown in Figure A.53. This method works by filtering the positive and negative sequence current responses out of the error signal. This error signal can then be combined with the fundamental for use as current regulator feedback. Additionally, the error term can be subtracted from the estimated negative sequence response to remove unwanted content from the signal which will be demodulated. In this work, the synchronous notch filters presented in 0 are used to remove the positive and negative sequences and are better shown in the Simulink implementation in Figure A.54.

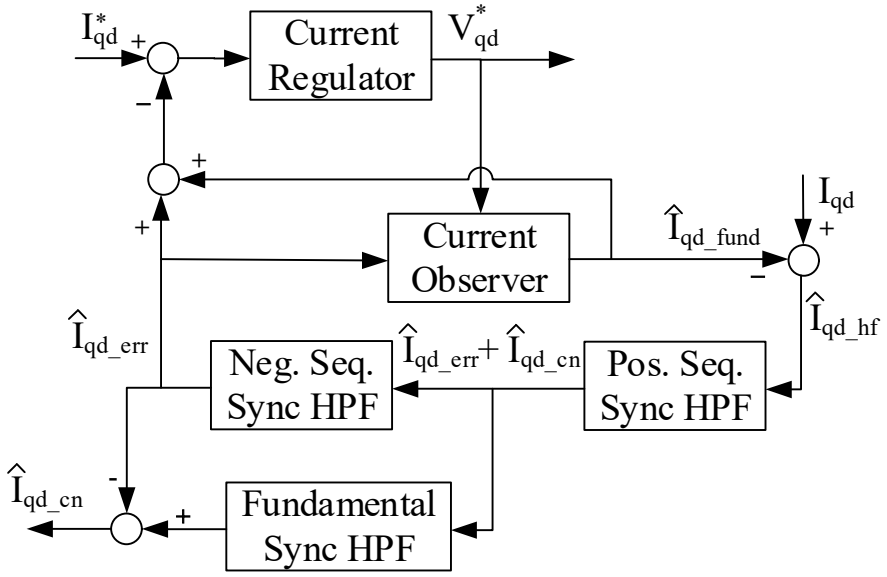

Figure A.53 – State block diagram of an observer based method of reducing high frequency content reaching the current regulator based on the structures presented in [59].

a)

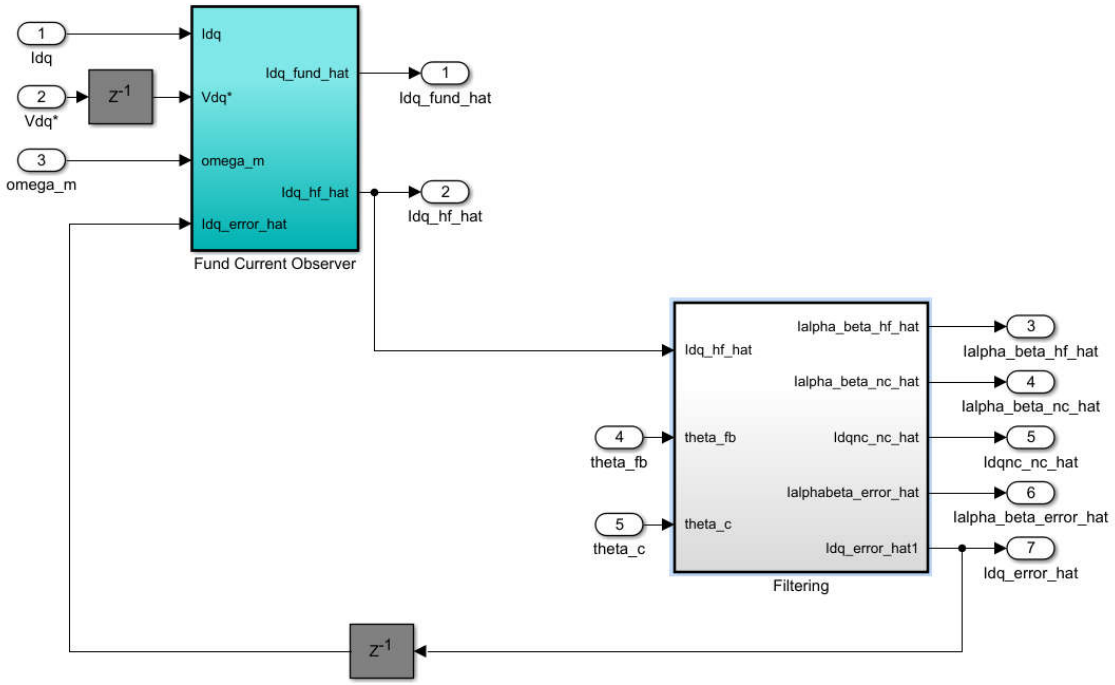

b)

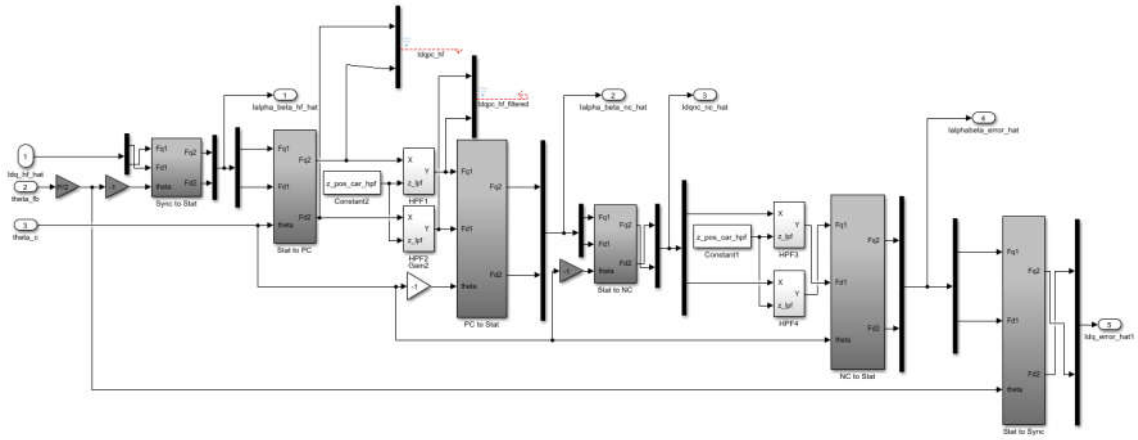

a) General structure of the current observer presented in Figure A.38
b) Internal structure to remove positive and negative sequence current

Figure A.54 – Simulink diagram of the structure presented in Figure A.53.

In Figure A.55 the synchronous frame currents which are described in Figure A.53 are shown to better illustrate the process. Between each step is a frequency synchronous notch filter as described in the previous section. This allows for very specific segments of the spectra to be removed, while extracting the error and negative sequence portions.

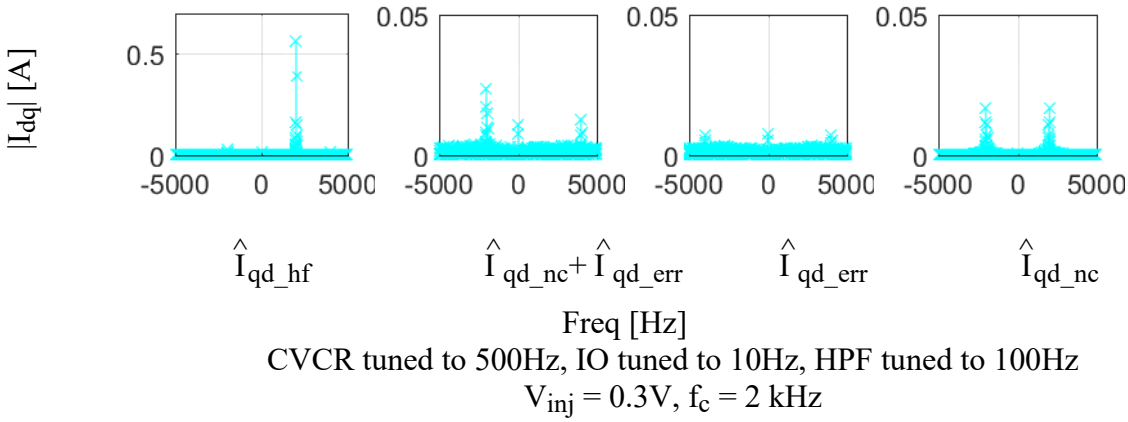

CVCR tuned to 500Hz, IO tuned to 10Hz, HPF tuned to 100Hz
V_{inj} = 0.3V, f_c = 2 kHz

Figure A.55 – Experimental results showing the spectrum of each step of the filtering process shown in Figure A.53.

A.10 Pulsating Voltage HFI Self-Sensing

In this section, a number of derivations will be shown which calculate the current response to a high frequency voltage with various forms of an impedance matrix. The general form of the derivation starts with the machine equation in the stationary frame as in (0.85). Next a rotation matrix is defined as in (0.86) with the inverse rotation matrix defined in (0.87). Equation (0.85) can be multiplied by (0.87) to transform it to the estimated synchronous reference frame as in (0.88). Substituting the definitions in (0.89) and (0.90) into (0.88) results in (0.91). Noting that this is the standard machine equation in the estimated synchronous reference frame, the inductance matrix can be redefined as in (0.92) and used to restate the machine equation as in (0.93). By integrating both sides, and multiplying by the inverse inductance matrix, the current can be solved for as in (0.94).

$$V_{dq} = L\, I_{dq} \frac{d}{dt} \tag{0.85}$$

$$R(x) = \begin{bmatrix} \cos(x) & -\sin(x) \\ \sin(x) & \cos(x) \end{bmatrix} \tag{0.86}$$

$$R^{-1}(x) = \begin{bmatrix} \cos(x) & \sin(x) \\ -\sin(x) & \cos(x) \end{bmatrix} \tag{0.87}$$

$$R^{-1}(\tilde{\theta})\, V_{dq} = R^{-1}(\tilde{\theta})\, L\, I_{dq} \frac{d}{dt} \tag{0.88}$$

$$R^{-1}(\tilde{\theta})\, V_{dq} = V_{dq}^{\hat{e}} \tag{0.89}$$

$$I_{dq} = R(\tilde{\theta})\, I_{dq}^{\hat{e}} \tag{0.90}$$

$$V_{dq}^{\hat{e}} = R^{-1}(\tilde{\theta})\, L\, R(\tilde{\theta})\, I_{dq}^{\hat{e}} \frac{d}{dt} \tag{0.91}$$

$$L^{\hat{e}} = R^{-1}(\tilde{\theta})\, L\, R(\tilde{\theta}) \tag{0.92}$$

$$V_{dq}^{\hat{e}} = L^{\hat{e}}\, I_{dq}^{\hat{e}} \frac{d}{dt} \tag{0.93}$$

$$I_{dq}^{\hat{e}} = L^{\hat{e}-1} \int V_{dq}^{\hat{e}}\, dt \tag{0.94}$$

A.10.1 Ideal current response, demodulation, and saliency tracking observer

Using the process developed above, the current response using an ideal inductance matrix as defined in (0.95) can be obtained. For reference, the inverted inductance matrix is shown in (0.96) and the injected pulsating voltage along the estimated d-axis is shown in (0.97). By plugging these into (0.94), the current response can be found as in (0.98).

$$L = \begin{bmatrix} L_q & 0 \\ 0 & L_d \end{bmatrix} \tag{0.95}$$

$$L^{\hat{e}-1} = \frac{1}{\Sigma L^2 - \Delta L^2} \left(\Sigma L \begin{bmatrix} 1 & 0 \\ 0 & 1 \end{bmatrix} + \Delta L \begin{bmatrix} -\cos(2\tilde{\theta}) & \sin(2\tilde{\theta}) \\ \sin(2\tilde{\theta}) & \cos(2\tilde{\theta}) \end{bmatrix} \right) \tag{0.96}$$

$$V_{dq}^{\hat{e}} = V_c \begin{bmatrix} 0 \\ \cos(\omega_c t) \end{bmatrix} \tag{0.97}$$

$$I_{dq}^{\hat{e}} = \frac{V_c}{\omega_c(\Sigma L^2 - \Delta L^2)} \begin{bmatrix} \Delta L \sin(2\tilde{\theta}) \sin(\omega_c t) \\ \Sigma L \sin(\omega_c t) + \Delta L \cos(2\tilde{\theta}) \sin(\omega_c t) \end{bmatrix} \tag{0.98}$$

$$I_{dq}^{\hat{e}} = \frac{V_c}{\omega_c(\Sigma L^2 - \Delta L^2)} \left(\Sigma L \begin{bmatrix} 0 \\ \sin(\omega_c t) \end{bmatrix} + \Delta L \begin{bmatrix} \sin(2\tilde{\theta}) \sin(\omega_c t) \\ \cos(2\tilde{\theta}) \sin(\omega_c t) \end{bmatrix} \right) \tag{0.99}$$

$$\hat{I}^{e}_{dq} = \frac{V_c}{\omega_c(\Sigma L^2 - \Delta L^2)}\left(\Sigma L\begin{bmatrix} 0 \\ \sin(\omega_c t)\end{bmatrix} + \frac{\Delta L}{2}\begin{bmatrix} \cos(2\tilde{\theta} - \omega_c t) - \cos(2\tilde{\theta} + \omega_c t) \\ \sin(2\tilde{\theta} + \omega_c t) - \sin(2\tilde{\theta} - \omega_c t)\end{bmatrix}\right) \quad (0.100)$$

This current response can be rewritten in several ways which are useful in viewing the response. The first can be separated into the portion which is based on the average inductance, and the portion based on the differential inductance as in (0.99). This is an interesting interpretation as it shows the relative importance of the differential inductance. Only the portion of the response based on the differential inductance contains position information. It also shows that along the q-axis only the response to the differential inductance is present. However, along the d-axis, the differential inductance is typically dwarfed by the average inductance response. Additionally, the current response can be rewritten as in (0.100). This form shows the response as two counter-rotating vectors based on the differential inductance.

$$\hat{I}^{e}_{q} = \frac{\Delta L\ V_c}{\omega_c(\Sigma L^2 - \Delta L^2)}\ \sin(2\tilde{\theta})\sin(\omega_c t) \quad (0.101)$$

$$\text{demod} = \frac{\Delta L\ V_c}{\omega_c(\Sigma L^2 - \Delta L^2)}\ \sin(2\tilde{\theta})\sin^2(\omega_c t) \quad (0.102)$$

$$\text{demod} = \frac{\Delta L\ V_c}{\omega_c(\Sigma L^2 - \Delta L^2)}\ \sin(2\tilde{\theta})\left(1 - \cos^2(\omega_c t)\right) \quad (0.103)$$

$$\text{demod}_{\text{filtered}} = \frac{\Delta L\ V_c}{\omega_c(\Sigma L^2 - \Delta L^2)}\ \sin(2\tilde{\theta}) \quad (0.104)$$

$$\tilde{\theta} = \frac{\omega_c(\Sigma L^2 - \Delta L^2)}{2\ \Delta L\ V_c}\,\text{demod}_{\text{filtered}} \quad (0.105)$$

To extract the position from the current response, first the q-axis current is isolated as in (0.101). Next, the q-axis current is multiplied by a sinusoid at the carrier to form (0.102) which is equivalent to (0.103). In (0.103) it is clear to see the frequency components. By applying a low-pass filter the high frequency content is removed leaving only the DC component as shown in (0.104). Finally, making a small angular error assumption and rearranging allows for the position error to be solved for as in (0.105). This error can be used as the error term for a

tracking observer which will drive the error to 0. This process is shown in the state block diagram in Figure A.56 and with the Simulink implementation used in this work shown in Figure A.57.

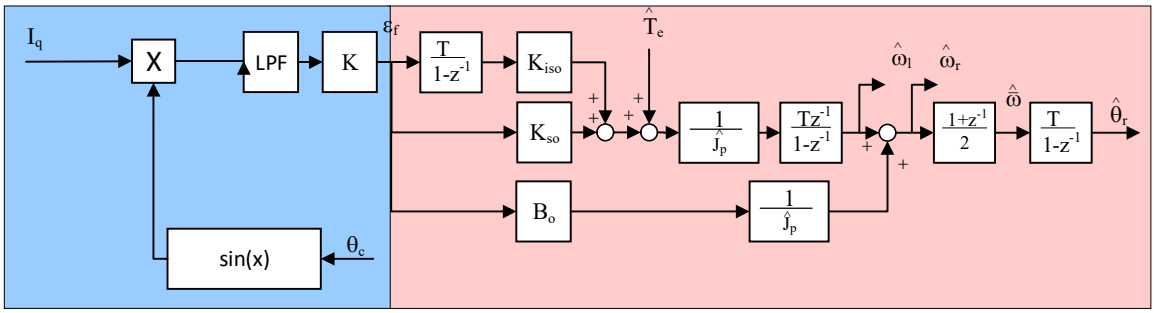

Figure A.56 – Demodulation process shown in blue which is suitable for use with a pulsating voltage injection, in red the cascaded saliency tracking observer is shown for zero-lag estimates of position.

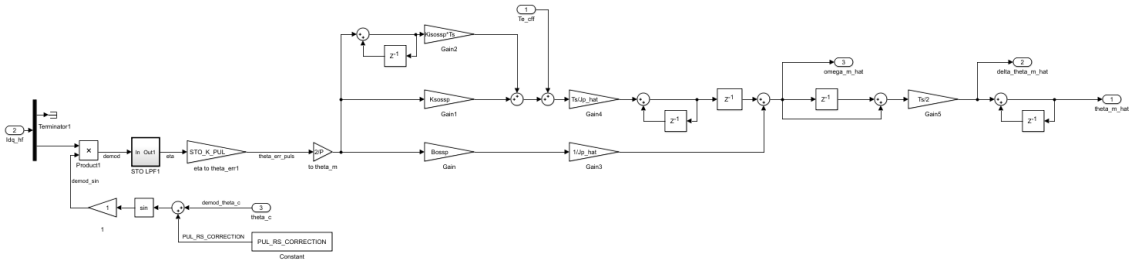

Figure A.57 – Simulink implementation of a pulsating vector HFI demodulation and saliency tracking observer.

The full pulsating self-sensing with an ideal inductance matrix is shown in Figure A.58. Here the voltage injection as in (0.97) is shown along with the q-axis current response from (0.101) with a small angular error of 5° is introduced. This is purely illustrative so that the q-axis current and subsequent demodulation steps are non-zero. Next the local oscillator which is used to demodulate the signal is shown for reference. Then the demodulated signal from (0.102) is shown and it is easy to see that the frequency content is moved to DC and $2\omega_c$. Finally, by

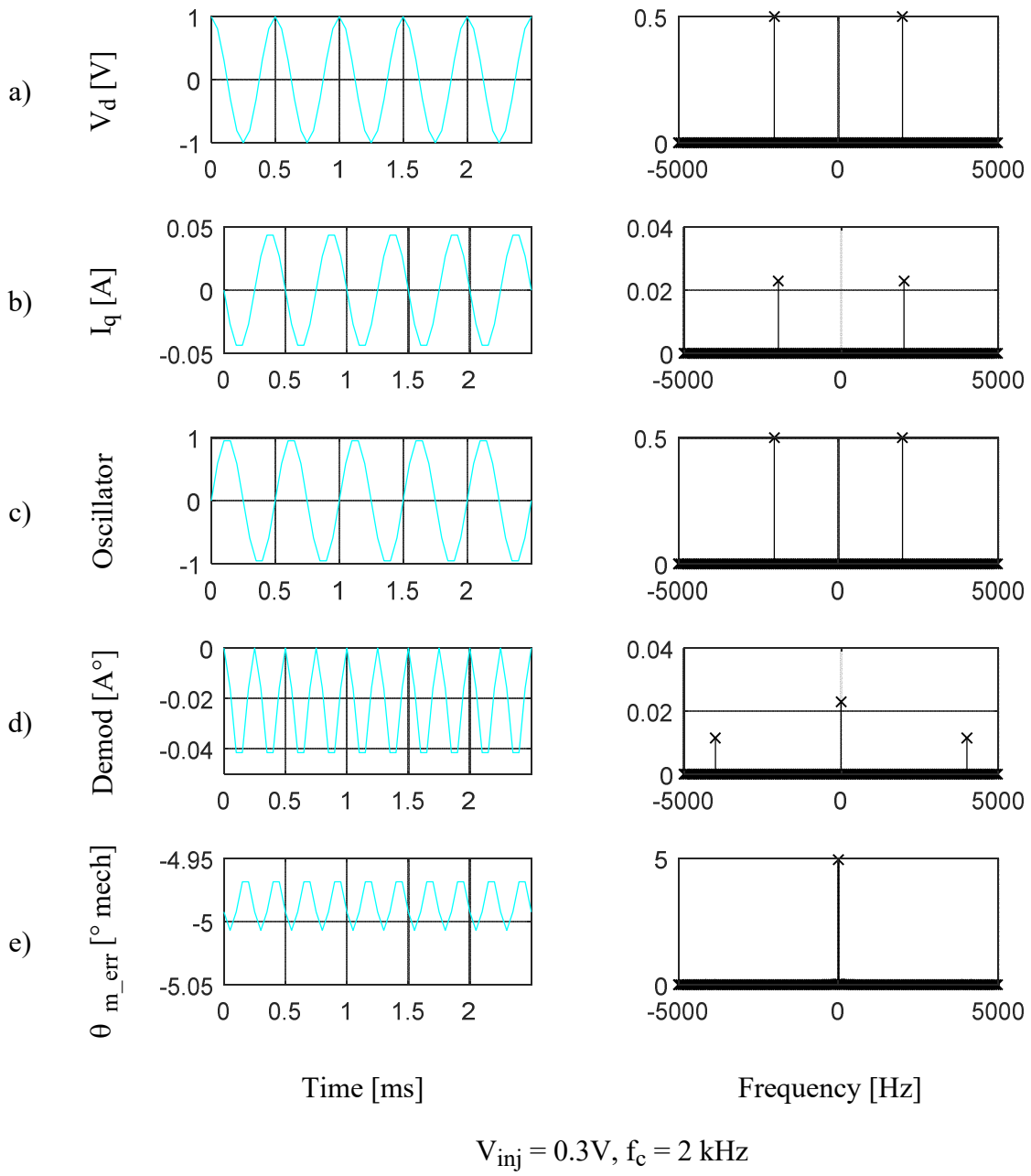

Figure A.58 – Analytical results showing the steps of the demodulation process in both the time and frequency domains.

applying a low-pass filter, the higher frequency content can be removed, and theta is estimated as in (0.105). To validate the process, the demodulated theta error that results is the expected 5° mechanical.

The full system including the voltage injection into the estimated d-axis, current separation, and saliency tracking observer is shown in Figure A.59. Viewing the system overview and the demodulation process it can be noted that the entire system forms a feedback loop between the injection into the estimated reference frame, and the tracking observer driving the error to 0.

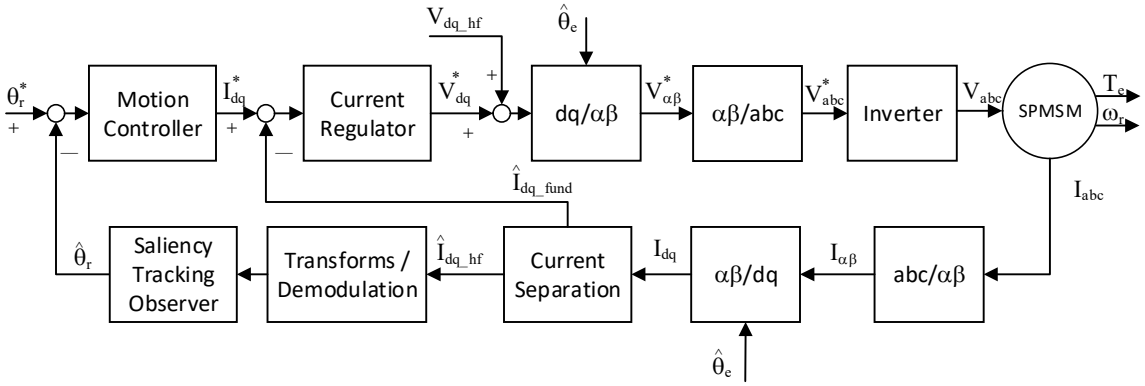

Figure A.59 – System overview of a pulsating voltage HFI self-sensing system with use of estimated position explicitly shown for feedback and reference frame transforms.

A.10.2 Non-ideal impedance, effects and compensation

This section will describe a number of non-ideal effects on pulsating voltage injection methods and where available, how to compensate for them. The first effect discussed is a non-ideal inductance matrix. By modifying the inductance matrix in (0.95) to account for the effects of cross-saturation, or an inductance coupling of the axes, the same process as before can be repeated. For reference, the inverted inductance matrix in the estimated synchronous frame is presented in (0.107). Which along with the same voltage injection presented in (0.97) can be plugged into (0.94) and evaluated to solve for the current response as presented in (0.108). Here it is presented in a form which can easily be compared to the ideal response to see the effects of the cross-saturation. Namely an additional phase and magnitude which rotate at the same

frequency. In (0.109) it is restated to show the effect on the counter-rotating vectors, again with a phase and magnitude shift but which rotate at the same frequency.

$$L = \begin{bmatrix} L_q & L_{dq} \\ L_{dq} & L_d \end{bmatrix} \tag{0.106}$$

$$L^{\hat{e}\text{-}1} = \frac{1}{\Sigma L^2 - \Delta L^2}\left(\Sigma L \begin{bmatrix} 1 & 0 \\ 0 & 1 \end{bmatrix} + \Delta L \begin{bmatrix} -\cos(2\tilde{\theta}) & \sin(2\tilde{\theta}) \\ \sin(2\tilde{\theta}) & \cos(2\tilde{\theta}) \end{bmatrix} + L_{dq} \begin{bmatrix} -\sin(2\tilde{\theta}) & -\cos(2\tilde{\theta}) \\ -\cos(2\tilde{\theta}) & \sin(2\tilde{\theta}) \end{bmatrix} \right) \tag{0.107}$$

$$I_{dq}^{\hat{e}} = \frac{V_c}{\omega_c(\Sigma L^2 - \Delta L^2 - L_{dq}^2)}\left(\Sigma L \begin{bmatrix} 0 \\ \sin(\omega_c t) \end{bmatrix} + \Delta L \begin{bmatrix} \sin(2\tilde{\theta})\sin(\omega_c t) \\ \cos(2\tilde{\theta})\sin(\omega_c t) \end{bmatrix} + L_{dq} \begin{bmatrix} -\cos(2\tilde{\theta})\sin(\omega_c t) \\ \sin(2\tilde{\theta})\sin(\omega_c t) \end{bmatrix} \right) \tag{0.108}$$

$$I_{dq}^{\hat{e}} = \frac{V_c}{\omega_c(\Sigma L^2 - \Delta L^2)}\left(\Sigma L \begin{bmatrix} 0 \\ \sin(\omega_c t) \end{bmatrix} + \frac{\Delta L}{2} \begin{bmatrix} \cos(2\tilde{\theta} - \omega_c t) - \cos(2\tilde{\theta} + \omega_c t) \\ \sin(2\tilde{\theta} + \omega_c t) - \sin(2\tilde{\theta} - \omega_c t) \end{bmatrix} + \frac{L_{dq}}{2} \begin{bmatrix} -\sin(2\tilde{\theta} + \omega_c t) + \sin(2\tilde{\theta} - \omega_c t) \\ \cos(2\tilde{\theta} - \omega_c t) - \cos(2\tilde{\theta} + \omega_c t) \end{bmatrix} \right) \tag{0.109}$$

The step-by-step process is again shown using analytical results as with the ideal case. At 5° mechanical error is introduced to force the signals to be non-zero. The voltage injection and oscillator are the same as for the ideal case. The current response shows a significant difference in both the phase and magnitude. This plays a role when the demodulation process is applied and results in significantly different demodulation and theta error terms when compared with the ideal case. It should also be noted that the estimated error is 10° when it should be 5°. This is because the q-axis current response is twice as large, and out of phase with the oscillator.

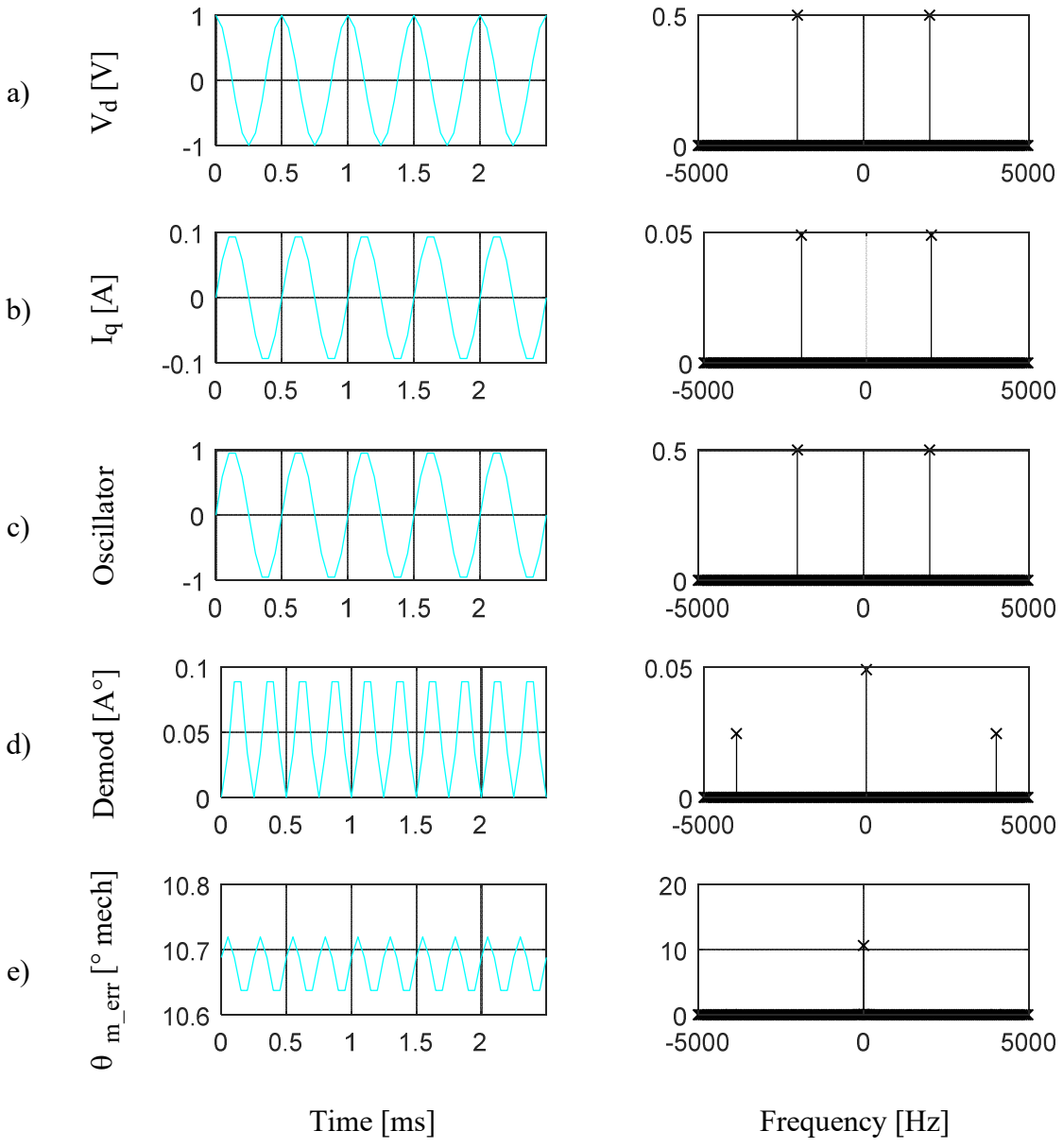

V_{inj} = 0.3V, f_c = 2 kHz, L_{dq} = 0.1*L_d

Figure A.60 – Analytical results showing the steps of the demodulation process in both the time and frequency domains when cross-saturation is included.

Following the same format as for ideal and cross-saturation. In the case of multiple saliencies, where the inductance a series of harmonics instead of simply the h=2 harmonic, the

inductance matrix can be given as in (0.110). Converting it to the estimated synchronous frame and inverting it leads to (0.111). Finally, plugging it and the voltage injection given in (0.97) into the estimated synchronous frame machine equation yields (0.112). First, there remains the average inductance-based component purely along the q-axis. Additionally, the previous ideal and cross-saturation models appear. For the ideal model, h only equals 2, and there is no phase shift in the matrix. For the cross-saturation model, again h only equals 2, and the cross-saturation appears in both the phase shift and the magnitude of the differential inductance for h=2. Finally, it should be noted that a term based on the actual position appears. This is an interesting piece as previously all information contained in the current was only relative to the injection axis, and subsequently related to the absolute position. However, here the phase of the response is partially based upon the position of the machine.

$$L = \Sigma L\begin{bmatrix} 1 & 0 \\ 0 & 1 \end{bmatrix} + \sum_{h} \Delta L_h \begin{bmatrix} \cos(h\theta+\phi_h) & -\sin(h\theta+\phi_h) \\ -\sin(h\theta+\phi_h) & -\cos(h\theta+\phi_h) \end{bmatrix} \tag{0.110}$$

$$L^{\hat{e}\text{-}1} = \frac{1}{\Sigma L^2 - (\sum_h \Delta L_h)^2}\left(\Sigma L\begin{bmatrix} 1 & 0 \\ 0 & 1 \end{bmatrix} + \sum_{h} \Delta L_h \begin{bmatrix} -\cos(h\theta+\phi_h-2\tilde{\theta}) & \sin(h\theta+\phi_h-2\tilde{\theta}) \\ -\sin(h\theta+\phi_h-2\tilde{\theta}) & \cos(h\theta+\phi_h-2\tilde{\theta}) \end{bmatrix} \right) \tag{0.111}$$

$$I_{dq}^{\hat{e}} = \frac{V_c \Sigma L}{\omega_c(\Sigma L^2 - (\sum_h \Delta L_h)^2)}\begin{bmatrix} 0 \\ \sin(\omega_c t) \end{bmatrix} + \sum_{h}\left(\frac{V_c \Delta L_h}{\omega_c(\Sigma L^2 - (\sum_h \Delta L_h)^2)} \begin{bmatrix} \sin(h\theta+\phi_h-2\tilde{\theta})\sin(\omega_c t) \\ \cos(h\theta+\phi_h-2\tilde{\theta})\sin(\omega_c t) \end{bmatrix} \right) \tag{0.112}$$

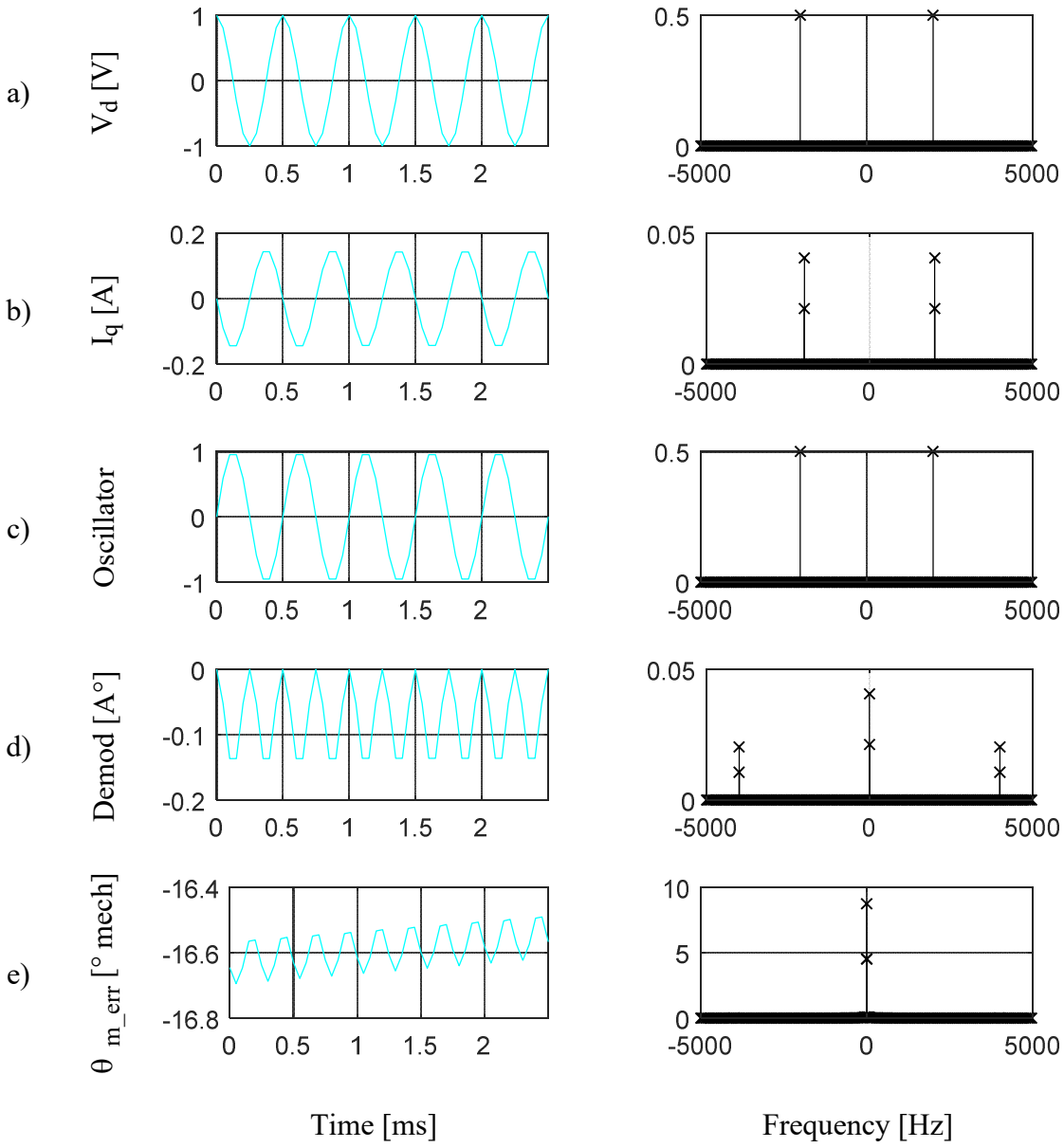

$V_{inj} = 0.3V$, $f_c = 2$ kHz, $\Delta L_3 = \Delta L_2$

Figure A.61 – Analytical results showing the steps of the demodulation process in both the time and frequency domains when a large multiple saliency is included.

Analytical results of each step of the injection and demodulation process are shown in Figure A.61. This can be compared to the results for the inductance matrix which is ideal and

when it contains cross-saturation. The voltage and demodulation signals are again the same. However, now there appear additional harmonics in the current governed by (0.112). This effect is highlighted in this test where the electrical speed is 1Hz to demonstrate the effect of the multiple saliency. If it weren't at speed, it would again show up as an additional component of the response at the positive and negative carrier frequency. Notice that after demodulation the effect is still seen near the DC component. This is evident in both the time and frequency domain and will generate an oscillating error as the machine spins.

Up to this point it has been assumed that the current response is based solely on the machine's inductance. In high frequency injection based self-sensing, this is often valid as the resistance is small relative to the inductance and has a tolerably small impact on the position estimate achieved from self-sensing. However, if the resistance is relatively large, this assumption is not valid, and the effects must be handled. In [64] the resistance effects were calculated and appear as a phase offset in the current response. If it is assumed that the resistance is not salient, e.g. that there are no reflection or loss differences between the two axes, the phase offset is given as (0.113). This can then be added to the phase of the local oscillator in the demodulation of the current signal as in Figure A.62. On the test bench used in this work, the phase correction is 23.6° and must be compensated. In the Simulink diagram presented in Figure A.57 this compensation is applied.

$$\phi_{nc} = \pi - \operatorname{atan}\left(\frac{\omega_c L_q}{R}\right) - \operatorname{atan}\left(\frac{\omega_c L_d}{R}\right) \tag{0.113}$$

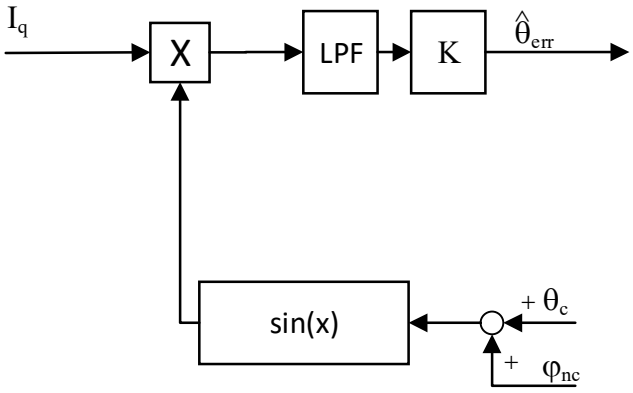

Figure A.62 – State block diagram of a modified demodulation process for pulsating high frequency voltage based self-sensing, which accounts for the phase offset due to resistance.

A further assumption which is commonly applied to self-sensing systems and has been applied thus far is that the cross-coupling of the electrical plant can be neglected. Even in this work the effects of cross-coupling are minor, however, to make the estimation as accurate as possible, the effects of cross-coupling on the high frequency injection can be decoupled. This can be achieved through the use of a high frequency current observer, and estimated voltage cross-coupling can be subtracted from the voltage command to effectively decouple the high frequency component. A state block diagram of this is shown in Figure A.63.

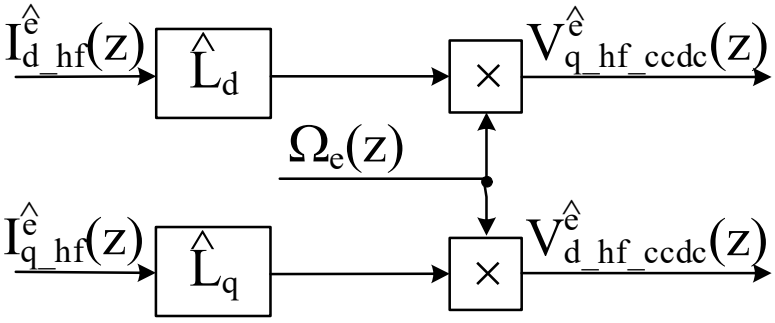

Figure A.63 – State block diagram of a method to compensate the high frequency voltage injection to account for the cross-coupling of the electric machine.

In Figure A.64 the initial closed-loop results are shown using an ideal inductance model. Notice that the estimate does not quite track the actual position and that an offset remains in steady-state. Identified sources of error have been discussed in this section and include the effects of resistance, high frequency voltage injection cross-coupling, and high frequency current remaining in the current regulator feedback signal. To address these problems, the discussed compensation methods were applied sequentially. The results are shown in Figure A.65 and remove 25% of the error. The remaining error is a result of the effects of the stationary frame latch and is discussed in Chapter 2.

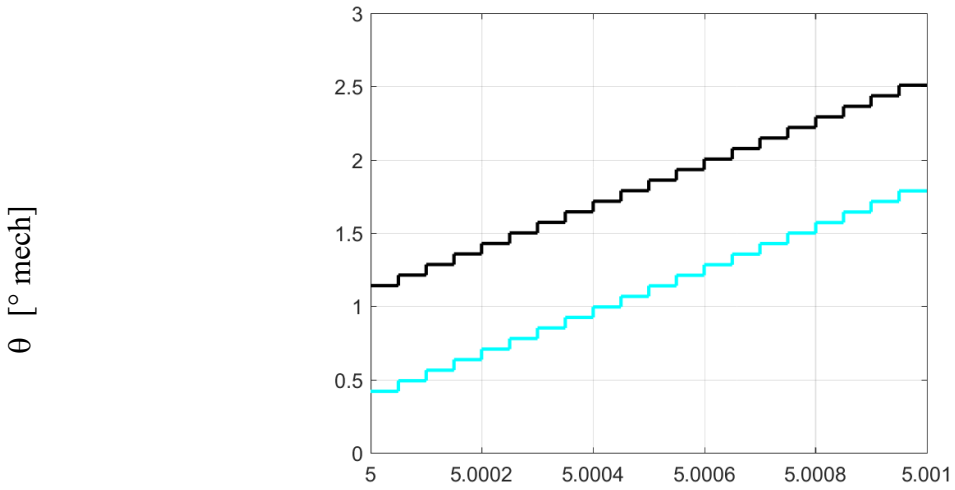

MC tuned to 50/10/5 Hz, STO tuned to 100/20/4 Hz, $|V_{inj}| = 0.1V$, $V_c = 2$ kHz

Figure A.64 – Simulated closed-loop pulsating feedback.

A similar experiment was performed on the test bench with all compensations applied. The results are shown in Figure A.66 and the pulsating system tracks well. The error is a little higher with 3° amplitude error, but minimal steady-state effects. The sources of this beyond

mechanical disturbances are likely a non-ideal inverter and a non-ideal inductance matrix. The error tends to oscillate at 8 ω_m, which would correspond to a relationship with the poles and points to a likely non-ideal inductance matrix.

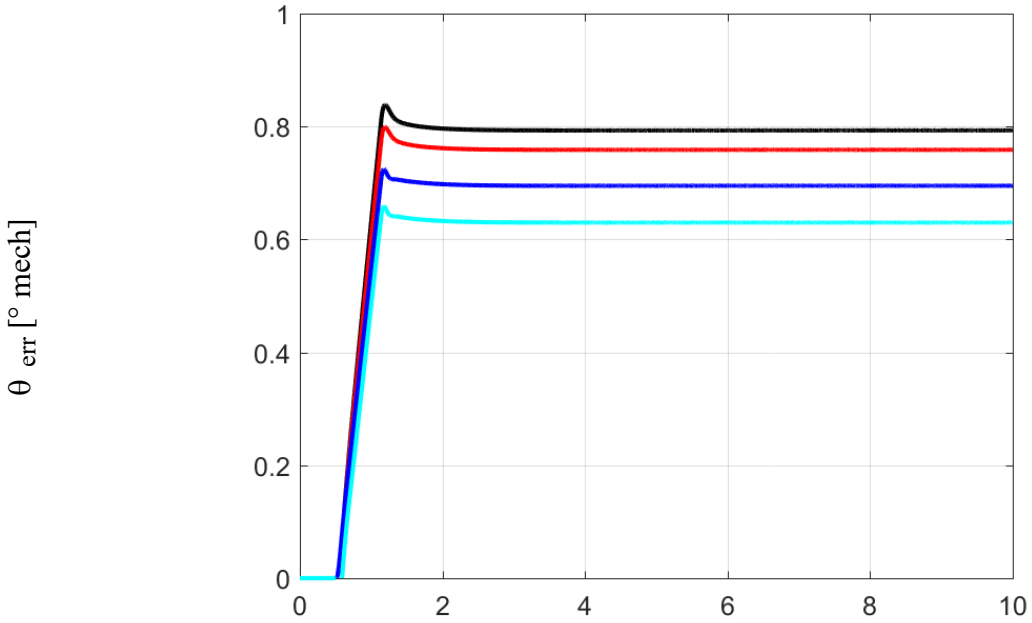

θ_{err} , θ_{err} w/ Rs Comp. , θ_{err} w/ Rs Comp. and Filtered IO Feedback ,
θ_{err} w/ Rs Comp., Filtered IO Feedback, and HF Cross-coupling Decoupling
MC tuned to 5/1/0.2 Hz, STO tuned to 10/2/0.4 Hz, $|V_{inj}| = 0.1V$, $V_c = 2$ kHz

Figure A.65 – Simulated closed-loop pulsating feedback with applied decoupling strategies.

The experimental qualities were further investigated by taking a dynamic stiffness FRF of the system using pulsating feedback. The overlaid asymptotes show the agreement between experimental and expected results. It should be noted though that the achievable bandwidth is markedly lower here than with the encoder used as feedback.

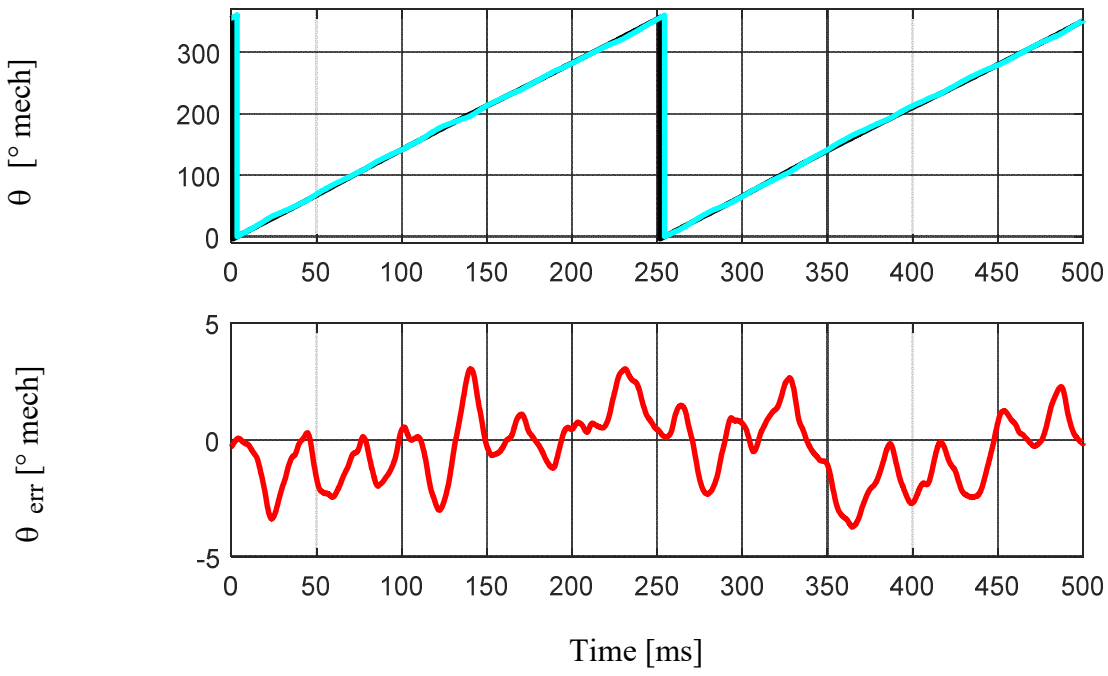

$\theta_{encoder}$, $\hat{\theta}_{pulsating}$, θ_{err}

MC tuned to 2/0.4/0.08 Hz, STO tuned to 10/2/0.4 Hz, $|V_{inj}| = 0.3V$, $V_c = 2$ kHz

Figure A.66 – Experimental closed-loop pulsating feedback.

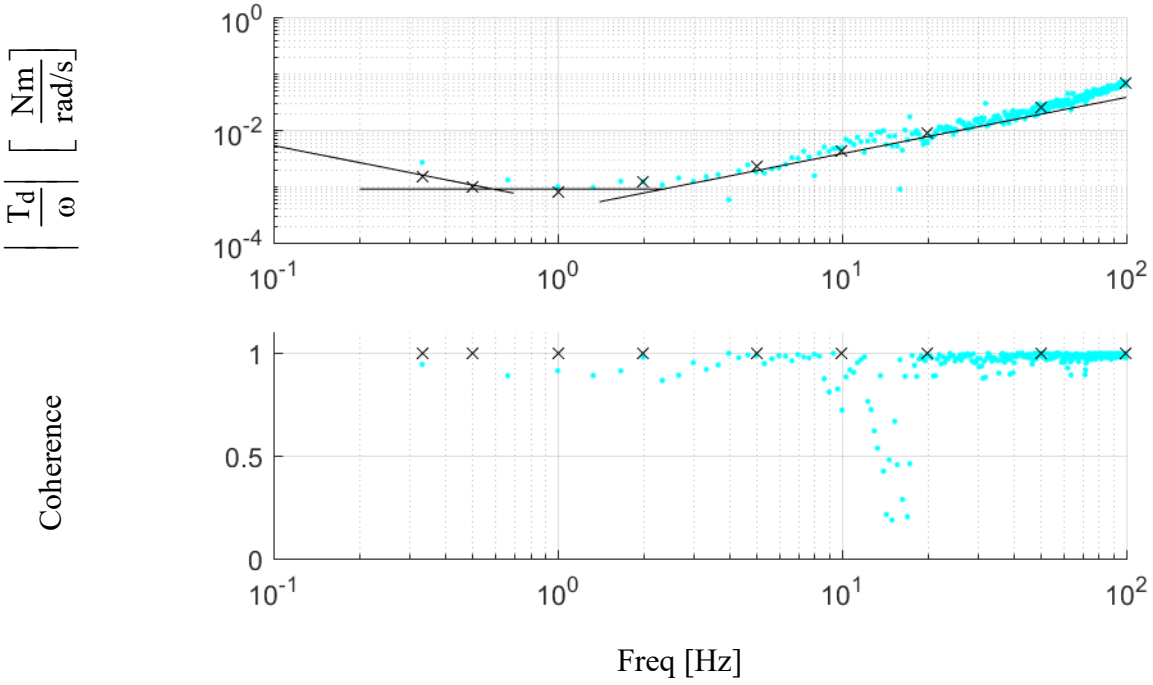

Dynamic stiffness from: Chirp FRF, Single Sine Test

MC tuned to 2/0.4/0.08 Hz, STO tuned to 10/2/0.4 Hz, $|V_{inj}| = 0.3V$, $V_c = 2$ kHz

T_d* chirp with $f_0 = 1$ Hz, $f_1 = 100$ Hz, T = 0.5s, magnitude 0.1PU

Overlaid asymptotes with $J_p = 60$ μNm, $B_o+B_p = 0.8$mNm/rad/s, $K_a = 0.0033$ Nm/rad, $K_{sa} = 0.0027$ Nms/rad

Figure A.67 – Dynamic stiffness FRF with pulsating self-sensing feedback.

A.11 High Frequency Flux Injection Self-Sensing

The concept of high frequency flux injection for an SPM machine is quite similar to pulsating voltage injection presented in section A.9 . The main difference is in the control method needed to generate the flux injection. This requires the implementation of DB-DTFC as described in section A.8 . The full system overview including torque and flux control, as well as self-sensing injection and demodulation is shown in Figure A.68.

The main difference from either DB-DTFC or self-sensing as presented earlier is the flux injection which is a pulsating flux along the torque line. This injection takes the form of (0.114)

which is identical to the form of (0.97). This only holds so long as the torque line is actually a line and is constant along the q-axis at a given operating point. This is true when M in (0.69) is 0, or further when $L_d = L_q$. This is not strictly true on an SPM but |M| will be small as long as the saliency ratio is small.

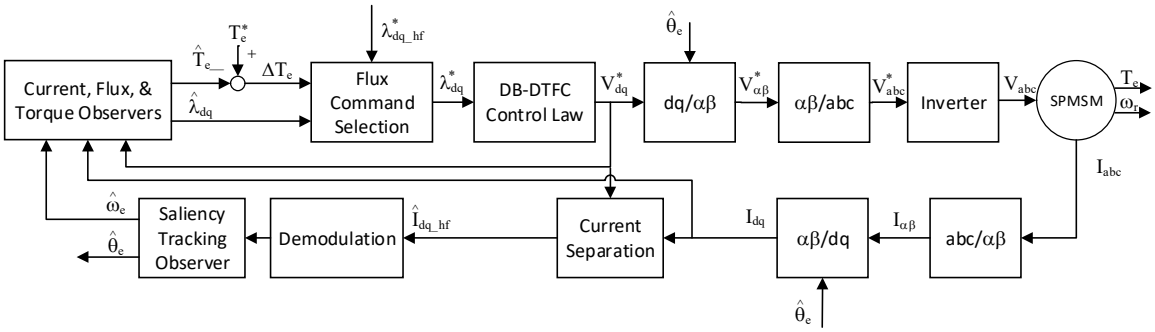

Figure A.68 – System overview of a HFFI with DB-DTFC self-sensing system.

$$\begin{bmatrix} \hat{V}_q^e \\ \hat{V}_d^e \end{bmatrix} = V_c \begin{bmatrix} 0 \\ \cos(\omega_c t) \end{bmatrix} = \frac{\lambda_c}{T_s} \begin{bmatrix} 0 \\ \cos(\omega_c t) \end{bmatrix} \tag{0.114}$$

A.12 Rotating Voltage HFI Self-Sensing

Using a similar process as for pulsating, the current response to a voltage rotating in the stationary frame can be found. Using the synchronous frame machine equation defined in (0.85) and multiplying by the rotation matrix defined in (0.87) equation (0.115) is formed. Using the definitions in (0.116) and (0.117) to substitute into (0.115), the machine equation in the stationary frame using the synchronous frame inductance is formed as in (0.118). By combining the inductance matrix in the synchronous frame with the adjacent matrixes, the inductance in the stationary frame can be defined as in (0.119) to form the stationary frame machine equation in (0.120). Finally, to solve for the current response, the stationary frame voltage can be integrated

and multiplied by the inverse of the stationary frame inductance matrix as in (0.121). This method will be used heavily in the rest of this chapter to find expected current and analyze the self-sensing response.

$$R^{-1}(\theta)\, V_{dq} = R^{-1}(\theta)\, L\, I_{dq} \frac{d}{dt} \tag{0.115}$$

$$R^{-1}(\theta)\, V_{dq} = V_{\alpha\beta} \tag{0.116}$$

$$I_{dq} = R(\theta)\, I_{\alpha\beta} \tag{0.117}$$

$$V_{\alpha\beta} = R^{-1}(\theta)\, L\, R(\theta)\, I_{\alpha\beta} \frac{d}{dt} \tag{0.118}$$

$$L_{\alpha\beta} = R^{-1}(\theta)\, L\, R(\theta) \tag{0.119}$$

$$V_{\alpha\beta} = L_{\alpha\beta} I_{\alpha\beta} \frac{d}{dt} \tag{0.120}$$

$$I_{\alpha\beta} = L_{\alpha\beta}^{-1} \int V_{\alpha\beta}\, dt \tag{0.121}$$

A.12.1 Ideal current response, demodulation, and saliency tracking observer

Using the equations developed in the previous section, the ideal current response to a rotating voltage in the stationary frame can now be solved for. Starting with the ideal synchronous frame inductance matrix as shown in (0.122) and proceeding to solve for the inverted stationary frame inductance matrix as in (0.123). Substituting the inverted stationary frame equation and the rotating voltage defined in (0.124) into the equation for the current solution in (0.121), simplifying, and separating the portions of the response dependent on the average and differential inductances results in (0.125). In this form, it is clear there will be a component at the carrier frequency dependent on the average inductance, but which does not contain any position information. More importantly, absolute position information is contained in the negative sequence with an amplitude dependent on the differential inductance.

$$L = \begin{bmatrix} L_q & 0 \\ 0 & L_d \end{bmatrix} \tag{0.122}$$

$$L_{\alpha\beta}^{-1} = \frac{1}{\Sigma L^2 - \Delta L^2} \left(\Sigma L \begin{bmatrix} 1 & 0 \\ 0 & 1 \end{bmatrix} + \Delta L \begin{bmatrix} -\cos(2\theta) & \sin(2\theta) \\ \sin(2\theta) & \cos(2\theta) \end{bmatrix} \right) \tag{0.123}$$

$$V_{\alpha\beta} = V_c \begin{bmatrix} \sin(\omega_c t) \\ \cos(\omega_c t) \end{bmatrix} \tag{0.124}$$

$$I_{\alpha\beta} = \frac{V_c}{\omega_c(\Sigma L^2 - \Delta L^2)} \left(\Sigma L \begin{bmatrix} \cos(\omega_c t) \\ -\sin(\omega_c t) \end{bmatrix} + \Delta L \begin{bmatrix} -\cos(2\theta - \omega_c t) \\ \sin(2\theta - \omega_c t) \end{bmatrix} \right) \tag{0.125}$$

To perform the demodulation the negative sequence current which is dependent on the position must be separated from the positive sequence. A detailed process for extracting this portion of the current spectra is outlined in section A.9 . Next a local oscillator based on the estimated position from the saliency tracking observer, and the carrier frequency is constructed as in (0.127). The current is cross-multiplied with the local oscillator to form the demodulated signal as in (0.128). In theory the demodulated signal could be used as an error signal, however in practice there will be additional harmonic content on the input current which will require low-pass filtering to remove. Assuming the error is small, the small angle assumption can be made, and the position error can be determined as in (0.130).

The demodulation process with attached saliency tracking observer is shown in state block diagram form in Figure A.69 with the Simulink implementation used in this project shown in Figure A.70.

$$I_{\alpha\beta\_nc} = \frac{\Delta L \, V_c}{\omega_c(\Sigma L^2 - \Delta L^2)} \begin{bmatrix} -\cos(2\theta - \omega_c t) \\ \sin(2\theta - \omega_c t) \end{bmatrix} \tag{0.126}$$

$$\text{oscillator} = \begin{bmatrix} -\cos(2\hat{\theta} - \omega_c t) \\ \sin(2\hat{\theta} - \omega_c t) \end{bmatrix} \tag{0.127}$$

$$\text{demod} = \frac{\Delta L \, V_c}{\omega_c(\Sigma L^2 - \Delta L^2)} \sin(2\theta) \tag{0.128}$$

$$\text{demod}_{\text{filtered}} = \frac{\Delta L \, V_c}{\omega_c(\Sigma L^2 - \Delta L^2)} \sin(2\theta) \tag{0.129}$$

$$\theta = \frac{\omega_c(\Sigma L^2 - \Delta L^2)}{2 \, \Delta L \, V_c} \text{demod}_{\text{filtered}} \tag{0.130}$$

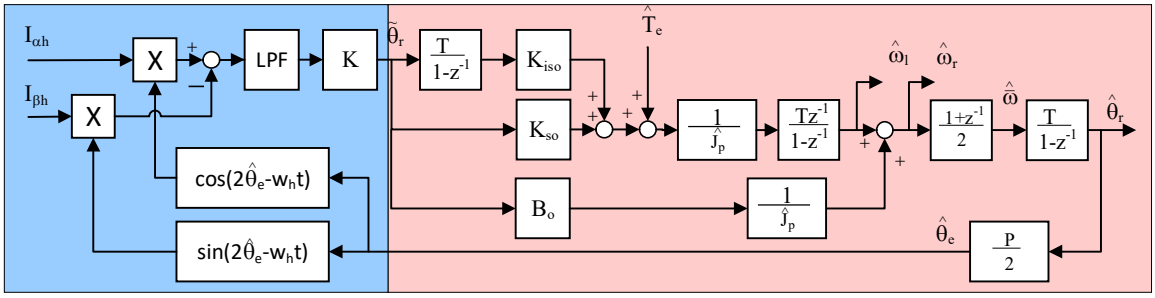

Figure A.69 – Demodulation process shown in blue which is suitable for use with a rotating voltage injection, in red the cascaded saliency tracking observer is shown for zero-lag estimates of position.

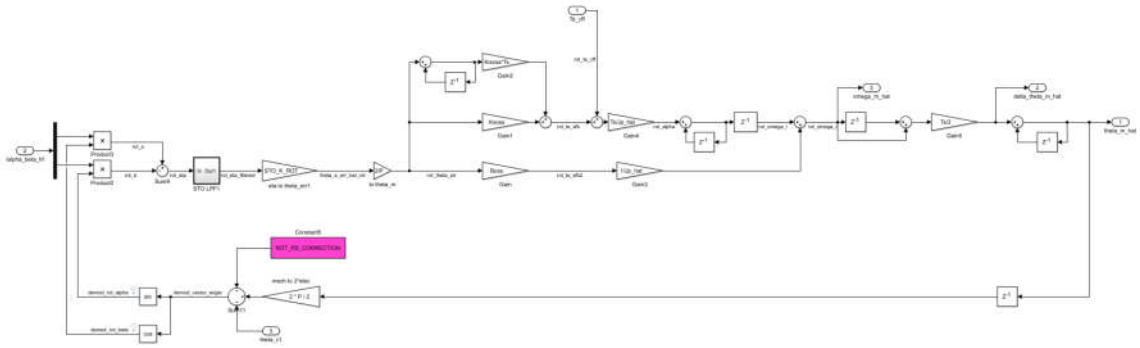

Figure A.70 – Simulink implementation of a rotating vector HFI demodulation and saliency tracking observer.

To demonstrate the injection, demodulation, and theta error estimation described, plots of the analytical solution are presented in Figure A.71 showing each step in time and frequency domains. Both the α- and β-axes are shown for the voltage injection, current response, and demodulation signal as the injection rotates across the entire stationary frame. Of particular interest is the full current response and the final theta error result. The current response shows the large response at the positive carrier which is based on the average inductance, and the smaller response at the negative sequence which is based on the differential inductance. The positive carrier is removed from the signal before demodulation leaving only the negative

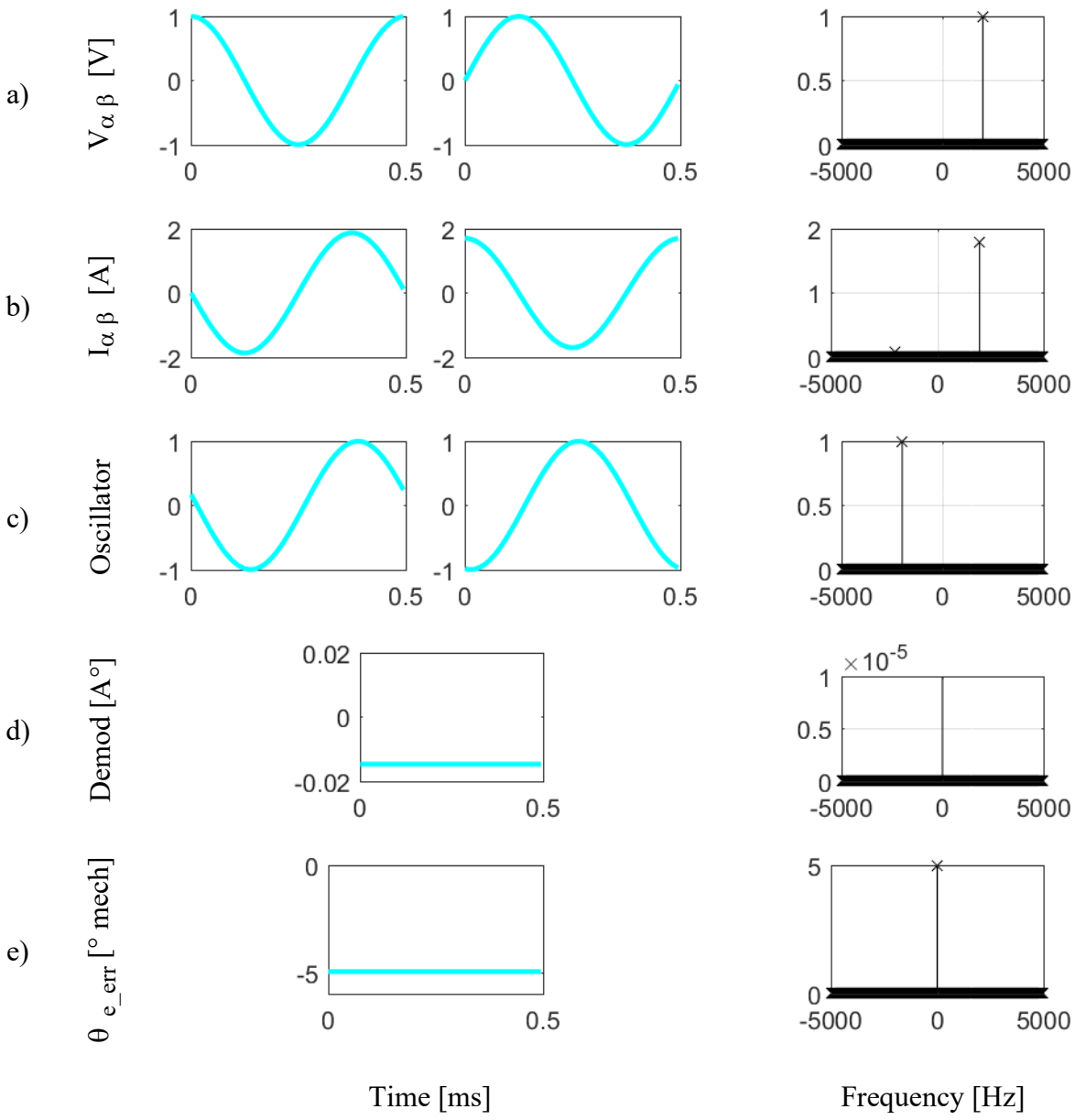

Figure A.71 – Analytical results showing the steps of the demodulation process in both the time and frequency domains.

sequence. In this case the demodulation signal is calculated with an estimated position which is 5° off to provide an interesting example. This in turn makes the cross-product demodulation non-zero, and after filtering and scaling results in a correctly estimated 5° theta error.

In Figure A.72 and overview of the full self-sensing system utilizing a rotating voltage injection in the stationary frame is shown. Of particular note is that in contrast to pulsating where the loop involves the entire system to estimate the reference frame and then inject into it, rotating is more compartmentalized with the injection being independent of the reference frame.

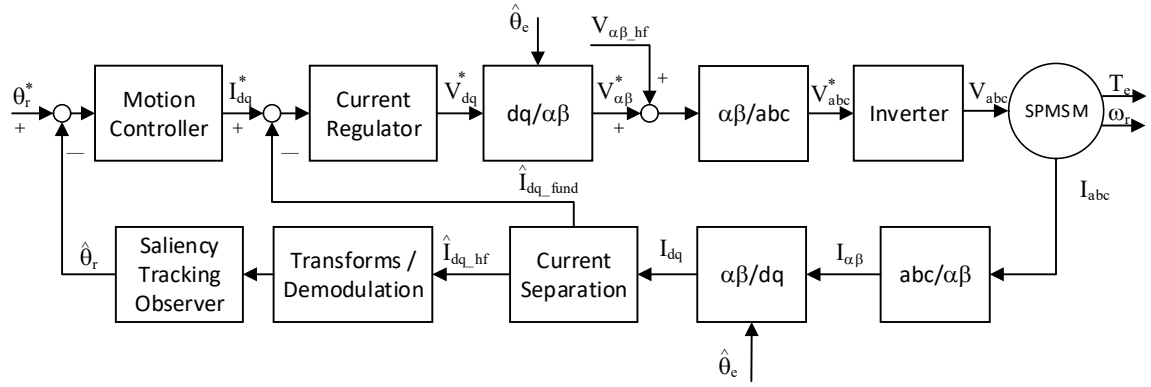

Figure A.72 – System overview of a rotating voltage HFI self-sensing system with use of estimated position explicitly shown for feedback and reference frame transforms.

A.12.2 Non-ideal impedance, effects, and compensation

The effects of non-ideal conditions on the current response to a rotating voltage injection will be explored in this section similar in a manner similar to the non-ideal conditions for pulsating. The effects of cross-saturation are evaluated first, as for pulsating this is the interaction between the axes due to cross-coupling inductance as in (0.131). Following the approach in (0.119) and inverting the matrix yields (0.132). Substituting the voltage injection as in (0.124) and this inverted inductance matrix into (0.121) yields (0.133). In this form it can be seen that the effects are a phase and magnitude alteration to the negative sequence portion of the current response.

To illustrate this process the time and frequency domain of the signals involved in the voltage injection, current response, and demodulation process are shown in Figure A.73. Of particular note is that the current response is at the same frequencies as for the ideal case as is

expected, however the amplitude of the current and the demodulation steps has been altered as is expected from the phase alteration of the current response. Here the 5° error which was introduced in the demodulation is estimated as 8° instead.

$$L = \begin{bmatrix} L_q & L_{dq} \\ L_{dq} & L_d \end{bmatrix} \tag{0.131}$$

$$L_{\alpha\beta}^{-1} = \frac{1}{\Sigma L^2 - \Delta L^2 - L_{dq}^2}\left(\Sigma L\begin{bmatrix} 1 & 0 \\ 0 & 1 \end{bmatrix} + \Delta L\begin{bmatrix} -\cos(2\theta) & \sin(2\theta) \\ \sin(2\theta) & \cos(2\theta) \end{bmatrix} - L_{dq}\begin{bmatrix} -\sin(2\theta) & -\cos(2\theta) \\ -\cos(2\theta) & \sin(2\theta) \end{bmatrix}\right) \tag{0.132}$$

$$I_{\alpha\beta} = \frac{V_c}{\omega_c(\Sigma L^2 - \Delta L^2 - L_{dq}^2)}\left(\Sigma L\begin{bmatrix} \cos(\omega_c t) \\ -\sin(\omega_c t) \end{bmatrix} + \Delta L\begin{bmatrix} -\cos(2\theta-\omega_c t) \\ \sin(2\theta-\omega_c t) \end{bmatrix} - L_{dq}\begin{bmatrix} -\sin(2\theta-\omega_c t) \\ -\cos(2\theta-\omega_c t) \end{bmatrix}\right) \tag{0.133}$$

Following the same process, the effects of a saliency that is characterized better by a series of harmonics than by single saliency is analyzed. The general form in the synchronous reference frame is shown in (0.134). Following the approach in (0.119) and inverting the matrix leads to (0.135). Substituting the voltage injection as in (0.124) and this inverted inductance matrix into (0.121) yields (0.136). The effects resolve into a series of harmonics in the negative sequence, each of which is dependent upon the position. It should be noted that the phase and magnitude are also dependent on any cross-coupling between the axes at that specific inductance harmonic.

To illustrate this process the time and frequency domain of the signals involved in the voltage injection, current response, and demodulation process are shown in Figure A.73. Of particular note is that the current response has additionally frequency content in the negative sequence which propagates through the demodulation process. Here the 5° error which was introduced in the demodulation is estimated as 8° instead.

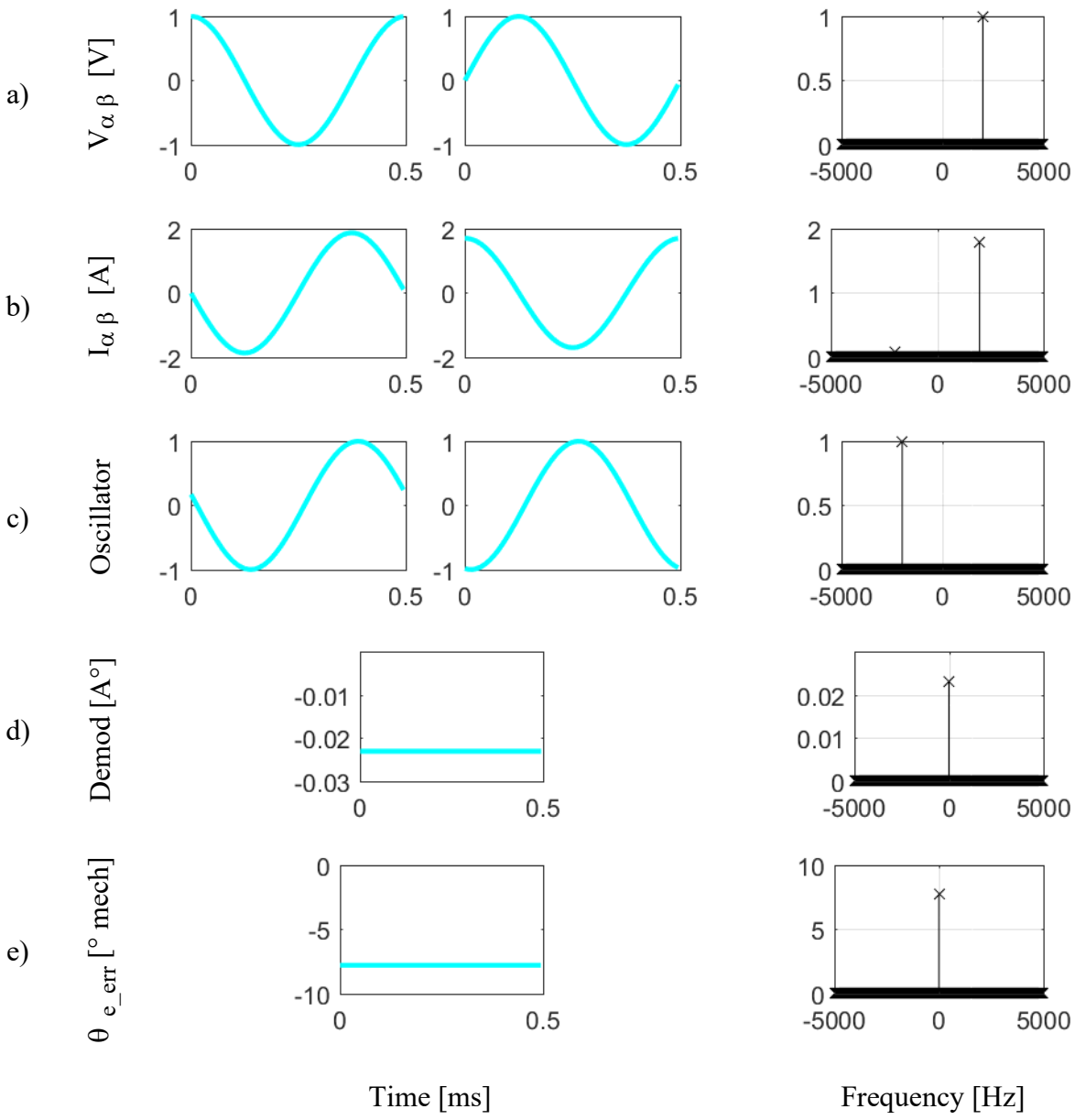

V_{inj} = 1V, f_c = 2 kHz, L_{dq} = 0.1*ΔL

Figure A.73 – Analytical results showing the steps of the demodulation process in both the time and frequency domains, showing the effects of cross-saturation. Where applicable, the left plot is the d-axis, and the right is the q-axis.

$$L = \Sigma L\begin{bmatrix} 1 & 0 \\ 0 & 1 \end{bmatrix} + \sum_{h} \Delta L_h \begin{bmatrix} \cos(h\theta+\phi_h) & -\sin(h\theta+\phi_h) \\ -\sin(h\theta+\phi_h) & -\cos(h\theta+\phi_h) \end{bmatrix} \tag{0.134}$$

$$L_{\alpha\beta}^{-1} = \frac{1}{\Sigma L^2 - (\sum_{h} \Delta L_h)^2} \left(\Sigma L\begin{bmatrix} 1 & 0 \\ 0 & 1 \end{bmatrix} + \sum_{h} \Delta L_h \begin{bmatrix} -\cos(h\theta+\phi_h) & \sin(h\theta+\phi_h) \\ \sin(h\theta+\phi_h) & \cos(h\theta+\phi_h) \end{bmatrix} \right) \tag{0.135}$$

$$I_{\alpha\beta} = \frac{V_c}{\omega_c \left(\Sigma L^2 - (\sum_{h} \Delta L_h)^2 \right)} \left(\Sigma L\begin{bmatrix} \cos(\omega_c t) \\ -\sin(\omega_c t) \end{bmatrix} + \sum_{h} \Delta L_h \begin{bmatrix} -\cos(h\theta-\omega_c t+\phi_h) \\ \sin(h\theta-\omega_c t+\phi_h) \end{bmatrix} \right) \tag{0.136}$$

The effects of resistance are the same as for pulsating as described in (0.113) again assuming that the resistance is constant. The decoupling factor is calculated the same, but due to the differences in demodulation process the compensation changes are shown in Figure A.74.

Additionally, the synchronous frame electrical plant model has cross-coupling. This effect is the same as for pulsating and is handled in the same manner. Namely decoupling utilizing a high bandwidth current observer as shown in Figure A.63.

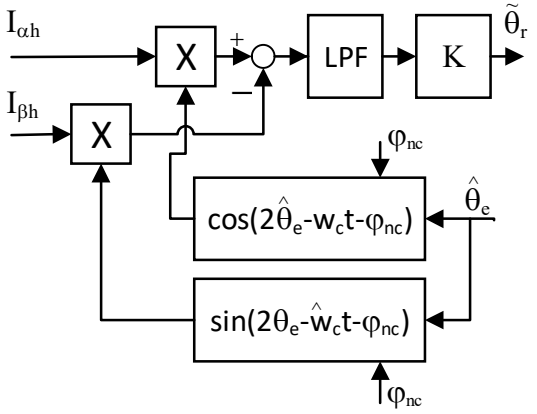

Figure A.74 – State block diagram of a modified demodulation process for rotating high frequency voltage based self-sensing, which accounts for the phase offset due to resistance.

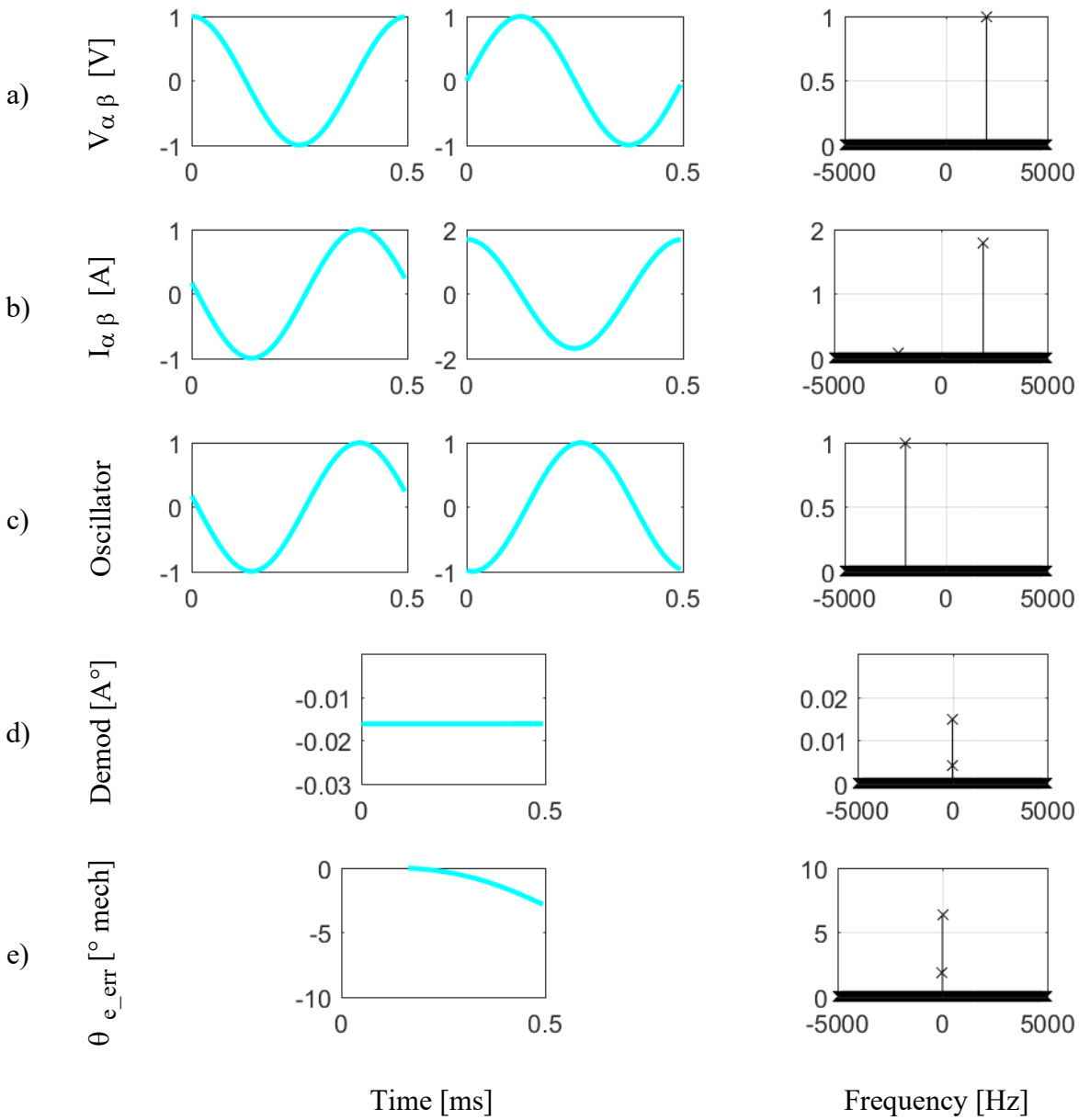

V_{inj} = 1V, f_c = 2 kHz, $\Delta L_3 = 0.1*\Delta L$

Figure A.75 – Analytical results showing the steps of the demodulation process in both the time and frequency domains, with effects of multiple saliencies. Where applicable, the left plot is the d-axis, and the right is the q-axis.

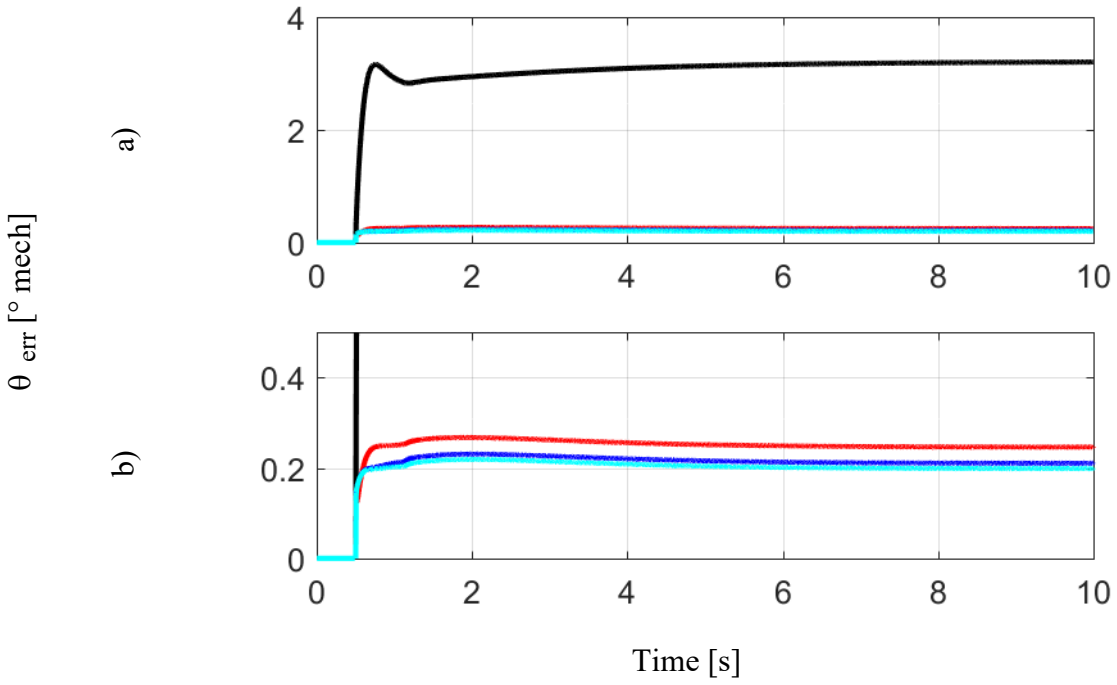

θ_{err} , θ_{err} w/ Rs Comp. , θ_{err} w/ Rs Comp. and Filtered IO Feedback ,
θ_{err} w/ Rs Comp., Filtered IO Feedback, and HF Cross-coupling Decoupling
MC tuned to 50/10/2 Hz, STO tuned to 100/20/4 Hz, V_{inj} = 1V, f_c = 2 kHz

Figure A.76 – Simulated closed-loop pulsating feedback comparing the effects of decoupling methods on the position estimation error.

To evaluate the performance of the controller utilizing a rotating voltage vector a simulation was performed using each of the compensation methods discussed. Initial error was quite substantial at greater than 3° mechanical offset as shown in Figure A.76. This can largely be reduced by compensating for the resistance effects, which reduces the error to less than 0.3° mechanical. Smaller improvements can be made by incorporating the filtered current observer feedback previously discussed, and the high frequency cross-coupling decoupling.

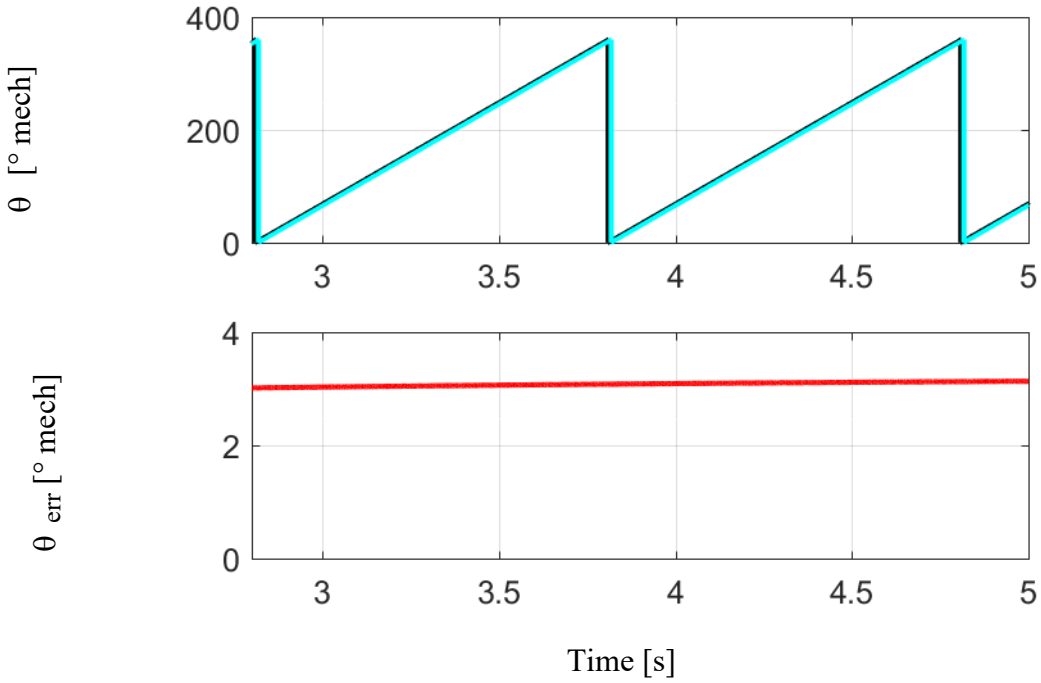

$\theta_{encoder}$, $\hat{\theta}_{rotating}$, θ_{err}
MC tuned to 50/10/2 Hz, STO tuned to 100/20/4 Hz, V_{inj} = 1V, f_c = 2 kHz

Figure A.77 – Simulated closed-loop rotating with injection cross-coupling decoupling and resistance decoupling.

The time-domain estimation accuracy captured on the bench is shown in Figure A.78. Here there is an offset which denotes likely cross-saturation. Additionally, there is harmonic content primarily synchronized with the mechanical position. This comes from a mechanical disturbance and the low bandwidth of the motion controller.

In Figure A.79 the experimental dynamic stiffness is shown. The overlaid asymptotes align well with the experimental data, particularly the data captured via single sinusoid tests. However, it should be noted that this controller only achieved a bandwidth of 2Hz.

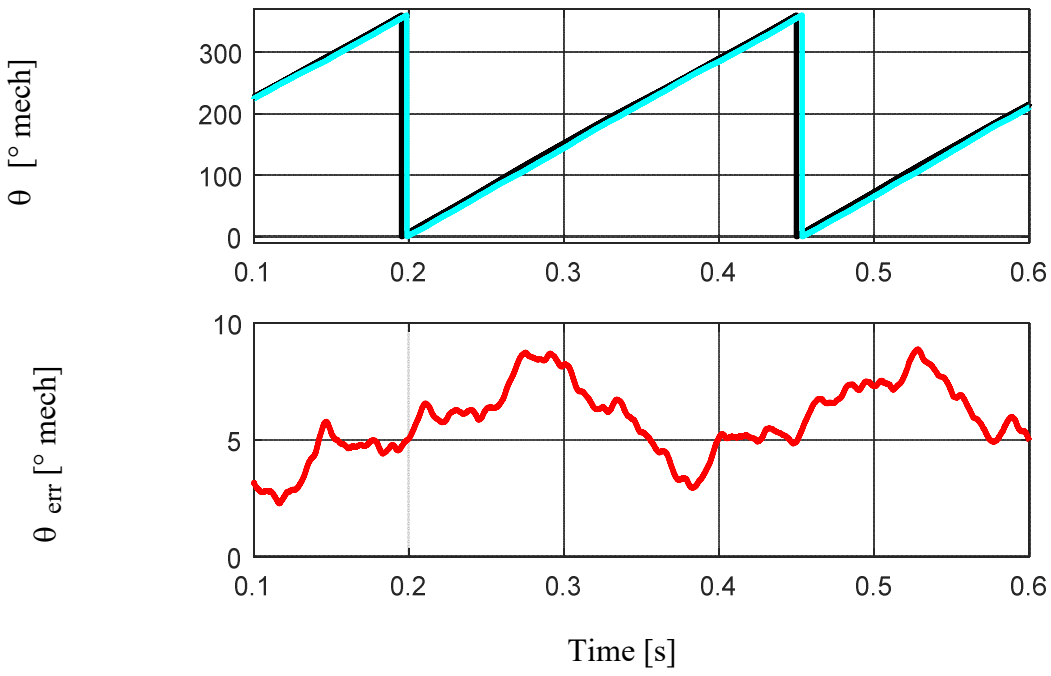

$\theta_{encoder}$, $\hat{\theta}_{pulsating}$, θ_{err}

MC tuned to 2/0.4/0.08 Hz, STO tuned to 10/2/0.4 Hz, V_{inj} = 0.3V, f_c = 2 kHz

Figure A.78 – Experimental closed-loop rotating feedback with resistance decoupling.

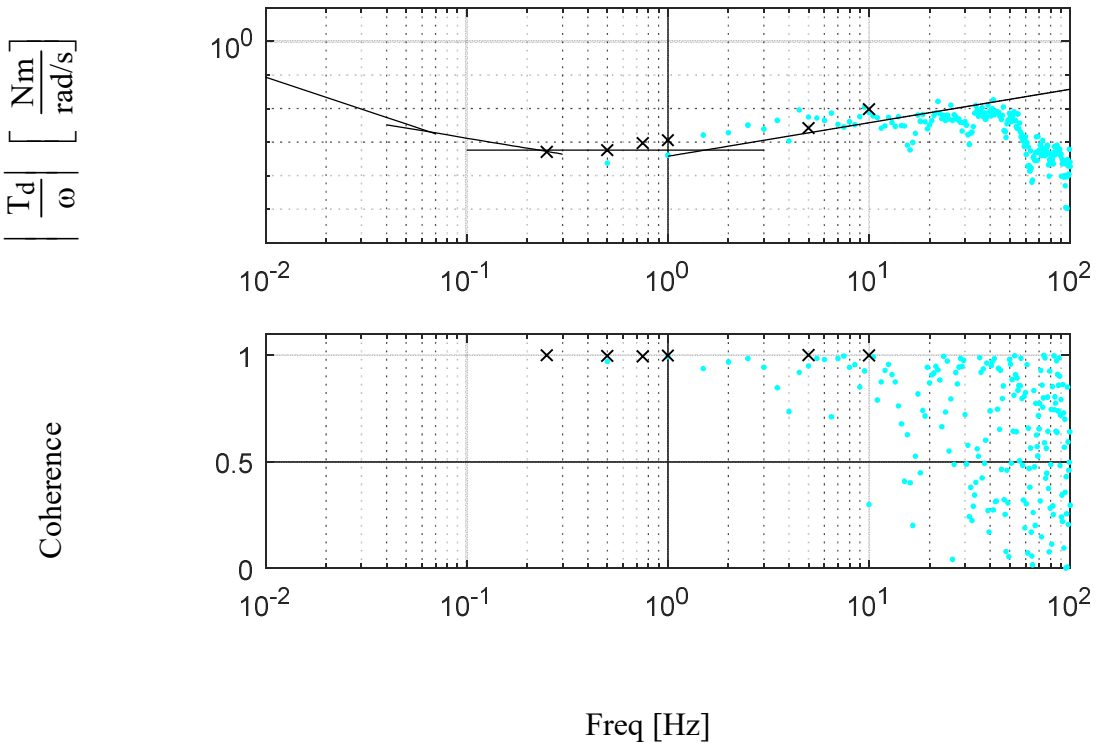

Dynamic stiffness from: Chirp FRF, Single Sine Test

MC tuned to 2/0.4/0.08 Hz, STO tuned to 10/2/0.4 Hz, V_{inj} = 0.3V, f_c = 2 kHz
T_d* chirp with f_0 = 1Hz, f_1 = 100Hz, T = 0.5s, magnitude 0.2PU
Overlaid asymptotes with J_p = 60 μNm, B_o+B_p = 0.8mNm/rad/s, K_a = 0.0033 Nm/rad, K_{sa} = 0.0027 Nms/rad.

Figure A.79 – Dynamic stiffness FRF with rotating self-sensing feedback.

A.13 Summary

This chapter described the electrical and mechanical models used throughout this work as well as documents methods used for parameter estimation of the bench. Sections describing the control methods, their design, and their evaluation were presented. The end of the chapter discusses self-sensing implementations, non-ideal effects, compensation strategies, and performance evaluation. Each section describes the estimation and tuning methods used in this work. The simulation and code used in this work is documented and any specific considerations and implementation details are documented.

Appendix B Control Structure Design and Implementation for Image Tracking

B.1 Introduction

A dynamometer bench to evaluate self-sensing on an SPMSM was developed as part of this project. The 3.7kW test machine, shown on the left in Figure B.1a, was specially designed to have a small saliency which is minimally dependent on load and was designed and the machine characteristics evaluated in [46, 47, 115].

a) b)

Figure B.1 – a) dynamometer with 3.7kW SPMSM test machine on left as designed in [115], with a 7.5kW SPMSM load machine on the right, b) underneath the shield are the couplers and a torque transducer.

Previous machine evaluating used other standalone power racks developed for other projects and based on the AIX controller. As part of this project was the evaluation of image tracking technologies and evaluation of the required computation in section 3.5 showed the AIX-

based system was incapable of performing the required computations, a new power rack was developed. This rack is shown in Figure B.2 features the inverters for both systems on the middle shelf, as well as a regenerative unit and EMI filter on the bottom shelf, finally a dSPACE MicroLabBox was chosen as the controller platform for its computation ability and ease of use.

Figure B.2 – Power rack based on two Delta C2000 inverters, a dSPACE MicroLabBox Controller, and accompanying hardware including a regenerative unit.

A number of connection boards were developed and integrated into this project. The C2000 inverters typically have a commercial control board for use driving a motor. As much of this project involves custom code a separate controller was required and so boards were designed to convert the control and sensor signals into usable signals by the external controllers. In Figure B.3a the C2000 inverter with the commercial controller removed is shown. In Figure B.3b the interface initially designed for use with the AIX controller is shown. However, as the project

continued the computational limitations of the AIX were evaluated and a new dSPACE MicroLabBox was procured. Signal levels and logic were either compatible between the two systems, or were configurable within the dSPACE MicroLabBox controller. However, a signal routing board was required to convert the output into dsub-50 package and coax cables suitable for sampling by the MicroLabBox. The interface board is shown in Figure B.3c, while the top of the MicroLabBox showing the connections is shown in Figure B.3d.

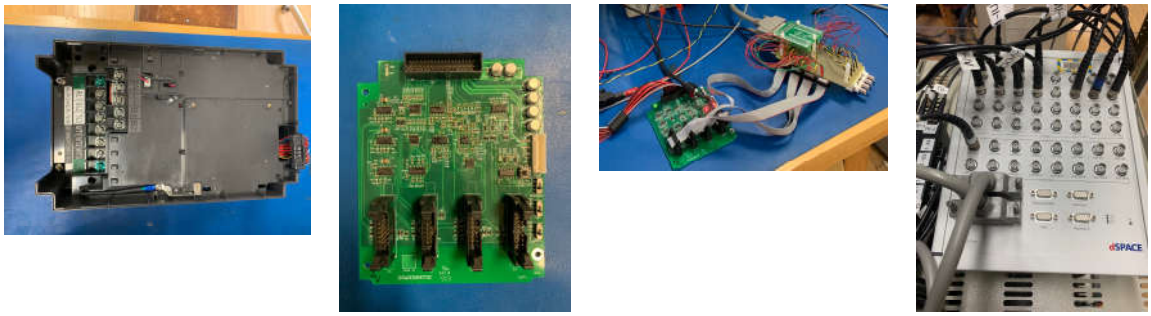

a) b) c) d)

Figure B.3 – a) C2000 inverter with commercial controller removed, b) interface board to connect C2000 to AIX controller, c) interface board to connect interface board from b) to the MicroLabBox Controller, d) MicroLabBox controller

B.2 Parameter Estimation

Parameter estimation follows the analytical process developed in section A.2

B.2.1 Dead-time Compensation

The first step toward developing the system is the analysis and compensation of dead-time effects. These effects are present to prevent the inverter from short circuiting during a switching event, and add a small amount of time where both switches within an inverter leg are closed. This section uses the process developed in [36, 37] to measure the dead-time effects by opening one phase of the motor, and then commanding a sinusoidal current across the other two

phases. The results of this are shown in Figure B.4a. Here the estimated voltage is calculated from the sensed current and estimated resistance as shown in (0.137), additionally the voltage commanded by the PI controller is shown. It is clear to see the two voltage signals do not overlap. The result of this is that if commanded voltage is used in further analytical steps in place of the actual voltage the calculations will contain errors. Additionally, in high frequency signal injection based self-sensing methods, the current response to a voltage command is used to determine position. If the actual applied voltage significantly differs from the commanded voltage, the resulting position estimates will contain associated error.

$$V_{uv}(t) = 2R_sI_{uv}(t) \tag{0.137}$$

$$d_{comp}(t) = \frac{V^*_{uv} - 2R_sI_{uv}(t)}{2V_{dc}(t)} \tag{0.138}$$

Using the equation in (0.138) a compensation can be developed which relates the commanded voltage with the voltage estimated from the current sensors. This results in a current dependent compensation as is shown in Figure B.5. Here a piecewise function is used where the high magnitude current regions should be the dead-time to sample time ratio, and the region near zero current is approximated with a linear relationship as the switches contain numerous secondary effects in this region.

The results of applying dead-time compensation are shown in Figure B.4b where now the commanded and measured voltages overlap. Noise on the measured voltage is a result of noise on the current sensors being amplified here, this effect is mitigated later in B.2.4 with a higher accuracy current sensor.

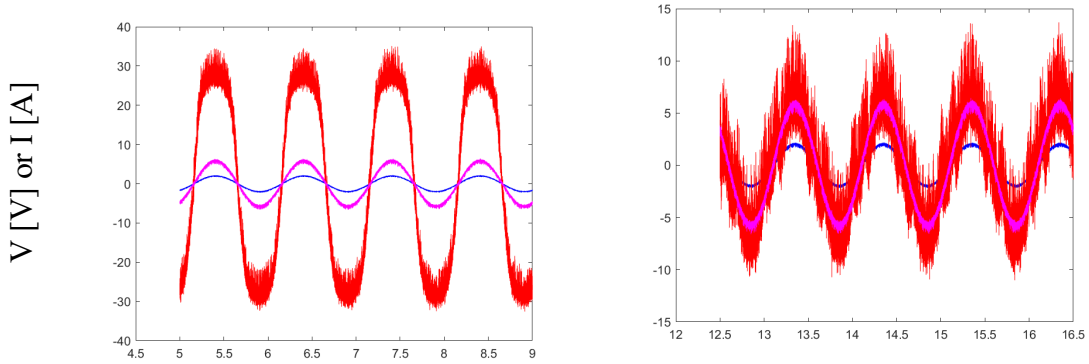

a) b)

$I^*_{uv} = 6\sin(2\pi)$, I_{uv}, V_{uv}, V_{uv}*

Figure B.4 – Voltage and current waveforms across phases u-v, with phase w open. a) No DTC applied. B) After DTC applied

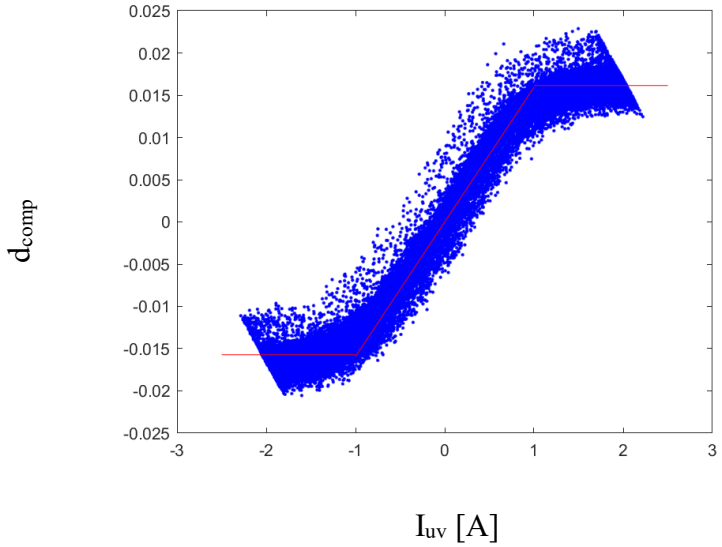

$I^*_{uv} = 6\sin(2\pi)$, Experimental, Piecewise DTC Fit

Figure B.5 – Estimated dead-time compensation as a function of current.

B.2.2 Electrical Parameter Estimation

Electrical parameter estimation follows the process outlined in section A.2.4 . The first test applied is to evaluate the offsets between the encoder and the synchronous reference frame. From the model developed in A.2.1 the back-EMF should appear solely along the q-axis. As such commanding zero d-axis current should result in zero d-axis voltage being applied. If the reference frames are misaligned a voltage will appear along the d-axis command to negate it. This can be used to tune the encoder offset as when they're fully aligned the effect will disappear. This process is shown in Figure B.6 for varied encoder offsets with the properly tuned value averaging to 0.

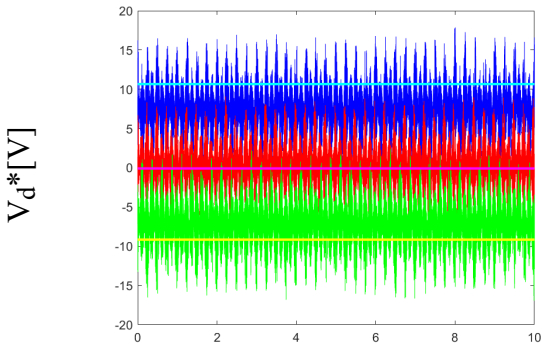

Figure B.6 – Voltage command resulting from the synchronous frame PI current regulator, when zero current is applied, and the machine is spun at a 2π rad/s with varied encoder-to-electrical position offsets.

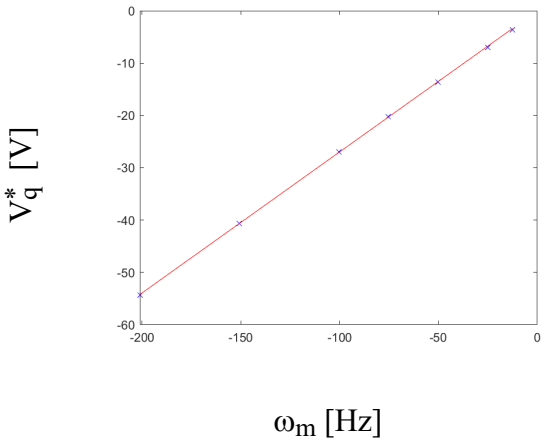

Figure B.7 – Estimation of λ_{pm} is done by relating the speed and voltage through equation (0.7) with estimated λ_{pm} of 0.2697 Wb overlaid for comparison.

Next the back-EMF can be estimated by realizing the back-EMF appears along the q-axis and is proportional to speed. By commanding zero current and observing the amount of q-axis voltage which is required to maintain this at different operating speeds the back-EMF can be calculated as in Figure B.7. A linear fit is applied which agrees well with the data points collected at several operating points.

Finally, the d- and q-axis impedences must be measured. This is done by holding the machine at zero speed with the load machine while applying a rotating chirp voltage. Observing the current and computing a frequency response function along each axis as is shown in Figure B.8 and Figure B.9 allows for asymptotes to be added which estimate the resistance and inductance. As each axis acts like a RL circuit, the low frequency portion is the conductance which can be inverted to find the resistance of the circuit. The two axes share the same resistance which can be used as a sanity check. The high frequency portion of Figure B.8 and Figure B.9 is the reluctance of the machine times 1/s resulting in a 1 decade per decade drop with zero-crossing relative to the reluctance. By fitting an asymptote to the high frequency data and inverting it, each axes' inductance can be found.

The values calculated in this section are summarized in Table B.1 and are shown with their nominal design parameters.

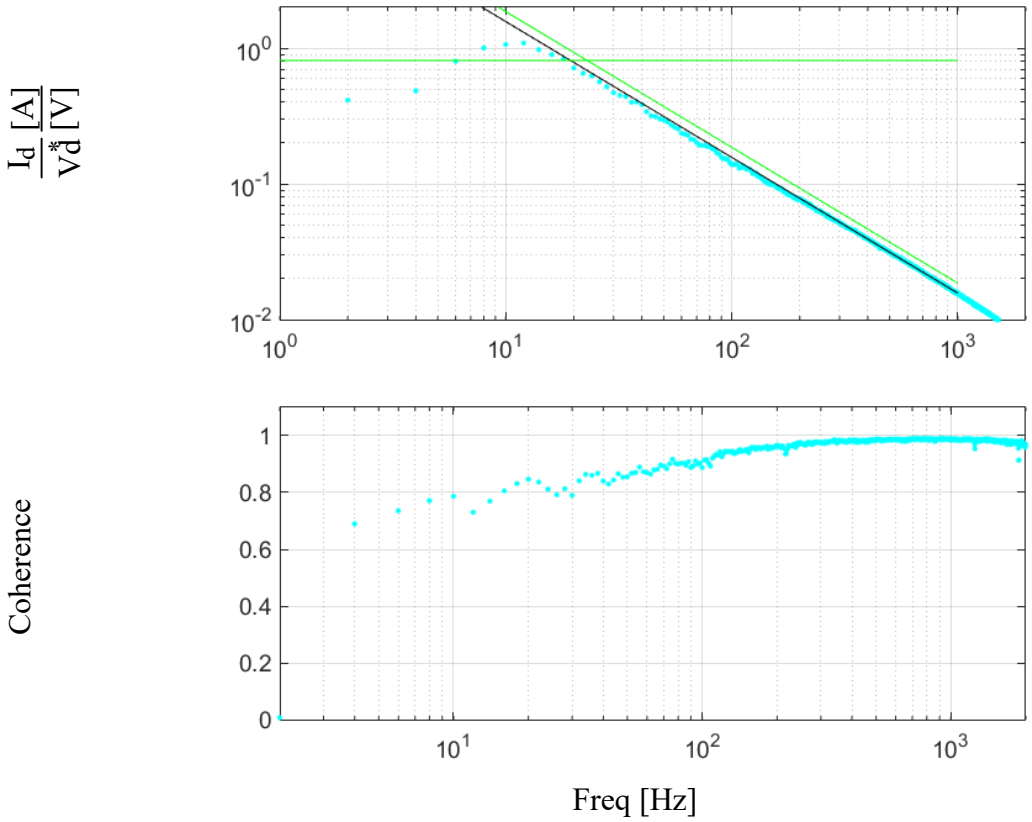

Inductance estimation FRF, Estimated Asymptotes, Datasheet Asymptotes
$\omega_m^* = 0$, V_{dq}^* chirp signal with f_0=1Hz, f_1=1kHz, T=5s, magnitude 10V
$R_s = 1.92\Omega$, $L_d = 10.8$mH

Figure B.8 – Estimation of d-axis parameters on test machine.

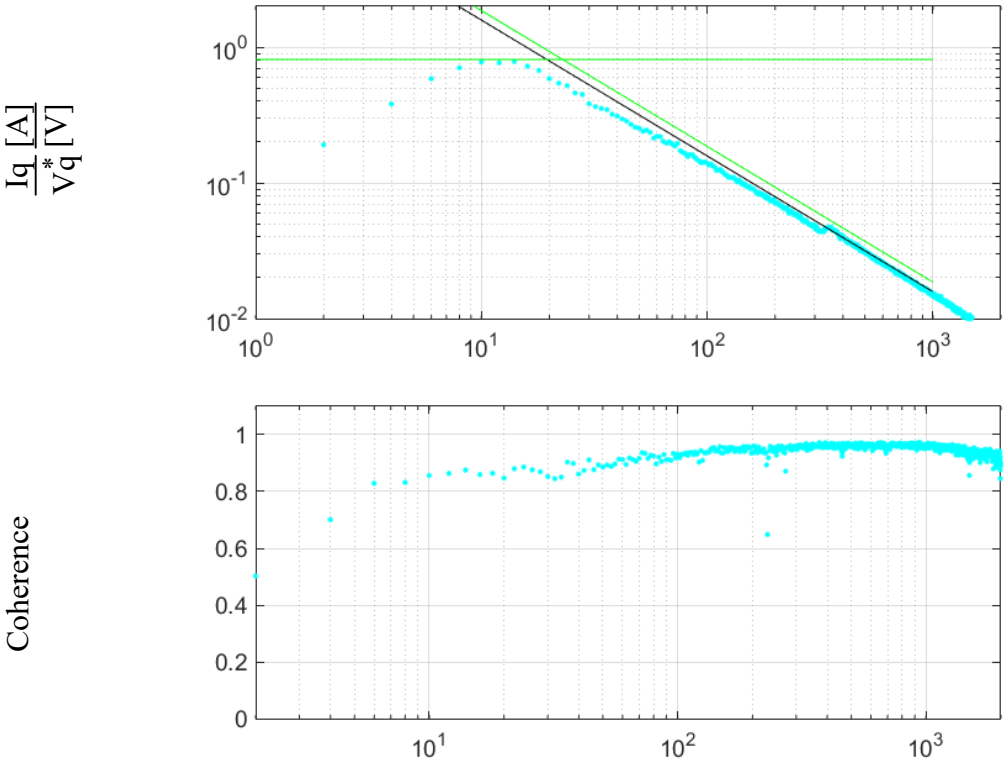

Inductance estimation FRF, Estimated Asymptotes, Datasheet Asymptotes
$\omega_m^* = 0$, V_{dq}^* chirp signal with f_0=1Hz, f_1=1kHz, T=5s, magnitude 10V
$R_s = 1.92\Omega$, $L_d = 10.8$mH

Figure B.9 – Estimation of q-axis parameters on test machine.

Table B.1 – Electrical Parameter Estimates

Parameter	Nominal From [115]	Obtained Experimentally
λ_{pm} [Wb]	0.2386	0.2697
L_d [mH]	7.8	10.9
L_q [mH]	9.9	10.8
R_s [Ω]	1.258	1.92

B.2.3 Mechanical Parameter Estimation

Mechanical estimation is done using the flag plot method described in A.2.6 . The parameters can be estimated directly from the raw data and can be further tuned by applying command feed-forward to null the components individually. The effects of adding friction, damping, and inertia terms respectively are shown in Figure B.10. Resulting parameter estimates along with their nominal values are shown in Table B.2. Note that datasheet values for the assembled bench are not available. However, datasheet values for the test and load machine are given for reference in Table B.2. The inertia measured here is the full system inertia which is expected to be higher as a result of the torque transducer, shaft, and two couplers on the dynamometer.

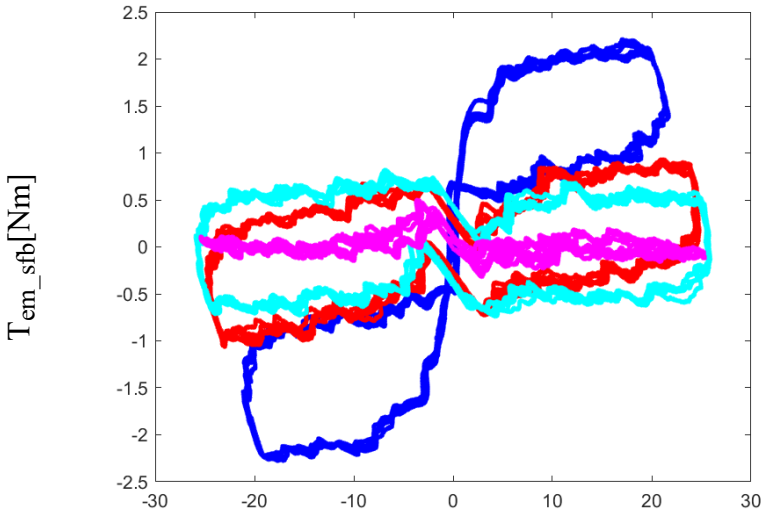

Torque from: Filtered Raw Data, Model (0.27), Model (0.28), Model (0.29)
$|\omega_m^*|$ = 8p Rad/s, alternating direction every 2s

Figure B.10 – Flag plot used to estimate mechanical parameters.

Table B.2 – Mechanical Parameter Estimation.

	Nominal from [115]	Estimated Value
J_p [mNs^2/rad]	13 (test), 18 (load)	5.58
B_p [Ns/rad]	-	0.0091
T_μ [N]	-	0.5526

B.2.4 Current Sensor Characterization

The current sensors must be characterized to verify the datasheet scaling as well as remove any DC bias from the circuitry. The DC bias is easily removed at runtime by collecting a short duration of current sensor data with the system idle, averaging the resulting value on each sensor, and subsequently subtracting that DC value from all measurements with that sensor. The scaling value requires an external sensor with known properties to validate the scaling expected by the data sheet. This was done by commanding a sinusoidal current of 5A, using a set of high accuracy current probes, overlaying the current sensor output with the current probe output, and adjusting the scaling until they match. The resulting values are shown in Table B.3 for the C2000 sensors.

Throughout the initial testing, significant noise from the current sensors or perhaps system noise coupling with the current sensors was identified. These effects can be seen in Figure B.12 with d-axis and q-axis spikes with magnitudes as high as 1.2A. In this project, with a 50V high frequency injection, the current response is expected to be less than 30mA. This magnitude of noise would prevent the self-sensing algorithms from enjoying a large enough SNR and so an additional set of sensors were added to the system. A simple board was developed and shown in Figure B.11 based on the LEM LA 55-p sensors. Initially 2 turns were used, this was later extended to ten turns to fully fill the window space of the sensor and improve the accuracy as far as possible. In Figure B.12 the results of the 2-turn LA 55-p board are overlaid and it is clear to see that the high frequency noise is minimized.

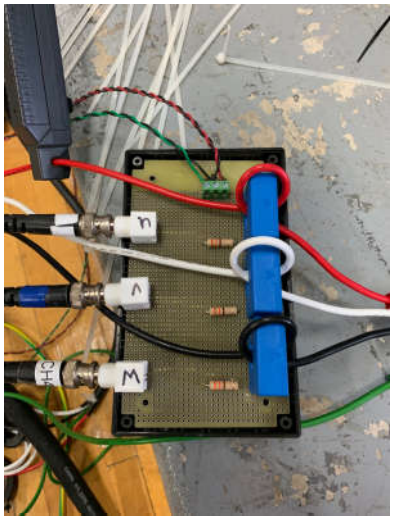

a)

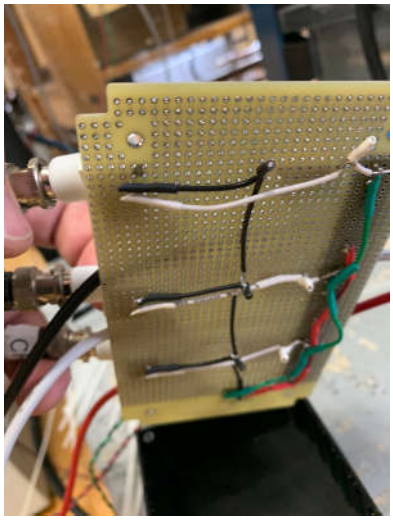

b)

Figure B.11 – Current sensor board to integrate LEM LA 55-P sensors for higher accuracy results.

Table B.3 – Current sensor characterization using C2000 sensors.

Machine/Phase	u	v	w
Gain from Spec Sheet/Turns	6.36	6.36	6.36
Tuned Gain	6.80	6.30	6.94

Table B.4 – Current sensor characterization using LEM LA 55-P sensors with 10 turns.

Machine/Phase	u	v	w
Gain from Spec Sheet/Turns	3.03	3.03	3.03
Tuned Gain	3.12	3.17	3.13

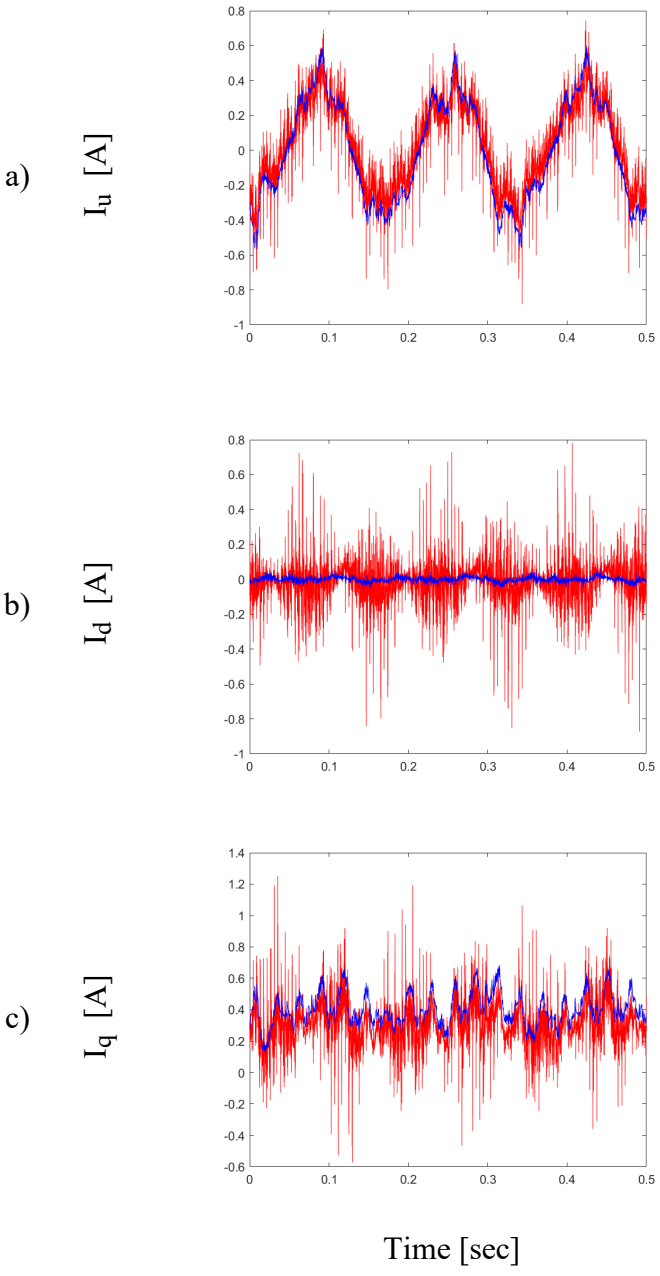

Figure B.12 – a) Raw current sensor output when zero voltage is commanded, b) and c) are the d- and q-axis currents respectively.

B.3 Current Regulation

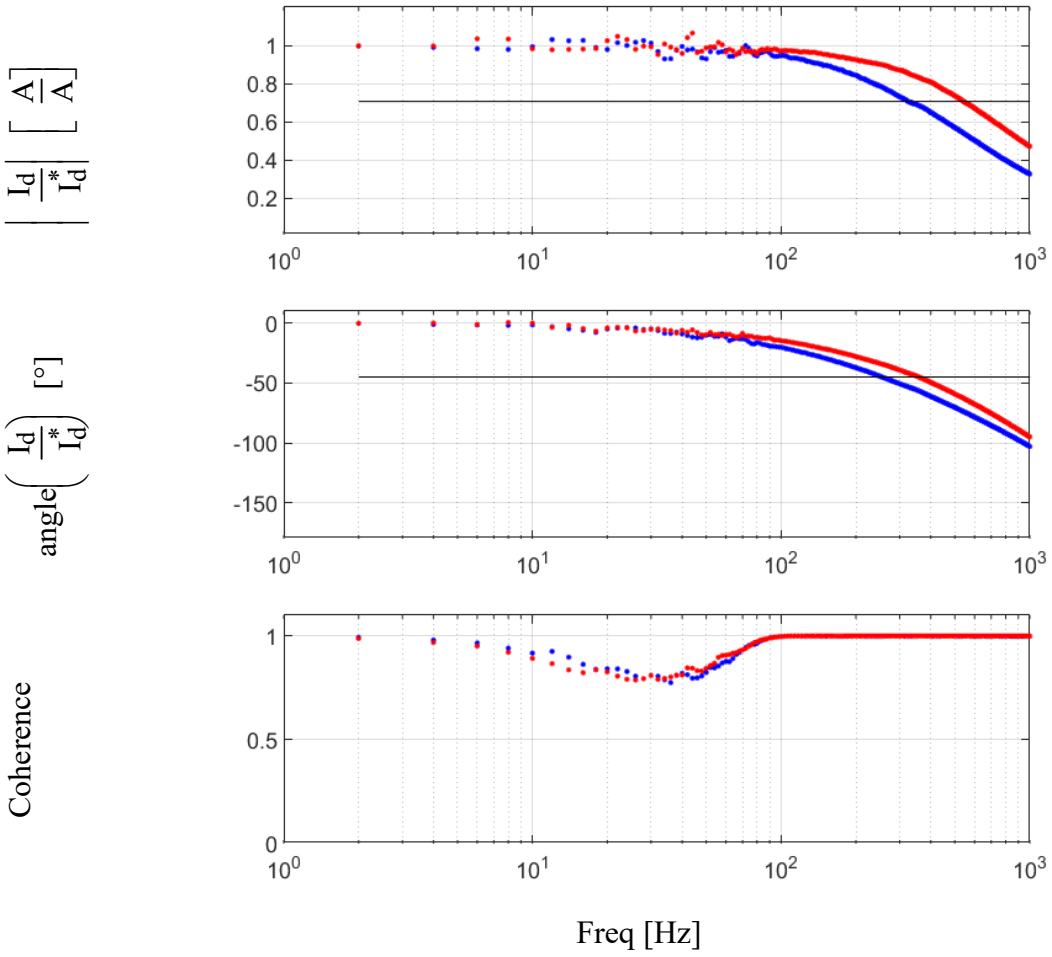

Command Tracking tuned to 500Hz using $0.7*\hat{L}$, $1*\hat{L}$
I_{dq}* chirp applied with f_0=1 Hz, f_1=1 kHz, T=5s, Magnitude = 1A

Figure B.13 – Experimental d-axis command tracking FRF.

The current regulator was created using the theory presented in section A.3 Frequency response plots of the current regulator response are shown in Figure B.13 and Figure B.14 for the d- and q-axis respectively. The d-axis when tuned to 500Hz achieves a bandwidth of 540Hz based on the angle and magnitude criteria of the FRF in Figure B.13. The q-axis however shows a higher order response in Figure B.14 as seen by the flattening of the response around 200Hz

before it resumes the expected decrease at high frequency. A value of $0.7L_q$ was required to achieve a bandwidth of 485Hz. This probably indicates a saturation effect in the machine as numerous saturation and cross-saturation properties were designed into the machine to generate the relatively stable saliency across the full operating space.

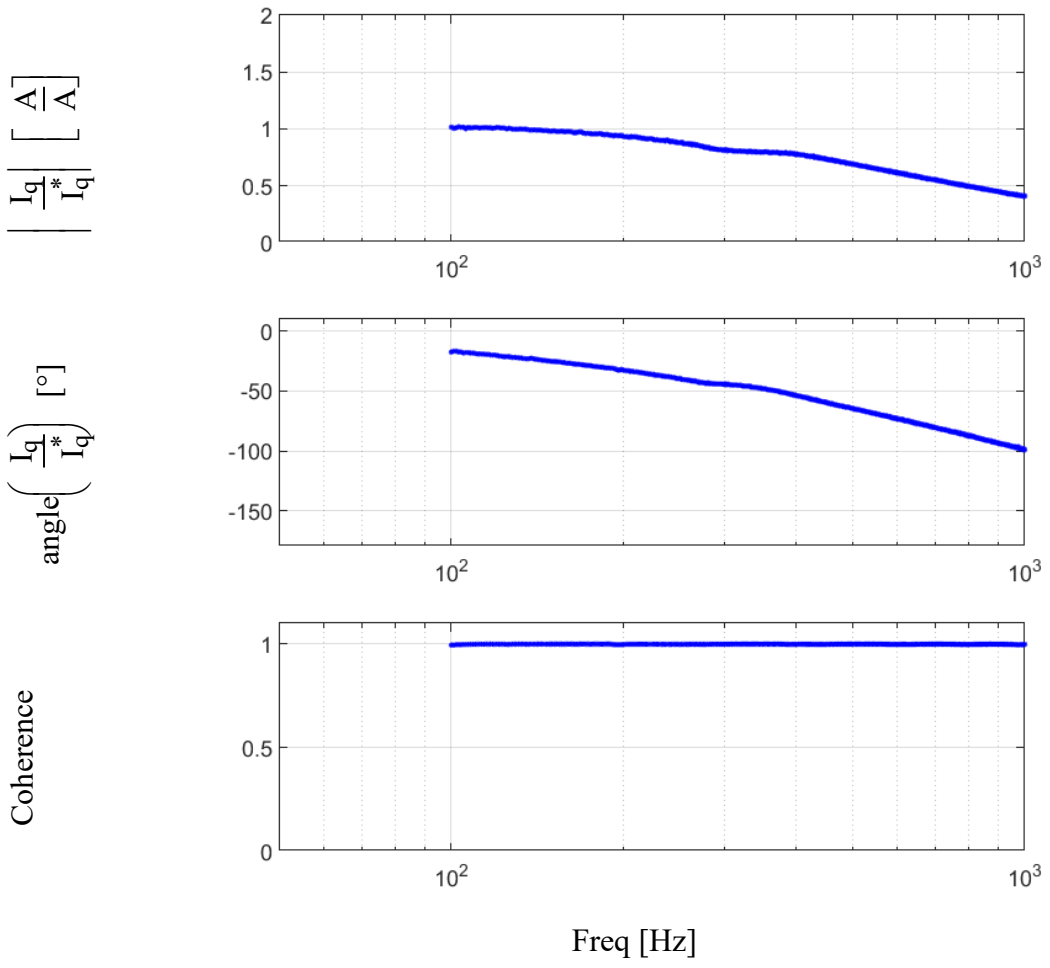

Command Tracking tuned to 500Hz using $0.7*\hat{L}$
I_{dq}* chirp applied with f_0=1 Hz, f_1=1 kHz, T=5s, Magnitude = 1A

Figure B.14 – Experimental d-axis command tracking FRF.

B.4 Motion Control

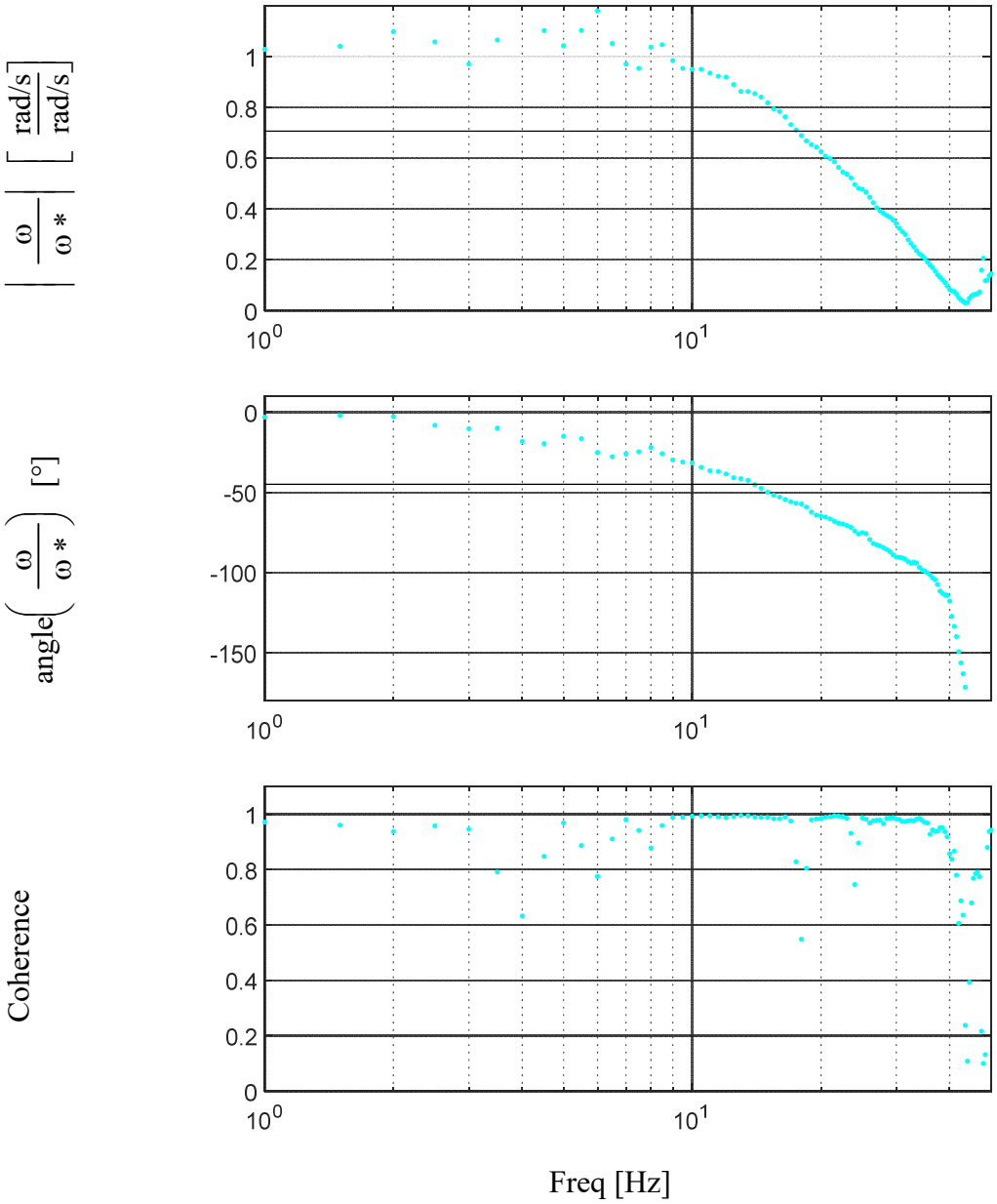

ω_m* chirp with f_0 = 1Hz, f_1= 400Hz, magnitude 0.8Hz, offset 1Hz

Figure B.15 – Command tracking FRF of a motion controller tuned to 20Hz.

The motion controller was designed using the theory presented in section A.4 In Figure B.15 the command tracking frequency response is shown for the controller without command feed-forward so that the eiganvalues can be evaluated. Here a tuning of 20Hz results in an achieved bandwidth of 18Hz. Next a dynamic stiffness frequency response plot is shown in Figure B.16 with overlaid asymptotes at the specified tuned values. In Figure B.16 the 50Hz tuning is confirmed with good agreement between the expected asymptotes and the experimental data.

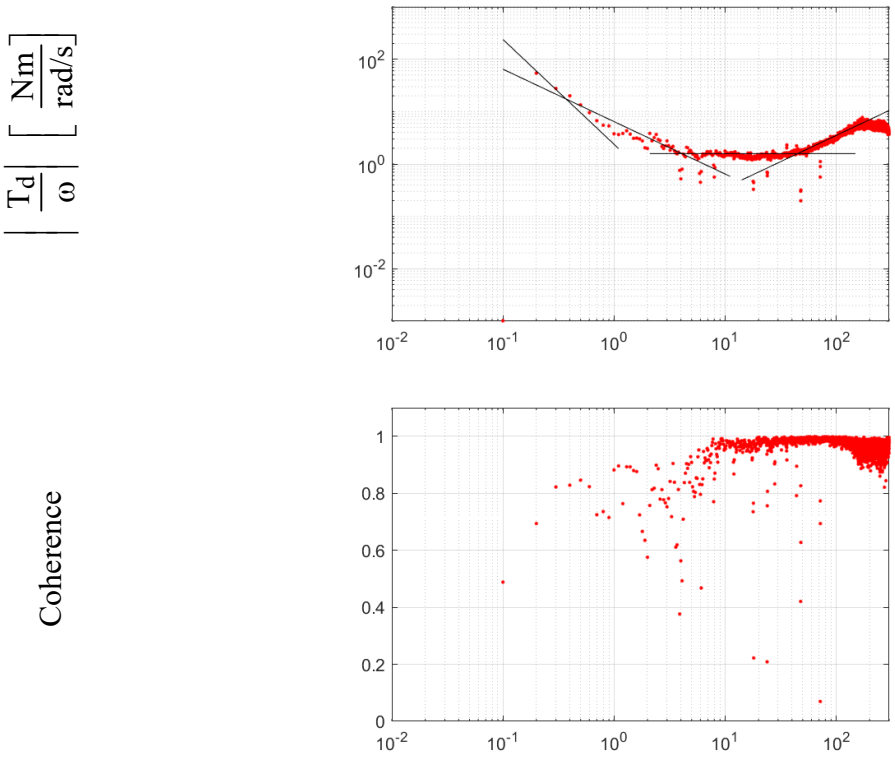

T_d* chirp with f_0 = 1Hz, f_1= 400Hz, magnitude 0.2PU
Overlaid asymptotes: J_p = 5.58 mNm, B_o+B_p = 0.92Nm/rad/s, K_a = 36.3 Nm/rad, K_{sa} = 112.9 Nms/rad

Figure B.16 – Dynamic stiffness FRF of a motion controller tuned to 50Hz

B.5 Current Separation

Current separation follows the same development as in section A.9 as first shown in Figure A.53 but copied to Figure B.17 for convenience with overlaid experimental current spectrum. The process uses a low bandwidth current observer to estimate the fundamental current. This fundamental current is subtracted from the total current, with the remainder being the high frequency components. Note that the fundamental component is mostly removed from

the high frequency component, but that portions remain near the fundamental which are similar amplitude to the negative sequence component. The high frequency current is passed through a high-pass filter which is synchronous to the positive carrier reference frame. As the positive carrier is well known with no variation it is effectively removed. The filtered result is passed through a negative carrier synchronous high-pass filter to remove the rest of the expected high frequency current response. This signal is used as a feedback to the current observer. Additionally it is added to the estimated fundamental to form the fundamental plus error signal which is suitable for use as a feedback signal to the current regulator. This form removes the high frequency components from the current regulator's path which allows the current regulator to be tuned to a higher bandwidth without reacting to and trying to compensate for the high frequency component.

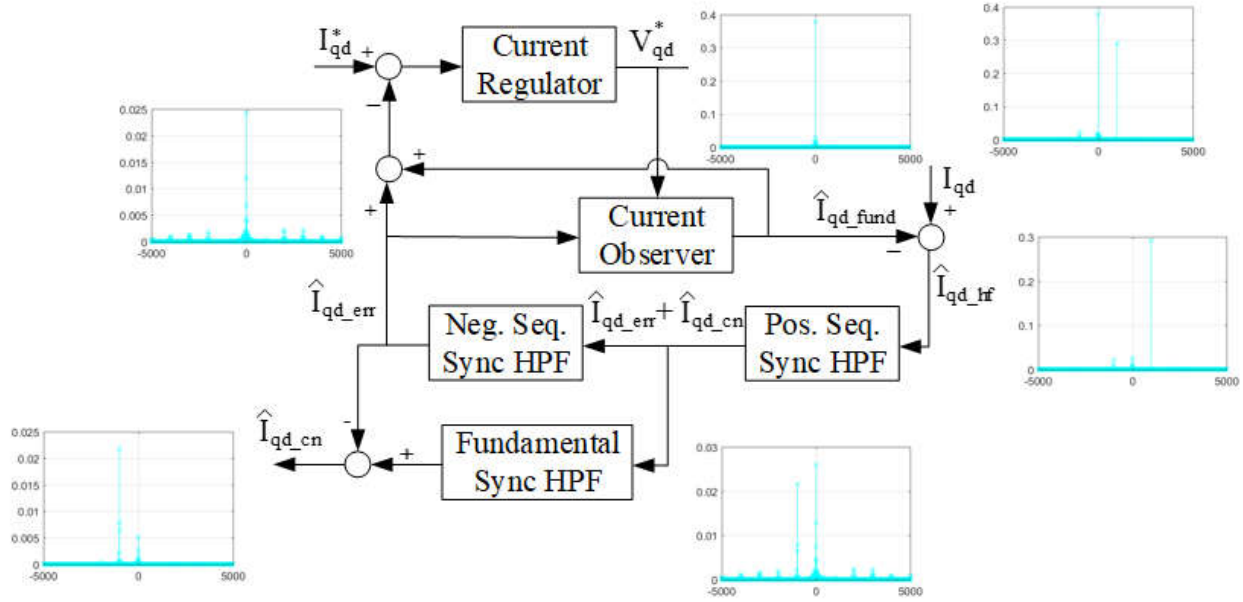

Figure B.17 – State block diagram from Figure A.53 with overlaid current frequency spectrum in hertz at each step showing the amplitude in Amperes.

It should be noted that the filtered high frequency current response has a fundamental synchronous high-pass filter applied to remove additional content from the high frequency component. However, even in the processed high frequency current response there is still

content near the fundamental of about one fourth the magnitude of the negative sequence. When this current is transformed to the negative carrier reference frame it appears as substantial magnitude high frequency content. To mitigate this, additional frequency synchronous high-pass filters were applied at harmonics near the fundamental. This effectively mitigates the remaining fundamental current, however care must be taken to ensure the high-pass filters applied near the fundamental are sufficiently low bandwidth so as not to interact with the current content near the negative sequence.

B.6 Pulsating Voltage HFI Self-Sensing

Pulsating voltage injection into the estimated synchronous reference frame with associated demodulation scheme was developed following the process outlined in section A.10 In Figure B.18 the time domain estimation accuracy is shown when the system is using the position estimate generated by the pulsating demodulation as feedback. The system is shown to be stable and track at steady state, however substantial electrical error offset is seen of 9 degrees, and an additional second harmonic can be observed with a magnitude of 6 degrees. This is further confirmed in the FFT of the error signal, shown in Figure B.19.

The source of this error is investigated in section B.6.1

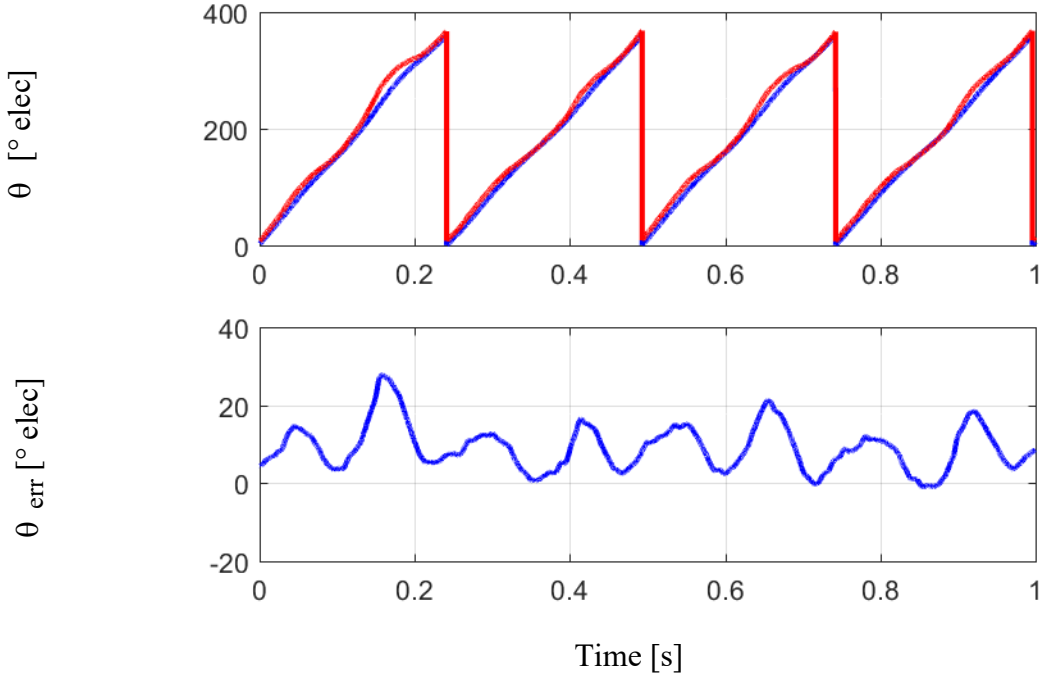

ω_m^*= 2π rad/s, MC tuned to 5Hz, $|V_{inj}|$ = 50V, V_c = 1 kHz, T_l = 0 Nm

Figure B.18 – Experimental closed-loop pulsating feedback.

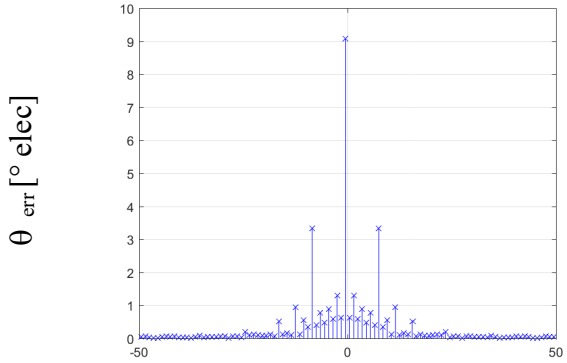

ω* = 2π [rad/s], T_{load} = 0 [Nm] V_c = 50V, f_c = 1 kHz.

Figure B.19 – FFT of the error of pulsating in steady-state.

B.6.1 Mechanical Disturbance Analysis and Characterization of Dynamometer

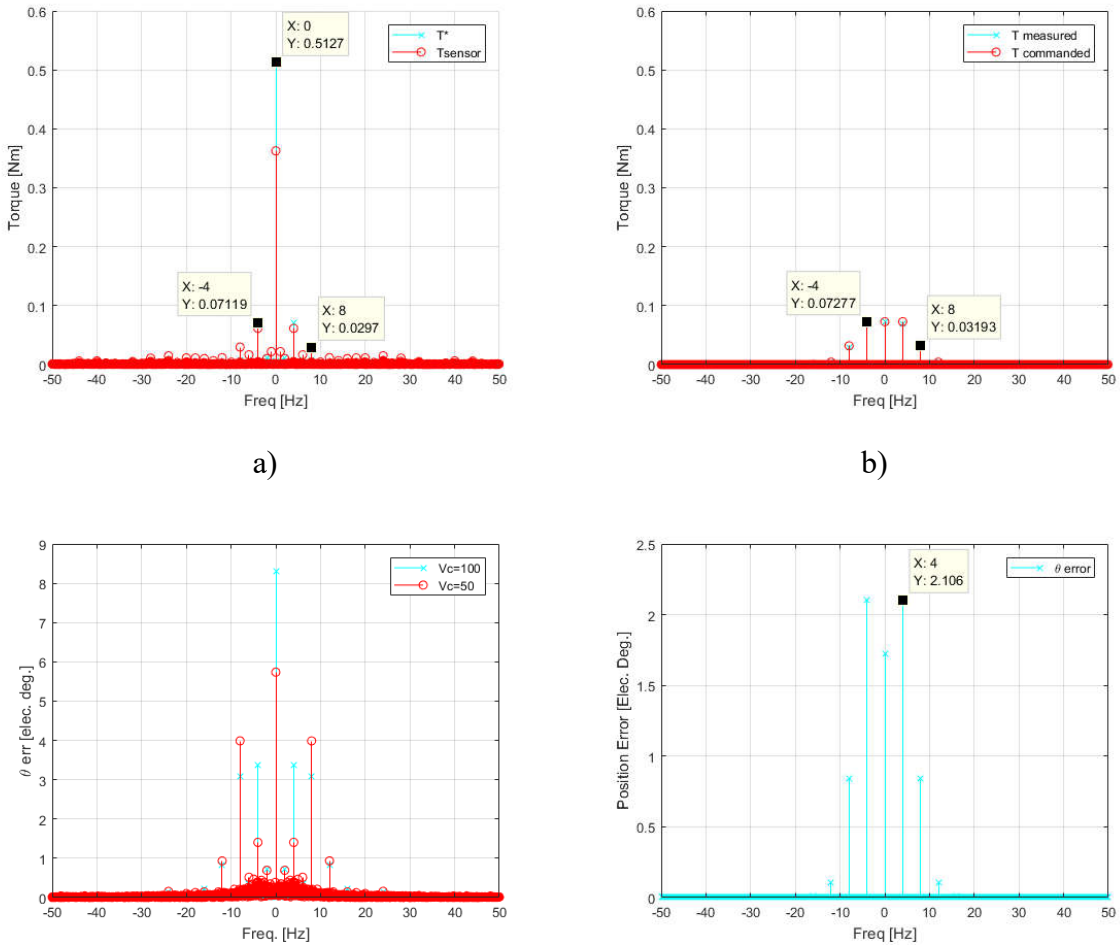

ω_m*= 2π rad/s, MC tuned to 5Hz, $|V_{inj}|$ = 50V, V_c = 1 kHz, T_l = 0 Nm

Figure B.20 – Dynamometer torque ripple analysis. a) measured torque from estimated by command and torque transducer using encoder feedback, b) simulation with commanded and measured disturbance torque added using position feedback, c) estimation error when using self-sensing feedback with varied injection size, d) simulated estimation error when using self-sensing feedback.

It should however be noted that error similar to the steady-state pulsating voltage self-sensing presented in section B.6 is seen in rotating voltage self-sensing as documented in B.7 and in the flux injection self-sensing method documented in [115]. In the flux injection method

a different power stack, controller, and control code were used. This isolates out the effects of inverter, controller, and control code bugs leaving machine and dynamoter effects to be investigated. Several of these effects are explored in Figure B.20 in experimental data in a) and c), and in simulation b) and d). In a) the torque from the torque transducer as well as the estimated disturbance torque from the motion controller are overlaid. These in general agree except at DC content. The discrepancy is caused by the location of the measurement relative to the friction where the transducer is in the center of the dyne and so measures less friction than the machine.

As the interest is in the harmonic content and not the DC component, the static friction is neglected for simulation. In Figure B.20b the harmonics are characterized in both magnitude and phase and applied as a disturbance. Figure B.20a and Figure B.20b show agreement in the harmonic frequency content present, which allows the impact on the self-sensing to be analyzed. In Figure B.20c and Figure B.20d the errors associated with pulsating estimation accuracy are shown. It is shown in simulation that the first harmonic has a magnitude of 4° and the second harmonic has a magnitude of 2°, while in compariable experimental data the first harmonic has a magnitude of 6° while the second harmonic has a magnitude of 6°. This shows that the torque disturbance on the dynamometer causes a portion of the estimation error, but does not account for all of the error. The source of the remaining error is explored with respect to rotating voltage injection in section B.7

B.7 Rotating Voltage HFI Self-Sensing

Self-sensing using a high frequency rotating voltage in the stationary reference frame following the methods documented in section A.12 was developed for the dynamometer. Time domain estimation accuracy when the system is using self-sensing position estimates for feedback is shown in Figure B.21. Similar to the pulsating results in section B.6 and the flux

injection results in [115], the resulting error in Figure B.21 has a 10° offset with at 10° second harmonic component.

Furthermore, a negative sequence decoupling scheme based on the methods presented in section A.12.2 using the negative sequence harmonics characterized in 5.4 was developed. This method decouples the harmonic components of the negative sequence current response before applying a heterodyning demodulation. The results of this process are shown in Figure B.22. The error resulting from this method reduces the DC offset to 0° while reducing the 2nd harmonic to 5°. This is a clear benefit and shows the achievable state-of-the-art performance on this test bench.

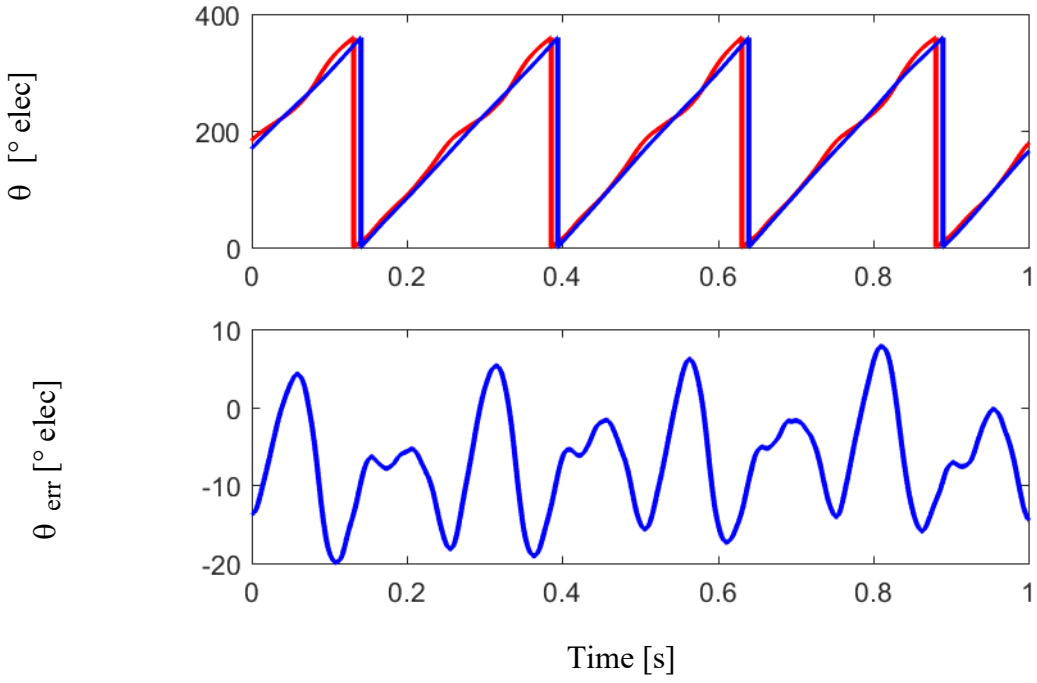

ω_m*= 2π rad/s, MC tuned to 5Hz, V_{inj} = 20V, f_c = 1 kHz, T_l = 0 Nm

Figure B.21 – Experimental closed-loop rotating feedback.

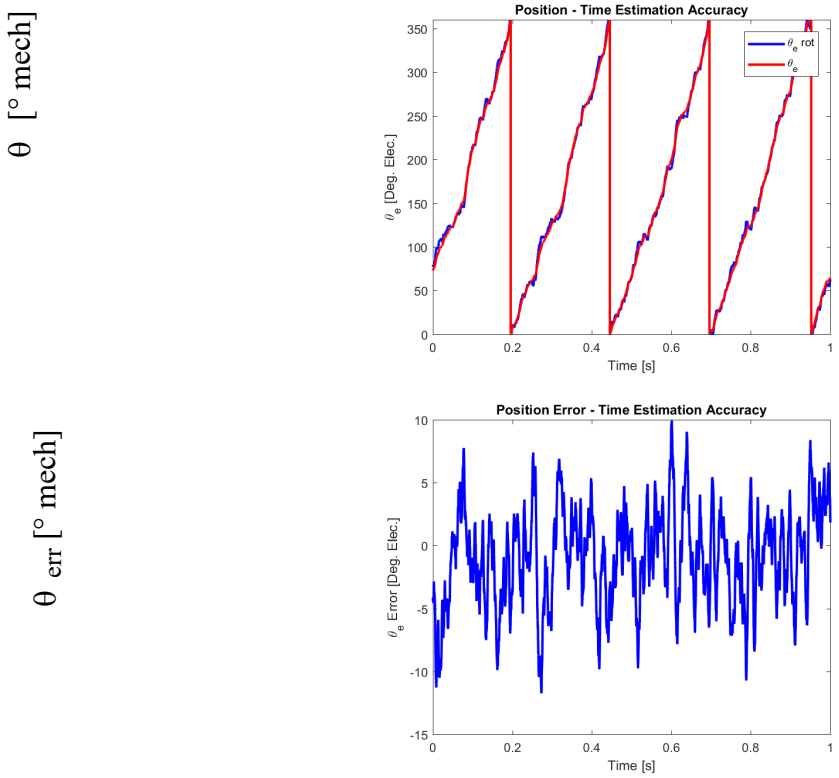

ω_m*= 2π rad/s, MC tuned to 5Hz, V_{inj} = 50V, f_c = 1 kHz, T_l = 0 Nm

Figure B.22 – Experimental closed-loop rotating feedback using negative sequence decoupling to decoupling harmonic saliencies using the method described in [60] with parameters given in Table 5.2.

B.7.1 Non-ideal Inductance Characterization

To further validate the multiple saliencies present in the machine, the load machine was used to hold the test machine at a constant position. The rotating voltage injection was then applied, and position estimates generated. Figure B.23a) shows the results over the full electric cycle with a -17° offset and 12° second harmonic component. Additionally, dead-time compensation is varied to evaluate the effects. As can be seen, dead-time compensation methods

have a large impact on the DC offset of the resulting position error, however the magnitude and phase of the second harmonic component is unchanged between tests. This further verifies that it is a spatial phenomena and not a speed or inverter dependent effect. In Figure B.23, selected positions are shown and plotted over the first 4.5s of each test to verify that the rotor is in fact stationary over the course of these tests and that no additional motion based effects are present.

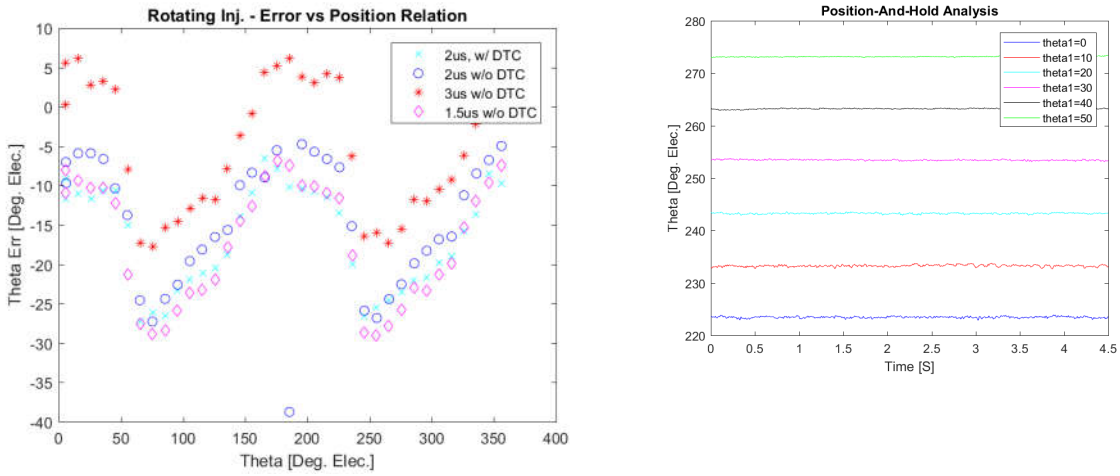

a) b)

ω_m*= 2π rad/s, MC tuned to 5Hz, V_{inj} = 20V, f_c = 1 kHz

Figure B.23 – Error spatial analysis using a rotating voltage injection with the load machine holding position. a) shows the error as a function of position with varied dead-time compensation schemes, b) shows the held position over the first few seconds of the experiment at selected positions.

Finally, the current response with with appropriate DTC at each held position is plotted in the negative carrier polar plane. This results in a figure similar to the templates generated in section 5.4 and verifies the presence of multiple inductance saliencies.

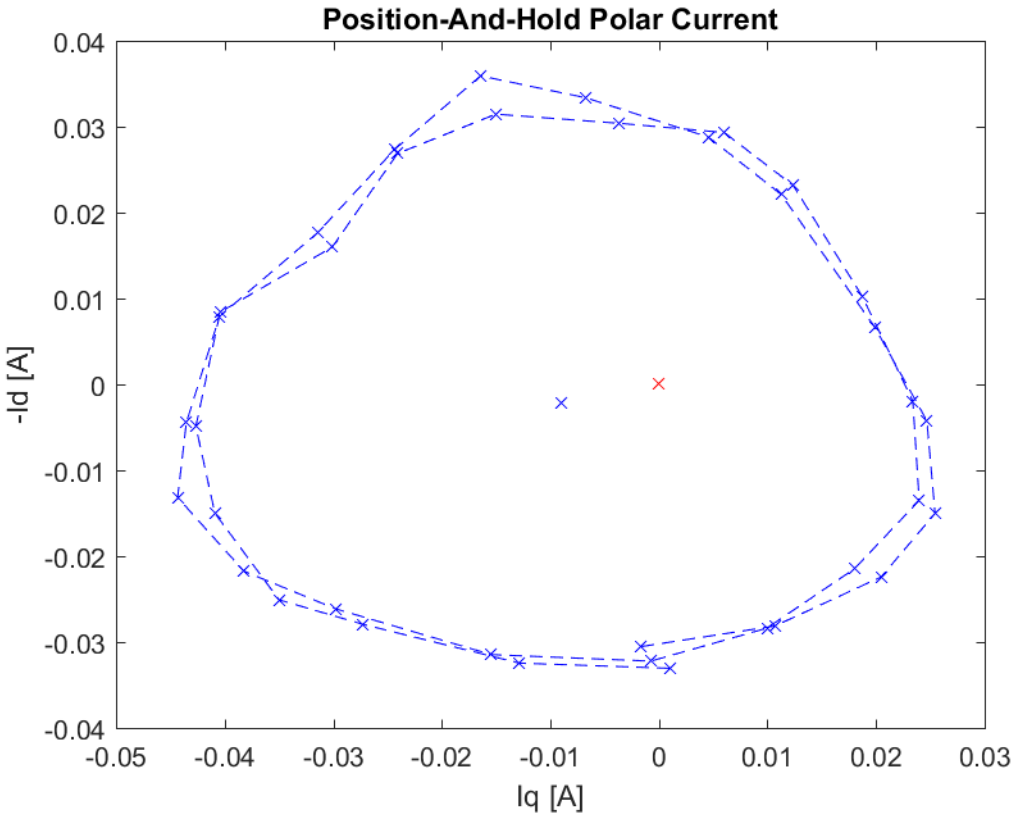

ω_m*= 2π rad/s, MC tuned to 5Hz, V_{inj} = 50V, f_c = 1 kHz

Figure B.24 – Spatial synchronously averaged current across a single electrical cycle when the position was held constant using the load machine.

B.7.2 Mechanical Disturbance Analysis and Characterization of Individual Motor

To further evaluate the machine, without the torque disturbance effects evaluated in section B.6.1 the machine was disconnected from the dynamometer and evaluated as a standalone machine. This prevents full system control of the torque and speed simultaneously, but removes any torque disturbances caused by couplers, the torque tranducer, or the load machine.

In Figure B.25 four tests with the same settings were repeated. In each test the system was brought down, turned off, and restarted. Data was collected for 30 seconds. In Figure

B.25a) an FFT of the position error is shown with the ame harmonics and approximately same magnitudes appearing in each test. In Figure B.25b) the error is plotted against the position it was collected at. This clearly identifies the spatial nature of the disturbance with both the phase and magnitude being consistent between tests.

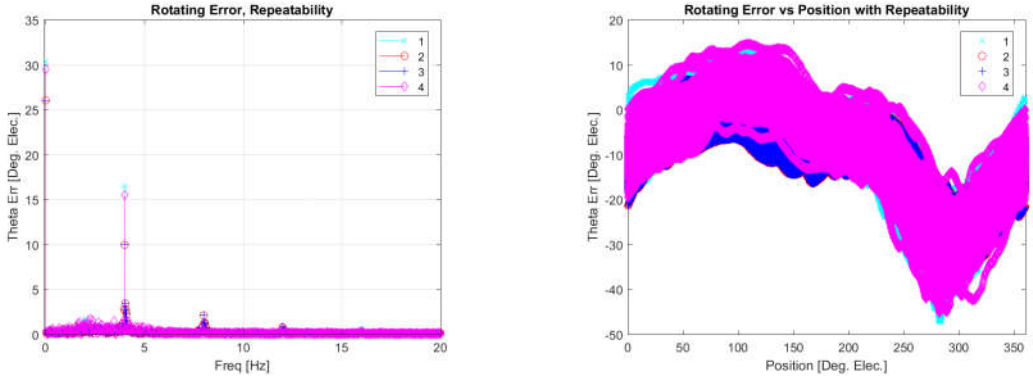

a) b)

ω_m*= 2π rad/s, MC tuned to 5Hz, V_{inj} = 20V, f_c = 1 kHz

Figure B.25 – Error spatial analysis using a rotating voltage injection with encoder feedback over four 1 minute long tests.

Next, a similar test was performed varying the speed at which the rotor was spinning was varied. In Figure B.26a the same harmonics, primarily at the second harmonic, show up within each test. It is noted that the magnitude decreases as the speed increases. This is due to the machine inertia damping the impact of the disturbances at higher speed. As with the previous test, the position error is plotted against the position in Figure B.26b. Againt the spatial phase aligns between all tests. The magnitude decreases with higher speed as was noted with the FFT in Figure B.26a.

Finally, in Figure B.27 the torque disturbance is characterized against position. This test was performed over a two hour period where the machine ran at 17Hz mechanical for the entire duration. Every 15 minutes, 30 seconds of data was collected to show the change in torque disturbance over time. The 30 seconds of data was then processed using the spatial synchronous averaging method described in section 5.4 and the number of times each position bin were

plotted, as well as the spatially averaged torque. To further isolate controller, inverter, or delay issues from mechanical issues, data was collected with the machine spinning in the positive direction in Figure B.27a, while in Figure B.27b the machine is spinning in the negative direction. In both Figure B.27a, and Figure B.27b the data is largely self-consistent. It should also be noted that the direction changes the torque disturbance. In these single-motor tests without couplers or other mechanical linkages, the few remaining moving pieces are the rotor and the bearings to keep it centered. Given that the direction of motion affects the torque disturbance this rules out things such as delays in the controller, inverter effects, and controller bugs as they are similar regardless of direction. The remaining source is likely the bearings.

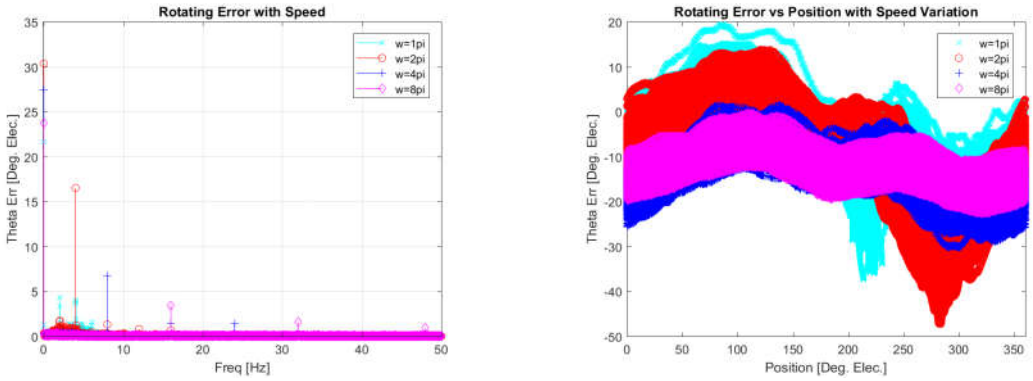

a) b)

ω_m*= 2π rad/s, MC tuned to 5Hz, V_{inj} = 20V, f_c = 1 kHz

Figure B.26 – Error spatial analysis using a rotating voltage injection with encoder feedback with mechanical speed varied speed.

There is a single test in the positive direction which varies in both phase and magnitude of the disturbance. This shows that the disturbance is spatial in nature, but can intermittently change. This effect was observed when decoupling of the spatial disturbance was attempted. Some tests would decouple very well, and a later run the decoupling would generate larger torque variations. The attempt was abandoned as the disturbance was deemed intermittent and this test confirms that observation. The best explanation for this given the single motor system is

that the bearings likely change configuration intermittently and change the phase and magnitude of the disturbances.

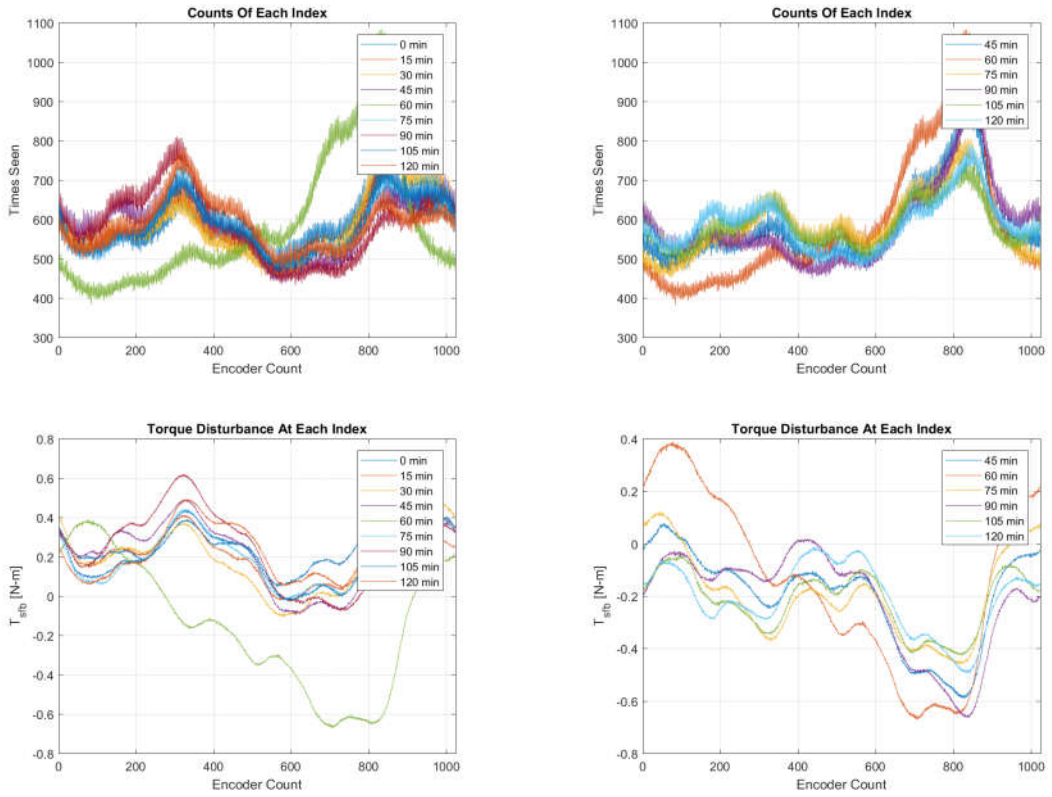

a) b)

$\omega_m^* = 2\pi$ rad/s, MC tuned to 5Hz, $V_{inj} = 50V$, $f_c = 1$ kHz

Figure B.27 – Torque disturbance analysis with system running continuous for 2 hours with periodic samples of spatial synchronously averaged torque disturbance over a 1 minute test. a) system spinning in positive direction, b) system spinning negative direction.

B.8 Summary

This chapter documents the electrical and mechanical systems through this work. Sections evaluating the parameter estimation and control methods were presented. The end of the chapter discussed self-sensing implementations and non-ideal effects of both the inductance and torque disturbances within the machine.